Mathematical morphology and statistical methods for the analysis of directional data with applications in civil engineering

Konstantin Hauch

Vom Fachbereich Mathematik
der Technischen Universität Kaiserslautern
zur Verleihung des akademischen Grades
Doktor der Naturwissenschaften
(Doctor rerum naturalium, Dr. rer. nat.)
genehmigte Dissertation

D 386

1. Gutachter:	Prof. Dr. Claudia Redenbach Technische Universität Kaiserslautern
2. Gutachter:	Dr. Jesus Angulo Lopez (HDR), Directeur de recherche Center for Mathematical Morphology, MINES Paris, PSL Research University
Datum der Disputation:	08.09.2022

TECHNISCHE UNIVERSITÄT
KAISERSLAUTERN

DEDICATED TO MY WIFE KATHRIN

Acknowledgements

I want to thank my supervisor Claudia Redenbach for her guidance and support during my research. Without her advice, this work would not have been possible. Whenever I encountered a problem or had a question about my research or writing, the door to her office was always open. Her mentoring has been essential in helping me to become a better professional.

Furthermore, I would like to thank Kasem Maryamh for giving me an exciting insight into the world of civil engineering. The joint discussions broadened my horizons in this field.

I would also like to thank my colleagues at the Technical University of Kaiserslautern and the Fraunhofer Institute for Industrial Mathematics (ITWM). I am grateful for their suggestions and support during my PhD. Thank you for the great time we spent together.

To my wife Kathrin, thank you for all the patience, understanding, support, and for motivating me to keep going in difficult times.

Contents

Introduction

We encounter directional data in numerous application areas such as astronomy, biology or engineering. Examples include the direction of arrival of cosmic rays, the direction of flight of migratory birds or the orientation of steel fibres in fibre-reinforced concrete.

In part I, we define and apply morphological operators, quantiles and depths for directional data. The morphological operators are defined for $\mathcal{S}^{d-1}$-valued images with $\mathcal{S}^{d-1} = \{x \in \mathbb{R}^d : \sqrt{x^T x} = 1\}$, $d \geq 2$. Since an ordered structure is necessary for a definition of these operators, which is not naturally given between vectors, an order is determined with the help of the theory of statistical depth functionals. This allows for defining the basic operators erosion and dilation as well as morphological (multi-scale) operators for $\mathcal{S}^{d-1}$-valued images based on them. The operators introduced are related to their grey value counterparts.

Furthermore, quantiles and the "angular Mahalanobis" depth for directional data introduced by Ley et al. (2014) are extended. The concept of Ley et al. (2014) provides useful geometric properties of the depth contours (such as convexity and rotational equivariance) and a Bahadur-type representation of the quantiles. Their concept is canonical for rotationally symmetric depth contours. However, it also produces rotationally symmetric depth contours when the underlying distribution is not rotationally symmetric. We solve this lack of flexibility for distributions with elliptical depth contours. The basic idea is to deform the elliptic contours by a diffeomorphic mapping to rotationally symmetric contours, thus reverting to the canonical case in Ley et al. (2014). Our results are confirmed by a Monte Carlo simulation study and applied to the analysis of fibre directions in fibre-reinforced concrete.

In Part II, we elaborate interdisciplinary results of statistical analysis and stochastic modelling in civil engineering. Our statistical analysis of the correlation between production parameters (fibre length, fibre diameter, fibre volume fraction as well as casting method, superplasticiser content and specimen size) of ultra-high performance fibre reinforced concrete and the fibre system (spatial arrangement and orientation of the fibres) provides users with a better understanding of this relatively new composite material. The fibre system is modelled by a Boolean model and the fibre orientation by a one-parameter distribution. In addition, the behaviour under tensile loading is modelled.

Part I

Mathematical morphology, quantiles and depths for directional data

Chapter 1

Mathematical morphology on directional images

1.1 Introduction

Mathematical morphology is a non-linear image processing technique that combines ideas from set theory, topology, and stochastic geometry. It is widely applied for the analysis of spatial structures, e.g. from geology, biology or materials science. The foundations of mathematical morphology are laid in the books by Matheron [1], Serra [2, 3], and Soille [4]. Sternberg [5] generalised mathematical morphology to numerical functions via the umbra method, i.e., the application of set morphology to the graph of the function. Ronse [6] and Goutsias et al. [7] derived a further generalisation to complete lattices, that is, partially ordered sets with the property that all subsets have a supremum and an infimum.

The development of imaging methods from binary via grey-scale images to vector-valued images, such as colour or ultra-spectral images, requires modified morphological operators. In mathematical morphology, the step from univariate to multivariate pixel values involves the challenging task of ordering vectors such that we can define the notions of minimum and maximum of a set of vectors. An ordering structure for vectors can be derived from the concept of depth. For a set of vectors, depth functions assign to each vector a value that measures its "centrality" within the set. The "centre" is the vector maximising the depth function. Thus, a centre-outward ordering based on the depth values of each vector yields a sound definition of minimum and maximum. Depth extends the univariate notion of a centre, e.g. the median, to a multivariate setting and enables a non-parametric robust data analysis.

Velasco-Forero et al. [8] defined multivariate mathematical morphological operators via random projection depth. They illustrated their approach on colour and hyperspectral images. Concepts of depth for directional data, i.e., unit vectors in $\mathbb{R}^d$, were investigated by Liu et al. [9] and Pandolfo et al. [10]. Ley et al. [11] introduced quantiles for directional data and the angular Mahalanobis depth.

Based on an ordering on the unit sphere $\mathcal{S}^{d-1}$, mathematical morphology was extended to directional images by several authors. Roerdink [12] introduced mathematical morphology on the sphere via generalised Minkowski operations. His motivation was to apply morphological operators to images of the earth, taking into account the surface curvature of the earth. Morphological operators for angle-valued images were introduced by Peters [13] and Hanbury et al. [14]. However, a generalisation from their results to the unit sphere $\mathcal{S}^{d-1}$ with $d \geq 2$ is not straightforward. Frontera-Pons and Angulo [15] defined morphological operators via a local partial ordering. They used the Fréchet-Karcher barycenter as a local origin $\mu \in \mathcal{S}^{d-1}$. The maximum and minimum of a set of vectors are then found via projecting the vectors into the tangent space at μ. A drawback of their approach is that the minimum and maximum derived this way are not necessarily elements of the given vector set, which seems unnatural.

Let $\overline{\mathbb{R}} = \mathbb{R} \cup \{-\infty, \infty\}$ the extended real numbers. Structuring functions $b : E \to \overline{\mathbb{R}}$ determine the effect of morphological operators. A standard example is $b(i) = 0$ if $i \in B$ and $b(i) = -\infty$ else, with the so-called structuring element B. Morphological operators are extended to multi-scale morphological operators if the structuring function is a parametric family $\{b_t\}_{t \geq 0}$ depending on the scale parameter t.

For instance, the scale of a structuring element B can be its size, and therefore $\{tB\}_{t\geq 0}$ determines the effect of a multi-scale morphological operator. Multi-scale morphological operators are based on the concept of scale-spaces, see Witkin [16]. The idea of scale-spaces is to use a continuous scale parameter for spatial filtering of image objects. A scale-space is not necessarily meant as a vector space or a comparable structure. It is a multi-scale representation of a signal or image I. A scale parameter $t = 0$ gives the original image I interpreted as the "finest scale". Higher values of t give a representation of I at a "coarser scale". A filtering example is smoothing an image by convolution with a scaled Gaussian kernel. Here, the scale parameter is the standard deviation σ in the Gaussian kernel (Gaussian scale-space). Small σ (fine-scale) preserves edges and large σ (coarse scale) smooths the image. Morphological scale-spaces for one-dimensional signals were discussed by Jackway [17, 18]. Heijmans [19] introduced an algebraic framework for linear and morphological scale-spaces with applications to grey-scale images. The basic idea is to scale the image to a unit scale for the application of a morphological operator and then re-scale it to the original image size. Vachier [20] defined multi-scale morphological operators via levellings which are operators preserving the grey-scale order. This approach preserves local extremes, which was used to extract and analyse image features, i.e., image objects of interest. Welk [21] stated families of generalised morphological scale-spaces obtained by algebraic operations related to l^p norms and generalised means. Their results are primarily of theoretical interest but offer an approach to a deeper understanding of scale-spaces.

Angulo [22] extended the concept of multi-scale morphological operators from $\mathbb{R}$-valued to $\mathbb{R}^d$-valued images. He defined morphological scale-space operators on metric Maslov-measurable spaces for images supported on point clouds. An application of their operators on RGB-valued point clouds, e.g. for object extraction, showed the usefulness of applying the theory of multi-scale morphological operators to $\mathbb{R}^d$-valued images.

It turns out that there are several possible definitions of multi-scale morphological operators to vector-valued images and there is no established solution to that issue. Theses definitions are often still abstract and further approaches in this direction are needed.

In this work, we introduce morphological operators for $\mathcal{S}^{d-1}$-valued images (called directional images). The morphological operators were defined via the theory of h-adjunctions which ensures a sound definition. Furthermore, we extend the operators to multi-scale operators where the structuring function corresponds to a rotation matrix. In this new approach for the structuring function, the scale parameter determines the angle of rotation. Our approach for the structuring function benefits from a simple interpretation, fulfils the semigroup property as well as further desired properties. Section 1.2 contains basics about mathematical morphology for grey-scale images and its relation to scale-space theory, and statistical depth functions on $\mathcal{S}^{d-1}$. The extension to multivariate mathematical morphology via h-ordering and h-adjunctions is stated. Furthermore, quantiles and depth for directional data from Ley et al. [11] are summarised. In Section 1.3, we introduce the concept of mathematical morphology on directional images using the directional projection depth. Basic image processing notions and operations, like a background/foreground representation and filters, are presented. The extension to multi-scale morphological operators for directional data is defined in Section 1.4. We illustrate and interpret our findings on generated and real-world $\mathcal{S}^2$-valued images in Section 1.5.

1.2 Basics and notation

1.2.1 Notation

We denote by $\mathcal{S}^{d-1} = \{x \in \mathbb{R}^d : \sqrt{x^T x} = 1\}$ the $(d-1)$-dimensional unit sphere. An image is a mapping $I : E \to S$ that is defined on a q-dimensional (spatial) domain E with $E \subset \mathbb{R}^q$ or $E \subset \mathbb{Z}^q$. The set S is the set of pixel values. We call I a binary image if $S = \{0, 1\}$, a grey-scale image if $S \subset \mathbb{R}$, a vector-valued image if $S \subset \mathbb{R}^d$ and a directional image if $S \subset \mathcal{S}^{d-1}$. Usually, $q, d \in \{2, 3\}$. We denote by

- $i \in E$ the position of a pixel with pixel value $I(i)$.

- $\max I$ the maximal possible pixel value of an image I. For instance, $\max I = 1$ if I is a binary image or $\max I = 255$ if I is a 8-bit grey-scale image.
- $|\cdot|$ the cardinality of a set.
- $||\cdot||_2$ the Euclidean norm for vectors and the spectral norm for matrices.
- 0_d the d-dimensional zero vector.
- 1_d the d-dimensional one vector.
- $0_{d\times d}$ the d-dimensional zero matrix.
- I_d the d-dimensional unit matrix.
- $Sym(d)$ the set of $d \times d$ symmetric matrices.
- $SO(d)$ the set of $d \times d$ rotation matrices.
- $\oplus$ the Minkowski addition.
- $\times$ the cross product.
- $\mathcal{S}^{d-2}_{\mu^\perp} = \{x \in \mathcal{S}^{d-1} : x^T\mu = 0\}$ the $(d-2)$-dimensional unit sphere with vectors orthogonal to $\mu \in \mathcal{S}^{d-1}$.
- $B_d(r) = \{x \in \mathbb{R}^d : ||x||_2 < r\}$ the d-dimensional open ball of radius $r > 0$ centred at the origin 0_d.
- $\stackrel{D}{=}$ equality in distribution.
- $\mathcal{F}_\mu$ the class of distributions on $\mathcal{S}^{d-1}$ with a bounded density that admit a unique modal direction μ.
- $B_i = i \oplus B$ a set $B \subset \mathbb{R}^q$ centred at pixel position i if B is centred at the origin.
- $\check{b}$ the reflection of a function $b : \mathbb{R}^q \to \overline{\mathbb{R}}$, i.e., $\check{b}(i) = b(-i)$ for all $i \in \mathbb{R}^q$, and by $\check{B}$ the reflection of a set $B \subset \mathbb{R}^q$, i.e., $\check{B} = -B$.

A function b is called symmetric if $b(i) = \check{b}(i)$ for all $i \in \mathbb{R}^q$ and a set B is called symmetric if $B = \check{B}$.

Furthermore, we define the unique geodesic [23] from $\mu \in \mathcal{S}^{d-1}$ to $x \in \mathcal{S}^{d-1}$ as a mapping

$$c^{\mu,x} : [0,1] \to \mathcal{S}^{d-1}, \tag{1.1}$$

starting at $c^{\mu,x}(0) = \mu$ with initial velocity $\dot{c}^{\mu,x}(0) = v$ and ending in $c^{\mu,x}(1) = x$, where v is a tangent vector at $\mu \in \mathcal{S}^{d-1}$.

1.2.2 Mathematical morphology

We first define morphological operators on grey-scale images I. See [1, 2, 4] for a detailed introduction. The two fundamental operations of mathematical morphology are erosion $\tilde{\varepsilon}_b$ and dilation $\tilde{\delta}_b$. They depend on a structuring function $b : \mathbb{R}^q \to \overline{\mathbb{R}}$ and are defined as

$$\tilde{\varepsilon}_b(I)(i) = \inf_{j\in E}\{I(j) - b(j+i)\}, \quad i \in E, \tag{1.2}$$

$$\tilde{\delta}_b(I)(i) = \sup_{j\in E}\{I(j) + b(j-i)\}, \quad i \in E. \tag{1.3}$$

In the discrete case, supremum and infimum can be replaced by maximum and minimum. We will not discuss edge effects here (see [17]).

A well known and widely used example for b is the flat structuring function. Given a structuring element $B \subset \mathbb{R}^q$, it is defined as

$$b(i) = \begin{cases} 0 & i \in B \\ -\infty & i \notin B. \end{cases}$$

Morphological operators with flat structuring functions are called flat operators. Symbols for flat operators will be written with index B rather than b, e.g., a flat erosion with structuring element B is denoted by $\tilde{\varepsilon}_B$.

Non-flat or volumic structuring functions assign non-constant weights to the pixel values [2]. For instance,

$$b(i) = -\left(\frac{||i||_2}{2}\right)^2$$

is a non-flat structuring function. Note that the grey-scale ranges of images dilated or eroded by non-flat structuring functions are not bounded [4]. For instance, an erosion with a non-flat structuring function of an image with non-negative pixel values can result in negative pixel values. Flat structuring functions do not suffer from that problem. The output of a flat erosion or dilation is bounded by the grey-scale range of the input image.

From now on, we assume that b is symmetric and that B is centred at the origin and symmetric. The composition of erosion and dilation yields the morphological operators opening $\tilde{\gamma}_b$ and closing $\tilde{\varphi}_b$

$$\tilde{\gamma}_b(I)(i) = \tilde{\delta}_b(\tilde{\varepsilon}_b(I))(i),$$
$$\tilde{\varphi}_b(I)(i) = \tilde{\varepsilon}_b(\tilde{\delta}_b(I))(i).$$

In applications the opening is used to remove bright noise and the closing to remove dark noise.

Let $i \in E$, I, I' grey-scale images and $\{I_l\}_{l\in\mathbb{N}}$ a family of grey-scale images. We write $I \leq I'$ if $I(i) \leq I'(i)$ for all $i \in E$. Furthermore, $\bigvee$ denotes the pixel-wise maximum operator and $\bigwedge$ the pixel-wise minimum operator. The complement $\tilde{\mathrm{C}}$ of a grey-scale image I is pixel-wise defined by

$$\tilde{\mathrm{C}}I(i) = \max I - I(i), \quad i \in E. \tag{1.4}$$

Some properties of morphological operators are summarised in the following [1, 2, 17].

1. All morphological operators are non-linear (in general), i.e.,

   $$\tilde{\Psi}(aI + bI') \neq a\tilde{\Psi}(I) + b\tilde{\Psi}(I'),$$

   where $a, b \in \mathbb{R}$ and $\tilde{\Psi} = \tilde{\delta}_b, \tilde{\varepsilon}_b, \tilde{\gamma}_b$, or $\tilde{\varphi}_b$.

2. Dilation and erosion are dual w.r.t. complementation $\tilde{\mathrm{C}}$, i.e.,

   $$\tilde{\delta}_b(I) = \tilde{\mathrm{C}}\tilde{\varepsilon}_b(\tilde{\mathrm{C}}I)$$

   with $b(i) = b(-i)$ due to symmetry.

3. Opening and closing are dual w.r.t. complementation $\tilde{\mathrm{C}}$, i.e.

   $$\tilde{\gamma}_b(I) = \tilde{\mathrm{C}}\tilde{\varphi}_b(\tilde{\mathrm{C}}I))$$

4. Opening and closing are idempotent, i.e.,

   $$\tilde{\gamma}_b(\tilde{\gamma}_b(I)) = \tilde{\gamma}_b(I),$$
   $$\tilde{\varphi}_b(\tilde{\varphi}_b(I)) = \tilde{\varphi}_b(I).$$

   The idempotence property means, that once such an operator is applied to an image, the result is not altered by an additional application of that operator.

5. The following distribution laws hold

$$\tilde{\delta}_b(\bigvee_l I_l) = \bigvee_l \tilde{\delta}_b(I_l),$$
$$\tilde{\varepsilon}_b(\bigwedge_l I_l) = \bigwedge_l \tilde{\varepsilon}_b(I_l).$$

6. Dilation is associative and erosion fulfils the chain rule, i.e.,

$$\tilde{\delta}_b(\tilde{\delta}_{b'}(I)) = \tilde{\delta}_{\tilde{\delta}_b(b')}(I),$$
$$\tilde{\varepsilon}_b(\tilde{\varepsilon}_{b'}(I)) = \tilde{\varepsilon}_{\tilde{\delta}_b(b')}(I).$$

7. All morphological operators are increasing, i.e.,

$$I \leq I' \Rightarrow \tilde{\Psi}(I) \leq \tilde{\Psi}(I'),$$

   where $\tilde{\Psi} = \tilde{\delta}_b, \tilde{\varepsilon}_b, \tilde{\gamma}_b$, or $\tilde{\varphi}_b$.

8. If b is defined at the origin and $b(0) \geq 0$, dilation is extensive and erosion is anti-extensive, i.e.,

$$\tilde{\varepsilon}_b(I) \leq I \leq \tilde{\delta}_b(I).$$

9. Closing is extensive and opening is anti-extensive, i.e.,

$$\tilde{\gamma}_b(I) \leq I \leq \tilde{\varphi}_b(I).$$

The latter two properties yield the ordering relation

$$\tilde{\varepsilon}_b(I) \leq \tilde{\gamma}_b(I) \leq I \leq \tilde{\varphi}_b(I) \leq \tilde{\delta}_b(I). \tag{1.5}$$

We introduce scaled structuring functions in Section 1.2.3 to extend the introduced operators to multi-scale morphological operators.

1.2.3 Morphological scale-space

In the context of mathematical morphology for grey-scale images, erosion and dilation can be written as scale-space operators [2, 24]

$$\tilde{\varepsilon}_{b_t}(I)(i) = \inf_{j \in E}\{I(j) - b_t(j+i)\} \tag{1.6}$$
$$\tilde{\delta}_{b_t}(I)(i) = \sup_{j \in E}\{I(j) + b_t(j-i)\}, \tag{1.7}$$

with a scaled structuring function

$$b_t : \mathbb{R}^q \to \overline{\mathbb{R}}, \quad t \geq 0 \tag{1.8}$$

with scale parameter t. We choose b_t [17, p.15] to fulfil the following properties:

1. $\{b_t\}_t$ is a one-parametric family of convex, continuous, symmetric functions and fulfils the semi-group property, i.e.

$$b_t \dot{+} b_s = b_{t+s} \qquad t, s \geq 0, \tag{1.9}$$

   where $\dot{+}$, $+$ are group operations [24]. For instance, choosing b_t to be a flat structuring function with structuring element tB the group operations are the Minkowski addition and the standard addition in $\mathbb{R}$:

$$tB \oplus sB = (t+s)B \qquad t, s \geq 0.$$

2. b_t is non-positive and monotonically decreasing with a global maximum at the origin of value zero, i.e.,

$$b_t(i) \leq 0 \qquad \forall\, t \geq 0, i \in \mathbb{R}^q, \tag{1.10}$$
$$b_t(i) \geq b_t(j) \quad ||i||_2 < ||j||_2, \tag{1.11}$$
$$b_t(0) = 0. \tag{1.12}$$

An example of a non-flat scaled structuring function is the Poweroid structuring function [17, p.14, Def. 5]

$$b_t(i) = -|t| \left(\frac{||i||_2}{|t|} \right)^a \qquad a \geq 0, t \neq 0. \tag{1.13}$$

1.2.4 Directional data

Directional data are a set of vectors on the unit sphere $\mathcal{S}^{d-1}$ for some $d \geq 2$. The vector $x = (x_1, \ldots, x_d)^T \in \mathcal{S}^{d-1}$ can be represented as a point on the surface of $\mathcal{S}^{d-1}$. For x in Cartesian coordinates a representation in angular coordinates for arbitrary d is given in [25].

For $d = 3$, we use the usual notation for spherical coordinates

$$x = \begin{pmatrix} \sin(\theta)\cos(\phi) \\ \sin(\theta)\sin(\phi) \\ \cos(\theta) \end{pmatrix} \tag{1.14}$$

with co-latitude $\theta \in [0, \pi]$ and longitude $\phi \in [0, 2\pi)$. A random vector $X \in \mathcal{S}^2$ can be represented in spherical coordinates by random variables Θ and Φ with realisations θ and ϕ.

Note that

$$(I_d - \mu\mu^T)X = X - \mu\mu^T X = X - (X^T\mu)\mu \tag{1.15}$$

with $X^T\mu = \mu^T X$. The tangent-normal decomposition of a random vector $X \in \mathcal{S}^{d-1}$ w.r.t. $\mu \in \mathcal{S}^{d-1}$ reads [26, 27]

$$X = (X^T\mu)\mu + (I_d - \mu\mu^T)X \tag{1.16}$$
$$= (X^T\mu)\mu + Z \tag{1.17}$$

with $Z = (I_d - \mu\mu^T)X$ the tangential part of X. Note that

$$||Z||_2 = \sqrt{1 - (X^T\mu)^2} \tag{1.18}$$

due to the Pythagorean theorem. Figure 1.1 illustrates the decomposition for $d = 3$.

1.2.5 Statistical depth functions

Depth functions are applied in multidimensional non-parametric robust data analysis and establish an ordering relation between vectors. See [28] for a detailed introduction. The definition of a centre within a multidimensional data set induces a centre-outward ordering. Furthermore, each vector of the data set has a depth value which is maximal at the centre. Denote by $\mathscr{F}$ the class of distributions on the Borel sets of $\mathbb{R}^d$ and by F_X the distribution of a random vector X. Note that some distributions in $\mathscr{F}$ exhibit a point of symmetry. Such a point is an example of a centre. Zuo and Serfling [28] claimed desirable properties of depth functions and provided a formal definition (the notation is slightly adapted):

Definition 1.2.1 (Definition 2.1 in [28])**.** *A statistical depth function $\mathcal{D}_\cdot(\cdot) : \mathscr{F} \times \mathbb{R}^d \to \mathbb{R}$ is a bounded, non-negative mapping satisfying*

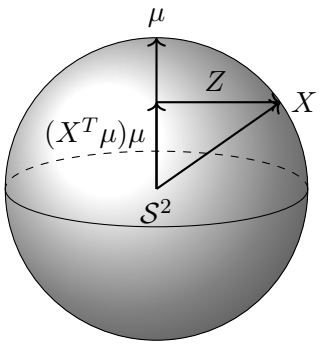

Figure 1.1: Tangent-normal-decomposition of $X = (X^T\mu)\mu + Z$ with $Z = (I_d - \mu\mu^T)X$ on $\mathcal{S}^2$.

1. $\mathcal{D}_{F_{AX+b}}(AX + b) = \mathcal{D}_{F_X}(X)$ *holds for any random vector* $X \sim F_X$*, any non-singular matrix* $A \in \mathbb{R}^{d\times d}$*, and any* $b \in \mathbb{R}^d$*,*

2. $\mathcal{D}_F(\mu) = \sup_{X\in\mathbb{R}^d} \mathcal{D}_F(X)$ *holds for any* $F \in \mathscr{F}$ *having centre* $\mu \in \mathbb{R}^d$*,*

3. *for any* $F \in \mathscr{F}$ *having centre* μ*,* $\mathcal{D}_F(X) \leq \mathcal{D}_F(\mu + \alpha(X - \mu))$ *holds for* $\alpha \in [0, 1]$*, and*

4. $\mathcal{D}_F(X) \to 0$ *for* $||X||_2 \to \infty$*, for each* $F \in \mathscr{F}$*.*

Property 1 implies that the depth of a vector should be independent of the underlying coordinate system or measurement scales. Property 2 means that for any F with unique centre μ, the depth function is maximal at μ. Property 3 indicates that the depth of X decreases monotonically if X moves away from μ along any fixed ray. Property 4 implies that the depth value of X tends to zero as its norm tends to infinity. The literature gives several depth functions, for instance halfspace depth [29], simplicial depth [30], projection depth [31], spatial depth [32], or the Mahalanobis depth [28].

For defining a depth for directional data, we initially restrict attention to the class $\mathcal{F}_\mu$ of distributions on $\mathcal{S}^{d-1}$ with a bounded density that admit a unique modal direction μ. We further assume that μ coincides with the Fisher spherical median [33], that is

$$\mu = \arg\min_{\gamma\in\mathcal{S}^{d-1}} E(\arccos(X^T\gamma)). \tag{1.19}$$

Examples of distributions in $\mathcal{F}_\mu$ are the von Mises–Fisher distribution and some Kent distributions (see Section 2.2.2) [34].

Ley et al. [11] adapted the Definition 1.2.1 for directional data as follows.

Definition 1.2.2. *Consider* $\mathcal{D}_\cdot(\cdot) : \mathcal{F}_\mu \times \mathcal{S}^{d-1} \to \mathbb{R}$*, a bounded, non-negative mapping satisfying*

1. $\mathcal{D}_{F_{AX}}(AX) = \mathcal{D}_{F_X}(X)$ *holds for any random unit vector* $X \sim F \in \mathcal{F}_\mu$ *and any rotation matrix* $A \in SO(d)$*,*

2. $\mathcal{D}_F(\mu) = \sup_{X\in\mathbb{R}^d} \mathcal{D}_F(X)$ *holds for any* $F \in \mathcal{F}_\mu$*,*

3. *for any* $F \in \mathcal{F}_\mu$*,* $\mathcal{D}_F(X) \leq \mathcal{D}_F(c^{\mu,X}(\alpha))$ *for the unique geodesic between* μ *and* X *given in* (1.1) *with* $\alpha \in [0, 1]$*, and*

4. $\mathcal{D}_F(-\mu) = 0$ *for each* $F \in \mathcal{F}_\mu$ *where* $-\mu$ *is the antipodal point of the centre* μ*.*

Then $\mathcal{D}_\cdot(\cdot)$ *is called a statistical depth function on* $\mathcal{S}^{d-1}$*.*

Depth functions for directional data are, for instance, directional distance-based depths (arc distance depth, cosine distance depth, chord distance depth) [10] or the angular Mahalanobis depth [11]. For defining morphological operators, we cannot use the latter since its application violates the ordering

property (1.5) for morphological operators. We rather use a re-scaled version of the cosine distance depth from [10] as defined in the following Section.

For $d = 3$, we define a great circle $\mathcal{GC}$ as a closed curve on the surface of $\mathcal{S}^2$ created by the intersection of $\mathcal{S}^2$ and a 2-dimensional hyperplane H passing through the origin 0_d [34]. We define

$$\mathcal{GC}_{\mu,x} = \{y \in \mathbb{R}^d | (x \times \mu)^T y = 0\} \cap \mathcal{S}^{d-1} \tag{1.20}$$

the great circle containing μ and the vector $x \in \mathcal{S}^{d-1} \setminus \{\mu\}$. Note that x and μ uniquely determine $\mathcal{GC}_{\mu,x}$. The geodesic in property 3 for points on $\mathcal{S}^2$ is embedded in $\mathcal{GC}_{\mu,x}$.

1.2.5.1 The angular projection depth

We define the angular projection depth for directional data by assigning the value

$$D_F^{proj}(x) = \frac{1 + x^T \mu}{2} \tag{1.21}$$

to each $x \in \mathcal{S}^{d-1}$. The angular projection depth is a re-scaled version of the cosine distance depth from Pandolfo et al. [10] restricted to μ given in (1.19). $D_F^{proj}(x)$ provides a centre-outward ordering with $D_F^{proj}(\mu) = 1$, $D_F^{proj}(-\mu) = 0$ and is decreasing on a geodesic from μ to $-\mu$. Let $A \in \mathbb{R}^{d \times d}$ be any rotation matrix. Then the distribution of the transformed vector AX has centre $A\mu$. It follows that

$$\begin{aligned} D_{F_{AX}}^{proj}(AX) &= \frac{1 + (AX)^T A\mu}{2} \\ &= \frac{1 + X^T A^T A\mu}{2} \\ &= \frac{1 + X^T \mu}{2} \\ &= D_{F_X}^{proj}(X). \end{aligned}$$

Thus, the properties of a directional depth function given in Definition 1.2.2 are fulfilled.

Let $X, X_1, \ldots, X_n \in \mathcal{S}^{d-1}$ be i.i.d. random vectors with $X \sim F \in \mathcal{F}_\mu$ and $\hat{\mu}$ the root-n consistent empirical Fisher spherical median [33]

$$\hat{\mu} = \arg\min_{\gamma \in \mathcal{S}^2} \sum_{i=1}^{N} \arccos(X_i^T \gamma). \tag{1.22}$$

The empirical angular projection depth reads

$$D^{proj}(x) = \frac{1 + x^T \hat{\mu}}{2}, \tag{1.23}$$

where $\hat{\mu}$ is given in (1.22).

1.2.5.2 Quantiles for directional data

The novel concept of quantiles for directional data from Ley et al. [11] is summarised in the following:

The quantile check function, known from quantile regression [35], reads $\rho_\tau(z) = z(\tau - 1[z \leq 0])$, where $z \in \mathbb{R}$, $\tau \in [0, 1]$ and $1[z \leq 0]$ the indicator function. The projection quantile is defined by [11, 36]

$$c_\tau = \arg\min_{c \in [-1,1]} E[\rho_\tau(X^T \mu - c)], \tag{1.24}$$

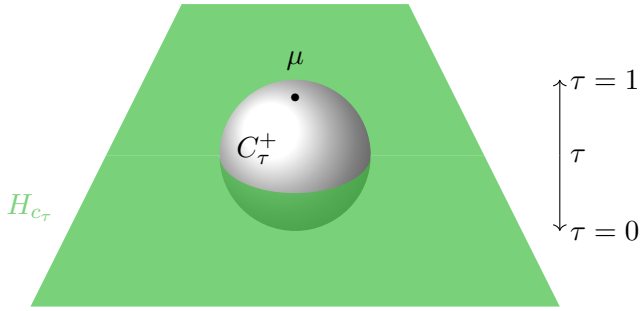

Figure 1.2: The hyperplane $H_{c_\tau\mu}$ divides the unit sphere $\mathcal{S}^2$ in the upper quantile cap C_τ^+ and lower quantile cap C_τ^-. The intersection of $H_{c_\tau\mu}$ with $\mathcal{S}^2$ corresponds to the τ-depth contour denoted by $C_{c_\tau\mu}$.

which is the univariate τ-quantile of $X^T\mu$. The partition of the sphere due to the hyperplane

$$H_{c_\tau\mu} = \{x \in \mathbb{R}^d | c_\tau = x^T\mu\} \tag{1.25}$$

defines the τ-depth contour

$$C_{c_\tau\mu} = H_{c_\tau\mu} \cap \mathcal{S}^{d-1}, \tag{1.26}$$

an upper quantile cap

$$C_\tau^+ = \{x \in \mathcal{S}^{d-1} | x^T\mu \geq c_\tau\},$$

and a lower quantile cap

$$C_\tau^- = \{x \in \mathcal{S}^{d-1} | x^T\mu < c_\tau\}.$$

For $d = 3$, Figure 1.2 illustrates $H_{c_\tau\mu}$, $C_{c_\tau\mu}$ and the quantile caps. Note that the $1/2$-quantile $c_{1/2\mu}$ is not related to the most central point. Its associated hyperplane $H_{c_{1/2}\mu}$ divides the probability mass into two equal halves. A value of $\tau = 1$ ($c_1 = 1$) is reached by μ and a value of $\tau = 0$ ($c_0 = -1$) is reached by $-\mu$ (provided that the neighbourhood of $-\mu$ has non-zero probability mass, otherwise an entire cap around $-\mu$ is associated with $\tau = 0$). The empirical projection quantile [11] reads

$$\hat{c}_\tau = \arg \min_{c \in [-1,1]} \sum_{i=1}^{N} [\rho_\tau(X_i^T\hat{\mu} - c)]. \tag{1.27}$$

Note that the authors in [11] transferred the projection quantile c_τ into a new definition of depth for directional data by assigning the value

$$D_F(x) = \arg \min_{\tau \in [0,1]} \{c_\tau \geq x^T\mu\}, \tag{1.28}$$

to each $x \in \mathcal{S}^{d-1}$. The angular Mahalanobis depth is a rescaled version of (1.28). Note that we return to this depth in Section 2.2.5. Here, we will not use this depth since its application contradicts the ordering property (1.5) for morphological operators. The contradiction results from the inequality in Equation (1.28).

1.2.6 Multivariate mathematical morphology, h-ordering and h-adjunctions

Mathematical morphology needs an ordering relation between pixel values for a sound definition of its operators. Defining maximum and minimum between d-dimensional vectors, $d \geq 2$, is not straightforward. One approach is to define a mapping h that maps the vectors into a space with a partial order. This approach has the advantage that we can define morphological operators for vectors over h-adjunctions.

We follow the notion of Goutsias et al. [7] for h-ordering and h-adjunctions: A space $\mathcal{L}$ with a partial order $\leq$ is called a complete lattice if every subset L of $\mathcal{L}$ has a supremum and an infimum. Note that the term lattice has nothing to do with the spatial domain of the image (known as grid or lattice for the discrete case in the image processing community). We denote a complete lattice with $(\mathcal{L}, \leq)$. Let $S \neq \emptyset$ and $h : S \to \mathcal{L}$ surjective. We define an equivalence relation on S, denoted by $=_h$, via

$$s =_h s' \Leftrightarrow h(s) = h(s') \qquad s, s' \in S. \tag{1.29}$$

An h-ordering $\leq_h$ is given by

$$s \leq_h s' \Leftrightarrow h(s) \leq h(s') \qquad s, s' \in S. \tag{1.30}$$

It is reflexive ($s \leq_h s$) and transitive ($s_1 \leq_h s_2$, $s_2 \leq_h s_3 \Rightarrow s_1 \leq_h s_3$). Note that $\leq_h$ is not a partial ordering: Let $s \leq_h s'$ and $s' \leq_h s$. Then, $s =_h s'$ but not necessarily $s = s'$.

Nevertheless, the surjectivity of h and the Axiom of Choice (existence of a least element) imply the existence of a mapping $h^{\leftarrow} : \mathcal{L} \to S$ such that [7]

$$hh^{\leftarrow}(l) = l, \qquad l \in \mathcal{L}. \tag{1.31}$$

The mapping $h^{\leftarrow}$ is unique if h is injective. Define a mapping $\Psi : S \to S$ to be

- h-increasing, if

$$s \leq_h s' \Rightarrow \Psi(s) \leq_h \Psi(s'). \tag{1.32}$$

- h-idempotent, if

$$\Psi^2 =_h \Psi. \tag{1.33}$$

- h-extensive, if for every $s \in S$

$$s \leq_h \Psi(s). \tag{1.34}$$

- h-anti-extensive, if for every $s \in S$

$$\Psi(s) \leq_h s. \tag{1.35}$$

For Ψ h-increasing, it holds that

$$h\Psi h^{\leftarrow}h = h\Psi. \tag{1.36}$$

Furthermore, Ψ is h-increasing if and only if there is an h-increasing mapping $\tilde{\Psi} : \mathcal{L} \to \mathcal{L}$ such that

$$\tilde{\Psi}h = h\Psi. \tag{1.37}$$

The mapping $\tilde{\Psi}$ is uniquely determined by Ψ via

$$\tilde{\Psi} = h\Psi h^{\leftarrow}. \tag{1.38}$$

An h-adjunction is a pair (ε, δ) of two mappings $\varepsilon, \delta : S \to S$ with

$$\delta(s) \leq_h s' \Leftrightarrow s \leq_h \varepsilon(s') \qquad s, s' \in S. \tag{1.39}$$

Let ε, δ be h-increasing mappings and $\tilde{\varepsilon} = h\varepsilon h^{\leftarrow}$ and $\tilde{\delta} = h\delta h^{\leftarrow}$. Then, (ε, δ) is an h-adjunction on S if and only if $(\tilde{\varepsilon}, \tilde{\delta})$ is an adjunction on $\mathcal{L}$. Note that ε is h-anti-extensive and δ is h-extensive.

Let (ε, δ) an h-adjunction. Then

$$\gamma(s) \leq_h s \leq_h \varphi(s) \qquad s \in S. \tag{1.40}$$

Thus, γ is h-anti-extensive and φ is h-extensive. Both are h-increasing and h-idempotent.

Via the h-adjunction argument we call

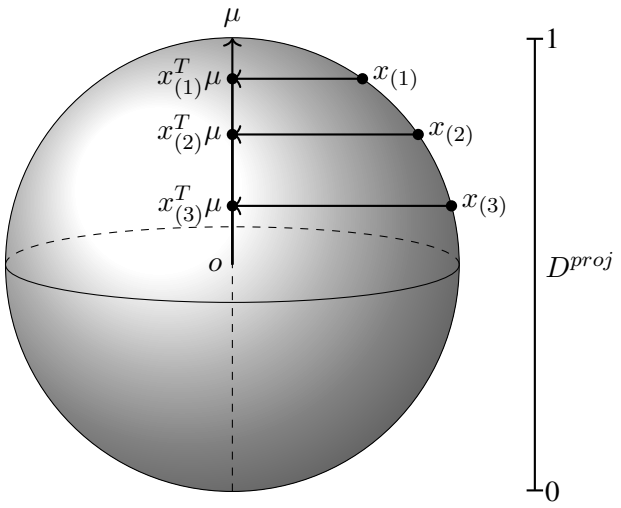

Figure 1.3: Vector ordering by directional projection depth. The indices in round brackets denote the order statistics.

- ε an h-erosion on S if $\tilde{\varepsilon}$ is an erosion on $\mathcal{L}$.
- δ an h-dilation on S if $\tilde{\delta}$ is a dilation on $\mathcal{L}$.
- $\gamma = \delta\varepsilon$ an h-opening on S if $\tilde{\gamma} = \tilde{\delta}\tilde{\varepsilon}$ is an opening on $\mathcal{L}$.
- $\varphi = \varepsilon\delta$ an h-closing on S if $\tilde{\varphi} = \tilde{\varepsilon}\tilde{\delta}$ is a closing on $\mathcal{L}$.

1.3 Mathematical morphology on directional images using directional projection depth

For directional images, we use the projection depth D_F^{proj} to define an ordering relation between unit vectors. Thus, we use D_F^{proj} as an h-ordering to inherit the h-adjunction properties. This allows for a definition of erosion and dilation, and the morphological operators derived from them as described below. For simplicity, we focus on flat morphological operators with structuring element B. We introduce non-planar structuring functions in Section 1.4.1.

Let $\mathcal{L} = [0, 1]$ and $S \subset \mathcal{S}^{d-1}$. $(\mathcal{L}, \leq)$ is a complete lattice. We define an h-ordering (denoted by $\leq_{h_I}$)

$$h_I(x) := D^{proj}(x), \quad (h_I\text{-depth}) \tag{1.41}$$

where I is a directional image with pixel values x and D_F^{proj} is given in Equation (1.21). Assume that x is a realisation of $X \sim F \in \mathcal{F}_\mu$.

In a given application, the assumption $F \in \mathcal{F}_\mu$ is not fulfilled. Nevertheless, a suitable central direction μ may be derived from the experimental setup. For example, the insertion direction of glass fibre reinforced materials or tension direction could be defined as μ. Hence, μ can be interpreted as a parameter. If that is the case we will write D_μ^{proj} for the projection depth using $\mu \in \mathcal{S}^{d-1}$ as centre. The parameter μ can be selected globally for the whole image or in a locally adaptive manner for parts of the image. The latter is not considered here.

The h_I-erosion ε_B of a directional image I at pixel position $i \in E$ is (implicitly) defined by

$$h_I(\varepsilon_B(I))(i) = \tilde{\varepsilon}_B(h_I(I))(i), \tag{1.42}$$

where $\tilde{\varepsilon}_B$ is the flat erosion of a grey-scale image. Analogously, the h_I-dilation δ_B of a directional image I at pixel position $i \in E$ is (implicitly) defined by

$$h_I(\delta_B(I)(i)) = \tilde{\delta}_B(h_I(I))(i), \tag{1.43}$$

where $\tilde{\delta}_B$ is the flat dilation of a grey-scale image. Note that (ε, δ) is an h_I-adjunction on S since $(\tilde{\varepsilon}, \tilde{\delta})$ is an adjunction on $\mathcal{L}$. Hence, a dilation will select the most central direction w.r.t. μ covered by the structuring element B while an erosion selects the most outlying direction.

The explicit definition reads

$$\varepsilon_B(I)(i) = h_I^{-1}\left(\tilde{\varepsilon}_B(h_I(I))\right)(i), \tag{1.44}$$

$$\delta_B(I)(i) = h_I^{-1}\left(\tilde{\delta}_B(h_I(I))\right)(i) \tag{1.45}$$

where h_I^{-1} refers to the preimage under h_I.

As h_I is not injective, the preimage may consist of more than one element. Consider vectors $x_1, x_2 \in \mathcal{S}^{d-1}$ with $x_1^T\mu = x_2^T\mu$. Then, $h_I(x_1) = h_I(x_2)$ but $x_1 = x_2$ is not necessarily the case. To resolve this issue we use a lexicographic order for vectors of same depth value which yields a total ordering [8]. Rotate the vectors such that $\mu = (0,0,1)^T$. Among the vectors $\{x_i\}_{i=1,\dots,n}$ with $h_I(x_i) = h_I(x_j)$ but $x_i \neq x_j$, $i \neq j$, we choose the vector $x^* \in \{x_i\}_{i=1,\dots,n}$ with the smallest longitude angle, i.e., $x^* = \arg\min_{x_i} \phi_i$ with (θ_i, ϕ_i) spherical coordinates of x_i, $i = 1, \dots, n$. Then rotate x^* back.

Let $(\varepsilon_B, \delta_B)$ be an h_I-adjunction. h_I-opening and h_I-closing are defined by

$$\gamma_B(I)(i) = \delta_B(\varepsilon_B(I))(i), \tag{1.46}$$

$$\varphi_B(I)(i) = \varepsilon_B(\delta_B(I))(i). \tag{1.47}$$

Of course, further morphological filters have their h_I-depth analogy. For instance, the scalar difference between the h_I-depth of h_I-dilation and h_I-erosion defines the morphological gradient

$$\mathrm{g}_{h_I,B}(I)(i) = h_I\left(\delta_B(I)\right)(i) - h_I\left(\varepsilon_B(I)\right)(i).$$

The gradient filter applied to a directional image results in a grey-scale image and identifies edges at which depth values change sharply. The morphological Laplacian is defined by

$$\Delta_{h_I,B}(I)(i) = \Delta_\delta(i) - \Delta_\varepsilon(i)$$

with $\Delta_\delta(i) = h_I\left(\delta_B(I)\right)(i) - h_I(I)(i)$ and $\Delta_\varepsilon(i) = h_I(I)(i) - h_I\left(\varepsilon_B(I)\right)(i)$. The shock filter is defined by

$$\mathrm{sf}_{h_I,B}(I)(i) = \begin{cases} \varepsilon_B(I)(i) & \Delta_{h_I,B}(I)(i) < 0, \\ \delta_B(I)(i) & \Delta_{h_I,B}(I)(i) > 0, \\ I(i) & \text{otherwise.} \end{cases}$$

Shock filtering is used to enhance edges. For grey-scale images, the idea is to dilate near local maxima and erode near local minima. Here, transitions in the spatial domain between regions of pixel values with high and low depth are enhanced.

1.3.1 Background/foreground representation of directional images

Let I be a directional image, X_I its set of pixel values and $I(i) \sim F \in \mathcal{F}_\mu, i \in E$. Using h_I-depth we can order the elements in X_I. As for binary or grey-scale images, one could assume that vector-valued images consist of two main parts [8]: background and foreground. An idea how to define such an division for an directional image is given in the following. We identify foreground pixel values with directions of small angular deviation to μ. Vice versa, the background pixels have pixel values with outlying directions w.r.t. μ.

A formal background/foreground representation (similar to [8]) is as follows: We assume that X_I has a disjoint decomposition in background pixel values (denoted by $X_{(B)}$) and foreground pixel values (denoted by $X_{(F)}$), i.e.,

$$X_I = X_{(B)} \dot{\cup} X_{(F)}. \tag{1.48}$$

We determine background and foreground pixel values in analogy to the thresholding for grey-scale images. Consider $\tau \in [0,1]$. The foreground pixel values are given by

$$X_{(F)} = \left\{x \in X_I : \; c_\tau \geq x^T \mu\right\} \tag{1.49}$$

and the background pixel values are given by

$$X_{(B)} = \left\{x \in X_I : \; c_\tau < x^T \mu\right\} \tag{1.50}$$

with c_τ given in (1.24). Thus, it follows that for all $x \in X_I$, $h_I(x) \leq h_I(x')$ for some $x' \in X_{(F)}$ and $h_I(x) \geq h_I(x')$ for some $x' \in X_{(B)}$. Analogous to grey-scale images, the largest pixel value is in the foreground ($\arg\max_{x \in X_I} h_I(x) \in X_{(F)}$), and the smallest pixel value is in the background ($\arg\min_{x \in X_I} h_I(x) \in X_{(B)}$).

The partition of the sphere in background and foreground pixel values due to a hyperplane $H_{c_\tau \mu}$ defines a foreground cap $C_{(F)} = \left\{x \in \mathcal{S}^{d-1} : c_\tau \geq x^T \mu\right\}$ and analogously a background cap $C_{(B)} = \left\{x \in \mathcal{S}^{d-1} : c_\tau < x^T \mu\right\}$. All foreground pixels, seen as points on the sphere, are contained in $C_{(F)}$ and all background pixels in $C_{(B)}$.

This background/foreground representation of directional images leads to the following interpretation of ε_B and δ_B: Consider that the threshold τ is fixed. ε_B leads to larger and δ_B to less angular deviations between the transformed pixel values and μ. Thus, ε_B could reduce the number of foreground pixel values. Furthermore, the component size of connected foreground pixels (seen from the spatial domain E) shrinks depending on B. Vice versa, δ_B could reduce the number of background pixel values and enlarges the component size of connected foreground pixels.

1.3.2 Complement operator C

The complement is a basic operator in image processing [4]. We define the complement of a directional image by reversing the sign of each vector coordinate, i.e., the complement of I reads

$$\mathrm{C}\, I(i) = -I(i), \qquad i \in E. \tag{1.51}$$

It follows for the h_I-depth value of $\mathrm{C}\, I(i)$ that

$$\begin{aligned} h_I(\mathrm{C}\, I)(i) &= h_I(-I)(i) && (1.52)\\ &= \frac{1 - I(i)^T \mu}{2} && (1.53)\\ &= 1 - \frac{1 + I(i)^T \mu}{2} && (1.54)\\ &= 1 - h_I(I)(i), && (1.55)\\ & && (1.56) \end{aligned}$$

where we see an analogy to (1.4) since $\max h_I = 1$.

Remark 1.3.1. *We give another approach of a complement operator which is based on D_F. The construction and an illustration are given in Appendix A.*

1.3.3 Properties

We saw that h_I-erosion ε_B and h_I-dilation δ_B for directional images from an h_I-adjunction. Thus, they inherit properties of morphological operators [2, 4, 7, 8, 37], see Section 1.2.2. In the following, we give some remarks about their properties which is useful for applications:

1.3.3.1 Duality

We illustrate the duality property between h_I-dilation and h_I-erosion. Due to the implicit definition of δ_B and ε_B, we show the duality via the h_I-depth:

$$\begin{aligned} h_I(\delta_B(\mathrm{C}\, I))(i) =& \tilde{\delta}_B(h_I(\mathrm{C}\, I))(i) \\ =& \sup_{j \in B_i} h_I(\mathrm{C}\, I)(j) \\ =& \sup_{j \in B_i} \frac{1 - I(j)^T \mu}{2} \\ =& \frac{1}{2} - \inf_{j \in B_i} \frac{I(j)^T \mu}{2} \\ =& 1 - \inf_{j \in B_i} \frac{1 + I(j)^T \mu}{2} \\ =& \max h_I - \inf_{j \in B_i} h_I(I)(j) \\ =& \tilde{C} \tilde{\varepsilon}_B(h_I(I))(i), \end{aligned}$$

with $\max h_I = 1$, C given in (1.51) and $\tilde{C}$ given in (1.4).

1.3.3.2 Ordering relation via geodesic lengths

The h_I-erosion ε_B is less than or equal to the h_I-dilation δ_B w.r.t. h_I, i.e., $\varepsilon_B \leq_{h_I} \delta_B$. This can be interpreted in terms of geodesic lengths as follows: Let $x = I(i), i \in B$, $c^{\mu,x}$ the geodesic on $\mathcal{S}^{d-1}$ from x to μ and $||c^{\mu,x}||$ its length. The length of the geodesic $c^{\mu,\delta_B(x)}$ on $\mathcal{S}^{d-1}$ from $\delta_B(x)$ to μ is less than or equal the length of the geodesic $c^{\mu,\varepsilon_B(x)}$ on $\mathcal{S}^{d-1}$ from $\varepsilon_B(x)$ to μ, i.e., $||c^{\mu,\delta_B(x)}|| \leq ||c^{\mu,\varepsilon_B(x)}||$. A smaller geodesic length to μ corresponds to a larger value h_I. Due to the definition of h_I-erosion and h_I-dilation it follows that

$$||c^{\mu,\delta_B(x)}|| \leq ||c^{\mu,x}|| \leq ||c^{\mu,\varepsilon_B(x)}||.$$

Thus, we have the same ordering relation as with h_I but reversed inequality signs.

From this view point of geodesic lengths, we could also define morphological operators: An erosion applied on a set of vectors would give the vector of the smallest and a dilation the vector of the largest geodesic length to μ. Thus, the interpretation of our introduced h_I-based morphological operators would be switched.

1.3.3.3 Invariance

Let X_I be a matrix whose column vectors correspond to the pixel values. For mathematical morphology, invariance to affine transformations is essential. The authors in [8] defined an h-ordering to be invariant to affine transformations if, for every positive definite matrix $A \in \mathbb{R}^{d \times d}$ and vector $b \in \mathbb{R}^d$, h-ordering is invariant to the transformation defined by $\Gamma(I) = AX_I + b$. Thus, $x_1 \leq_{h_I} x_2 \Rightarrow x_1 \leq_{h_{\Gamma(I)}} x_2$ for all $x_1, x_2 \in \mathbb{R}^d$.

With $x \in \mathcal{S}^{d-1}$ it turns out that the rotation group replaces the Euclidean translation group [12]. Note that the Euclidean translation group is commutative, but the rotation group $SO(d)$, $d > 2$, is not. An approach is to move the points on $\mathcal{S}^{d-1}$ such that the the geodesic distance to μ is unchanged. Thus, $x_1 \leq_{h_I} x_2 \Rightarrow x_1 \leq_{h_{\Gamma(I)}} x_2$ for all $x_1, x_2 \in \mathcal{S}^{d-1}$, $\Gamma(I) = AX_I$, $A \in SO(d)$ with $A\mu = \mu$. The restriction $A\mu = \mu$ ensures that the X_I are rotated around μ. Thus, if the X_I are interpreted as points on the surface of $\mathcal{S}^{d-1}$ these points are shifted along a contour line, which does not change their geodesic distance to μ.

1.3.3.4 Local knowledge

The local knowledge property [4] means that applying transformations on an image $I : E \to S$ or on $I : E' \to S$ with $E' \subset E$ give identical results. More precisely, for $E' \subset E$ it holds $\Psi(I) = \Psi(I|E')$, with Ψ an image transformation and $I|E'$ the restriction of the spatial domain E of image I to a subset E'. Due to the definition, the value of $h_I(I)(i)$, $i \in E' \subset E$, does not differ if the depth function is calculated using all $i \in E$ or only all $i \in E'$. It differs if we need to estimate μ by $\hat{\mu}$. This is because $\hat{\mu}$ could change if just the vectors $I(i)$ with E' are considered. Of course, if we use D_μ^{proj} with globally fixed μ the local knowledge property is preserved.

1.3.4 Connection to rank filters

Rank filters are non-linear filters using a (local) ordering. Ranking is trivial in the one-dimensional real-valued case, in contrast to higher dimensions. However, c_τ is an approach for the computation of rank values (such as the infimum and supremum for erosion and dilation, respectively). Keep in mind that the meaning of rank τ differs from the usual rank interpretation (see Section 1.2.5.2): The sphere is divided by a hyperplane $H_{c_\tau \mu}$ such that $(1-\tau) \cdot 100$-percent of the data points are closer to μ than the τ-depth contour $C_{c_\tau \mu}$. Therefore, it is formidable in trimming (removing extreme values called outliers): Choosing a rank τ can be used to delete all $I(i) \in \mathcal{S}^{d-1}$ "below" the τ-depth contour $C_{c_\tau \mu}$.

1.4 Morphological multi-scale operators for directional images

Here, we introduce morphological multi-scale operators for directional images. As with $\mathbb{R}^d$-valued images, multi-scale operators cannot be straightforwardly transferred from their counterparts for grey-scale images (see [8, 22]). Our approach gives a structuring function which has a meaningful interpretation, fulfils the semi-group property and delivers bounded non-flat operators.

The latter is briefly discussed here: In general, structuring functions $b_t : E \to \overline{\mathbb{R}}$ are unbounded. Thus, multi-scale h_I-dilation and h_I-erosion inherit this unboundedness if we use $h(I(i)) + b_t(i)$ and $h(I(i)) - b_t(i)$, respectively. Furthermore, we can not associate a vector with a depth value outside $[0, 1]$ since no unit vector could be found as preimage. In our approach we redefine structuring functions $b_t : E \to SO(d)$. We will define the operation $I(i) + b_t(i)$ and $I(i) - b_t(i)$ to be a vector rotation of $I(i)$ where the rotation angle depends on the scale t. Therefore, the h_I-depths of $I(i) + b_t(i)$ and $I(i) - b_t(i)$ are both bounded.

The main idea is to rotate a pixel value $x = I(i)$, $i \in E$, about $x \times \mu$ towards μ or away from μ on a great circle $\mathcal{GC}_{\mu,x}$. This increases or decreases the h_I-depth value of the rotated x which gives our approach also a meaningful interpretation. Note that $I(i) + b_t(i)$ and $I(i) - b_t(i)$, $i \in E$, result again in directional images which seems natural.

1.4.1 Structuring function for directional images

In the following, we will redefine the structuring function. In particular, our structuring function no longer maps into $\overline{\mathbb{R}}$. Let $i \in E$, $x = I(i) \in \mathcal{S}^{d-1}$ and $R_{\mu,x} \in SO(d)$ be a rotation matrix which rotates x about $\mu \times x$, $R_{\mu,x}(\theta)x = \mu$ and $\theta = \arccos(x^T \mu)$. We define a structuring function b_t for directional images by a mapping

$$\begin{aligned} b_t : E &\to SO(d) \\ i &\mapsto b_t(i) = R_{\mu,x}(\alpha_t(i)), \end{aligned} \tag{1.57}$$

with rotation angle $\alpha_t(i)$, $t \geq 0$. Since $R_{\mu,x}$ depends on x, the structuring function is locally adaptive. We choose

$$\alpha_t(i) = \frac{||i||_2^2}{2t} \tag{1.58}$$

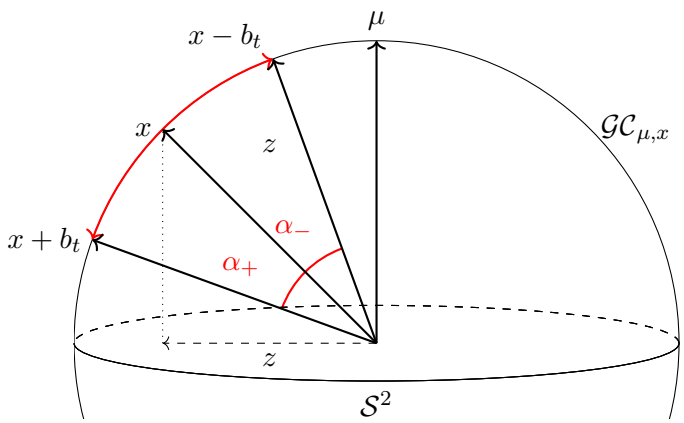

Figure 1.4: Illustration of the operation $x - b_t = R_{\mu,x}(\alpha_-)x$ and $x + b_t = R^T_{\mu,x}(\alpha_+)x$. A rotation from x to $x + b_t$ increases the geodesic distance to μ by α_+. A rotation from x to $x - b_t$ decreases the geodesic distance to μ by α_-. The rotation moves x on the great circle $\mathcal{GC}_{\mu,x}$.

following the Poweroid structuring function given in (1.13) with $a = 2$. Let $f \square g$ be the infimal convolution of two functions $f, g : E \mapsto \mathbb{R}$ [38], i.e.,

$$(f \square g)(i) = \inf_{j \in E} \{f(i - j) + g(j)\} \tag{1.59}$$

with function $f, g : E \mapsto \mathbb{R}$. Furthermore, let $\overline{oi}$ be the line segment from the origin $o \in E$ to $i \in E$. For $E \subset \mathbb{R}^q$ and $t, s > 0$, let j^* be a point on $\overline{oi} \subset E$ such that

$$||j^*||_2 = \frac{s}{t+s}||i||_2 \tag{1.60}$$

$$||i - j^*||_2 = \frac{t}{t+s}||i||_2. \tag{1.61}$$

Then,

$$\begin{aligned}
(\alpha_t \square \alpha_s)(i) &\overset{(1.59)}{=} \inf_{j \in E} \{\alpha_t(i - j) + \alpha_s(j)\} \\
&\overset{(1.58)}{=} \inf_{j \in E} \left\{ \frac{||i - j||_2^2}{2t} + \frac{||j||_2^2}{2s} \right\} \\
&\overset{j^* \in \overline{oi}}{=} \frac{||i - j^*||_2^2}{2t} + \frac{||j^*||_2^2}{2s} \qquad (1.62) \\
&\overset{(1.60),(1.61)}{=} \frac{t||i||_2^2}{2(t+s)^2} + \frac{s||i||_2^2}{2(t+s)^2} \\
&= \frac{||i||_2^2}{2(t+s)} \\
&\overset{(1.58)}{=} \alpha_{t+s}(i). \qquad (1.63)
\end{aligned}$$

Let

$$(b_t \dot{+} b_s)(i) = R_{\mu,x}((\alpha_t \square \alpha_s)(i)). \tag{1.64}$$

The structuring element b_t fulfils the semi-group property as follows

$$\begin{aligned}
b_t(i) \dot{+} b_s(i) &\overset{(1.64)}{=} R_{\mu,x}((\alpha_t \square \alpha_s)(i)) \qquad (1.65) \\
&\overset{(1.63)}{=} R_{\mu,x}(\alpha_{t+s}(i)) \qquad (1.66) \\
&\overset{(1.57)}{=} b_{t+s}(i) \qquad (1.67)
\end{aligned}$$

Remark 1.4.1. *Note that for $E \subset \mathbb{Z}^q$ it follows that $\overline{oi} \not\subset E$. Thus, the equality* (1.62) *does only hold for $j^* \in E$ and some $t, s > 0$. If $j^* \notin E$ it holds that*

$$\inf_{j \in E} \left\{ \frac{||i-j||_2^2}{2t} + \frac{||j||_2^2}{2s} \right\} \geq \frac{||i-j^*||_2^2}{2t} + \frac{||j^*||_2^2}{2s}.$$

We illustrate the construction for $d = 3$: The rotation matrix $R_{\mu,x}$ rotates x on the great circle $\mathcal{GC}_{\mu,x}$. Thus, the structuring function is symmetric since a rotation on $\mathcal{GC}_{\mu,x}$ can be represented by a rotation matrix in $SO(2)$ and $b_t(i) = b_t(-i)$ due to (1.58). We use $R_{\mu,x}$ to move a pixel value $x \in \mathcal{S}^2$ towards μ or away from μ on $\mathcal{GC}_{\mu,x}$. Therefore, we define the operation $x - b_t$ and $x + b_t$, which are illustrated in Figure 1.4, as follows:

$$x - b_t(i) := R_{\mu,x}(\alpha_-)x \tag{1.68}$$

with

$$\alpha_- = \begin{cases} \alpha_t(i), & \text{for } \alpha_t(i) \in [0, \theta] \\ \theta, & \text{for } \alpha_t(i) \in (\theta, 2\pi). \end{cases}$$

$$x + b_t(i) := R_{\mu,x}^T(\alpha_+)x \tag{1.69}$$

with

$$\alpha_+ = \begin{cases} \alpha_t(i), & \text{for } \alpha_t(i) \in [0, \pi - \theta] \\ \pi - \theta, & \text{for } \alpha_t(i) \in (\pi - \theta, 2\pi). \end{cases}$$

Note that $x - b_t$ has a smaller geodesic distance to μ as x, and $x + b_t$ has a larger geodesic distance to μ as x.

Remark 1.4.2 (Fixation of a vector)**.** *We need the restriction of α_- to θ if $\alpha_t(i) \in (\theta, 2\pi)$ and of α_+ to $\pi - \theta$ if $\alpha_t(i) \in (\pi - \theta, 2\pi)$ to achieve the ordering relation in* (1.70)*. Otherwise it would be possible to rotate x beyond μ which would decrease $h_I(x - b_t(i))$ or it would be possible to rotate x beyond $-\mu$ which would increase $h_I(x + b_t(i))$. This can be interpreted as fixing the vector at μ or $-\mu$, respectively. If we fix the vector at μ or $-\mu$, the semi-group property is no longer valid.*

With these restrictions it follows that

$$h_I(x + b_t) \leq h_I(x) \leq h_I(x - b_t). \tag{1.70}$$

We obtain (in some sense) analogue properties to (1.10)−(1.12):

1. b_t is non-positive w.r.t. h_I in the sense that for rotations of x away from μ its h_I-depth decreases, i.e.

$$h_I(x + b_t(i)) - h_I(x) \leq 0. \tag{1.71}$$

2. b_t is monotonically decreasing w.r.t. h_I in the sense that for increasing distance between pixel positions the h_I-depth decreases, i.e.

$$h_I(x + b_t(i)) \geq h_I(x + b_t(i')), \quad ||i||_2 < ||i'||_2. \tag{1.72}$$

3. b_t has a global maximum at the origin w.r.t. h_I in the sense that $x + b_t(i) = x$ if $i = 0 \in E$ and the h_I-depth is unchanged, i.e.

$$h_I(x + b_t(0)) - h_I(x) = 0. \tag{1.73}$$

Note that the rotation matrix $R_{\mu,x}$ is not necessary to calculate $x + b_t$ and $x - b_t$, respectively: The projection of $x + b_t$ on μ is

$$(x + b_t(i))^T \mu = \cos(\theta + \alpha_+) \tag{1.74}$$

and the projection of $x - b_t$ on μ is

$$(x - b_t(i))^T \mu = \cos(\theta - \alpha_-), \tag{1.75}$$

see Figure 1.4. Let z_+ be the tangential part of $x + b_t$, i.e.,

$$z_+ = (I_d - \mu\mu^T)(x + b_t(i)) \tag{1.76}$$

with length

$$||z_+||_2 \overset{(1.18),(1.74)}{=} \sqrt{1 - \cos^2(\theta + \alpha_+)}, \tag{1.77}$$

and let z_- be the tangential part of $x - b_t$, i.e.,

$$z_- = (I_d - \mu\mu^T)(x - b_t(i)) \tag{1.78}$$

with length

$$||z_-||_2 \overset{(1.18),(1.75)}{=} \sqrt{1 - \cos^2(\theta - \alpha_-)}. \tag{1.79}$$

The tangential part z of x points in the same direction as the tangential part z_+ (z_-) of $x + b_t$ ($x - b_t$), see Figure 1.4. Thus,

$$\frac{z_+}{||z_+||_2} = \frac{z_-}{||z_-||_2} = \frac{z}{||z||_2}. \tag{1.80}$$

Then,

$$z_+ \overset{(1.77)}{=} \frac{z_+}{||z_+||_2}\sqrt{1 - \cos^2(\theta + \alpha_+)} \overset{(1.80)}{=} \frac{z}{||z||_2} \cdot \sin(\theta + \alpha_+) \tag{1.81}$$

and

$$z_- \overset{(1.79)}{=} \frac{z_-}{||z_-||_2}\sqrt{1 - \cos^2(\theta - \alpha_-)} \overset{(1.80)}{=} \frac{z}{||z||_2} \cdot \sin(\theta - \alpha_-). \tag{1.82}$$

Finally, $x + b_t$ can be derived from

$$x + b_t(i) \overset{(1.17)}{=} \left((x + b_t(i))^T \mu\right)\mu + z_+ \tag{1.83}$$

$$\overset{(1.74)(1.81)}{=} \cos(\theta + \alpha_+)\mu + \frac{z}{||z||_2}\sin(\theta + \alpha_+) \tag{1.84}$$

and $x - b_t$ can be derived from

$$x - b_t(i) \overset{(1.17)}{=} \left((x - b_t(i))^T \mu\right)\mu + z_- \tag{1.85}$$

$$\overset{(1.75)(1.82)}{=} \cos(\theta - \alpha_-)\mu + \frac{z}{||z||_2}\sin(\theta - \alpha_-). \tag{1.86}$$

1.4.2 Morphological multi-scale operators for directional images

Let b_t be as in Equation (1.57). The multi-scale h_I-erosion ε_{b_t} of a directional image I at pixel position $i \in E$ is (implicitly) defined by

$$h_I(\varepsilon_{b_t}(I))(i) = \inf_{j \in E}\{h_I(I(j) - b_t(j-i))\}, \tag{1.87}$$

where $I(j) - b_t(j-i)$ is defined in Equation (1.68). Analogously, the multi-scale h_I-dilation δ_{b_t} of a directional image I at pixel position $i \in E$ is (implicitly) defined by

$$h_I(\delta_{b_t}(I))(i) = \sup_{j \in E}\{h_I(I(j) + b_t(j-i))\}, \tag{1.88}$$

where $I(j) + b_t(j-i)$ is defined in Equation (1.69).

The interpretation of the multi-scale operators is as follows: We want to rotate the vector $I(j)$ depending on $||i-j||_2$ and the scale t towards μ (h_I increases) or towards $-\mu$ (h_I decreases).

Multi-scale h_I-opening, h_I-closing, morphological gradient and shock filter can be defined as analogue to their flat counterparts.

Remark 1.4.3. *Note that* (1.87) *and* (1.88) *reduce to* (1.42) *and* (1.43)*, respectively, if*

$$b_t(j-i) = \begin{cases} R_{\mu,x}(0), & j - i \in B \\ R_{\mu,x}^T(\pi - \theta), & \text{if } j - i \notin B \text{ and we calculate } h_I(I(j) + b_t(j-i)) \\ R_{\mu,x}(\theta), & \text{if } j - i \notin B \text{ and we calculate } h_I(I(j) - b_t(j-i)) \end{cases}$$

with B the structuring element and $\theta = \arccos\left((I(j))^T\mu\right)$.

1.4.2.1 Properties

The properties of the multi-scale operators are analogous to their flat counterparts. Furthermore, it holds that ε_{b_t} and δ_{b_t} are h_I-ordered w.r.t. scale, i.e., if $0 < s < t$ then

$$\varepsilon_{b_t}(I)(i) \leq_{h_I} \varepsilon_{b_s}(I)(i) \leq_{h_I} I(i) \leq_{h_I} \delta_{b_s}(I)(i) \leq_{h_I} \delta_{b_t}(I)(i) \tag{1.89}$$

for all $i \in E$.

1.5 Applications

In this section, we investigate the effect of the morphological operators on generated $\mathcal{S}^2$-valued images and compare them to their standard grey-scale counterparts. As real application example, we enhance changes in the displacement field of a compressed glass foam.

1.5.1 Flat morphological operators

To investigate the newly defined flat morphological operators, we generate a 2-dimensional $\mathcal{S}^2$-valued image I mimicking direction vectors obtained from two fibres on a homogeneous background. That is, the image contains two objects consisting of vectors with a small angular deviation from μ, see Figure 1.5. The background is formed by vectors directed along a plane perpendicular to μ. Flat h_I-dilation and flat h_I-erosion (Figure 1.6) show a similar behaviour as their standard grey-scale counterparts. Dilation expands objects. That is, directions of background pixels that are close to the edge of objects are rotated to match the directions of the objects. An erosion shrinks objects, i.e., object vectors at the edge are rotated so that they are assigned to the image background.

In a similar manner, the flat h_I-opening removes foreground objects that are smaller than the structuring element. Figure 1.7 reveals that object vectors in an object of size smaller than the structuring

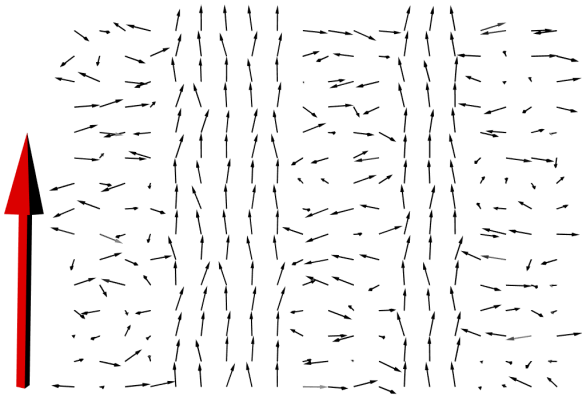

Figure 1.5: Original $\mathcal{S}^2$-valued image I. The direction vectors within the fibres are rotationally symmetric around μ (large red vector). Their angular deviation from μ is uniformly drawn from $(0, \pi/8)$. Background vectors are also rotationally symmetric around μ. Their angular deviation from μ is uniformly drawn from $[\pi/8, 7\pi/10]$.

element B are rotated such that we assign them to the image background. The flat h_I-closing removes small holes in the foreground. Vectors with large angular deviation from μ within a background object of size smaller than B are rotated to become part of the image foreground.

The results of shock filtering of I is shown in Figure 1.8. The edges between the two objects and the background pixels are enhanced.

1.5.1.1 Duality with respect to C

The property of duality between erosion and dilation w.r.t. the complement operator C is illustrated in Figure 1.9. We apply on $\mathrm{C}\, I$ (Figure 1.9a) the h_I-dilation which results in Figure 1.9b. Furthermore, we apply on $\varepsilon_B(I)$ (Figure 1.9c) the complement C which results in Figure 1.9d. We observe that Figure 1.9b corresponds to Figure 1.9d which illustrates $\delta_B(\mathrm{C}\, I) = \mathrm{C}\, \varepsilon_B(I)$.

1.5.2 Morphological multi-scale operators

We illustrate the multi-scale h_I-dilation and h_I-erosion on I. $\delta_{b_t}(I)$ and $\varepsilon_{b_t}(I)$ behave like their grey-scale counterparts: Figure 1.10 shows that $\delta_{b_t}(I)$ enlarges objects in the foreground and Figure 1.11 shows that $\varepsilon_{b_t}(I)$ shrinks objects in the foreground. Of course, the enlargement and shrinkage depend on the continuous scale parameter t. Note that fixation at μ or $-\mu$, respectively, in the sense of Remark 1.4.2 was needed. The behaviour of multi-scale h_I-dilation and h_I-erosion reminds of quadratic scaling, especially due to the definition of α_t in (1.58). For an example of quadratic scaling of an erosion scale-space (resp. a parabolic morphological scale-space), see [19, Figure 5.1].

1.5.3 Enhancement of fault zones in compressed glass foam

To characterise the structural behaviour of complex materials during loading, mechanical tests and simultaneous micro-computed tomography imaging (in situ μCT) can be used to estimate local displacements of the material on the micro scale. We analyse a glass foam which consists of very thin struts, see Figure 1.12a.

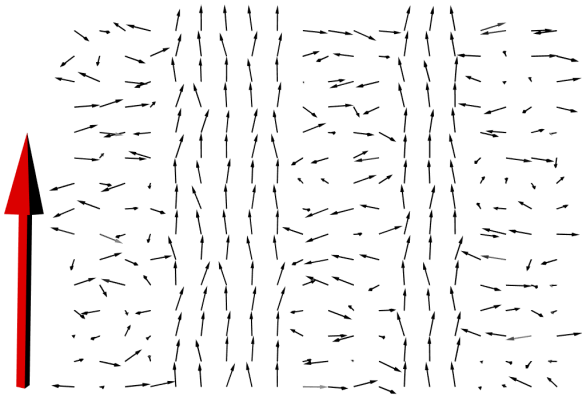

(a) Original image I

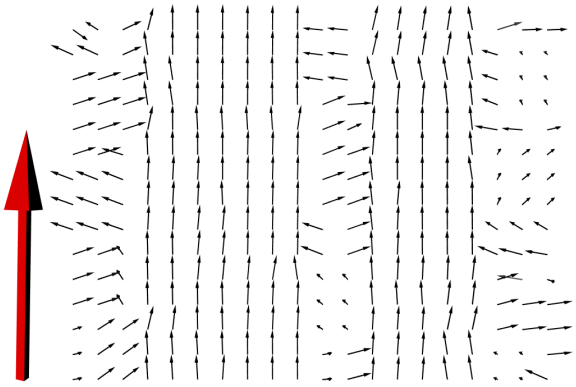

(b) $\delta_B(I)$, B is 3×3

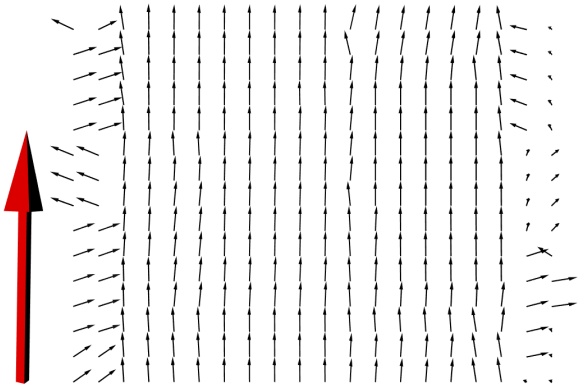

(c) $\delta_B(I)$, B is 5×5

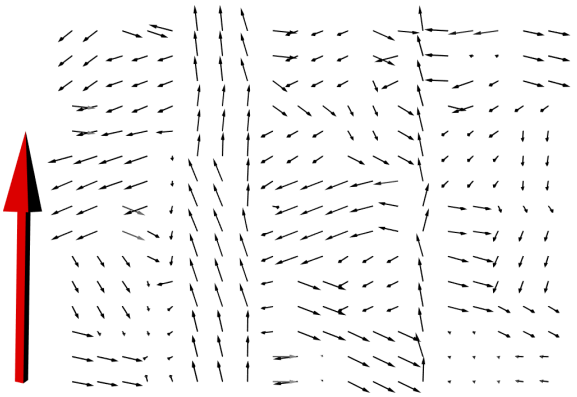

(d) $\varepsilon_B(I)$, B is 3×3

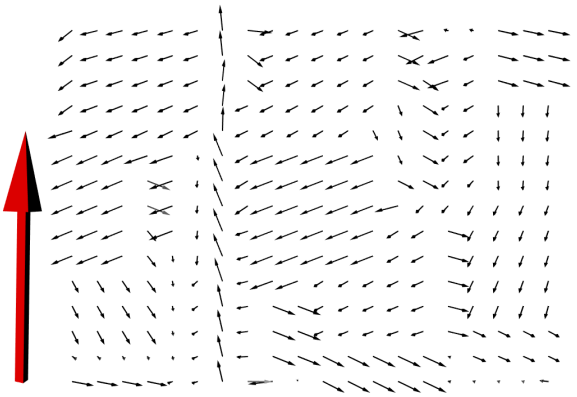

(e) $\varepsilon_B(I)$, B is 5×5

Figure 1.6: Original $\mathcal{S}^2$-valued image I (a), flat h_I-dilation δ_B (b,c) and flat h_I-erosion ε_B (d,e) with B a square as structuring element. The large red vector corresponds to μ.

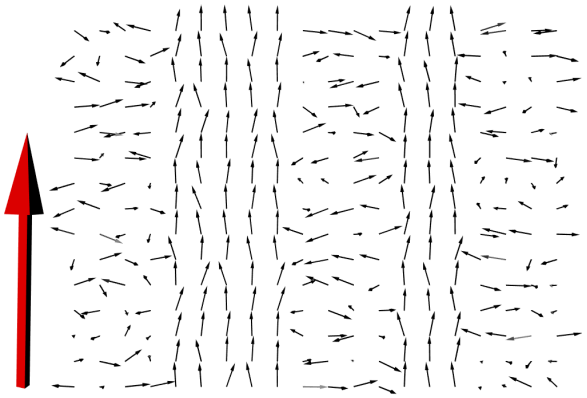

(a) Original image I

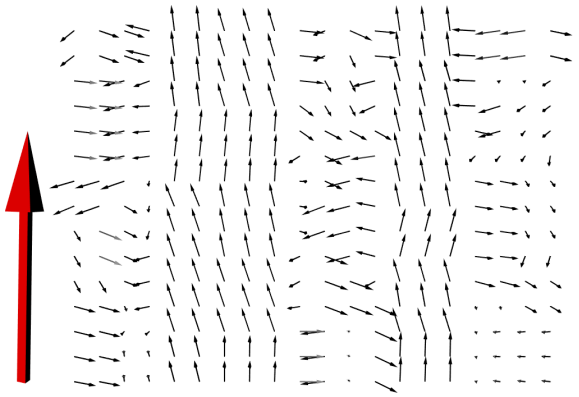

(b) $\gamma_B(I)$, B is 3×3

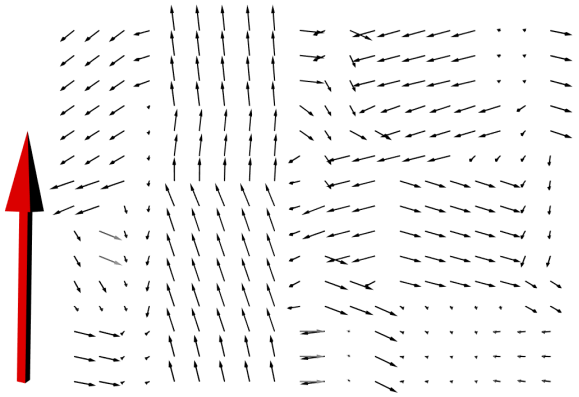

(c) $\gamma_B(I)$, B is 5×5

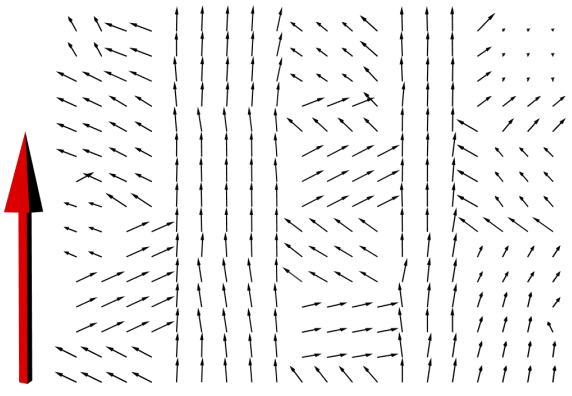

(d) $\varphi_B(I)$, B is 3×3

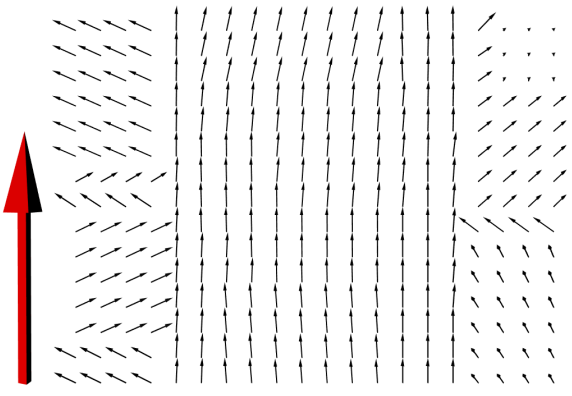

(e) $\varphi_B(I)$, B is 5×5

Figure 1.7: Original $\mathcal{S}^2$-valued image I (a), flat h_I-opening γ_B (b,c) and flat h_I-closing φ_B (d,e) with B a square as structuring element. The large red vector corresponds to μ.

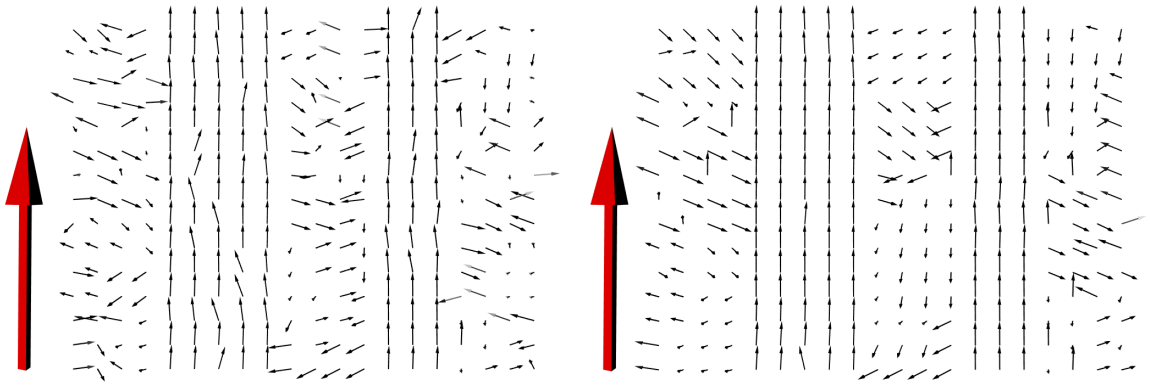

(a) $\mathrm{sf}_B(I)$, B is 3×3 (b) $\mathrm{sf}_B(I)$, B is 5×5

Figure 1.8: Flat shock filter $\mathrm{sf}_B(I)$ with B a square as structuring element.

The μCT images were recorded while the glass foam was compressed in Z-direction. The foam is expected to fail very suddenly due to its thin struts. Nogatz et al. [39] computed the displacement field for the transition from strain level 1% (Figure 1.12b) to strain level 3.8% (Figure 1.12c) which is shown in Figure 1.13a. During compression, a fault zone forms which is now post-processed by directional morphology. To this end, our flat morphological operators are applied to the directional component of the displacement vectors. That is, the vectors were normalised for the calculation of the morphological operators and were subsequently scaled back to their original length. As we mostly expect compression along the compression direction, we choose $\mu = (0, 0, 1)$ and define $h_I = D_\mu^{proj}$. Here, the analysis is limited to one slice of the 3D image.

We enhance the fault zone with the morphological gradient, see Figure 1.13b. If motion estimation algorithms fail to reconstruct these sharp edges, we can enhance them by an h_I-erosion, as shown in Figure 1.13c. Some other materials however are known to show creep before failure. Here, a smoother transition seems more reasonable, which is obtained by a h_I-dilation, see Figure 1.13d.

h_I-opening (Figure 1.13f) and h_I-closing (Figure 1.13e) remove misalignment in the transition between the two regions.

1.6 Conclusion

We have formulated the theory of mathematical morphology for directional images. The required ordering for unit vectors is derived from the directional projection depth which enables a sound definition of $\mathcal{S}^{d-1}$-valued morphological (multi-scale) operators and filters. Furthermore, we gave a background/-foreground representation of directional images and rank filters using directional quantiles from [11]. Relations of introduced morphological operators to their grey-scale counterparts are emphasised. Furthermore, we used the operators to enhance regions of significant changes in a displacement field of a glass foam under compression.

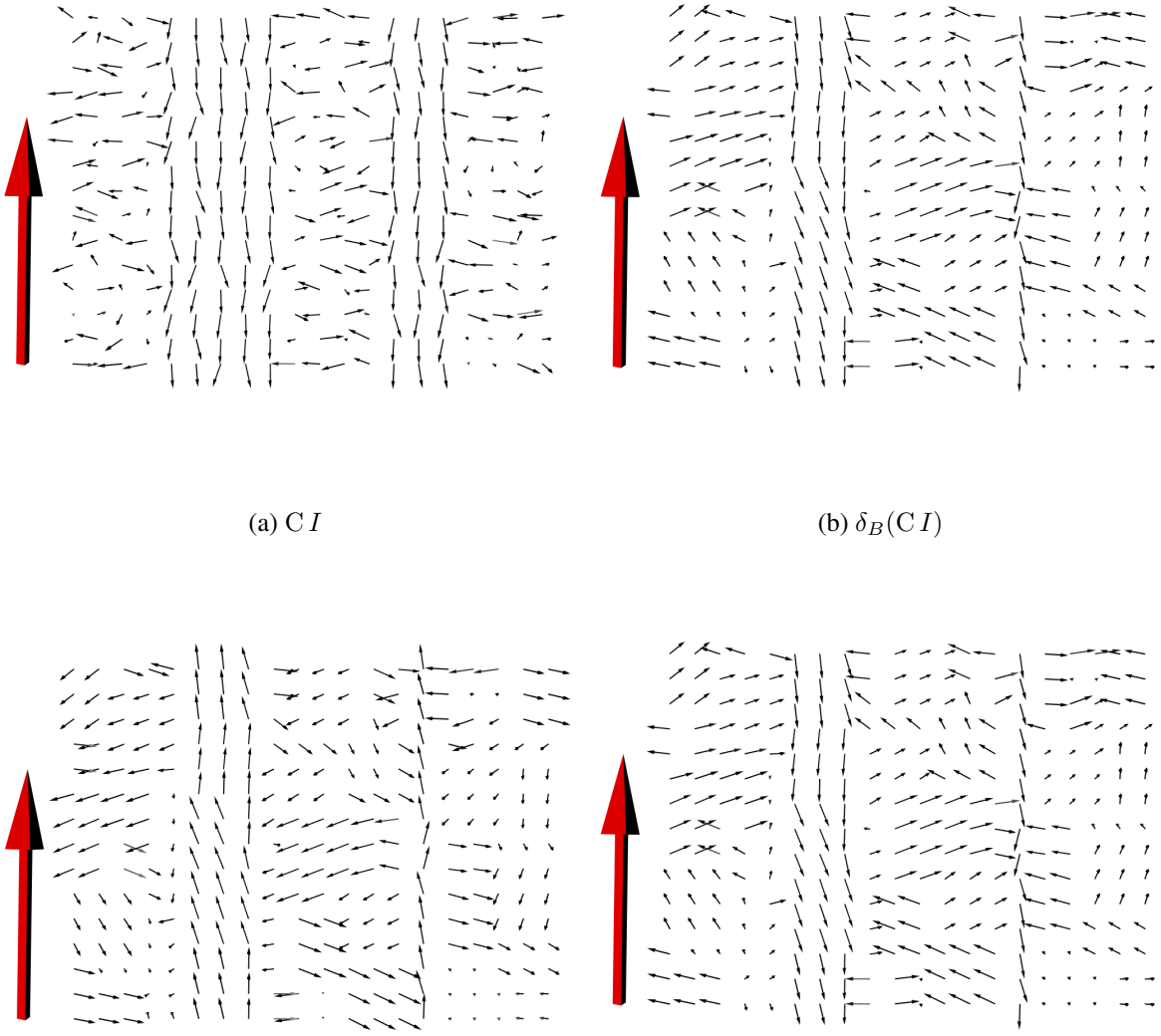

(a) $\mathrm{C}\, I$ (b) $\delta_B(\mathrm{C}\, I)$

(c) $\varepsilon_B(I)$ (d) $\mathrm{C}\, \varepsilon_B(I)$

Figure 1.9: Duality between erosion and dilation w.r.t. the complement operator C. Complement of I (a), flat dilation of $\mathrm{C}\, I$ (b), flat erosion of I (c), and complement of $\varepsilon_B(I)$ (d). B is a 3×3-square centred at the origin.

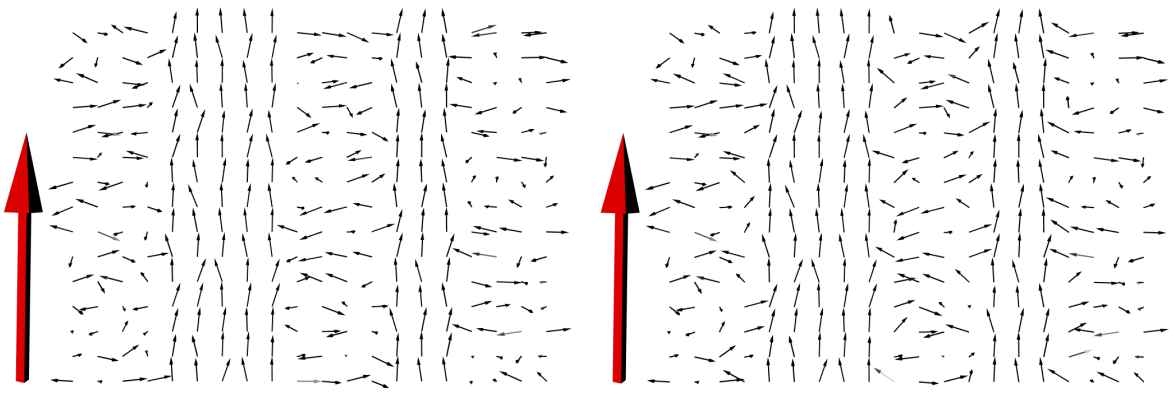

(a) $t = 0.1$ (b) $t = 0.5$

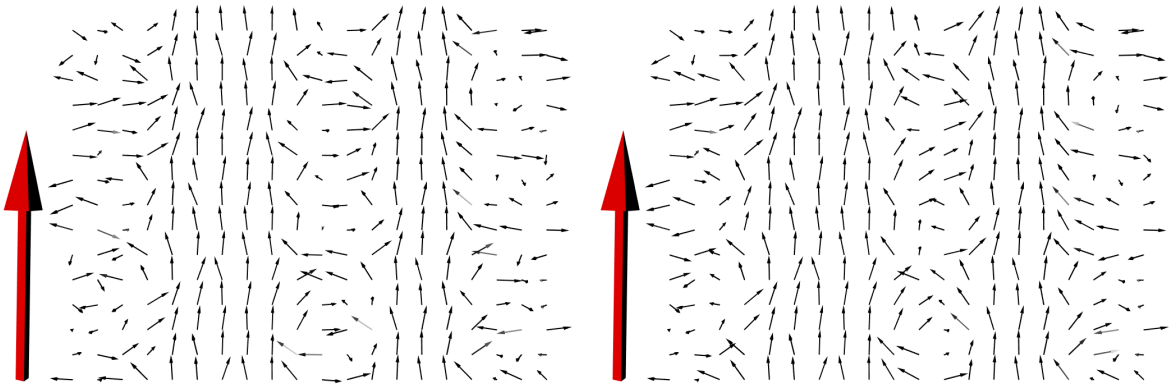

(c) $t = 0.7$ (d) $t = 0.9$

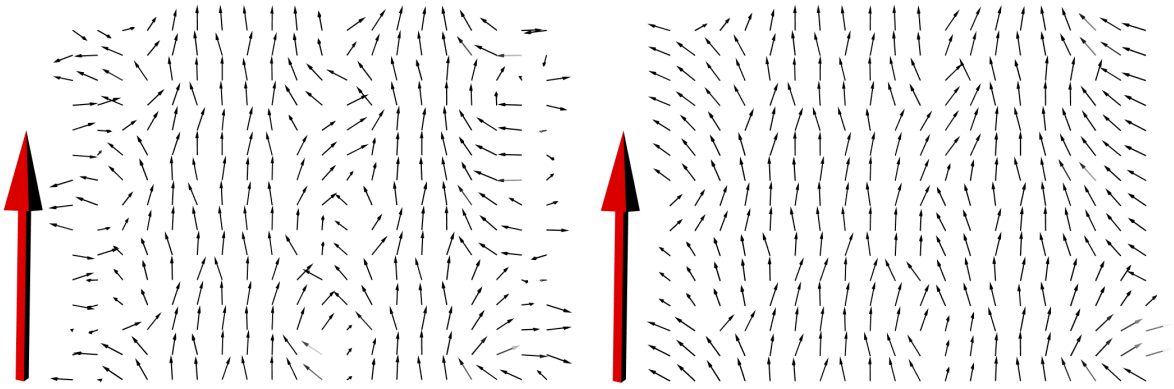

(e) $t = 1.1$ (f) $t = 2$

Figure 1.10: $\delta_{b_t}(I)$ at scales $t = 0.1, 0.5, 0.7, 0.9, 1.1, 2$. The large red vector corresponds to μ.

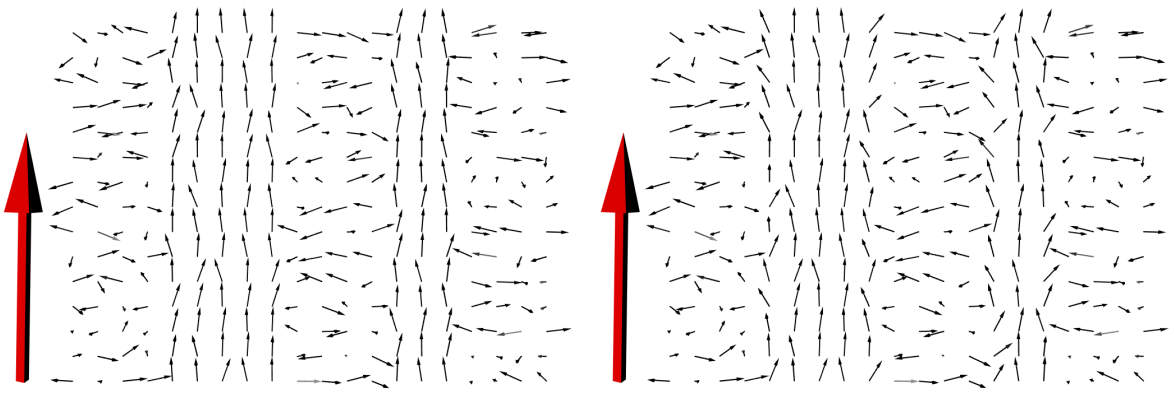

(a) $t = 0.1$ (b) $t = 0.5$

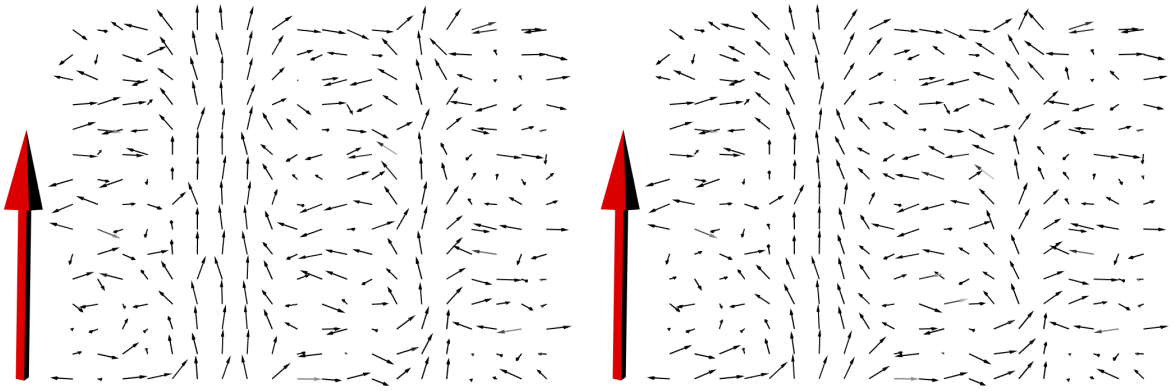

(c) $t = 0.7$ (d) $t = 0.9$

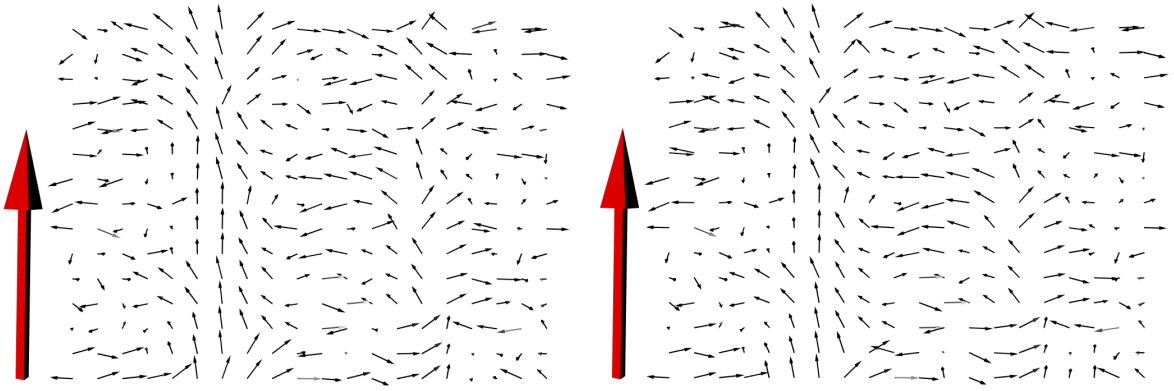

(e) $t = 1.1$ (f) $t = 2$

Figure 1.11: $\varepsilon_{b_t}(I)$ at scales $t = 0.1, 0.5, 0.7, 0.9, 1.1, 2$. The large red vector corresponds to μ.

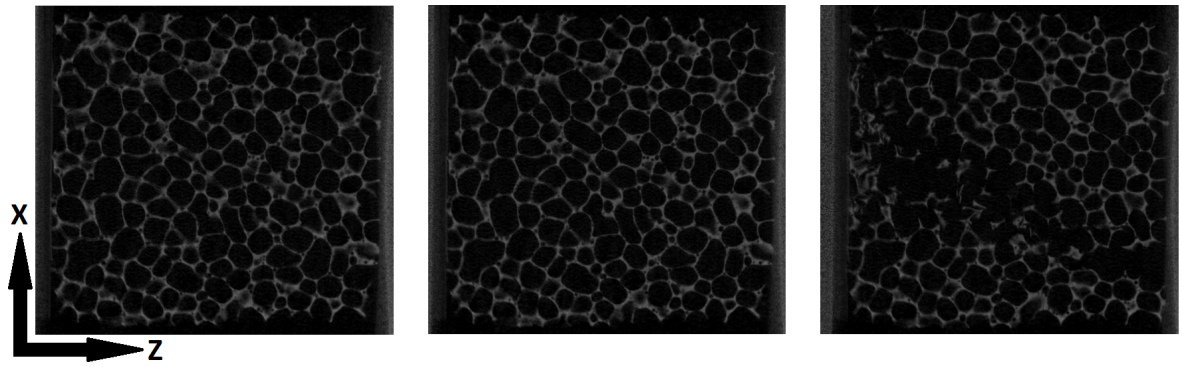

(a) Unloaded glass foam (b) Strain level 1% (c) Strain level 3.8%

Figure 1.12: XZ-slice of the unloaded (a) and loaded (b,c) glass foam analysed in [39]. The thin struts are bright. The displacement field is was estimated between image (b) and (c) where the strain level was increased from 1% to 3.8%. Sample, in situ testing and imaging by TU Bergakademie Freiberg.

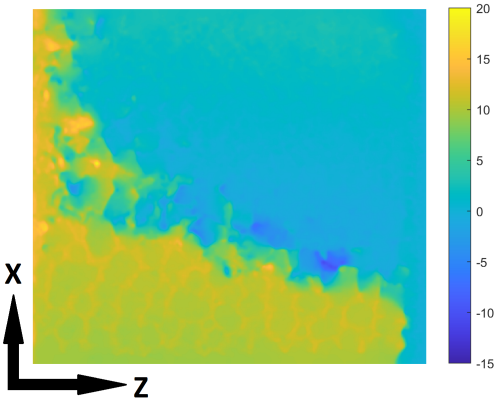

(a) Displacement field

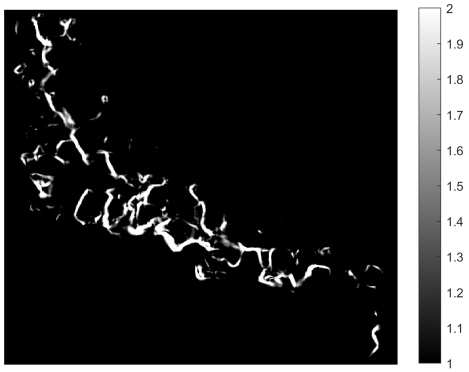

(b) Morphological gradient

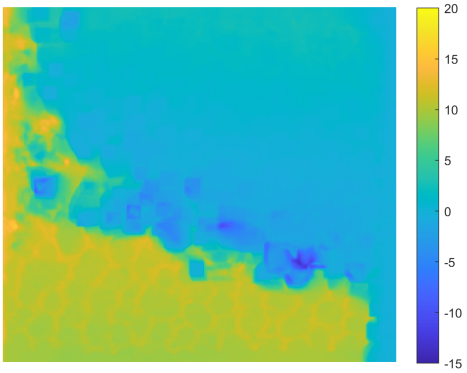

(c) h_I-erosion

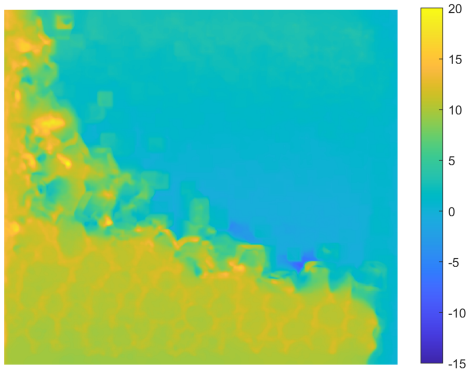

(d) h_I-dilation

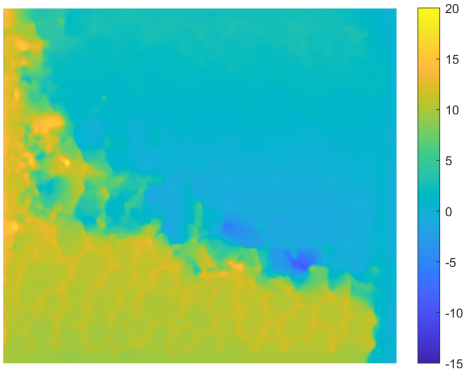

(e) h_I-opening

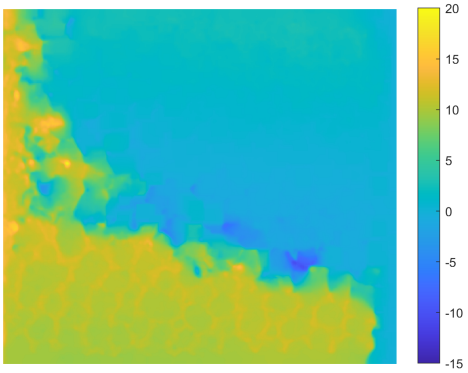

(f) h_I-closing

Figure 1.13: XZ-slice of the displacement field from Nogatz et al. [39]. Yellow colour indicates movement along the Z-direction, and blue refers to the opposite direction. The computed displacement field reflects the influence on the microstructure during compression (a). The morphological gradient (with B a 3×3 square) enhances the fault zone (b). The results of other morphological operators are given in (c-f) with B a 15×15 square.

Chapter 2

Quantiles and depth for directional data from elliptically symmetric distributions

2.1 Introduction

The classes of rotationally symmetric distributions and elliptically symmetric distributions in $\mathbb{R}^d$ have been well investigated by Kelker [40], Cambanis et al. [41] and Fang et al. [42]. A random vector $X \in \mathbb{R}^d$ has a rotationally symmetric distribution if the distribution of X is identical to the distribution of OX for all $O \in SO(d)$. Rotationally symmetric distributions are often regarded as the most natural non-uniform distributions in $\mathbb{R}^d$. For instance, the charge distribution of an electric field is rotationally symmetric around its source. In practice, not all real phenomena can be represented by symmetric models. Elliptically symmetric distributions extend the class of rotationally symmetric distributions. Note that a random vector with an elliptically symmetric distribution can be transformed into a random vector with a rotationally symmetric distribution via a linear transformation.

These concepts of symmetry transfer to the sphere $\mathcal{S}^{d-1}$ for the description and analysis of directional data. Distributions on $\mathcal{S}^{d-1}$ which are rotationally symmetric about a direction $\mu \in \mathcal{S}^{d-1}$ are also often regarded as a natural non-uniform distribution on $\mathcal{S}^{d-1}$ [27]. In most cases, rotationally symmetric distributions have tractable normalising constants (compared with other non-rotationally symmetric models). Note that the density $f(x)$ of a rotationally symmetric distribution is proportional to a function $f(x^T\mu)$. Thus, a projection on μ enables a one-dimensional analysis of the distribution, for example, its concentration around μ. The class of rotationally symmetric distributions about a direction $\mu \in \mathcal{S}^{d-1}$ is denoted by $\mathcal{R}_\mu$.

In practice, however, symmetric models are often too restrictive. For instance, Leong and Carlile [43] illustrated that rotational symmetry about a direction is a too strong assumption for a directional data set from neurosciences. Kent [44] has fitted his elliptical model to a data set of 34 measurements of the directions of magnetisation for samples from the Great Whin Sill (Northumberland, England). As in $\mathbb{R}^d$, distributions that are elliptically symmetric about a direction μ on $\mathcal{S}^{d-1}$ are an extension of the rotationally symmetric distributions. The contours are more flexible to form elliptical shapes. Due to the curved shape of the sphere, the transition from distributions which are rotationally symmetric about $\mu \in \mathcal{S}^{d-1}$ to distributions which are elliptically symmetric about μ is not obvious. A remedy to this problem is to linearise $\mathcal{S}^{d-1}$ at some base point μ. The linear space resulting from this is called the tangent space at μ and denoted by $T_\mu\mathcal{S}^{d-1}$. Then, we can provide a transformation between the two distributions in the tangent space analogous to $\mathbb{R}^d$.

Ley et al. [11] introduced a concept of quantiles and depth for directional data. They showed that their quantiles are asymptotically normal and established a Bahadur-type representation [45] for directional data $X \sim F_X \in \mathcal{R}_\mu$. A Monte Carlo simulation study corroborated their theoretical results. Statistical tools, like directional DD- and QQ-plots and a quantile-based goodness-of-fit test, were defined and illustrated on a data set of cosmic rays. Their results are canonical for rotationally symmetric distributions. But their concept suffers from the disadvantage of producing rotationally symmetric depth

contours, even if the underlying distribution has elliptical contours.

In this chapter, we present a procedure solving the latter issue if the underlying distribution has elliptical contours. The chapter is organised as follows. In Section 2.2, we first introduce the considered distributions. Following Pennec [46], we relate the directional density contours on $\mathcal{S}^{d-1}$ with their projection into a tangent space $T_\mu\mathcal{S}^{d-1}$, and extend the notation of Mahalanobis transformation to $\mathcal{S}^{d-1}$. Furthermore, we summarise the findings of Ley at al. [11]. Section 2.3 contains our main contribution. The idea is to map the unit vectors into the tangent space $T_\mu\mathcal{S}^{d-1}$ where μ is the median direction of the unit vectors. The mapped vectors are elliptically symmetric around the origin in $T_\mu\mathcal{S}^{d-1}$. The multivariate Mahalanobis transformation [46, 47] is applied to the mapped vectors in $T_\mu\mathcal{S}^{d-1}$. The transformed vectors are rotationally symmetric distributed around the origin in $T_\mu\mathcal{S}^{d-1}$. These are mapped back to $\mathcal{S}^{d-1}$. This procedure results in unit vectors which are rotationally symmetric about μ. Thus, we can exploit the results from [11]. All transformations are diffeomorphic such that we can trace back the results to the original unit vectors. Section 2.4 affirms our findings by a Monte Carlo study. Furthermore, we apply our approach to a real-world data set from [48]: Directions of short steel fibres crossing a crack in ultra-high performance fibre-reinforced concrete (UHPFRC).

2.2 Basics

The notation is as in Section 1.2.1.

2.2.1 Rotational and elliptical symmetric distributions in $\mathbb{R}^d$

Before we restrict our attention to distributions on the sphere, we give the definition of rotationally and elliptically symmetric distributions in $\mathbb{R}^d$. These will be used when we linearise the sphere $\mathcal{S}^{d-1}$ at μ and transfer density contours from $\mathcal{S}^{d-1}$ into the (flat) tangential space $T_\mu\mathcal{S}^{d-1}$. See [41] for a detailed introduction.

Definition 2.2.1 (Rotationally symmetric distribution)**.** *Let $V \in \mathbb{R}^d$ be a random vector. The distribution of V is rotationally symmetric if and only if*

$$V \overset{D}{=} OV \tag{2.1}$$

for every $O \in SO(d)$.

Every random vector $V \in \mathbb{R}^d$ following a rotationally symmetric distribution can be represented as

$$V \overset{D}{=} RU \tag{2.2}$$

where $U \sim Unif(\mathcal{S}^{d-1})$ (uniformly distributed on $\mathcal{S}^{d-1}$) and independent of the real-valued random variable R with distribution F_R. U gives the direction of V and R is the length of V.

Definition 2.2.2 (Elliptically symmetric distribution)**.** *Let $W \in \mathbb{R}^d$ be a random vector. The distribution of W is elliptically symmetric if and only if*

$$W \overset{D}{=} m + R\Sigma^{1/2}U \tag{2.3}$$

with $m \in \mathbb{R}^d$, $U \sim Unif(\mathcal{S}^{d-1})$, R real-valued with distribution F_R and $\Sigma \in \mathbb{R}^{d\times d}$ a symmetric, positive definite matrix, and U and R are independent.

If $W \in \mathbb{R}^d$ has an elliptically symmetric distribution, we write $W \sim E(m, \Sigma, F_R)$. The centre of W is m and $\Sigma^{1/2}U$ produces the elliptical density contours. From now on, let $m = 0_d$ such that $W \sim E(0_d, \Sigma, F_R)$ is centred at the origin. The matrix Σ is called the dispersion or scatter matrix of W. Since Σ is symmetric, positive definite it follows that $\Sigma^{1/2}, \Sigma^{-1}$ and $\Sigma^{-1/2}$ are well defined. The spectral decomposition of Σ describes the semi-axes of the elliptical contours. For $\Sigma = I_d$, we are in the rotationally symmetric case.

Elliptical symmetry is connected to rotational symmetry as follows.

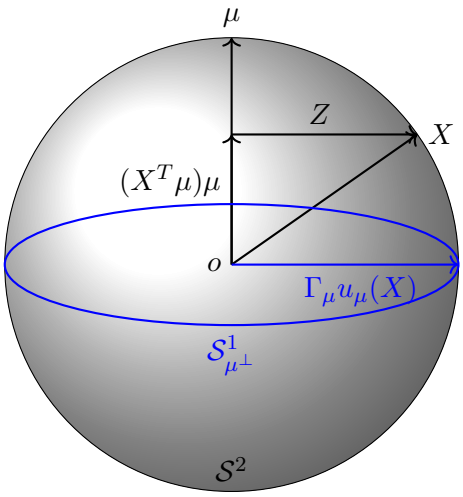

Figure 2.1: Illustration of $\Gamma_\mu u_\mu(X)$ for $d = 3$. $\Gamma_\mu u_\mu(X)$ to corresponds to the direction of Z.

Proposition 2.2.1. *$W \sim E(0_d, \Sigma, F_R)$ if and only if $V = \Sigma^{-1/2}W \sim E(0_d, I_d, F_R)$.*

Proof. Let $W \sim E(0_d, \Sigma, F_R)$. By Definition 2.2.2 follows that $W \overset{D}{=} R\Sigma^{1/2}U$. Then,

$$V = \Sigma^{-1/2}W \overset{D}{=} R\Sigma^{-1/2}\Sigma^{1/2}U = RU. \tag{2.4}$$

Thus, $V \sim E(0_d, I_d, F_R)$. The other direction follows analogously. □

2.2.2 Rotational and elliptical symmetry about a direction on $\mathcal{S}^{d-1}$

We follow the notation of García-Portugués et al. [27]. Let $\Gamma_\mu = \left(\Gamma_\mu^{(1)}, \ldots, \Gamma_\mu^{(d-1)}\right) \in \mathbb{R}^{d\times d-1}$, where the columns $\Gamma_\mu^{(i)} \in \mathbb{R}^d,\ i = 1, \ldots, d-1$, build an orthonormal basis of the orthogonal complement to μ so that

$$\Gamma_\mu^T\Gamma_\mu = I_{d-1}, \tag{2.5}$$
$$\Gamma_\mu\Gamma_\mu^T = I_d - \mu\mu^T. \tag{2.6}$$

Define

$$u_\mu(X) := \frac{\Gamma_\mu^T X}{||\Gamma_\mu^T X||_2} = \frac{\Gamma_\mu^T X}{\sqrt{(1-(X^T\mu)^2}} \in \mathcal{S}^{d-2}_{\mu^\perp}. \tag{2.7}$$

$||\Gamma_\mu^T X||_2 = \sqrt{(1-(X^T\mu)^2}$ holds since

$$\Gamma_\mu u_\mu(X) = \frac{\Gamma_\mu\Gamma_\mu^T X}{||\Gamma_\mu^T X||_2}, \qquad \text{(apply } \Gamma_\mu \text{ on both sides of (2.7))} \tag{2.8}$$
$$\Rightarrow ||\Gamma_\mu u_\mu(X)||_2 = \frac{||\Gamma_\mu\Gamma_\mu^T X||_2}{||\Gamma_\mu^T X||_2}, \qquad \text{(apply } ||\cdot||_2 \text{ on both sides of (2.8))} \tag{2.9}$$
$$||\Gamma_\mu^T X||_2 = \frac{||\Gamma_\mu\Gamma_\mu^T X||_2}{||\Gamma_\mu u_\mu(X)||_2}, \qquad \text{(rearranged terms of (2.9))}$$
$$\overset{(2.6)}{=} \frac{||(I_d - \mu\mu^T)X||_2}{||\Gamma_\mu u_\mu(X)||_2} \overset{(1.17)}{=} \frac{||Z||_2}{||\Gamma_\mu u_\mu(X)||_2} = \sqrt{(1-(X^T\mu)^2}.$$

The last equality holds with $||\Gamma_\mu u_\mu(X)||_2 = 1$ due to the fact that the columns of Γ_μ build an orthonormal basis of $\mathcal{S}_{\mu^\perp}^{d-2}$ and $u_\mu(X) \in \mathcal{S}_{\mu^\perp}^{d-2}$, and Z the tangential part of X as given in (1.17) has norm $||Z||_2 = \sqrt{(1-(X^T\mu)^2}$. The connection between $u_\mu(X)$ and Z reads

$$Z \overset{(1.17)}{=} (I_d - \mu\mu^T)X \overset{(2.6)}{=} \Gamma_\mu \Gamma_\mu^T X \overset{(2.7)}{=} \sqrt{1-(X^T\mu)^2}\Gamma_\mu u_\mu(X). \tag{2.10}$$

Thus, $\Gamma_\mu u_\mu(X)$ corresponds to the direction of Z, see Figure 2.1.

Definition 2.2.3 (Rotational symmetry about a direction)**.** *Let $X \in \mathcal{S}^{d-1}$ be a random vector and $\mu \in \mathcal{S}^{d-1}$. The distribution of X is rotationally symmetric about μ on $\mathcal{S}^{d-1}$ if and only if $X \overset{D}{=} OX$ for every $O \in SO(d)$ fulfilling $O\mu = \mu$.*

Let $\mathcal{R}_\mu$ be the class of distributions which are rotationally symmetric about $\mu \in \mathcal{S}^{d-1}$.

Theorem 2.2.1 (Watson 1983 [49])**.** *Let $X \sim F_X \in \mathcal{R}_\mu$. Then,*

$$X^T\mu \text{ and } \Gamma_\mu u_\mu(X) \text{ are independent} \tag{2.11}$$

and

$$\Gamma_\mu u_\mu(X) \sim Unif(\mathcal{S}_{\mu^\perp}^{d-2}). \tag{2.12}$$

Projecting X onto a vector space orthogonal to μ yields rotationally symmetric contours. Distributions $F_X \in \mathcal{R}_\mu$ are characterised by densities of the form

$$x \mapsto f_{\mathcal{R}_\mu}(x) = c_d f(x^T\mu), \quad x \in \mathcal{S}^{d-1}, \tag{2.13}$$

where $f : [-1,1] \to \mathbb{R}_{\geq 0}$ is absolutely continuous and c_d a normalising constant [11]. The distribution of $X^T\mu$ is absolutely continuous w.r.t the Lebesgue measure on $[-1,1]$ [26]. The density of $X^T\mu$ reads

$$\tilde{f}(t) = \omega_{d-1}c_d(1-t^2)^{\frac{d-3}{2}}f(t), \tag{2.14}$$

where

$$\omega_{d-1} = \frac{2\pi^{(d-1)/2}}{\Gamma\left(\frac{d-1}{2}\right)} \tag{2.15}$$

is the surface area of $\mathcal{S}^{d-2}$ [27]. A widely known distribution in $\mathcal{R}_\mu$ is the von Mises-Fisher distribution $M_d(\mu,\kappa)$ with

$$f(t) = \exp(\kappa t) \tag{2.16}$$

in (2.13).

Definition 2.2.4 (von Mises-Fisher distribution $M_d(\mu,\kappa)$)**.** *The probability density function of the von Mises–Fisher distribution for a random vector $X \in \mathcal{S}^{d-1}$ is given by*

$$f_{vMF}(x) = c_d \exp(\kappa x^T\mu), \tag{2.17}$$

where $\kappa \geq 0$, $\mu \in \mathcal{S}^{d-1}$, and the normalising constant is equal to

$$c_d = \frac{\kappa^{d/2-1}}{(2\pi)^{d/2}I_{d/2-1}(\kappa)}. \tag{2.18}$$

$I_\nu(z)$ is the order-v modified Bessel function of the first kind

$$I_\nu(z) = \frac{1}{\pi}\int_0^\pi e^{z\cos\theta}\cos\nu\theta\, d\theta - \frac{\sin\nu\pi}{\pi}\int_0^\infty e^{-z\cosh t-\nu t}\, dt, \quad z > 0.$$

The parameters μ and κ are called the mean direction and concentration parameter, respectively. The concentration around μ increases with κ. The $M_d(\mu,\kappa)$ is unimodal for $\kappa > 0$, and is uniform on the sphere for $\kappa = 0$.

A generalisation of the von Mises-Fisher distributions are the Fisher-Bingham distributions [26]. The idea is to add a general quadratic equation in the exponent of the density in (2.13). An example of the Fisher-Bingham distributions is the Kent distribution $K(\mu, \kappa, A)$ [44].

Definition 2.2.5 (Kent distribution $K(\mu, \kappa, A)$)**.** *The probability density function of the Kent distribution for a random vector $X \in \mathcal{S}^{d-1}$ is given by*

$$f_K(x) = c_{d,K} \exp(\kappa x^T \mu + x^T A x), \tag{2.19}$$

where $\kappa \geq 0$, $\mu \in \mathcal{S}^{d-1}$, $A \in Sym(d)$ with $A\mu = 0_d$ and the normalising constant $c_{d,K}$. The parameters μ, κ and A are called the mean direction, concentration and shape parameter, respectively. The concentration around μ increases with κ. $A \in Sym(d)$ controls the shape of the density contours.

For large κ, the Kent distribution has a mode at μ and density contours which are elliptical [34, p.177].

Remark 2.2.1. *Note that the definition of the class $\mathcal{R}_\mu$ does not include that μ is the unique modal direction. However, we restrict our attention to distributions in $\mathcal{R}_\mu \cap \mathcal{F}_\mu$ from now on, where $\mathcal{F}_\mu$ was the class of distributions on $\mathcal{S}^{d-1}$ with a bounded density that admit a unique modal direction μ equal to the Fisher spherical median given in* (1.19) *as described in Section 1.2.5. $M_d(\mu, \kappa) \in \mathcal{R}_\mu \cap \mathcal{F}_\mu$ for $\kappa > 0$, and $K(\mu, \kappa, A) \in \mathcal{F}_\mu$ for $\kappa > 0$ and some matrices $A \in Sym(d)$ given in the next Section.*

2.2.2.1 Examples on $\mathcal{S}^2$

We assume that μ corresponds to the north pole, i.e. $\mu = (0, 0, 1)^T$. Otherwise, we rotate the data by a rotation matrix $O \in SO(3)$ with $O\mu = (0, 0, 1)^T$. We choose

$$\Gamma_\mu = \begin{pmatrix} 1 & 0 \\ 0 & 1 \\ 0 & 0 \end{pmatrix}. \tag{2.20}$$

Then,

$$\Gamma_\mu \Gamma_\mu^T = \mathrm{diag}(1, 1, 0). \tag{2.21}$$

We describe the random vector $X \in \mathcal{S}^{d-1}$ by spherical coordinates as given in Equation (1.14). Thus, the co-latitude Θ equals the angle between X and μ.

Example 2.2.1 (Standardised Kent distribution)**.** *Consider $A = \beta(\xi_1 \xi_1^T - \xi_2 \xi_2^T)$, where $\beta \geq 0$ and (μ, ξ_1, ξ_2) forms an orthogonal matrix. Choosing $\mu = (0, 0, 1)^T$, $\xi_1 = (1, 0, 0)^T$ and $\xi_2 = (0, 1, 0)^T$, we have*

$$A = \mathrm{diag}(\beta, -\beta, 0) \tag{2.22}$$

and get the so-called standardised Kent distribution [34, Section 4.4.5]. Its density reads [34, Eq.(4.443)]

$$f_K(\theta, \phi) = c_{d,\mu,A} \exp\left(\kappa \cos(\theta) + \beta \sin^2(\theta) \cos(2\phi)\right) \sin(\theta), \tag{2.23}$$

where β, with $0 \leq 2\beta < \kappa$, determines the ellipticity of the contours of equal probability. β is called the ovalness parameter. The major and minor axis of the elliptical contours are ξ_1 and ξ_2, respectively. The normalising constant is given by [34, Section 4.4.5]

$$c_{d,\mu,A} = \left[(2\pi)^{\frac{3}{2}} \kappa^{-\frac{1}{2}} \sum_{r=0}^{\infty} \frac{(2r)!}{(r!)^2} \left(\frac{\beta}{\kappa}\right)^{2r} I_{2r+\frac{1}{2}}(\kappa) \right]^{-1} \overset{\kappa \text{ large}}{\approx} \frac{1}{2\pi} \exp(-\kappa) \sqrt{\kappa^2 - 4\beta^2}.$$

Example 2.2.2 (Standardised von Mises-Fisher distribution)**.** *For $\beta = 0$, we derive from (2.23) the density of $M_3(\mu, \kappa)$ the von Mises-Fisher distribution in standardised form [34, Eq.(4.28)]*

$$f_{vMF}(\theta, \phi) = \frac{\kappa}{2\pi(\exp(\kappa) - \exp(-\kappa))} \exp(\kappa \cos(\theta)) \sin(\theta). \tag{2.24}$$

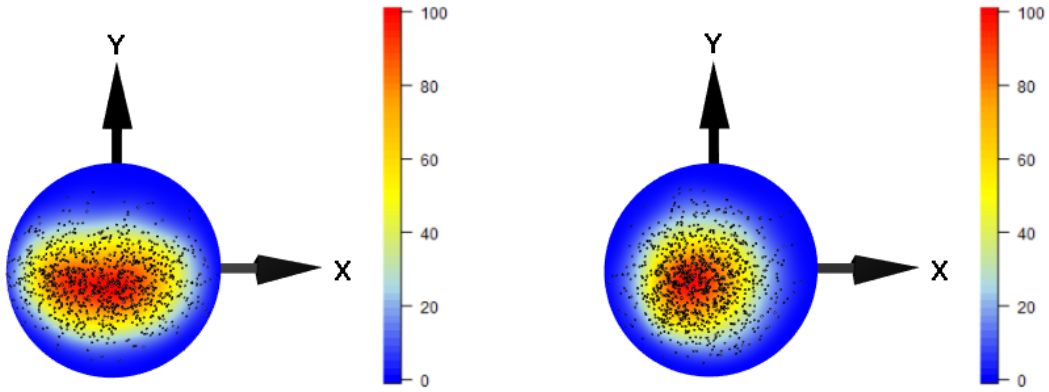

(a) $K(\mu, \kappa, A)$ (b) $M_3(\mu, \kappa)$

Figure 2.2: (a) 500 realisations of a standardised Kent $K(\mu, \kappa, A)$-distributed random vector with $\kappa = 12$ and $\beta = 5$. (b) 500 realisations of a standardised von Mises-Fisher $M_3(\mu, \kappa)$-distributed random vector with $\kappa = 12$. The Z-direction points out of the page.

See Figure 2.2 for an illustration of the standardised Kent and standardised von Mises-Fisher distribution. The marginal densities of $M_3(\mu, \kappa)$ can be used to check whether the model fitting of a von Mises-Fisher distribution to a data set is reasonable.

Remark 2.2.2 (Section 4.4.3 in [34])**.** *The joint density $f_{vMF}(\theta, \phi)$ in* (2.24) *can be decomposed in its marginal densities*

$$f_\phi(\phi) = \frac{1}{2\pi} \tag{2.25}$$

and

$$f_\theta(\theta) = \frac{\kappa}{\exp(\kappa) - \exp(-\kappa)} \exp(\kappa \cos(\theta)) \sin(\theta) \tag{2.26}$$

with $0 \leq \theta \leq \pi$. In particular, Θ and Φ are independent.

The distribution of $H = 1 - \cos(\Theta)$ has density

$$f_h(h) = \frac{\kappa}{1 - \exp(-2\kappa)} \exp(-\kappa h) \tag{2.27}$$

with $0 \leq h \leq 2$. Thus, $H \sim Exp(\kappa)$ truncated at $h = 2$ with $E(H) = \frac{1}{\kappa}$. For $\kappa > 2$, the truncation is negligible as $\frac{1}{1-\exp(-2\kappa)}$ tends towards 1. Thus, $H \sim Exp(\kappa)$.

2.2.3 Differential geometry

Differential geometry examines smooth manifolds using differential and integral calculus as well as linear and multi-linear algebra. It originates in studying spherical geometries related to astronomy and the geodesy of the earth. For an introduction to differential geometry, see e.g. [50].

We saw in Proposition 2.2.1 that a linear transformation Σ transforms a random vector which is from a rotationally symmetric distribution into a random vector which is from an elliptically symmetric distribution in $\mathbb{R}^d$. We want to proceed analogously for distributions on the sphere. However, it is not clear that such a linear transformation applied to a vector on $\mathcal{S}^{d-1}$ leads to a vector on $\mathcal{S}^{d-1}$. A remedy is provided by linearising the sphere $\mathcal{S}^{d-1}$ at a base point $\mu \in \mathcal{S}^{d-1}$.

Definition 2.2.6 (Tangent space $T_\mu\mathcal{S}^{d-1}$)**.** *The tangent space $T_\mu\mathcal{S}^{d-1}$ to the manifold $\mathcal{S}^{d-1}$ at a base point $\mu \in \mathcal{S}^{d-1}$ is the collection of all tangent vectors to $\mathcal{S}^{d-1}$ at μ.*

$T_\mu\mathcal{S}^{d-1}$ is a local Euclidean vector space with local origin in μ. Given $\mu \in \mathcal{S}^{d-1}$ and a tangent vector $v \in T_\mu\mathcal{S}^{d-1}$, there is a unique geodesic $c^{\mu,x}$ as defined in (1.1). In the following, we define mappings between the tangent space and the sphere.

Definition 2.2.7 (Riemannian exponential map)**.** *Let $T_\mu\mathcal{S}^{d-1}$ be the tangent space to $\mathcal{S}^{d-1}$ at $\mu \in \mathcal{S}^{d-1}$ and $c^{\mu,x}$ as in* (1.1)*. The Riemannian exponential map,*

$$Exp_\mu : T_\mu\mathcal{S}^{d-1} \to \mathcal{S}^{d-1} \tag{2.28}$$

maps a vector $v \in T_\mu\mathcal{S}^{d-1}$ on $\mathcal{S}^{d-1}$ along a geodesic such that $x = Exp_\mu(v) = c^{\mu,x}(1)$.

The exponential map is locally diffeomorphic onto a neighbourhood $V(\mu)$ of μ. For $\mathcal{S}^{d-1}$, it follows $V(\mu) = \mathcal{S}^{d-1} \setminus \{-\mu\}$, where $-\mu$ is called cut point and the set $\{-\mu\}$ is called cut locus. Within $V(\mu)$ the exponential map Exp_μ has an inverse, the Riemannian logarithmic map.

Definition 2.2.8 (Riemannian logarithmic map)**.** *Let Exp_μ be as in* (2.28)*. The Riemannian logarithmic map,*

$$Log_\mu : V(\mu) \to T_\mu\mathcal{S}^{d-1} \tag{2.29}$$

maps a vector $x \in \mathcal{S}^{d-1}$ into $T_\mu\mathcal{S}^{d-1}$ with $Exp_\mu(Log_\mu(x)) = x$.

The mapping from $\mathcal{S}^{d-1}$ into $T_\mu\mathcal{S}^{d-1}$ can be seen as a linearisation of $\mathcal{S}^{d-1}$ onto $T_\mu\mathcal{S}^{d-1}$ at μ along all geodesics with initial velocity $v \in T_\mu\mathcal{S}^{d-1}$.

The distance between μ and a point on the sphere is described by the Riemannian distance function.

Definition 2.2.9 (Riemannian distance function)**.** *Let Log_μ as in* (2.29)*. For any point $x \in V(\mu)$, the Riemannian distance function is given by*

$$d_{GD}(\mu, x) = ||Log_\mu(x)||_2 = \arccos(x^T\mu) \in [0, \pi). \tag{2.30}$$

It holds that $Log_\mu(x) \in B_{d-1}(\pi) \subset T_\mu\mathcal{S}^{d-1}$.

For calculations in local coordinates, we need a local representation of the Riemannian metric.

Remark 2.2.3 (Local representation of the Riemannian metric)**.** *Let*

$$\frac{\partial}{\partial\tilde{x}} = \left(\frac{\partial}{\partial\tilde{x}_1}, \ldots, \frac{\partial}{\partial\tilde{x}_n}\right) \tag{2.31}$$

be a basis of $T_\mu\mathcal{S}^{d-1}$. The local representation of the Riemannian metric reads

$$G_\mu = \left[\left(\frac{\partial}{\partial\tilde{x}_i}\right)^T \left(\frac{\partial}{\partial\tilde{x}_j}\right)\right]_{i,j}, \tag{2.32}$$

i.e. each element of G_μ is given by the scalar product of two tangent basis vectors. G_μ is symmetric and positive definite.

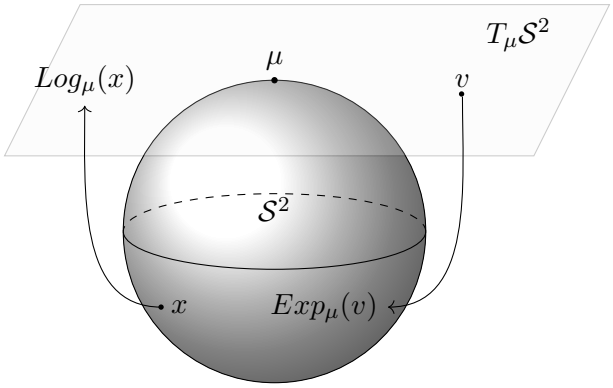

Figure 2.3: The tangent space $T_\mu\mathcal{S}^2$ of the sphere $\mathcal{S}^2$ and related operators.

2.2.3.1 Examples on $\mathcal{S}^2$

Consider $d = 3$. The locally diffeomorphic exponential map reads [15, 51]

$$\begin{aligned} Exp_\mu : T_\mu\mathcal{S}^2 &\to \mathcal{S}^2 \setminus \{-\mu\}, \\ v &\mapsto \mu\cos\left(||v||_2\right) + \frac{v}{||v||_2}\sin\left(||v||_2\right). \end{aligned} \tag{2.33}$$

The locally diffeomorphic logarithmic map reads [15, 51]

$$\begin{aligned} Log_\mu : \mathcal{S}^2 \setminus \{-\mu\} &\to T_\mu\mathcal{S}^2, \\ x &\mapsto \Gamma_\mu\Gamma_\mu^T x\frac{d_{GD}(x,\mu)}{\sin\left(d_{GD}(x,\mu)\right)} \end{aligned} \tag{2.34}$$

with $\frac{0}{\sin(0)} = 1$. See Figure 2.3 for an illustration. With $\mu = (0,0,1)^T$ the logarithmic map in spherical coordinates reads

$$Log_\mu(x) \overset{(1.14)}{=} \begin{pmatrix} \cos(\phi)\sin(\theta) \\ \sin(\phi)\sin(\theta) \\ 0 \end{pmatrix} \frac{\theta}{\sin(\theta)} = \theta \begin{pmatrix} \cos(\phi) \\ \sin(\phi) \\ 0 \end{pmatrix} \in T_\mu\mathcal{S}^2, \tag{2.35}$$

with $d_{GD}(x,\mu) = \arccos\left(\cos(\theta)\right) = \theta$. Thus, the length of any vector $Log_\mu(x) \in T_\mu\mathcal{S}^2,\ x \in \mathcal{S}^{d-1}$, is already given by the (co-latitude) angle $\theta \in [0,\pi)$.

Remark 2.2.4. *Mapping a random vector $X \sim F_X \in \mathcal{R}_\mu$ (with spherical coordinates Θ and Φ) into a tangent space $Log(X) \in T_\mu\mathcal{S}^2$ gives us an interpretation of Theorem 2.2.1: Since $\Phi \sim Unif(S^1_{\mu^\perp}) = Unif[0,2\pi]$ and Φ, Θ independent, $Log_\mu(X)$ has circular density contours in $T_\mu\mathcal{S}^2$. The radius of a contour line of equal probability depends on the value of the density of Θ.*

Remark 2.2.5 (Local representation of the Riemannian metric in $\mathbb{R}^3$)**.** *Let $d = 3$, $\mu = (0,0,1)^T$ and $Exp_\mu(v)$ given in (2.33). For calculating G_μ, consider*

$$\tilde{x} = R(\sin(\theta)\cos(\phi), \sin(\theta)\sin(\phi), \cos(\theta))^T.$$

The partial derivatives are

$$\begin{aligned} \frac{\partial\tilde{x}}{\partial R} &= (\sin(\theta)\cos(\phi), \sin(\theta)\sin(\phi), \cos(\theta))^T, \\ \frac{\partial\tilde{x}}{\partial\theta} &= (\cos(\theta)\cos(\phi), \cos(\theta)\sin(\phi), -\sin(\theta))^T, \\ \frac{\partial\tilde{x}}{\partial\phi} &= (-\sin(\theta)\sin(\phi), \sin(\theta)\cos(\phi), 0)^T. \end{aligned}$$

For $R = 1$,

$$G_\mu = \mathrm{diag}(1, 1, \sin^2(\theta))$$

$$\sqrt{|G_\mu|} = \sin(\theta). \tag{2.36}$$

The representation of densities in the tangent space is given in the next section.

2.2.3.2 Relation between densities on $\mathcal{S}^{d-1}$ and $T_\mu\mathcal{S}^{d-1}$

Following the work of [46], we can transfer densities from $\mathcal{S}^{d-1}$ into $T_\mu\mathcal{S}^{d-1}$ for some $\mu \in \mathcal{S}^{d-1}$: Let $X \in \mathcal{S}^{d-1}$ be random vector with density f. Furthermore, let $v \in T_\mu\mathcal{S}^{d-1}$ and G_μ in (2.32) the corresponding local representation of the Riemannian metric. The connection between the density f on $\mathcal{S}^{d-1}$ and $f_{T_\mu\mathcal{S}^{d-1}}$ in $T_\mu\mathcal{S}^{d-1}$ (defined w.r.t. the Lebesgue measure) reads [46, Equation (9)]

$$f_{T_\mu\mathcal{S}^{d-1}}(v) = f(Exp_\mu(v))\sqrt{|G_\mu|}. \tag{2.37}$$

Note that $f_{T_\mu\mathcal{S}^{d-1}}$ depends on the chosen exponential map on the contrary to f [46].

2.2.3.2.1 Examples for the relation between densities on $\mathcal{S}^2$ and $T_\mu\mathcal{S}^2$

Here, we apply (2.37) on the von Mises-Fisher and Kent density for $d = 3$.

Remark 2.2.6 (Transferred von Mises-Fisher density)**.** *Let $v \in T_\mu\mathcal{S}^2$ with $||v||_2 < \pi$. The transferred von Mises-Fisher density reads*

$$\begin{aligned}
f_{vMF,T_\mu\mathcal{S}^2}(v) &\overset{(2.37)}{=} f_{vMF}(Exp_\mu(v))\sqrt{|G_\mu|} \\
&\overset{(2.17)}{=} c_d \exp\left(\kappa \left(Exp_\mu(v)\right)^T \mu\right)\sqrt{|G_\mu|} \\
&\overset{(2.33)}{=} c_d \exp\left(\kappa \left(\mu\cos\left(||v||_2\right) + \frac{v}{||v||_2}\sin\left(||v||_2\right)\right)^T \mu\right)\sqrt{|G_\mu|} \\
&= c_d \exp\left(\kappa(\mu^T\mu\cos\left(||v||_2\right) + \frac{v^T\mu}{||v||_2}\sin\left(||v||_2\right))\right)\sqrt{|G_\mu|}, \qquad \mu^T\mu = 1,\ v^T\mu = 0 \\
&= c_d \exp\left(\kappa\cos\left(||v||_2\right)\right)\sqrt{|G_\mu|} \\
&= c_d \exp\left(\kappa\cos\left(\theta\right)\right)\sin\left(\theta\right),
\end{aligned} \tag{2.38}$$

where the last line follows using polar coordinates

$$v = \theta \begin{pmatrix} \cos(\phi) \\ \sin(\phi) \\ 0 \end{pmatrix} \in T_\mu\mathcal{S}^2, \tag{2.39}$$

with $||v||_2 = \theta$ and (2.36)*. Note that Equation (2.38) equals Equation (2.24).*

Remark 2.2.7 (Transferred Kent density)**.** *Let $v \in T_\mu\mathcal{S}^2$ with $||v||_2 < \pi$. With* (2.37) *and* (2.36)*, the transferred Kent density reads*

$$\begin{aligned}
f_{K,T_\mu\mathcal{S}^2}(v) &\overset{(2.37)}{=} f_K(Exp_\mu(v))\sqrt{|G_\mu|} \\
&\overset{(2.19)}{=} c_{d,K}\exp\left(\kappa Exp_\mu(v)^T\mu + Exp_\mu(v)^T A Exp_\mu(v)\right)\sqrt{|G_\mu|}
\end{aligned} \tag{2.40}$$

Note that

$$Exp_\mu(v)^T\mu \overset{(2.33)}{=} \cos(||v||_2) \tag{2.41}$$

and

$$\begin{aligned} AExp_\mu(v) &\overset{(2.33)}{=} A\left(\mu\cos\left(||v||_2\right) + \frac{v}{||v||_2}\sin\left(||v||_2\right)\right) \\ &= A\mu\cos\left(||v||_2\right) + \frac{Av}{||v||_2}\sin\left(||v||_2\right) \\ &\overset{A\mu=0}{=} \frac{Av}{||v||_2}\sin\left(||v||_2\right). \end{aligned} \tag{2.42}$$

Then,

$$f_{K,T_\mu\mathcal{S}^2}(v) \overset{(2.40),(2.41)}{=} c_{d,K}\exp\left(\kappa\cos\left(||v||_2\right)\right) + Exp_\mu(v)^T AExp_\mu(v)\Big)\sqrt{|G_\mu|}. \tag{2.43}$$

$$\overset{(2.42)}{=} c_{d,K}\exp\left(\kappa\cos\left(||v||_2\right) + \left(\frac{\sin\left(||v||_2\right)}{||v||_2}\right)^2 v^TAv\right)\sqrt{|G_\mu|} \tag{2.44}$$

The contours are controlled by the quadratic form v^TAv.

For $A = \mathrm{diag}(\beta, -\beta, 0)$, it follows that

$$\begin{aligned} v^TAv &\overset{(2.39)}{=} \beta\theta^2(\cos^2(\phi) - \sin^2(\phi)) \\ &= \beta\theta^2\cos(2\phi). \end{aligned} \tag{2.45}$$

Thus,

$$\begin{aligned} f_{K,T_\mu\mathcal{S}^2}(v) &\overset{(2.44)}{=} c_{d,K}\exp\left(\kappa\cos\left(||v||_2\right) + \left(\frac{\sin\left(||v||_2\right)}{||v||_2}\right)^2 v^TAv\right)\sqrt{|G_\mu|} \\ &\overset{(2.45),(2.36)}{=} c_{d,K}\exp\left(\kappa\cos\left(\theta\right) + \beta\sin^2\left(\theta\right)\cos(2\phi)\right)\sin\left(\theta\right) \end{aligned} \tag{2.46}$$

with $\cos\left(||v||_2\right) = \theta$. Note that Equation (2.46) equals Equation (2.23).

We have seen that densities can be transferred between $\mathcal{S}^{d-1}$ and $T_\mu\mathcal{S}^{d-1}$. In our examples in Remark 2.2.6 and Remark 2.2.7, the transformation (2.37) corresponds to the density transformation from Cartesian to spherical coordinates. The tangent space is easier tractable due to its linear structure. Thus, we examine the contours in $T_\mu\mathcal{S}^{d-1}$ instead of on the curved surface of $\mathcal{S}^{d-1}$.

2.2.4 The Mahalanobis transformation

2.2.4.1 The Mahalanobis transformation in $\mathbb{R}^d$

The idea of the Mahalanobis transformation is to linearly transform a real-valued data matrix $\mathcal{W}_{\mathbb{R}^d}$ in a centred, standardised and uncorrelated data matrix $\mathcal{V}_{\mathbb{R}^d}$, see e.g. [47]. Consider $\mathcal{W}_{\mathbb{R}^d} = (w_1, \ldots, w_n)^T \in \mathbb{R}^{n\times d}$ with d-dimensional row vectors $w_1, \ldots, w_n \in \mathbb{R}^d$. In particular, if the w_i, $i = 1, \ldots, n$, are realisations from a $E(0, \Sigma, F_R)$-distributed random vector, we can use the Mahalanobis transformation to estimate Σ. The vector $\bar{w}$ of the sample means

$$\bar{w}_j = \frac{1}{n}\sum_{i=1}^n w_{ij}, \quad j = 1, \ldots, d,$$

reads

$$\bar{w} = (\bar{w}_1, \ldots, \bar{w}_d)^T = \frac{1}{n}\mathcal{W}_{\mathbb{R}^d}^T 1_n.$$

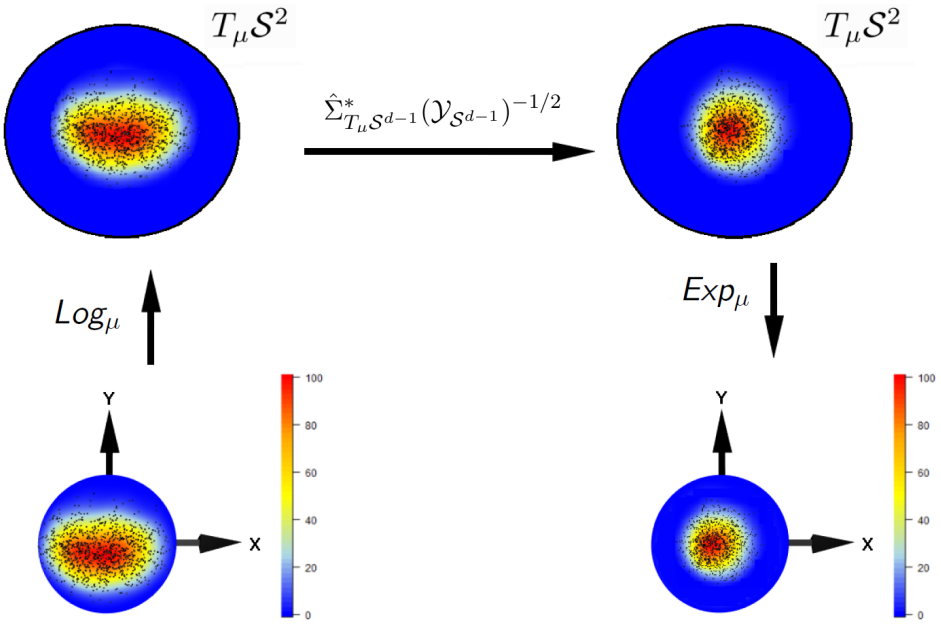

Figure 2.4: The Mahalanobis transformation of $y_1, \ldots, y_{500} \in \mathcal{S}^{d-1}$. The realisations are from a random vector Y which is standardised Kent distributed with $\kappa = 12$ and $\beta = 5$, see Example 2.2.1. The Z-direction points out of the page.

The empirical covariance matrix of $\mathcal{W}_{\mathbb{R}^d}$ reads

$$\hat{\Sigma}(\mathcal{W}_{\mathbb{R}^d}) = \frac{1}{n}\mathcal{W}_{\mathbb{R}^d}^T \mathcal{H} \mathcal{W}_{\mathbb{R}^d}$$

with the centring matrix

$$\mathcal{H} = 1_n - \frac{1}{n} 1_n 1_n^T. \tag{2.47}$$

$\hat{\Sigma}(\mathcal{W}_{\mathbb{R}^d}) \in \mathbb{R}^{d\times d}$ is symmetric and positive semi-definite.

The Mahalanobis transformation of $w_i \in \mathbb{R}^d$ reads

$$v_i = \hat{\Sigma}(\mathcal{W}_{\mathbb{R}^d})^{-1/2}(w_i - \bar{w}). \tag{2.48}$$

2.2.4.2 The Mahalanobis transformation on $\mathcal{S}^{d-1}$

The Mahalanobis transformation can be generalised to the Riemannian manifold $\mathcal{S}^{d-1}$, see [46]. Here, the row vectors $y_1, \ldots, y_n \in \mathcal{S}^{d-1} \setminus \{-\mu\}$ of a data matrix $\mathcal{Y}_{\mathcal{S}^{d-1}} \in \mathbb{R}^n \times \mathcal{S}^{d-1}$ are mapped onto $T_\mu\mathcal{S}^{d-1}$. The sample mean reads

$$\bar{y}_{T_\mu\mathcal{S}^{d-1}} = \frac{1}{n}\sum_{i=1}^n Log_\mu(y_i) \in T_\mu\mathcal{S}^{d-1}.$$

Remark 2.2.8. *For realisations $y_i, i = 1, \ldots n$, from a random unit vector following a distribution which is rotationally or elliptically symmetric about $\mu \in \mathcal{S}^{d-1}$, it follows that*

$$\bar{y}_{T_\mu\mathcal{S}^{d-1}} = \frac{1}{n}\sum_{i=1}^n Log_\mu(y_i) \approx 0_{d-1} \tag{2.49}$$

if the sample size is large.

The empirical covariance matrix reads

$$\hat{\Sigma}_{T_\mu\mathcal{S}^{d-1}} = \hat{\Sigma}_{T_\mu\mathcal{S}^{d-1}}(\mathcal{Y}_{\mathcal{S}^{d-1}}) = \frac{1}{n}\sum_{i=1}^{n} Log_\mu(y_i)Log_\mu(y_i)^T. \tag{2.50}$$

In analogy to (2.48) and with (2.49), the transformed vector in $T_\mu\mathcal{S}^{d-1}$ reads

$$v_i = \hat{\Sigma}_{T_\mu\mathcal{S}^{d-1}}(\mathcal{Y}_{\mathcal{S}^{d-1}})^{-1/2}Log_\mu(y_i). \tag{2.51}$$

Note that it is not clear that we can apply Exp_μ to map $v_i \in T_\mu\mathcal{S}^{d-1}$ onto the sphere $\mathcal{S}^{d-1}$ since $||v_i||_2 < \pi$ is maybe not the case.

We normalise $\hat{\Sigma}_{T_\mu\mathcal{S}^{d-1}}(\mathcal{Y}_{\mathcal{S}^{d-1}})^{-1/2}$ to ensure that the Riemannian exponential map Exp_μ is locally diffeomorphic. Let

$$\hat{\Sigma}^*_{T_\mu\mathcal{S}^{d-1}}(\mathcal{Y}_{\mathcal{S}^{d-1}})^{-1/2} = \frac{\hat{\Sigma}_{T_\mu\mathcal{S}^{d-1}}(\mathcal{Y}_{\mathcal{S}^{d-1}})^{-1/2}}{||\hat{\Sigma}_{T_\mu\mathcal{S}^{d-1}}(\mathcal{Y}_{\mathcal{S}^{d-1}})^{-1/2}||_2}. \tag{2.52}$$

Then it holds that

$$||v_i||_2 \overset{(2.51)}{=} ||\hat{\Sigma}^*_{T_\mu\mathcal{S}^{d-1}}(\mathcal{Y}_{\mathcal{S}^{d-1}})^{-1/2}Log_\mu(y_i)||_2 \leq ||\hat{\Sigma}^*_{T_\mu\mathcal{S}^{d-1}}(\mathcal{Y}_{\mathcal{S}^{d-1}})^{-1/2}||_2 \cdot ||Log_\mu(y_i)||_2 \overset{(2.30)}{<} \pi,$$

Thus, we can apply the locally diffeomorphic Riemannian exponential map Exp_μ on v_i.

Remark 2.2.9. *Note that using* (2.52) *in* (2.51) *could increase the concentration of the points around* μ*.*

The Mahalanobis transformation of $y_i \in \mathcal{S}^{d-1}$ reads

$$x_i = Exp_\mu(\hat{\Sigma}^*_{T_\mu\mathcal{S}^{d-1}}(\mathcal{Y}_{\mathcal{S}^{d-1}})^{-1/2}Log_\mu(y_i)). \tag{2.53}$$

For $d = 3$, the Mahalanobis-transform is illustrated in Figure 2.4.

Let

$$\hat{\Sigma}^*_{T_\mu\mathcal{S}^{d-1}}(\mathcal{Y}_{\mathcal{S}^{d-1}})^{1/2} = ||\hat{\Sigma}_{T_\mu\mathcal{S}^{d-1}}(\mathcal{Y}_{\mathcal{S}^{d-1}})^{-1/2}||_2 \cdot \hat{\Sigma}_{T_\mu\mathcal{S}^{d-1}}(\mathcal{Y}_{\mathcal{S}^{d-1}})^{1/2} \tag{2.54}$$

the inverse of (2.52) such that

$$\hat{\Sigma}^*_{T_\mu\mathcal{S}^{d-1}}(\mathcal{Y}_{\mathcal{S}^{d-1}})^{1/2}\hat{\Sigma}^*_{T_\mu\mathcal{S}^{d-1}}(\mathcal{Y}_{\mathcal{S}^{d-1}})^{-1/2} = I_{d-1} \tag{2.55}$$

Then, we can invert (2.53) by

$$\begin{aligned}
&Exp_\mu(\hat{\Sigma}^*_{T_\mu\mathcal{S}^{d-1}}(\mathcal{Y}_{\mathcal{S}^{d-1}})^{1/2}Log_\mu(x_i)) \\
&\overset{(2.53)}{=} Exp_\mu(\hat{\Sigma}^*_{T_\mu\mathcal{S}^{d-1}}(\mathcal{Y}_{\mathcal{S}^{d-1}})^{1/2}Log_\mu\left(Exp_\mu(\hat{\Sigma}^*_{T_\mu\mathcal{S}^{d-1}}(\mathcal{Y}_{\mathcal{S}^{d-1}})^{-1/2}Log_\mu(y_i))\right)) \\
&\overset{*}{=} Exp_\mu(\hat{\Sigma}^*_{T_\mu\mathcal{S}^{d-1}}(\mathcal{Y}_{\mathcal{S}^{d-1}})^{1/2}\hat{\Sigma}^*_{T_\mu\mathcal{S}^{d-1}}(\mathcal{Y}_{\mathcal{S}^{d-1}})^{-1/2}Log_\mu(y_i)) \\
&\overset{(2.55)}{=} Exp_\mu(Log_\mu(y_i)) \\
&\overset{*}{=} y_i
\end{aligned}$$

where $*$ holds with $Log_\mu(Exp_\mu(x)) = x$.

We will use (2.53) to Mahalanobis-transform realisations $y_1, \ldots, y_n \in \mathcal{S}^{d-1}$ from a random vector Y which has elliptical density contours about μ. If the Mahalanobis-transformed vectors result in vectors which are rotationally symmetric about μ, we treat them as realisations from a random vector X with rotationally symmetric density contours about μ. Then, we will use the results of Ley at al. [11] which are canonical in the rotationally symmetric case. Their results are summarised in the following section.

2.2.5 The angular Mahalanobis depth

As stated in Section 1.2.5.2, the authors in [11] transferred the projection quantile c_τ in (1.24) into a directional depth by assigning the value $D_F(x)$ given in (1.28) to each $x \in \mathcal{S}^{d-1}$. $D_F(x)$ provides a centre-outward ordering with $D_F(\mu) = 1$, $D_F(-\mu) = 0$ and is decreasing on a geodesic from μ to $-\mu$. The angular Mahalanobis depth (AMHD) is defined by

$$AMHD_F(x) = \frac{1}{1 + 1/D_F(x)} = \frac{D_F(x)}{1 + D_F(x)} \in [0, 1/2]\,, \tag{2.56}$$

where $AMHD_F(\mu) = 1/2$, $AMHD_F(-\mu) = 0$. As D_F, $AMHD_F$ decreases on a geodesic from μ to $-\mu$. The angular Mahalanobis depth is leaned on the Classical Mahalanobis depth

$$MHD_F = \frac{1}{1 + (x - \mu(F))^T(\Sigma(F))^{-1}(x - \mu(F))} \tag{2.57}$$

with $x \in \mathbb{R}^d$. $\mu(F)$ and $\Sigma(F)$ are location and scatter functionals under F, respectively. The spherical centre μ corresponds to the centre $\mu(F)$. MHD_F is suited for elliptically symmetric distributions on $\mathbb{R}^d$ since $\Sigma(F)$ contains all necessary information about the principal axes. $AMHD_F$ is not suited for distributions which are elliptically symmetric about $\mu \in \mathcal{S}^{d-1}$ since information about the shape of the distribution is lost due to the projection $X^T\mu$ in the definition of $D_F(x)$ in (1.28).

The empirical angular Mahalanobis depth reads

$$AMHD(x) = \frac{1}{1 + 1/\hat{D}(x)}, \tag{2.58}$$

with

$$\hat{D}(x) = \arg\min_{\tau \in [0,1]} \{\hat{c}_\tau \geq x^T\hat{\mu}\}, \tag{2.59}$$

where the empirical projection quantile $\hat{c}_\tau$ is given in (1.27).

2.2.5.1 Asymptotic properties

Let $\{X_n\}_{n\in\mathbb{N}}$ be a family of random variables. The order in probability notation [52] $X_n \in o_P(1)$ is defined as $\lim_{n\to\infty} P(|X_n| \geq \varepsilon) = 0$, for all $\varepsilon > 0$, which corresponds to convergence in probability with limit $X = 0$.

The following Bahadur-type representation of $\hat{c}_\tau$ given in (1.27) is shown in [11] (with slightly differing notation).

Proposition 2.2.2 (Proposition 3.1 in [11])**.** *Let $F \in \mathcal{F}_\mu$ and f_{proj} stand for the common density of the projections $X_i^T\mu$, $i = 1, \ldots, n$ and set $\Delta_{c_\tau} := f_{proj}(c_\tau)$. Then there exists a d-vector Δ_{μ,c_τ} such that*

$$n^{1/2}(\hat{c}_\tau - c_\tau) = \frac{n^{1/2}}{\Delta_{c_\tau}} \sum_{i=1}^{N} (\tau - 1[X_i^T\mu \leq c_\tau])] - \frac{\Delta_{\mu,c_\tau}^T}{\Delta_{c_\tau}} n^{1/2}(\hat{\mu} - \mu) + o_P(1) \tag{2.60}$$

as $n \to \infty$ under the joint distribution of $X_1, \ldots, X_n$.

Note that (2.60) gives us that a rather complicated non-linear estimator $\hat{c}_\tau$ can be represented as a sum of i.i.d. random variables and the scaled difference between μ to its estimator $\hat{\mu}$. However, the calculation of $\Delta_{\mu,c_\tau} = \frac{d}{dc} E\left((\tau - 1[X_i^T\mu \leq c])X_i\right)_{|c=c_\tau}$ (see the proof of Proposition 3.1 in [11]) is not straightforward.

The representation in Equation (2.60) simplifies in the rotationally symmetric case:

Proposition 2.2.3 (Proposition 3.2 in [11]). *Let $F \in \mathcal{R}_\mu$. Then*

$$n^{1/2}(\hat{c}_\tau - c_\tau) = \frac{n^{1/2}}{\Delta_{c_\tau}} \sum_{i=1}^{N} (\tau - 1[X_i^T \mu \leq c_\tau])] + o_P(1) \tag{2.61}$$

as $n \to \infty$ under the joint distribution of $X_1, \ldots, X_n$. Therefore, letting f_{proj} stand for the density of $X_i^T \mu$, we have that $n^{1/2}(\hat{c}_\tau - c_\tau)$ is asymptotically normal with mean zero and variance $\frac{(1-\tau)\tau}{f_{proj}(c_\tau)}$.

The reason for the simplification in Equation (2.60) is that $\Delta_{\mu,c_\tau}^T n^{1/2}(\hat{\mu} - \mu) \in o_P(1)$ for $F \in \mathcal{R}_\mu$. The absence of $\hat{\mu}$ in Equation (2.61) means that any root-n consistent estimator (empirical Fisher spherical median $\hat{\mu}$, spherical mean $\sum_{i=1}^n X_i / || \sum_{i=1}^n X_i ||_2$, etc.) can substitute μ with no asymptotic effect, independent of the dimension d. Furthermore, (2.60) is a Bahadur-type representation for univariate sample quantiles [45]. Hence, the directional quantiles of [11] have similar asymptotic properties as the quantiles in $\mathbb{R}$. Therefore, the directional quantiles of [11] can be regarded as canonical for $F \in \mathcal{R}_\mu$.

Remark 2.2.10. *Ley et al. [11] derived from Proposition 2.2.3 a goodness-of-fit test which is summarised in Appendix B. For $X \sim M_3(\mu, \kappa)$, the projected density f_{proj} given in (2.14) and a simple expression of the covariance matrix in the goodness-of-fit test statistic is given Appendix C.*

2.3 Quantiles for directional data from elliptically symmetric distributions and the elliptical Mahalanobis depth

As mentioned, Ley et al. [11] introduced quantiles and a depth which are canonical for directional data from distributions $F \in \mathcal{R}_\mu$ with rotational symmetric density contours. But their concept suffers from the disadvantage of producing rotationally symmetric depth contours even if the underlying distribution $F \notin \mathcal{R}_\mu$, for instance, if F has elliptically symmetric depth contours. We solve this problem by transforming the elliptical contours in the tangent space to rotationally symmetric contours, such that we are again in the canonical case of Ley et. [11].

In the following, we consider random vectors $Y, Y_1, \ldots, Y_n \in \mathcal{S}^{d-1}$ i.i.d. with $Log_\mu(Y) \sim E(0_{d-1}, \Sigma, F_R)$. With Remark 2.2.1 follows that $\Sigma^{-1/2} Log_\mu(Y) \sim E(0_{d-1}, I_{d-1}, F_R)$. Let

$$(\Sigma^*)^{-1/2} = \frac{\Sigma^{-1/2}}{||\Sigma^{-1/2}||_2} \tag{2.62}$$

and

$$(\Sigma^*)^{1/2} = ||\Sigma^{-1/2}||_2 \cdot \Sigma^{1/2} \tag{2.63}$$

Then,

$$||(\Sigma^*)^{-1/2} Log_\mu(Y)||_2 \leq ||(\Sigma^*)^{-1/2}||_2 \cdot ||Log_\mu(Y)||_2 \overset{(2.30)}{<} \pi \tag{2.64}$$

and, therefore,

$$\mathcal{G}(Y) = Exp_\mu((\Sigma^*)^{-1/2}(Log_\mu(Y))) \tag{2.65}$$

is locally diffeomorphic since Exp_μ and Log_μ are locally diffeomorphic, and $(\Sigma^*)^{-1/2}$ is invertible. We denote the inverse of (2.65) by

$$\mathcal{G}^{-1}(Y) = Exp_\mu((\Sigma^*)^{1/2}(Log_\mu(Y))). \tag{2.66}$$

2.3.1 Quantiles for directional data from elliptically symmetric distributions

We define the elliptical projection quantile by

$$c_\tau^{\mathcal{G}} = \arg\min_{c\in[-1,1]} E[\rho_\tau(\mathcal{G}(Y)^T\mu - c)], \tag{2.67}$$

where $\mathcal{G}(Y)$ is given in (2.65). The partition of the sphere due to the hyperplane $H_{c_\tau^{\mathcal{G}}\mu} = \{x \in \mathbb{R}^d | c_\tau^{\mathcal{G}} = \mathcal{G}(Y)^T\mu\}$ defines the τ-th-depth contour $C_{c_\tau^{\mathcal{G}}\mu}$, an upper and lower quantile cap as in Section 1.2.5.2. Note that $c_\tau^{\mathcal{G}} = c_\tau$ if $\Sigma^* = I_{d-1}$ since $\mathcal{G}(Y) = Y$.

We denote by $C^{\mathcal{E}}_{c_\tau^{\mathcal{G}}\mu}$ the τ-th-depth contour of the random vector Y which we derive from $C_{c_\tau^{\mathcal{G}}\mu}$ as follows. Map all vectors on the contour line $C_{c_\tau^{\mathcal{G}}\mu}$ into $T_\mu\mathcal{S}^{d-1}$. Then, transform the mapped vectors by $(\Sigma^*)^{1/2}$ given in (2.63) which inverts the transformation in (2.62). Finally, map the transformed vectors back onto the sphere $\mathcal{S}^{d-1}$. These vectors build $C^{\mathcal{E}}_{c_\tau^{\mathcal{G}}\mu}$ defined as

$$C^{\mathcal{E}}_{c_\tau^{\mathcal{G}}\mu} = \left\{\mathcal{G}^{-1}(Y) | Y \in C_{c_\tau^{\mathcal{G}}\mu}\right\} \tag{2.68}$$

with $\mathcal{G}^{-1}(Y)$ given in (2.66). Note that $C^{\mathcal{E}}_{c_\tau^{\mathcal{G}}\mu}$ can be elliptically shaped which is not the case for $C_{c_\tau^{\mathcal{G}}\mu}$.

Let

$$\operatorname{minor} c_\tau^{\mathcal{E}} = \max_{x\in C^{\mathcal{E}}_{c_\tau^{\mathcal{G}}\mu}} x^T\mu \tag{2.69}$$

$$\operatorname{major} c_\tau^{\mathcal{E}} = \min_{x\in C^{\mathcal{E}}_{c_\tau^{\mathcal{G}}\mu}} x^T\mu. \tag{2.70}$$

The intrinsic small semi-axis of $C^{\mathcal{E}}_{c_\tau^{\mathcal{G}}\mu}$ is $\arccos\left(\operatorname{minor} c_\tau^{\mathcal{E}}\right)$ and the intrinsic large semi-axis of of $C^{\mathcal{E}}_{c_\tau^{\mathcal{G}}\mu}$ is $\arccos\left(\operatorname{major} c_\tau^{\mathcal{E}}\right)$. (2.69) and (2.70) contain the main information about the concentration and shape of the distribution of Y around μ. A large difference between $\operatorname{minor} c_\tau^{\mathcal{E}}$ and $\operatorname{major} c_\tau^{\mathcal{E}}$ indicates a strong deviation from a rotationally symmetric distribution, whereas $\operatorname{minor} c_\tau^{\mathcal{E}} = \operatorname{major} c_\tau^{\mathcal{E}}$ indicates that we are in the rotationally symmetric case. Note that $\operatorname{major} c_\tau^{\mathcal{E}} \le c_\tau \le \operatorname{minor} c_\tau^{\mathcal{E}}$.

The empirical elliptical projection quantile reads

$$\hat{c}_\tau^{\mathcal{G}} = \arg\min_{c\in[-1,1]} \frac{1}{N}\sum_{i=1}^{N}[\rho_\tau(\hat{\mathcal{G}}(Y_i)^T\hat{\mu} - c)] \tag{2.71}$$

with

$$\hat{\mathcal{G}}(Y) = Exp_\mu((\hat{\Sigma}^*)^{-1/2}(Log_\mu(Y))) \tag{2.72}$$

and $(\hat{\Sigma}^*)^{-1/2}$ given in (2.52).

The empirical versions of (2.68), (2.69) and (2.70) are denoted by $C^{\mathcal{E}}_{\hat{c}_\tau^{\mathcal{G}},\mu}$, $\operatorname{minor}\hat{c}_\tau^{\mathcal{E}}$ and $\operatorname{major}\hat{c}_\tau^{\mathcal{E}}$, respectively.

If $\mathcal{G}(Y)$ results in a random vectors with a distribution which is rotationally symmetric about $\mu \in \mathcal{S}^{d-1}$, we can use the findings of Ley et al. [11] from Section 2.2.5.1.

2.3.2 The elliptical Mahalanobis depth

Analogously to Ley et al. [11], we define

$$D_F^{\mathcal{G}}(y) = \arg\min_{\tau\in[0,1]}\{c_\tau^{\mathcal{G}} \ge \mathcal{G}(y)^T\mu\} \tag{2.73}$$

using the elliptical projection quantile $c_\tau^{\mathcal{G}}$ in (2.67). $D_F^{\mathcal{G}}(y)$ provides a centre-outward ordering with $D_F^{\mathcal{G}}(\mu) = 1$, $D_F^{\mathcal{G}}(-\mu) = 0$ and is decreasing on a geodesic from μ to $-\mu$. Following [11], we rescale $D_F^{\mathcal{G}}(y)$ which yields the elliptical Mahalanobis depth (EMHD)

$$EMHD_F(y) = \frac{1}{1 + 1/D_F^{\mathcal{G}}(y)} = \frac{D_F^{\mathcal{G}}(y)}{1 + D_F^{\mathcal{G}}(y)} \in [0, 1/2]\,, \tag{2.74}$$

where $EMHD_F(\mu) = 1/2$, $EMHD_F(-\mu) = 0$. Furthermore, $EMHD_F$ decreases on a geodesic from μ to $-\mu$. As $AMHD_F$, the elliptical Mahalanobis depth is leaned on the Classical Mahalanobis depth MHD_F given in Equation (2.57). $EMHD_F$ contains $AMHD_F$ as a special case. They are equal if the depth contours are rotationally symmetric.

The empirical elliptical Mahalanobis depth reads

$$EMHD(y) = \frac{1}{1 + 1/\hat{D}^{\mathcal{G}}(y)}, \tag{2.75}$$

with

$$\hat{D}^{\mathcal{G}}(y) = \arg\min_{\tau \in [0,1]} \{\hat{c}_\tau^{\mathcal{G}} \geq \hat{\mathcal{G}}(y)^T \hat{\mu}\}. \tag{2.76}$$

2.4 Applications

To confirm our findings, we perform a Monte Carlo simulation study. We generated N = 1500 independent replications of four independent samples (with sample size n = 200) of standardised $K(\mu, \kappa, A)$-distributed random vectors

$$Y_{l,i}, \quad l = 1, 2, 3, 4, \quad i = 1, \ldots, n,$$

with $\kappa = 5$, $\beta = 2$ ($Y_{1,i}$), $\kappa = 7$, $\beta = 3$ ($Y_{2,i}$), $\kappa = 10$, $\beta = 4$ ($Y_{3,i}$), $\kappa = 12$, $\beta = 5$ ($Y_{4,i}$), respectively. We denote by $Y_{l,\cdot}$ all $Y_{l,i}$, $i = 1, \ldots, n$ for a fixed l. Furthermore, we denote by $y_{l,i}$ the observation of $Y_{l,i}$. Using (2.51), the Mahalanobis-transformed $y_{l,i}$ are denoted by $x_{l,i}$. Furthermore, we denote by $\Phi_{y_{l,\cdot}}$ the longitudes of $y_{l,\cdot}$ and by $\Phi_{x_{l,\cdot}}$ the longitudes of $x_{l,\cdot}$.

Figure 2.5 shows histograms of $\Phi_{y_{l,\cdot}}$ and $\Phi_{x_{l,\cdot}}$, $l = 1, 2, 3, 4$, indicating that the transformation leads to uniformly distributed longitudes. This supports that Mahalanobis-transformed $Y_{l,i}$ are rotationally symmetric about $\mu = (0, 0, 1)^T$. To confirm this visual impression, we test the hypothesis of uniform longitudes. We use Watson's test [54, p. 156] implemented in the R-package $Directional$ [53]. Watson's test applied on ϕ_{y_i} gave p-values less than 0.004 for all designs $l = 1, 2, 3, 4$. The p-values for the Mahalanobis-transformed angles ϕ_{x_i} were 0.7086 ($l = 1$), 0.5132 ($l = 2$), 0.3436 ($l = 3$), 0.5268 ($l = 4$) which supports an assumption of uniform longitudes.

2.4.1 Quantiles for directional data

Directional quantiles extend single value statistics measuring the concentration of unimodal directional distributions like the mean resultant length $R := \sqrt{E(X)^T E(X)}$ [34]. For directional data from $F \in \mathcal{R}_\mu$, directional quantiles c_τ were introduced and investigated in Ley et al. [11]. For distributions with elliptical contours, we introduced $\operatorname{minor} c_\tau^{\mathcal{E}}$ in (2.69) and $\operatorname{major} c_\tau^{\mathcal{E}}$ in (2.70) which contain the main information about the concentration and shape of the distribution around μ. Furthermore, $\operatorname{minor} c_\tau^{\mathcal{E}}$ and $\operatorname{major} c_\tau^{\mathcal{E}}$ can be used as a tool to measure the deviation from rotational symmetry around μ, where a large difference between $\operatorname{minor} c_\tau^{\mathcal{E}}$ and $\operatorname{major} c_\tau^{\mathcal{E}}$ indicates a strong deviation from rotational symmetry and a small difference indicates rotational symmetry about μ. For illustration, we provide in Figure 2.6 and Table 2.1 empirical quartiles $\hat{c}_\tau$, $\operatorname{minor} \hat{c}_\tau^{\mathcal{E}}$ and $\operatorname{major} \hat{c}_\tau^{\mathcal{E}}$ of $y_{4,i}$, $i = 1, \ldots, n$. It becomes clear that $\operatorname{minor} c_\tau^{\mathcal{E}}$ and $\operatorname{major} c_\tau^{\mathcal{E}}$ provide more insight into the concentration and shape of the distribution than c_τ.

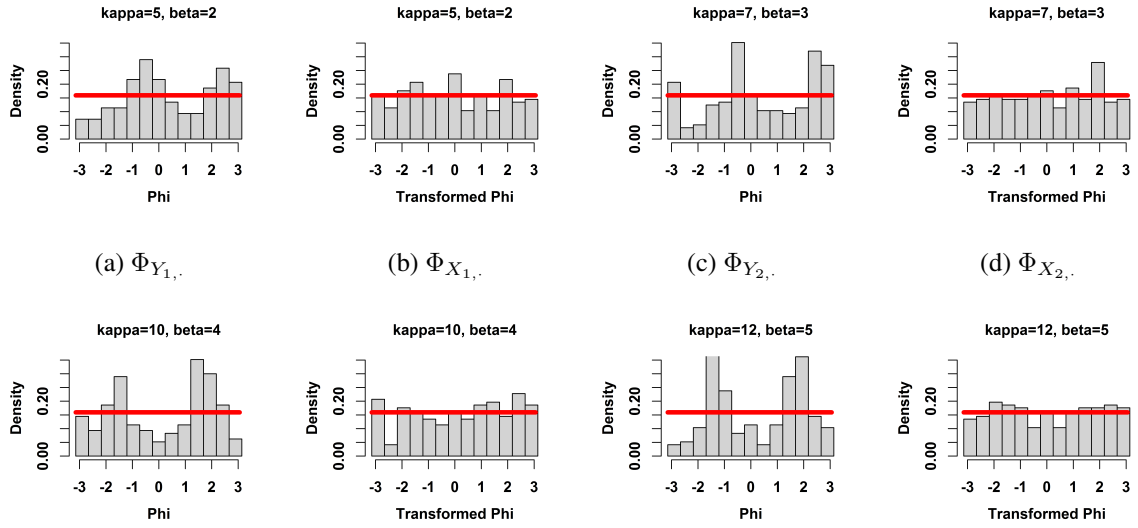

(a) $\Phi_{Y_{1,\cdot}}$ (b) $\Phi_{X_{1,\cdot}}$ (c) $\Phi_{Y_{2,\cdot}}$ (d) $\Phi_{X_{2,\cdot}}$

(e) $\Phi_{Y_{3,\cdot}}$ (f) $\Phi_{X_{3,\cdot}}$ (g) $\Phi_{Y_{4,\cdot}}$ (h) $\Phi_{X_{4,\cdot}}$

Figure 2.5: Histograms of the longitudes $\Phi_{Y_{l,\cdot}}$ and $\Phi_{X_{l,\cdot}}$, $l = 1, 2, 3, 4$. The red line corresponds to the density of $Unif(\mathcal{S}^1)$.

τ	0.25	0.5	0.75
$\hat{c}_\tau$	0.8110	0.9090	0.9660
minor $\hat{c}^{\mathcal{E}}_\tau$	0.9370	0.9677	0.9870
major $\hat{c}^{\mathcal{E}}_\tau$	0.6847	0.8347	0.9245

Table 2.1: The empirical quartiles minor $\hat{c}^{\mathcal{E}}_\tau$, major $\hat{c}^{\mathcal{E}}_\tau$ and $\hat{c}_\tau$ of $y_{4,i}$, $i = 1, \ldots, n$, illustrated in Figure 2.6.

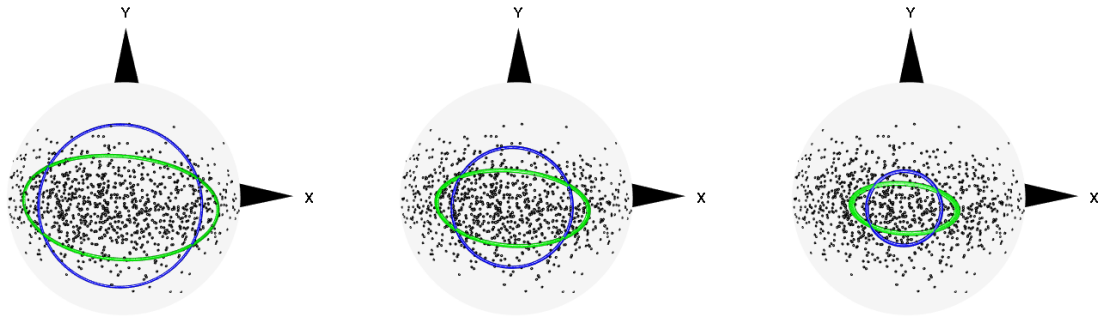

(a) $\tau = 0.25$ (b) $\tau = 0.5$ (c) $\tau = 0.75$

Figure 2.6: Realisations $y_{4,i}$, $i = 1, \ldots, n$, are given as points on $\mathcal{S}^2$ with empirical τ-depth contours, $\tau = 0.25, 0.5, 0.75$. The blue circle corresponds to the empirical τ-depth contour $C_{\hat{c}_\tau \mu}$. The green ellipse corresponds to the empirical τ-depth contour $C^{\mathcal{E}}_{\hat{c}^{\mathcal{G}}_\tau, \mu}$. The values minor $\hat{c}^{\mathcal{E}}_\tau$, major $\hat{c}^{\mathcal{E}}_\tau$ and $\hat{c}_\tau$ are summarised in Table 2.1. The Z-direction points out of the page.

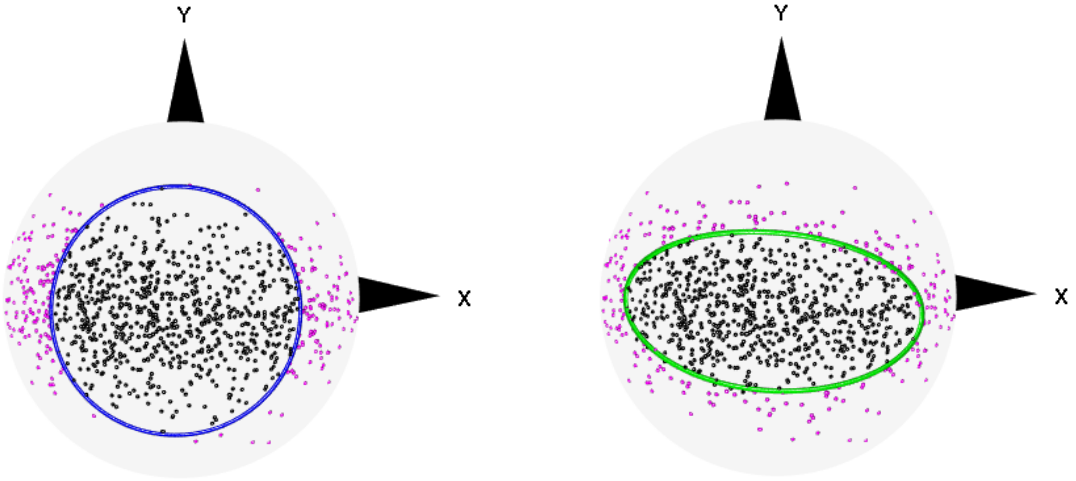

(a) $C_{c_\tau,\mu}$ (b) $C^{\mathcal{E}}_{c^{\mathcal{G}}_\tau,\mu}$

Figure 2.7: Realisations $y_{4,i}$, $i = 1, \ldots, n$, are given as points on $\mathcal{S}^2$. The blue circle corresponds to $C_{\hat{c}_\tau,\mu}$ (left) and the green ellipse corresponds to $C^{\mathcal{E}}_{\hat{c}^{\mathcal{G}}_\tau,\mu}$ with $\tau = 0.25$ of $y_{4,i}$, $i = 1, \ldots, n$. Trimmed points are purple. The Z-direction points out of the page.

2.4.2 Trimming of directional data

The angular Mahalanobis depth $AMHD_F$ is canonical for trimming of directional data from $F \in \mathcal{R}_\mu$. The trimming corresponds to deleting the points on $\mathcal{S}^{d-1}$ below the τ-depth contour $C_{c_\tau,\mu}$ given in (1.26) with $\tau \in [0, 1]$. If the underlying distribution has elliptical contours trimming results into circular contours at some τ when using $AMHD_F$. Here, the elliptical Mahalanobis depth $EMHD_F$ is the obvious choice. The trimming deletes points below $C^{\mathcal{E}}_{c^{\mathcal{G}}_\tau,\mu}$ and preserves the elliptical shape of the contours. See Figure 2.7 for an illustration.

2.4.3 Empirical illustration: Directional data of short steel fibres in ultra-high performance fibre-reinforced concrete

Ultra-high performance fibre-reinforced concrete (UHPFRC) is a relatively new material in civil engineering. If cracks appear in the concrete due to loading, crossing fibres counteract the crack propagation. Note that straight fibres are without a directional sense. A fibre has an orientation represented as two opposite points on the unit sphere. However, in the following, we restrict ourselves to the upper hemisphere of $\mathcal{S}^2$ to mimic fibre directions. We analyse a data set from [48] which consists of $n = 598$ measurements of fibre directions. The n fibres crossed a crack in a bended UHPFRC-specimen. The tension axis corresponds to the Z-axis used in the analysis. The fibre directions are denoted by y_i and the Mahalanobis-transformed fibre directions are denoted by x_i, $i = 1, \ldots, n$. Furthermore, we denote by ϕ_{y_i} the longitudes of y_i and ϕ_{x_i} the longitudes of x_i.

2.4.3.1 Visual inspection, rotational symmetry and quartiles

First, we start by visually inspecting the fibre directions. Figure 2.8 shows a kernel density estimation of the original (Figure 2.8a) and Mahalanobis-transformed (Figure 2.8b) fibre directions. The distribution of the y_i is uni-modal with empirical Fisher spherical median $\hat{\mu} \approx (0, 0, 1)^T$. We used $mediandir()$ from the R-package $Directional$ [53] for calculating the empirical Fisher spherical median [33] given in (1.22).

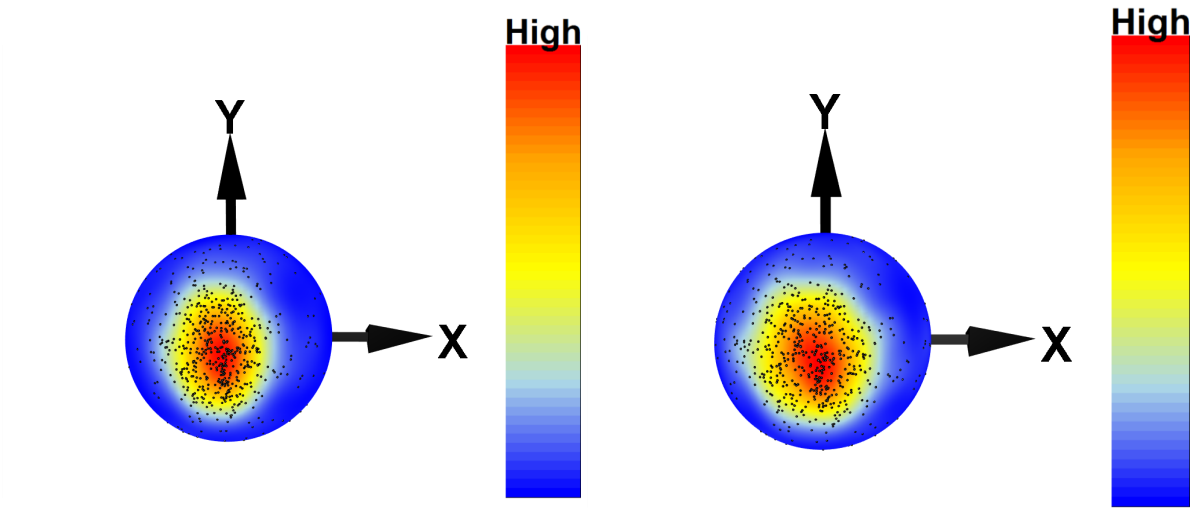

(a) Original fibre directions y_i

(b) Transformed fibre directions x_i

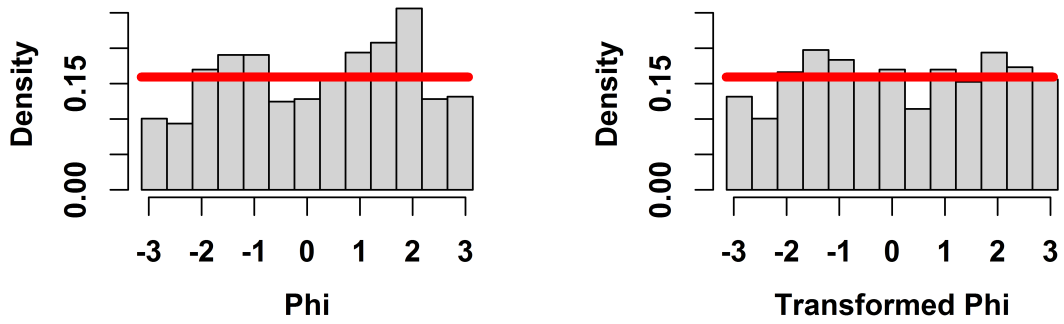

(c) ϕ_{y_i}

(d) ϕ_{x_i}

Figure 2.8: Fibre directions y_i in UHPFRC before (a) and after (b) Mahalanobis transformation. The Z-direction points out of the page. Histograms of the longitudes ϕ_{y_i} (c) and ϕ_{x_i} (d). The red line corresponds to the density of $Unif(\mathcal{S}^1)$.

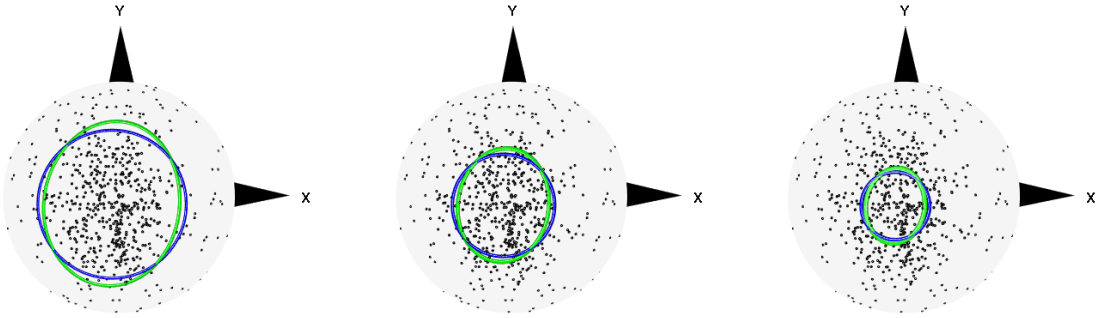

(a) $\tau = 0.25$ (b) $\tau = 0.5$ (c) $\tau = 0.75$

Figure 2.9: The empirical projection quartiles of the fibre directions y_i. The blue circle corresponds to the empirical τ-depth contour $C_{\hat{c}_\tau \mu}$. The green ellipse corresponds to the empirical τ-depth contour $C^{\mathcal{E}}_{\hat{c}^{\mathcal{G}}_\tau, \mu}$. The values $\operatorname{minor} \hat{c}^{\mathcal{E}}_\tau, \operatorname{major} \hat{c}^{\mathcal{E}}_\tau$ and $\hat{c}_\tau$ are summarised in Table 2.2. The Z-direction points out of the page.

Figures 2.8c and 2.8d indicate that the Mahalanobis-transformed fibre directions have uniformly distributed longitudes. Despite this visual impression, we want to test the hypothesis of uniform longitudes. We use Watson's test [54, p. 156] implemented in the R-package $Directional$ [53]. Watson's test applied on ϕ_{y_i} gave a p-value of less than 10^{-4} such that the null hypothesis is always rejected at any meaningful nominal level. Applying Watson's test on ϕ_{x_i} gave a p-value of 0.2660. Thus, the transformed fibre directions could be compatible with the assumption of rotational symmetry about $\hat{\mu}$.

In Figure 2.9, we illustrate the empirical τ-depth contours $C_{\hat{c}_\tau \mu}$ given in (1.26) and $C^{\mathcal{E}}_{\hat{c}^{\mathcal{G}}_\tau, \mu}$ given in (2.68) for $\tau = 0.25, 0.5, 0.75$. The values $\operatorname{minor} \hat{c}^{\mathcal{E}}_\tau, \operatorname{major} \hat{c}^{\mathcal{E}}_\tau$ and $\hat{c}_\tau$ are summarised in Table 2.2. It holds that $\operatorname{major} \hat{c}^{\mathcal{E}}_\tau \lesssim \hat{c}^{\mathcal{E}}_\tau \lesssim \operatorname{minor} \hat{c}^{\mathcal{E}}_\tau$ for all $\tau = 0.25, 0.5, 0.75$. Thus, the shape of the underlying density seems to be slightly better fitted by a distribution which is elliptically symmetric than rotationally symmetric about $\hat{\mu}$.

τ	0.25	0.5	0.75
$\hat{c}_\tau$	0.8489	0.9349	0.9729
$\operatorname{minor} \hat{c}^{\mathcal{E}}_\tau$	0.8785	0.9507	0.9808
$\operatorname{major} \hat{c}^{\mathcal{E}}_\tau$	0.7986	0.9128	0.9629

Table 2.2: The empirical projection quartiles $\operatorname{minor} \hat{c}^{\mathcal{E}}_\tau, \operatorname{major} \hat{c}^{\mathcal{E}}_\tau$ and $\hat{c}_\tau$ of the fibre directions y_i illustrated in Figure 2.9.

2.4.3.2 Goodness-of-fit test and trimming

We investigate, whether we can fit a specific rotationally symmetric directional distribution, more precisely a von Mises-Fisher distribution $F_0 = M_3(\mu, \kappa)$, to the transformed data x_i following a unknown distribution F. First, we estimate κ by the MLE $\hat{\kappa} = 6.97$ using the function $vmf.mle()$ implemented in the R-package $Directional$. We fix $\mu = (0, 0, 1)^T$ and $\kappa = 6, 7, 8$ and perform the goodness-of-fit test given Appendix B based on the projection quartiles $(\hat{c}_{0.25}, \hat{c}_{0.5}, \hat{c}_{0.75})$. The null hypothesis $H_0 : F = F_0$ against $H_1 : F \neq F_0$ is always rejected at any meaningful nominal asymptotic level α for all $\kappa = 6, 7, 8$. The resulting p-values are less than 10^{-4}. Denote by (Θ, Φ) the spherical coordinates of X and by (θ_i, ϕ_i) the spherical coordinates of x_i. A closer investigation of the co-latitude angle θ_i revealed that $1 - \cos(\theta_i)$ has a heavy tail (see Figure 2.10a). Due to Remark 2.2.2, we know that $1 - \cos(\Theta) \sim Exp(\kappa)$ under H_0. Trimming the directions x_i below the τ-depth contour $C_{c_\tau, \mu}, \tau = 0.15$, removes the heavy tail as Figure 2.10b shows. We think that the strong directional deviation from the

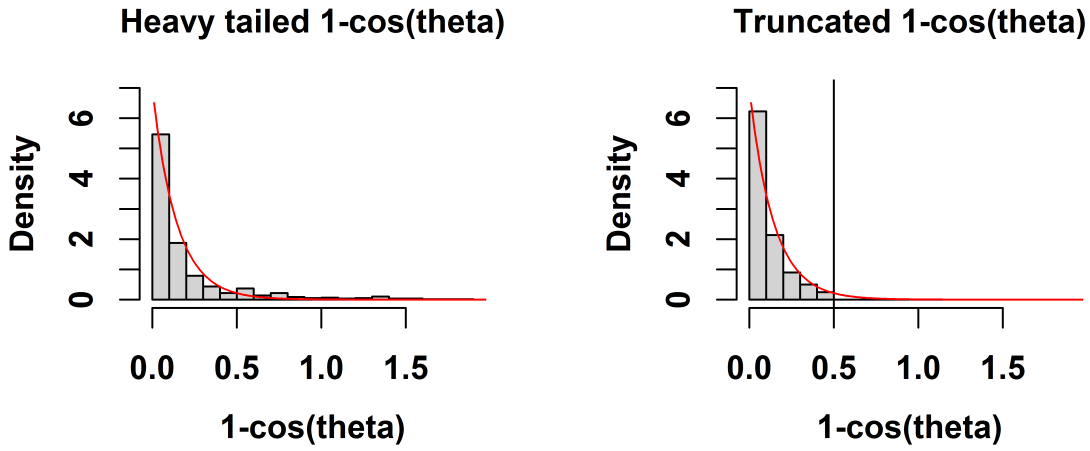

(a) Heavy tailed $1-\cos(\theta_i)$

(b) Truncated $1-\cos(\theta_i)$ at approx. 0.5

Figure 2.10: Histograms of $1-\cos(\theta_i)$, $i = 1, \ldots, n$, before (a) and after (b) truncation due to trimming. The solid line corresponds to the theoretical density of $Exp(\kappa)$, $\kappa = 7$.

tensile axis of almost $\tau = 15$-percent of the fibres favoured the cracking at this position. A possible modelling approach here would be a mixture: $\tau \cdot 100$-percent of fibre directions extremely deviate from the tensile axis and $(1-\tau) \cdot 100$-percent directions are such that $1-\cos(\Theta) \sim Exp(\kappa)$. We focus on the $(1-\tau) \cdot 100$-percent directions with $1-\cos(\Theta) \sim Exp(\kappa)$. Let x_i^{trim} be the trimmed directions. Again, we performed the goodness-of-fit test with $F_0 = M_3(\mu, \kappa)$ based on the projection quartiles $(\hat{c}_{0.25}, \hat{c}_{0.5}, \hat{c}_{0.75})$ of the trimmed set x_i^{trim}. We chose $\mu = (0,0,1)^T$ and $\kappa = 8, 9, 10$ because we expect a higher concentration parameter needed due to trimming. The asymptotic p-values are 0.0130 ($\kappa = 8$), 0.2854 ($\kappa = 9$) and 0.1288 ($\kappa = 10$). Thus, $\kappa = 9$ provides the best fit to the trimmed data.

2.5 Conclusion

We extended the concept of quantiles and depth for directional data from Ley et. al. [11]. Their concept provides useful geometric properties of the depth contours (such as convexity and rotational equivariance) and a Bahadur-type representation of the quantiles. However, a disadvantage is that rotationally symmetric depth contours are always produced, even if the underlying distribution is not rotationally symmetric. Our extension solves this lack of flexibility for distributions with elliptical depth contours. The main idea was to transform the elliptical contours in the tangent space to rotationally symmetric contours, such that we are in the canonical case of Ley et. [11]. In view of similarities with the classical Mahalanobis depth, our depth was called elliptical Mahalanobis depth ($EMHD_F$). The usefulness of our results was confirmed by a Monte Carlo simulation study. Furthermore, we applied our quantiles and depth to analyse fibre directions in fibre-reinforced concrete.

Part II

Statistical analysis, stochastic modelling and prediction of the tensile behaviour of ultra-high performance fibre-reinforced concrete (UHPFRC)

Chapter 3

Introduction

Ultra-high performance concretes (UHPCs) are new types of cementitious materials combining a compressive strength of more than 150 N/mm^2 with a high bulk density and a low porosity. The latter are explained by the packing density and the low water content with a water-binder ratio lower than 0.25. Maximum grain sizes in UHPC are mostly limited to 0.6 to 1 mm. However, experiments with maximal grain sizes up to 8 or 16 mm have also been performed [55]. In practice, the optimisation of the packing density of the cementitious paste is crucial. The optimum concrete can be produced by the combination of the optimum paste with the optimum aggregates for different maximum grain sizes [55, 56].

Many researchers [55, 57, 58, 59, 60] have shown that the addition of steel fibres to the UHPC is indispensable to increase the ductility of the material. As standard, micro wire fibres are used in fibre-reinforced UHPC (UHPFRC). The mechanical behaviour of the UHPFRC under different loading cases critically depends on the spatial arrangement of the fibres. For an optimal performance, fibres should be aligned along the tension axis [61].

For analysing the influence of production parameters on the resulting spatial distribution and orientation of the steel fibres (fibre geometry), the fibre system has to be observed and characterised. This is possible by using photo-optical, magnetic or micro-computed tomography (μCT) methods. The most accurate characterisation is obtained by quantitative analysis of μCT images which allow for a reconstruction of the whole fibre system in 3D [62, 63].

UHPCs are typically produced with a very flowable consistency. The continuous development of PCE-plasticisers allows for a control of the viscosity of the mixture such that concrete with a wide range of consistencies can be produced. Moreover, rheological adjustments of the binder paste have been applied to optimise the deaeration behaviour of the mixture [64].

Besides optimisation of the packing density, the rheological properties of the UHPFRC yield an important parameter that can be varied in concrete production. The fibre geometry is significantly influenced by the rheological properties of the mixture. Fibre orientation in a preferred direction can usually only be achieved by a very fluid consistency, which, however, enhances the tendency of the fibres to sediment. A homogeneous spatial distribution over the component height may then no longer be ensured [60]. Wang et al. (2017) [65] studied the dependence of the fibre distribution on the concrete rheology which was modified by varying the water-binder ratio and the amount of superplasticiser. Fibre systems were analysed by using 2D images of sections through the samples. It turned out that moderate rheology parameters yield the most homogeneous fibre systems. Stähli et al. (2008) [66] present a study analysing the fibre systems in three different concrete mixtures. Concrete samples were imaged by computed tomography. The analysis, however, was restricted to sectional images.

Various further production parameters may also influence the fibre geometry. Vandewalle et al. (2008) [67] investigated the influence of the flow distance, the type of concrete, and the fibre length. The latter was shown to have a negligible influence on the fibre alignment. In the work by Ferrara et al. (2011) [68], 30 mm thin concrete slabs were produced using different casting directions. Their results indicate that the casting process is an additional factor influencing the resulting fibre geometry and, hence, the bending performance. As in Wang et al. (2017) [65] the fibre orientations were determined in 2D cross

sections of the specimens.

In Section 6, we investigate the influence of production parameters on the fibre geometry and the elastic flexural strength of UHPFRC. For this purpose, a large number of prismatic UHPFRC specimens were produced by varying the diameter and volume fraction of the steel fibres, the consistency of the mixture and the casting point. Subsequently, the specimens were imaged by μCT to characterise the resulting fibre geometries. Finally, correlations between production parameters, the fibre geometry, and the load-bearing behaviour observed in four-point bending tests were derived. The results are published in [48].

If a production parameter configuration is fixed, the influence of specimen size on the fibre geometry and the mechanical properties are of interest. In particular, whether it is possible to conclude the fibre geometry and mechanical behaviour from small specimens to larger specimens. Typical specimen sizes used for compression tests are cubes with an edge length ranging from 40 to 150 mm or cylinders with a diameter ranging from 50 to 100 mm and a length between 150 and 300 mm. For bending tests, prisms in the size range 40 x 40 x 160 mm^3 to 100 x 100 x 400 mm^3 are common while dog bone shapes are preferred for tensile tests. In most studies, specimen size and shape were constant. As a consequence, the influence of these parameters, henceforth termed size effect, on the mechanical concrete behaviour is less well understood [69, 70, 71, 72].

Experimental results investigating the effect of specimen size in compression or bending tests are reported in [70, 71, 72, 73, 74]. In these studies, a decrease of flexural strength for increasing sample size is reported. Attempts to explain this finding include both a statistical and a deterministic approach [71, 73]. The statistical approach according to Weibull's theory [75] basically states that larger specimens are more likely to contain severe flaws or defects that reduce the strength of the specimen. The deterministic effect is based on the fact that deformation is concentrated in a localisation band whose size depends on the maximum aggregate size in concrete. In small specimens, the size of this zone is significant compared to the specimen size while it is negligible in reasonably large specimens. This effect is considered in Bažant's theory which is based on fracture mechanics [76, 77]. An additional effect that is still poorly acknowledged is that a change of specimen size may also result in local variations in the fibre geometry. In particular, the degree of edge effects due to the interaction of the fibres with the edges of the formwork or sedimentation of fibres may differ when producing specimens of different size.

A first publication investigating this effect is [74]. The authors study the size effect on the flexural performance of UHPFRC by using three different specimen sizes. Distribution and orientation of fibres in the specimens were investigated by image analysis of two-dimensional cross-sections at the crack surfaces. The investigation revealed that the flexural performance noticeably decreases with an increase in the specimen size resulting from an inhomogeneous spatial fibre distribution and a poor fibre alignment along the tension axis. For specimens of different size but with comparable fibre distribution properties, an insignificant size effect on the flexural strength was observed for UHPC with 2 % steel fibre volume fraction.

In Section 7, we aim at a characterisation of size effects in the local fibre geometry in UHPFRC specimens in a fully three-dimensional manner. To this end, specimens of different size are produced and μCT-scanned. We chose the production parameter combination resulting in the concrete with the highest flexural strength based on the findings in Section 6. The fibre systems were characterised locally and the results have been correlated to the tensile strength of the specimens. The results are published in [78].

The statistical information about the fibre system and the mechanical behaviour of UHPFRC from Section 6 and 7 can be used for further investigations like predicting the tensile behaviour. The force contribution of individual fibres can be determined from single-fibre pull-out tests for selected fibre orientations and embedded lengths [79, 80, 81, 82]. For modelling purposes, the force response of single fibres is idealised as piecewise linear with cut points equal to the tensile force at the end of the linear phase and the ultimate force [83, 84, 85].

Several authors [79, 80, 86, 87, 88, 89, 90, 91, 92] proposed prediction models for the tensile be-

haviour where the pull-out curves for individual fibres form a basic ingredient. Wuest et al. [93] introduced a meso-mechanical model depending on fibre characteristics and mechanical matrix properties. Choi et al. [86] and Kang et al. [94] proposed analytical models to predict the tensile behaviour depending on the fibre orientation distribution. Habel et al. [89] and Yoo [91] considered bilinear models for UHPFRC with short straight steel fibres. Kang et al. [92] and Yoo et al. [88] introduced trilinear models for various UHPFRC types of varying volume fractions and fibre lengths under the common assumption of an isotropic fibre orientation, see also [79, 86, 95, 96]. In practice, the fibre orientation distribution deviates significantly from a uniform (isotropic) distribution [48]. This should be taken into account for formulating more realistic models.

For the prediction of tensile behaviour, characteristics of fibres intersecting the crack plane are required. Therefore, 2D images of cross sections of concrete specimens are frequently studied. However, the fibre orientation can only be roughly determined from such sections [65, 66, 96], and the measurement of the embedded length is not possible at all [86]. A more accurate characterisation is obtained by quantitative analysis of μCT images which allow for a reconstruction of the whole fibre system in 3D [62, 63, 97].

In Section 8, we present a tensile prediction model for UHPFRC-specimens based on a stochastic model for the 3D fibre system and an extensive single-fibre pull-out study. Input parameters for the fibre model are the distribution of fibre orientations, the fibre volume fraction, and the dimensions (length, diameter) of the fibres. The fibre orientation distribution is modelled by a one-parametric distribution family whose parameter β controls the fibre anisotropy, i.e., the scatter of orientations about the preferred direction. The parameter can be estimated either from a sample of fibres observed in a 3D specimen (3D case) or from fibres crossing a planar section of the specimen (2D case).

We fitted the fibre model to a reconstructed 3D fibre system of a μCT-scanned UHPFRC-specimen. This way, embedded length and orientation of the fibres intersecting the crack observed in a mechanical test of the specimen could be determined. A model for the single fibre contributions to the tensile behaviour is obtained by fitting piecewise linear functions to the force-slip curves observed in single-fibre pull-out tests. Following [95, 98], the predicted tensile curve is the sum of all single-fibre pull-out force contributions of crack-crossing fibres. In practice, the tensile behaviour of individually embedded fibres (as used in the pull-out tests) may show deviations from the behaviour of fibres in a larger UHPFRC sample [96]. To take this effect into account, scaling and shifting parameters are introduced which allow for a calibration of the prediction model to stress-strain curves recorded in experimental tensile tests. Randomising some of the model components yields more realistic curve shapes than a deterministic model.

Chapter 4

Experimental program

4.1 Production of the UHPFRC-specimens

UHPC mixtures based on the M3Q-mixture with a maximum grain size of 1 mm were used. The mixture mass fractions for mixture M00 are provided in Table 4.1. To vary the rheology of the concrete, also specimens with an increased amount of PCE-plasticiser were considered. In the mixtures M02 and M04, the PCE content was increased by 10 %, resulting in 30.25 g/l, and 20 %, resulting in 33 g/l, respectively, compared to M00.

An Eirich-Intensiv Vacuum mixer of 5 litre volume capacity was used. Dry components were first mixed for approximately 2 minutes with a rotation velocity of 250 r/min. After that, both water and PCE were added after increasing the velocity to 500 r/min. Mixing was continued for 2 minutes, followed by a break of 2 minutes to scrape off dry particles. Finally, the mixture was mixed at a low velocity of 100 r/min for 7 minutes for deaeration. During the deaeration phase, straight brass coated wire steel fibres were added to the mixture through the shaft on top of the mixer. The fibre diameters were either d_f = 0.2 mm (denoted by 02) or d_f = 0.3 mm (denoted by 03), the fibre length was l_f = 12.5 mm (l_f/d_f = 12.5/0.2 [mm/mm] and 12.5/0.3 [mm/mm]), and the fibre volume fraction was chosen as either V_V = 1% (denoted by F1) or V_V = 2% (denoted by F2). The fibre material has an ultimate tensile strength of 2.800 N/mm^2 and an elasticity modulus of 200 GPa.

Spread flow, bulk density and air void content of each configuration were measured for the fresh concrete directly after mixing. The spread flow was determined by using a Hagermann cone. As illustrated in Figure 4.1a, the spread flow increases when increasing the PCE-amount. The spread flow of the mixtures with 03-fibres was always greater than the mixtures with 02-fibres when fixing the remaining parameters. This can be explained by the increased specific fibre surface area in the systems with thinner fibres. The surface will be covered with a water film during the mixing procedure. The water is absorbed from the pore solution resulting in a lower spread flow.

The air void content (Figure 4.1b) and the bulk density (Figure 4.1c) were measured by using a 1 litre bowl and pressure gauge method. The minimal air void content is observed for F1. Decreasing the viscosity of the concrete reduces the air void content. The mixture F1-03 shows an exceptional behaviour.

Table 4.1: Constituents of the UHPC-mixture M00

Material	**Amount [g/l]**
Cement CEM I 52.5 R SR3- NA (Sulfo 5R)	825
Quarz Sand 0.125/0.5 Haltern	975
Quarz Flour-MILLISIL-W12	200
Silica fume: Sika Silicoll P uncompacted	175
Water	179
PCE-plasticiser - Sika Viscocrete 2810	27.5

Table 4.2: Overview and notation of specimens produced to study the influence of production parameters on the fibre geometry and the elastic flexural strength of UHPFRC. The specimens were bended as described in Section 4.3. The specimens were of size 40 × 40 × 160 mm^3.

fibre content	**fibre dimension**		**casting method**	**consistency**		
volume fraction [%]	length l_f [mm]	diameter d_f [mm]	s=side, m=middle	M00 100% PCE	M02 110% PCE	M04 120% PCE
1	12.5	0.2	s	M00F1s02	M02F1s02	M04F1s02
1	12.5	0.2	m	M00F1m02	M02F1m02	M04F1m02
2	12.5	0.2	s	M00F2s02	M02F2s02	M04F1s02
2	12.5	0.2	m	M00F2m02	M02F2m02	M04F1m02
1	12.5	0.3	s	M00F1s03	M02F1s03	M04F1s03
1	12.5	0.3	m	M00F1m03	M02F1m03	M04F1m03
2	12.5	0.3	s	M00F2s03	M02F2s03	M04F1s03
2	12.5	0.3	m	M00F2m03	M02F2m03	M04F1m03

Table 4.3: Bending and uniaxial tensile strength and compression strength of the mixtures without fibre-reinforcement

Mixture / Consistency	**M00**	**M02**	**M04**
Bending tensile strength [MPa]	11.58	13.77	15.46
Compression strength [MPa]	157.5	150.2	150.7
Strain at uniaxial tensile strength (ϵ_r) [mm/mm]		0.00087	
Uniaxial tensile strength [MPa]		6.4 MPa	

The bulk density slightly increases when reducing the viscosity of concrete without fibres. In mixtures with fibres, bulk densities are nearly independent of the viscosity (with the exception of mixture F1-03).

For every configuration, six specimens of size 40 × 40 × 160 mm^3 were produced, three cast from the side (denoted by s) and three from the middle (denoted by m) of the formwork, see Table 4.2 for a summary. After production, the specimens were cured in a climate chamber for 28 days. Additionally, control specimens without fibre-reinforcement were produced and tested to determine the mechanical properties of the three mixtures. Tensile strengths and compression strengths are given in Table 4.3. The modulus of elasticity is about 50 GPa for all three mixtures.

Besides the 24 configurations described in Table 4.2, we produced M02F2s02 production equivalent specimens of five different sizes, see Table 4.4 for a summary. To ensure the uniformity of the concrete flow over the different widths of the specimens, a chute with an adjustable casting width (Figure 4.2) was designed and produced at the lab of the Department of Concrete Structures and Structural Design, University of Kaiserslautern, Germany. The chute enables a variation of the casting width from 4 up to 15 cm with nearly similar flow velocity.

Table 4.4: Overview and notation of specimens produced to study the influence of specimen size on the fibre geometry and tensile strength of UHPFRC. The specimens are production equivalent to M02F2s02 and were tensioned as described in Section 4.4

specimen	**specimen dimension**		
	width [mm]	height [mm]	length [mm]
4x4x16	40	40	160
8x4x16	80	40	160
4x4x32	40	40	320
4x8x32	40	80	320
8x8x32	80	80	320

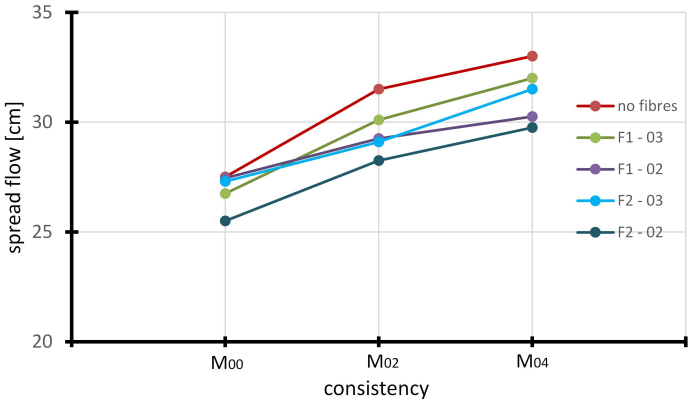

(a) Spread flow

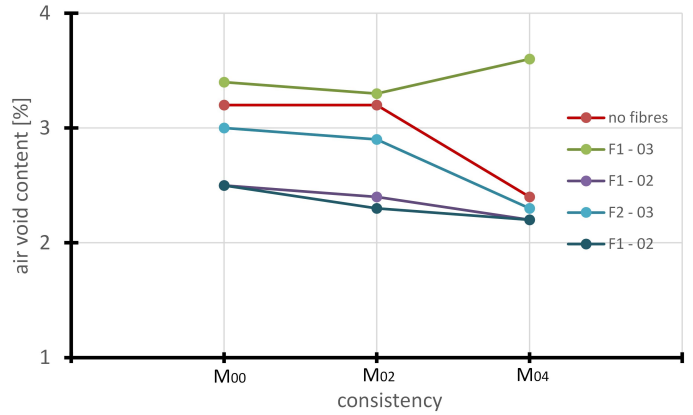

(b) Air void content

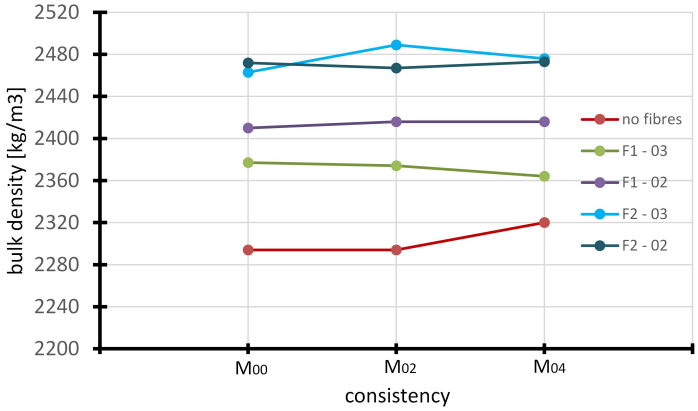

(c) Bulk density

Figure 4.1: Spread flow, air void content and Bulk density of the fresh UHPFRC mixture of each configuration.

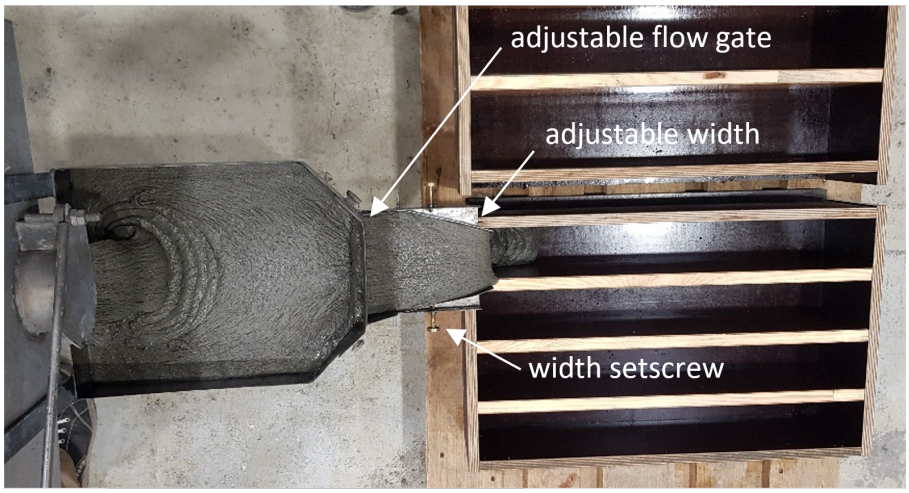

Figure 4.2: Production of the specimens using a chute with adjustable casting width.

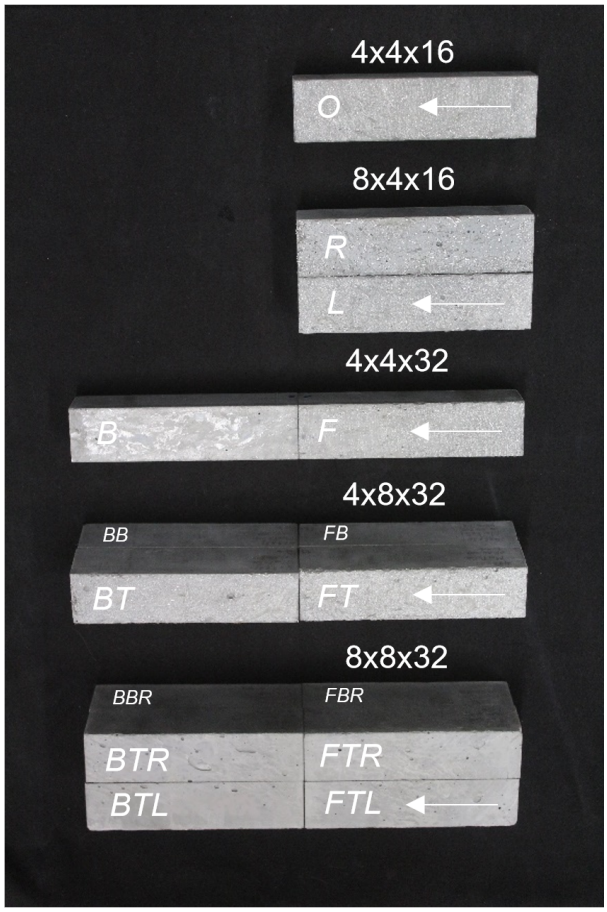

Figure 4.3: The sawed specimens with the notation of the subspecimens according to position: O: original specimen size, R: right, L: left, F: front, B: back, T: top and B: bottom. Arrows indicate the casting direction.

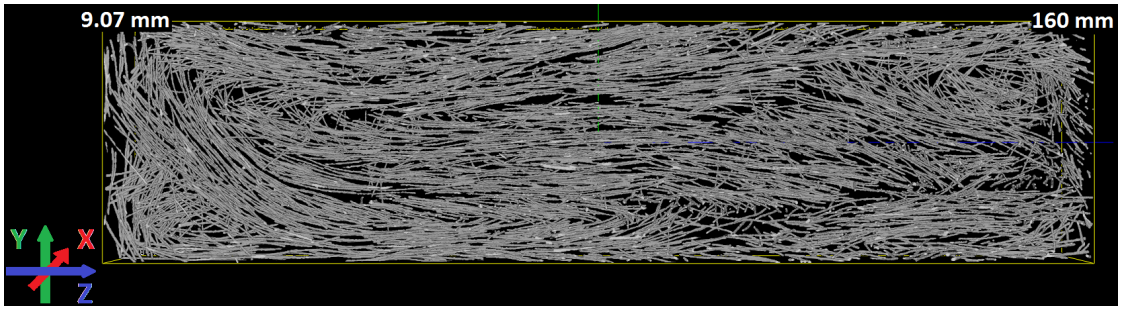

Figure 4.4: 3D coordinate system and fibre system reconstruction of a subvolume of specimen 4x4x16. The visualised volume corresponds to 100 × 441 × 1766 pixels.

Since the maximal specimen size for computed tomography imaging is 40 × 40 × 160 mm^3, the larger specimens were sawn into subvolumes of this size. Water jet technology with a beam width of approximately 1 mm was used to cut the specimens. This method causes nearly no microcracks in the specimens compared to the conventional sawing method. Figure 4.3 shows the specimens after cutting.

4.2 Micro-computed tomography imaging

The specimens were scanned by micro-computed tomography (μCT) at the Fraunhofer Institut für Techno- und Wirtschaftsmathematik (ITWM) in Kaiserslautern, Germany. To reduce grey value variations in the images, we placed the prismatic specimens in a cylindrical UHPC shell during the scanning process. Table 4.5 summarises the CT specifications and imaging parameters. A specimen of size 40 × 40 × 160 mm^3 corresponds to a reconstructed image of 441 × 441 × 1766 pixels. Figure 4.4 shows a visualisation of one specimen together with the coordinate system used for the analysis: depth, height, and length of the specimen correspond to the X, Y and Z coordinate axis, respectively. The plane Y = 0 mm represents the bottom of the sample. The casting point is located at Z = 0 mm, X = 20 mm (40 mm) for depth 40 mm (80 mm), and Y = 40 mm or 80 mm corresponding to the top of the specimens. The flow direction of the UHPFRC was along the Z-coordinate direction.

Table 4.5: CT specifications and imaging parameters

CT tube	Feinfocus FXE 225.51
Maximum acceleration	225 kV
Maximum power	20 W
Detector	Perkin Elmer XRD 1621
Detector size	2048 × 2048 pixel
Tube voltage	190 kV
Target electricity	65 μA
Applied power	12 W
No. of projections	800
Voxel edge length	90.6 μm

4.3 Bending tests

The bending behaviour of specimens given in Table 4.2 was investigated by four point bending tests on unnotched specimens as shown in Figure 4.5. For testing, specimens were rotated by 90° about the Z-axis such that the concrete surface pointed to the front. The bending tests were carried out in a displacement-controlled manner. The load rate was chosen very low at 0.1 mm/min to be able to follow the crack formation. The displacement in the midspan was measured by using an extensometer. The test

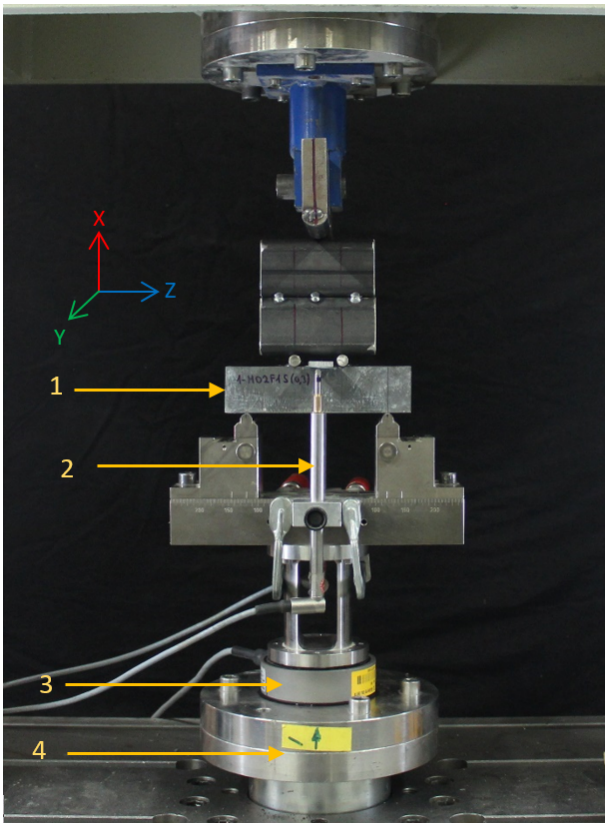

Figure 4.5: Setup of the four-point bending test (1 = the specimen, 2 = extensometer on both sides to measure the deflection in the midspan, 3 = force gauge, 4 = load cell)

ended as soon as a deflection of 5 mm in the midspan was reached.

For further comparison of the specimens, the elastic flexural load F_{el} was considered. It corresponds to the force value at which the curve enters the non-linear phase. From F_{el}, the elastic flexural strength f_{el} can be computed by

$$f_{el} = \frac{3F_{el}}{a^2} \tag{4.1}$$

where $a = 4$ cm is the specimens‘ cross section edge length.

4.4 Tensile tests

The specimens given in Table 4.4 had to be cut for the μCT imaging. Thus, testing the tensile strength of the complete specimens is no longer possible. However, uniaxial tensile tests were performed on the 17 subspecimens to determine the (local) tensile strength.

A challenge was to develop a test setup, which enables to apply an uniaxial tension on specimens of prism form, the main point being the fixation of the specimens at the ends. The test set up shown in Figure 4.6 provided a reasonable result regarding fixing rigidity and convenient handing. The specimen was placed in the gripping jaws with a contact area of 40 $\times$ 60 mm^2 and fixed by six bolts, which were pulled by a moment of 110 Nm. This pull moment was determined as the maximum so that no cracks occur in the clamping area. After fixing both ends, the set was fixed in the pull machine by two nuts. In this set up, a field of length 40 mm located in the middle of the specimens was tensioned.

The tests were carried out in a displacement-controlled manner. A low load rate of 0.1 mm/min was chosen. The lengthening of the 40 mm field was measured by using two extensometers. The test was stopped as soon as the lengthening of the field reached 2 mm. During the uniaxial tensile tests, load-

lengthening curves were recorded. Since the subspecimens have a small difference in the cross-section, the uniaxial stress-strain curves were determined to compare the results consistently.

It is known that eccentricity occurs in the internal resisting forces due to non-uniform distribution of fibres in the cross-section. However, the stress distribution over the cross-section was assumed to remain uniform during the initial cracking phase and after crack localisation. Thus, the uniaxial equivalent stress reads

$$\sigma = \frac{F}{A}, \tag{4.2}$$

where F is the force value and A is the area of the cross-section. The strain reads

$$\epsilon = \frac{\Delta L}{L}, \tag{4.3}$$

where the measured lengthening ΔL is divided by the tensioned length L = 40 mm.

Two strength values were computed for every specimen: the elastic post-crack tensile strength (σ_{el}^{exp}), which corresponds to the force at the end of the linear phase in the curve (limit of proportionality) in sense of [99], and the ultimate post-crack tensile strength (σ_{ult}^{exp}) which corresponds to the maximum force reached.

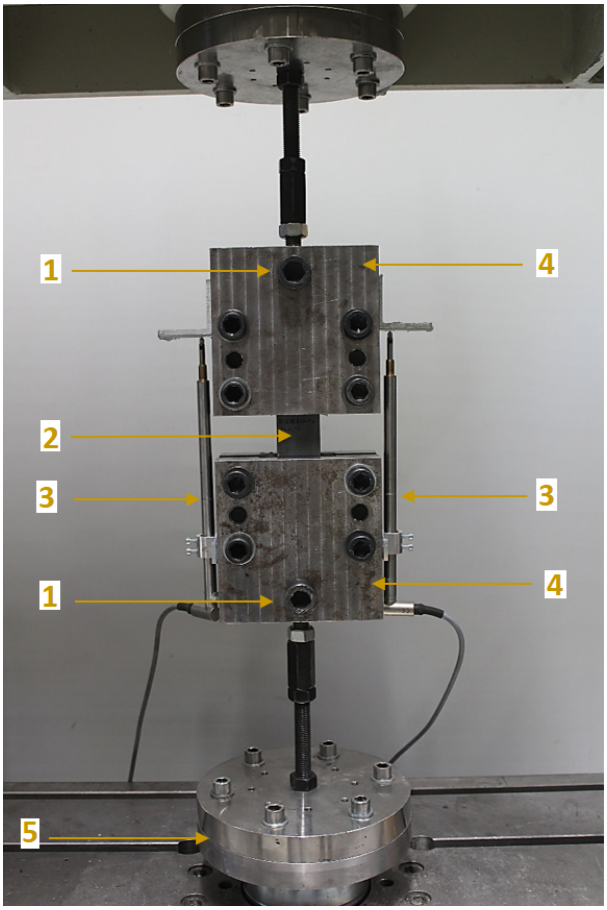

Figure 4.6: Setup of the uniaxial tensile test: rotatable hinge (1), specimen (2), extensometer on both sides to measure the elongation (3), griping jaw (4), and load cell (5).

Chapter 5

Image analysis

5.1 Image processing

For image processing, we used the software tools MAVI (Modular Algorithms for Volume Images) [100] and ToolIP (Tool for Image Processing) [101]. The CT images contain illumination gradients from the edges of the specimen to the centre [102]. Hence, an illumination correction was necessary to reconstruct the fibre system correctly, see Figure 5.1 for an illustration.

The following chain of image processing steps was applied:

1. Filtering of the initial image by a mean filter [103]. The size of the cubic filter mask is chosen such that the largest object (typically an air pore) in the initial image is covered.

2. Subtraction of the filtered image from the initial image

3. Division of the image into cylinders whose bases form concentric rings/discs in the XY-plane, see Figure 5.2.

4. Segmentation of the fibres in the image parts by using Otsu's method[104].

5. Merging of the image parts.

The choice of subdivision was validated by checking whether the segmented fibres have a constant diameter throughout the image. This is done by comparing the values of local maxima of the Euclidean distance transform [105]. The subdivision shown in Figure 5.2 was used for specimens given in Table 4.4. Figure 5.3 shows a sectional image of specimen 4x4x16 obtained by μCT and its binarisation.

5.2 Fibre content

We assessed the homogeneity of the fibre content along the coordinate directions. For this purpose, we computed area fraction profiles (AFP) which represent the area fraction of the fibres in each slice orthogonal to a coordinate direction. In macroscopically homogeneous microstructures, the expected area fraction A_A in a 2D slice is equal to the volume fraction V_V of the complete specimen [106, p. 414]. Spatial inhomogeneities such as layer structures or varying fibre density lead to significant variations of the area fraction. The partial volume effect [107] in CT imaging and the low resolution of the images (2-3 pixels per fibre diameter) led to deviations between the estimated fibre volume fraction and the nominal value of 2%. To be able to compare the specimens with each other, the AFPs were centred. That is, the volume fraction of the complete specimen was subtracted from the area fraction in the slices. To compare the centred AFPs visually, the curves were smoothed by exponential smoothing with the parameter $\alpha = 0.05$ (R-function HoltWinters, R-packet statistics [108]), see Figure 5.4.

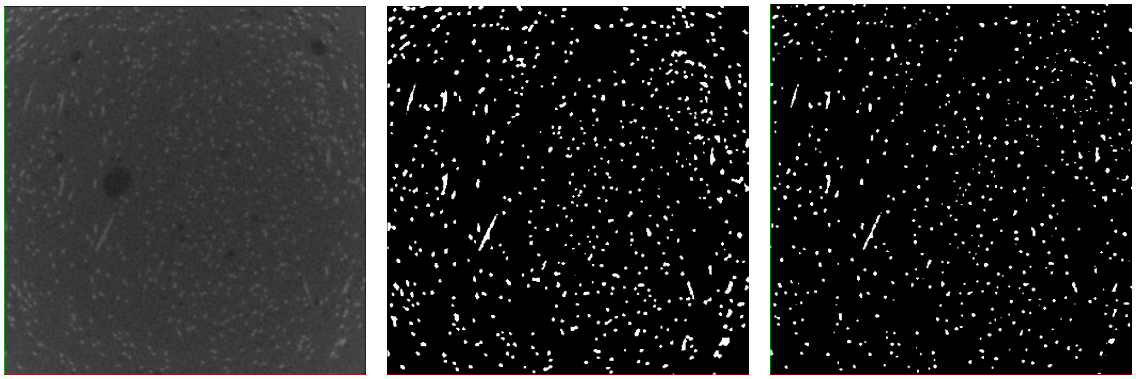

(a) Sectional μCT image. (b) Binarisation without illumination removal. (c) Binarisation with illumination removal.

Figure 5.1: Sectional μCT image of specimen 4x4x16 (a). Binarisation without removal of the illumination gradients resulting in over-segmentation in the edge areas (b). Binarisation by using the procedure detailed in the text (c).

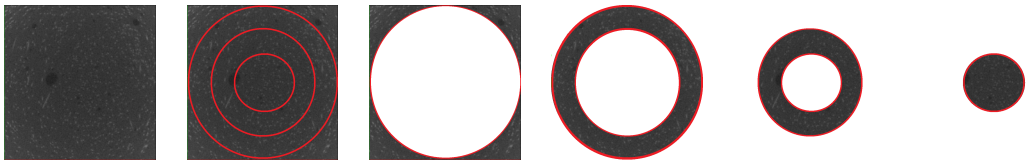

Figure 5.2: From left to right: The initial image, the cylindrical subdivision of the image and the single image parts after cropping.

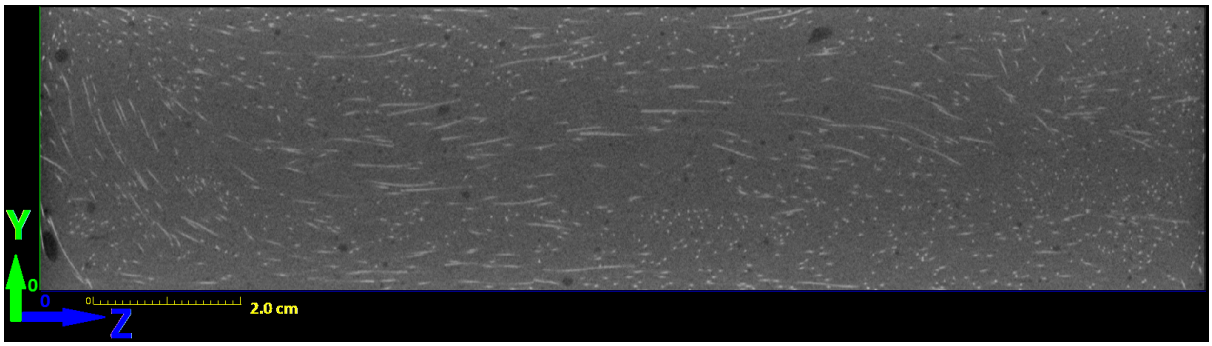

(a) Sectional μCT image of 4x4x16.

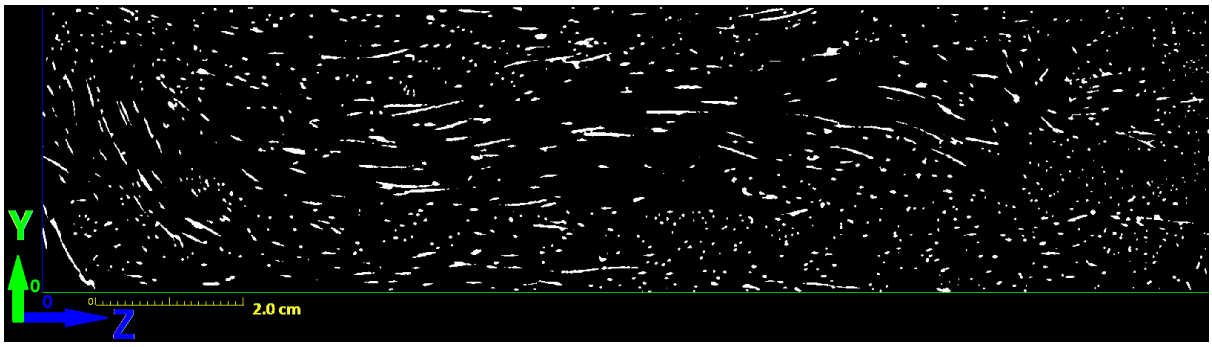

(b) Binarisation.

Figure 5.3: Sectional μCT image of specimen 4x4x16 (a). Fibres are white, concrete matrix is grey, and air pores are black. Binarisation of the fibre system (b).

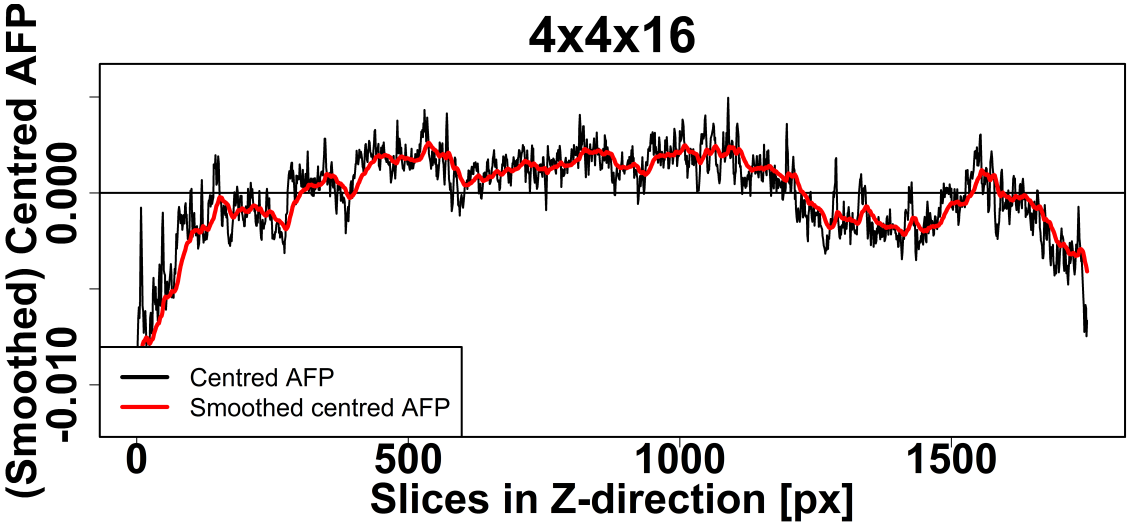

(a) Centred AFP.

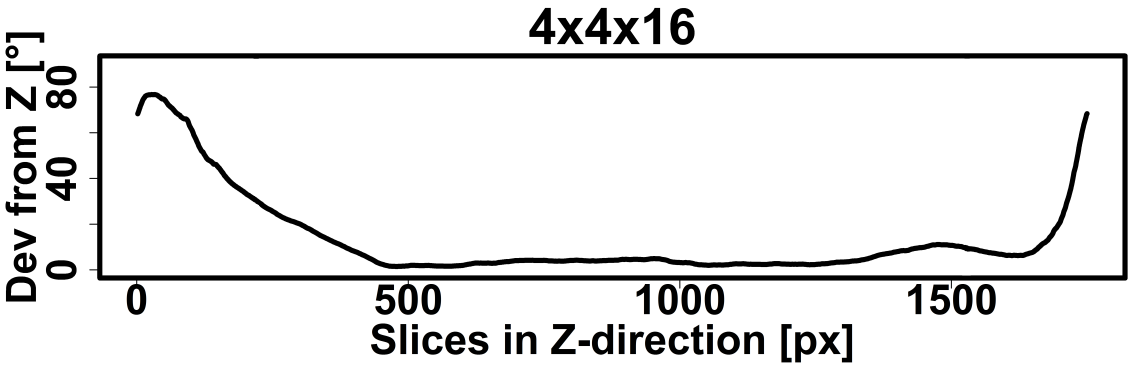

(b) Dev.

Figure 5.4: Centred area fraction profile of specimen 4x4x16 before (black) and after (red) smoothing (a). Deviation (Dev) of the fibre orientation from the Z-axis (in degrees) in each slice of specimen 4x4x16 along the Z-direction (b).

5.3 Fibre orientation

The local orientation of the fibres in the concrete was estimated based on partial second derivatives [109, 110]. For this purpose, the initial image f is smoothed by applying an isotropic Gaussian convolution filter with kernel g_σ at scale σ to reduce noise in the grey values. The convolution is denoted by $\star$. For the resulting image, the Hessian matrix

$$H(f) = \begin{pmatrix} f_{xx} & f_{xy} & f_{xz} \\ f_{yx} & f_{yy} & f_{yz} \\ f_{zx} & f_{zy} & f_{zz} \end{pmatrix} \tag{5.1}$$

is computed, where

$$f_{ij} = \frac{\partial^2}{\partial i \partial j}(f \star g_\sigma), \quad i,j \in \{x,y,z\} \tag{5.2}$$

are the second order derivatives of the smoothed image.

We follow the recommendation of Wirjadi et al. [110] and set σ equal to the fibre radius. For each fibre pixel p, the eigenvector corresponding to the smallest eigenvalue of $H(f)$ estimates the local fibre orientation in p. The fibre orientations $v_i = \pm(v_i^{(x)}, v_i^{(y)}, v_i^{(z)})$, $i = 1, \ldots, N$, in a slice of the 3D image are averaged by using the orientation matrix [34]

$$T = \sum_{i=1}^{N} v_i \otimes v_i = \sum_{i=1}^{N} \begin{pmatrix} v_i^{(x)} v_i^{(x)} & v_i^{(x)} v_i^{(y)} & v_i^{(x)} v_i^{(z)} \\ v_i^{(x)} v_i^{(y)} & v_i^{(y)} v_i^{(y)} & v_i^{(y)} v_i^{(z)} \\ v_i^{(x)} v_i^{(z)} & v_i^{(y)} v_i^{(x)} & v_i^{(z)} v_i^{(z)}, \end{pmatrix} \tag{5.3}$$

with $\otimes$ the outer product. The eigenvector of T with the largest eigenvalue represents the main fibre orientation within the slice. A fibre orientation along the tension axis, here the Z-axis, is desirable. Therefore, we compute the deviation of the main fibre orientation from the Z-axis (see Figure 5.4). As for the AFP, we smoothed the curves by exponential smoothing.

The large deviations at the edges of the specimen can be explained by formwork effects. Hence, on each side an edge area of 2 cm width (220 slices) is neglected in the statistical analysis.

Chapter 6

Influence of production parameters on the fibre geometry and the elastic flexural strength of UHPFRC

6.1 Results

6.1.1 Image analysis

Figure 6.1 shows a comparison of specimens with different consistencies (controlled by the amount of PCE-plasticiser) while the other parameters (fibre volume fraction, fibre diameter and casting point) are fixed. The M02-specimen shows the most homogeneous fibre system w.r.t. the AFP and the fibre orientation. The very fluid consistency of M04 results in fluctuations in the spatial distribution and orientation of the fibres. The volume rendering also clearly shows the sedimentation of the fibres. The more viscous M00-specimen shows some inhomogeneities close to the casting point and a more homogeneous structure in the second half of the specimen.

Figure 6.2 shows the centred AFPs along the Y-direction, i.e., from the bottom to the top of the specimens. All specimens show sedimentation of the fibres which is most pronounced for the M04-specimens. The M00- and M02-specimens often show a similar behaviour. The sedimentation is most pronounced for the thicker, hence heavier, fibres (d_f = 0.3 mm). The casting method does not seem to have any influence.

AFPs along the X-direction, i.e. from right to left, are shown in Figure 6.3. The specimens generally show some wall effects close to the boundary of the formwork. Specimens with high volume fraction (F2) and thin fibres (d_f = 0.2 mm) are most affected. Consistency and casting method do not seem to contribute to the wall effect.

Finally, AFPs along the Z-direction are shown in Figure 6.4. The strongest variations are observed for the M04-specimens. Casting from the middle leads to an almost symmetric AFP with an accumulation of fibres in the centre of the specimens. M02-specimens cast from the side show less fluctuations except for F2s02-specimens.

For studying the alignment of the fibres we plot the local deviations of the fibre orientation from the Z-axis in Figure 6.5. The maximal deviation was approximately 45°. Casting from the side results in a more homogeneous fibre orientation distribution than casting from the middle. In the latter case, the deviation of the fibres from the Z-axis is low just in a narrow region around the casting point and increases in the flow directions towards the sides. This deviation seems to be stronger for viscous mixtures with few, thin fibres. For more and/or thicker fibres this effect is reduced. The fibre orientation of s03-specimens is highly affected by the consistency (independent of the volume fraction). Fluid mixtures lead to more fluctuations. For 02-specimens, the correlation between fibre orientation and consistency is not pronounced. The orientation of fibres in s02-specimens deviates least from the Z-axis for all consistencies and fibre volume fractions.

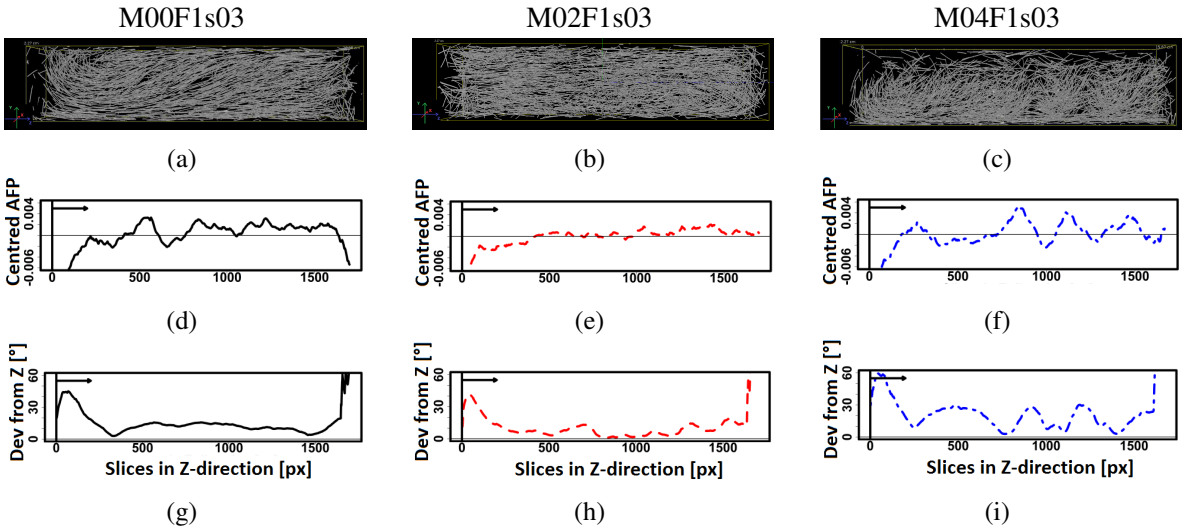

Figure 6.1: Volume rendering (a, b, c), centred AFP along the Z-direction (d, e, f), and deviation of the fibre orientations from the Z-axis along the Z-direction (g, h, i) of specimens M00F1s03, M02F1s03 and M04F1s03

To measure the variation in the spatial distribution and orientation of the fibres in a specimen, the sample standard deviation (SSD) of the centred AFPs and the orientation deviations in Z-direction (Figures 6.4 and 6.5) were calculated. The results are visualised in Figure 6.6. Again, M04-specimens are found to be most heterogeneous. The SSDs are maximal in this group. Additionally, they show the highest differences between the four sets of fibre parameters used. In total, fibre systems are more homogeneous when casting from the side than when casting from the middle. With respect to the fibre orientation, the s-specimens are clearly more aligned to the Z-axis than the m-specimens. Figure 6.7 showing the SSDs along the Y-direction confirms the visual impression that the spatial fibre distribution and fibre orientation of M04-specimens are inhomogeneous compared to M00- and M02-specimens for all fibre volume fractions, fibre diameters, and casting methods considered.

In summary, M00- and M02-specimens cast from the side are most homogeneous w.r.t. fibre orientation and spatial distribution.

6.1.2 Bending tests

During the testing of the 72 specimens (three specimens for each of the 24 parameter combinations), load-midspan deflection curves were recorded (see Figures 6.8 and 6.9). All specimens showed deflection-hardening performance to different extent.

In the initial phase, the bending behaviour of the specimens is linear elastic. When the load exceeds the matrix tensile strength, a first crack occurs in the weakest point of the matrix in the middle third of the specimen. After crack initiation, the fibres crossing the crack get activated and avoid propagation of the crack opening. The response curve remains in the linear elastic range and the tensile stress increases at the bottom of the specimen. In the same manner, the specimen may develop three to four visible cracks. Crack propagation occurs at different scales. The response behaviour of the specimen is still elastic or elastoplastic but linear. This will be followed by non-linear behaviour, where many cracks propagate simultaneously until reaching the maximum load. A mean strain constitutive law can be assumed, because the complete cross sections are strained along the specimen, which concur with the AFGC-Recommendation (2013) [99].

When reaching the maximum load, the crack which requires a minimum energy to develop break down dominates the process. That is, crack propagation progresses only in the dominating crack and the response behaviour is non-linear and plastic. Simultaneously, other cracks reduce in width causing a stress relief on both sides of the dominating crack. Thus, a rigid body motion of the two parts of the

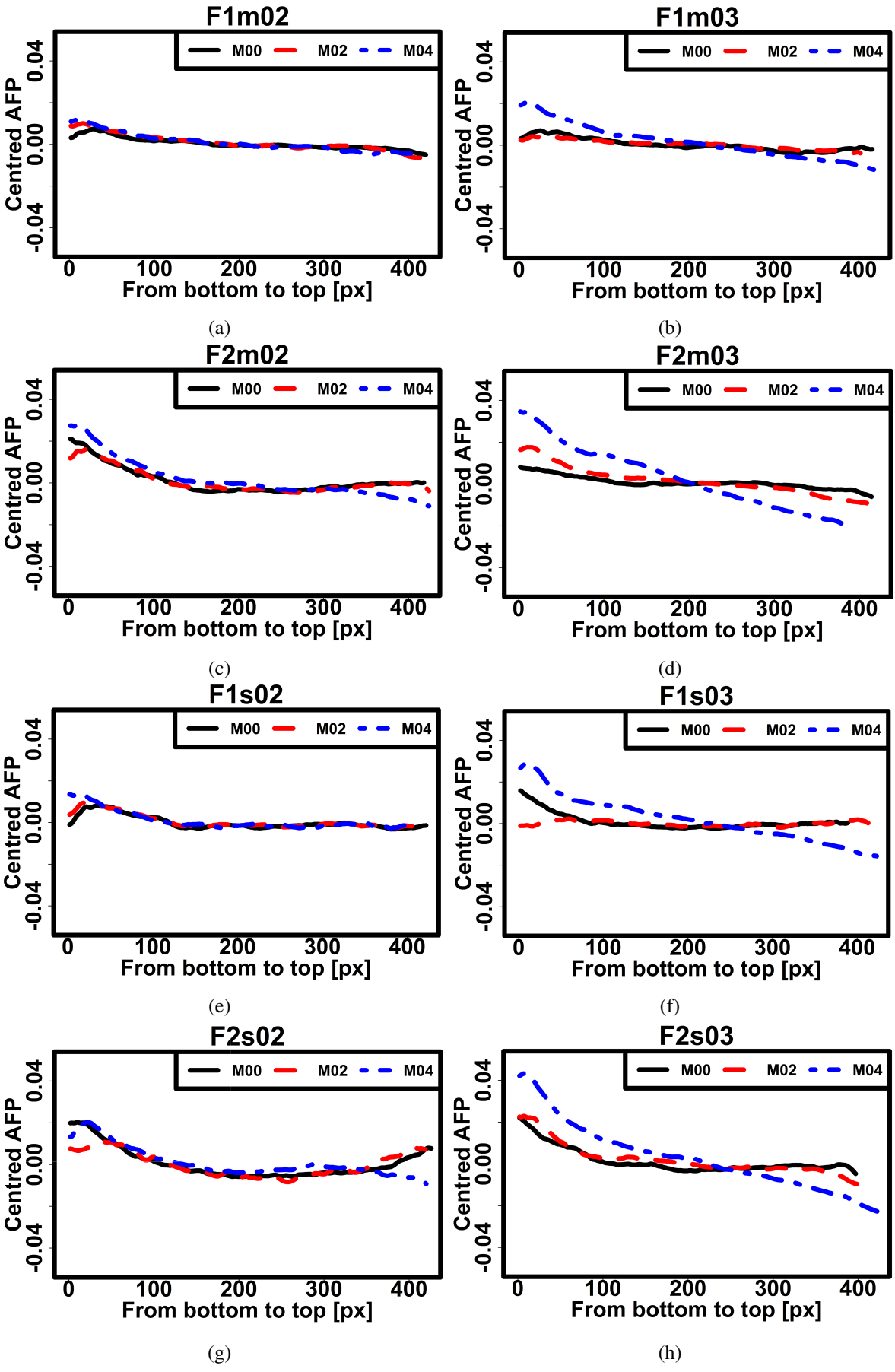

Figure 6.2: Centred AFPs along the Y-direction (from bottom to top)

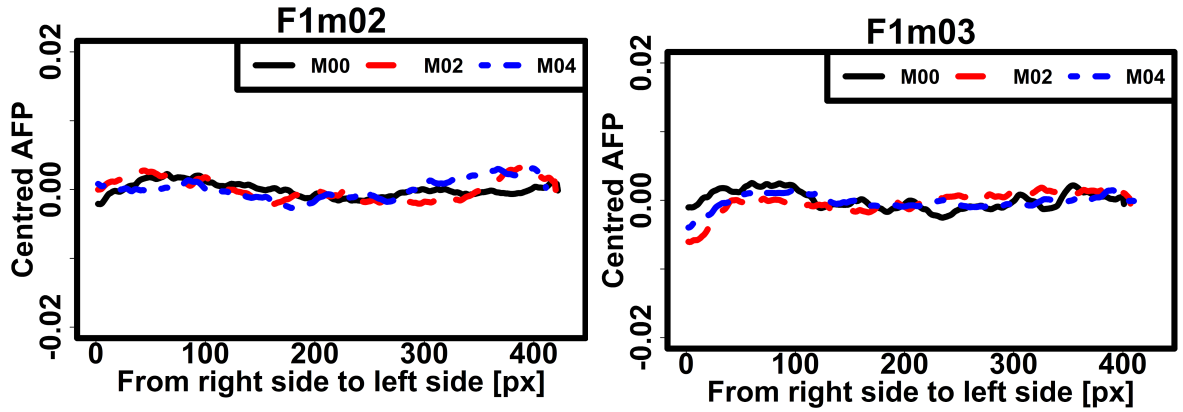

(a)

(b)

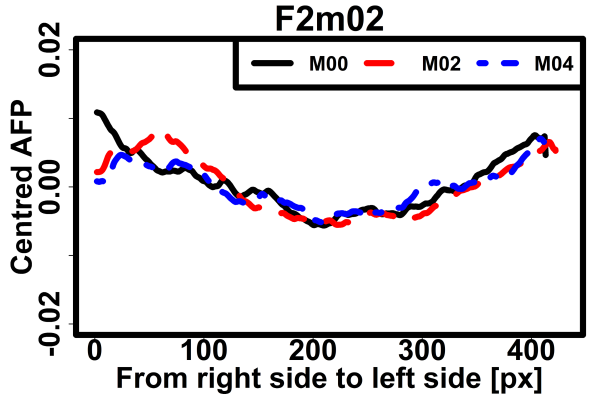

(c)

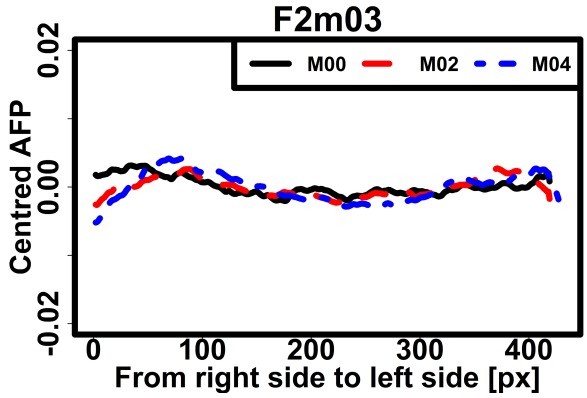

(d)

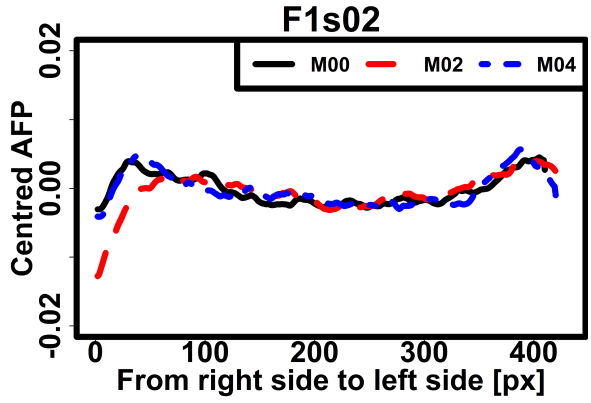

(e)

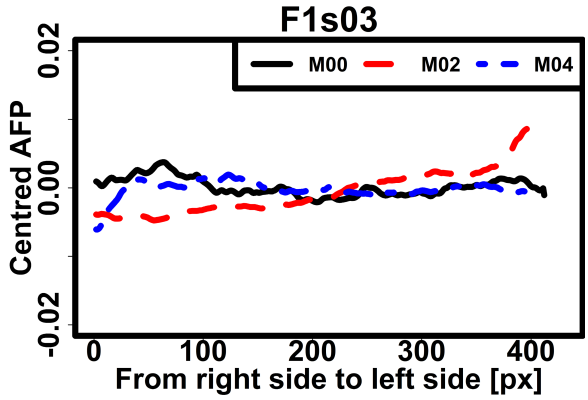

(f)

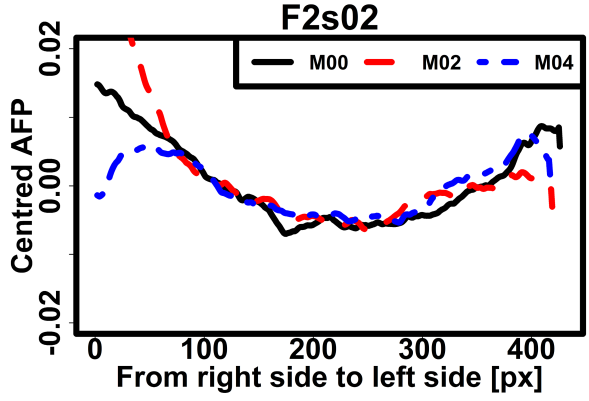

(g)

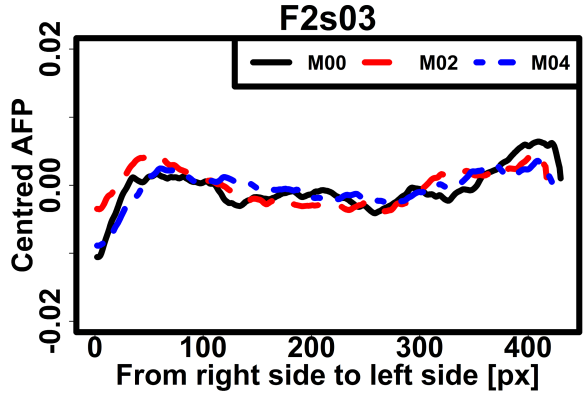

(h)

Figure 6.3: Centred AFP along the X-direction (from right side to left side)

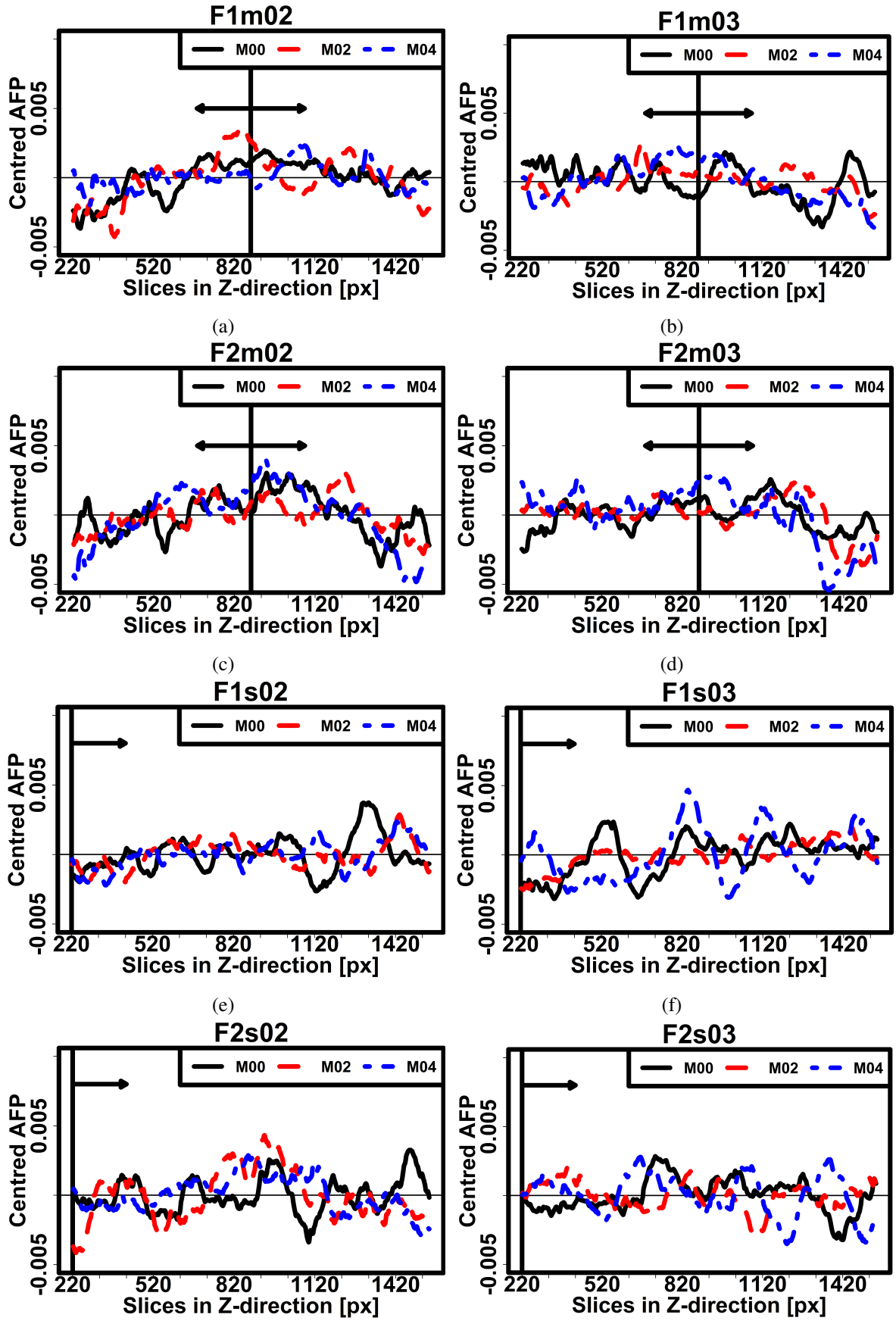

Figure 6.4: Centred AFP along to the Z-direction without edge area. The casting point is marked with a vertical line and the flow direction is illustrated by arrows.

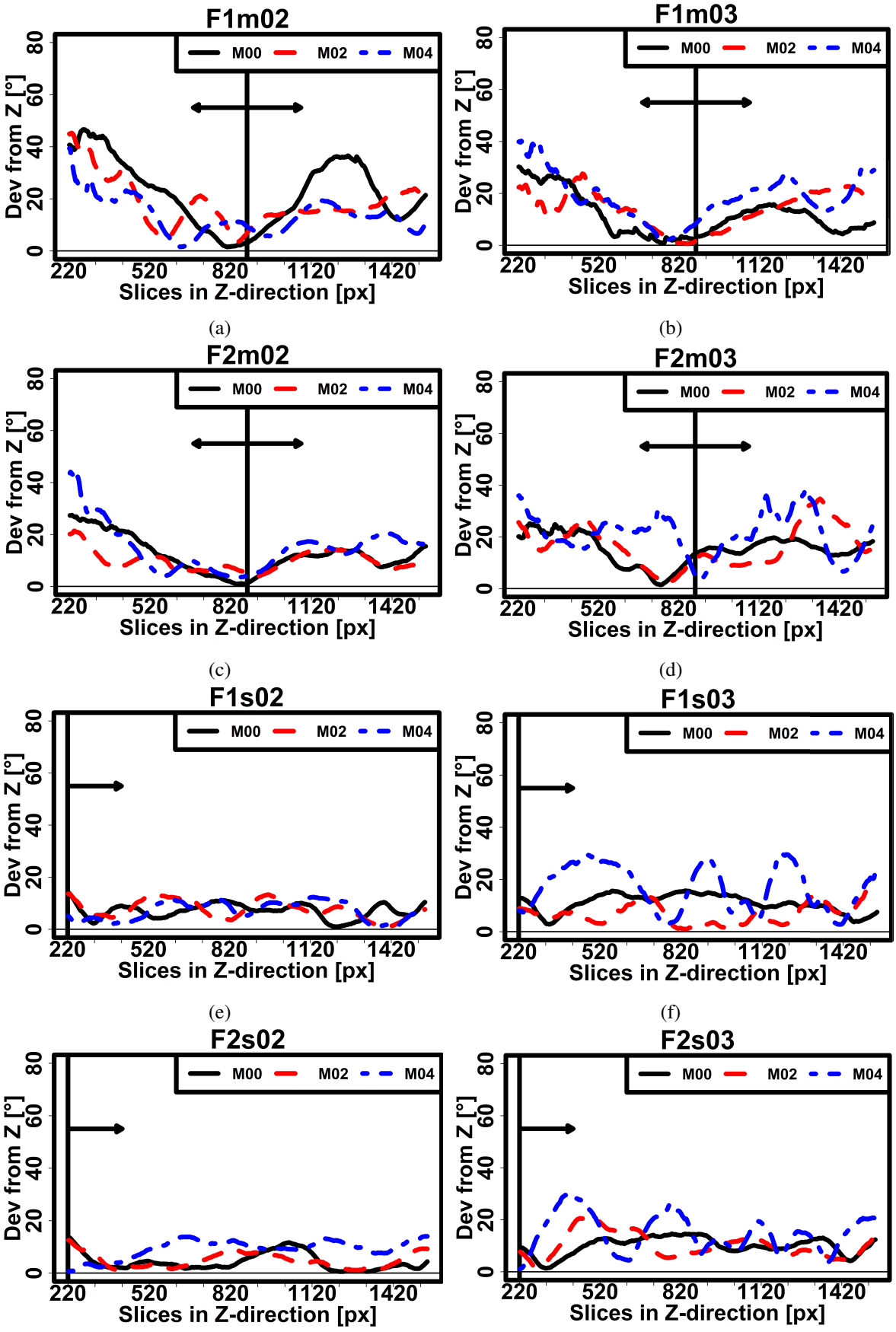

Figure 6.5: Deviation of the fibre orientations from the Z-axis along the Z-direction (without edge area). The casting point is marked with a vertical line and the flow direction is illustrated by arrows.

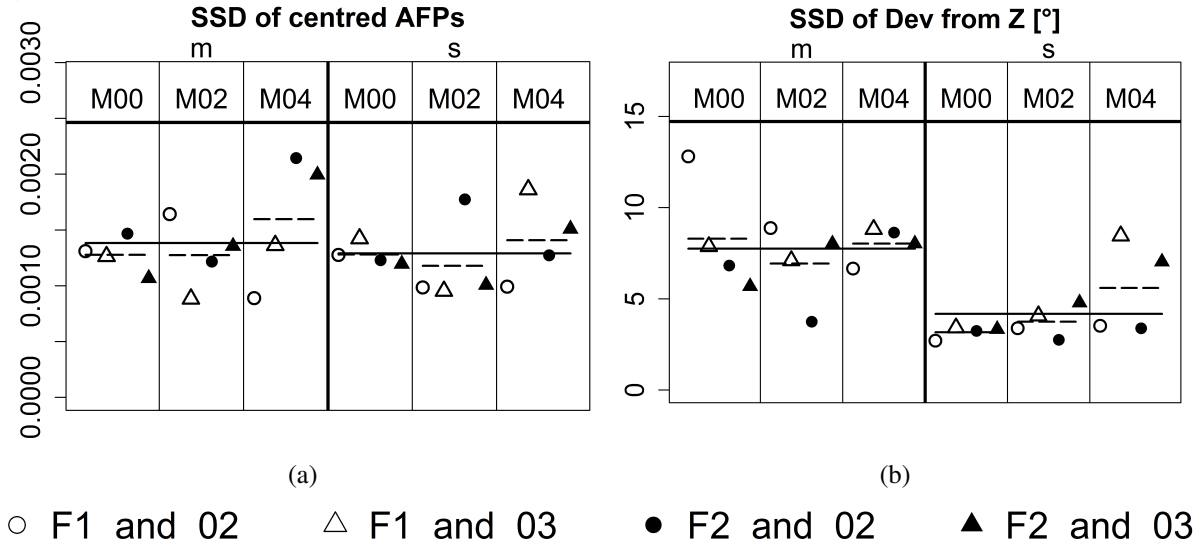

Figure 6.6: SSD of the centred AFP (a) and the deviation of the fibre orientation from the Z-axis (b) along the Z-direction. The mean value over all specimens with the same casting method is given as solid horizontal line. Dashed lines describe mean values in subgroups with fixed casting point and plasticiser content but varying fibre parameters.

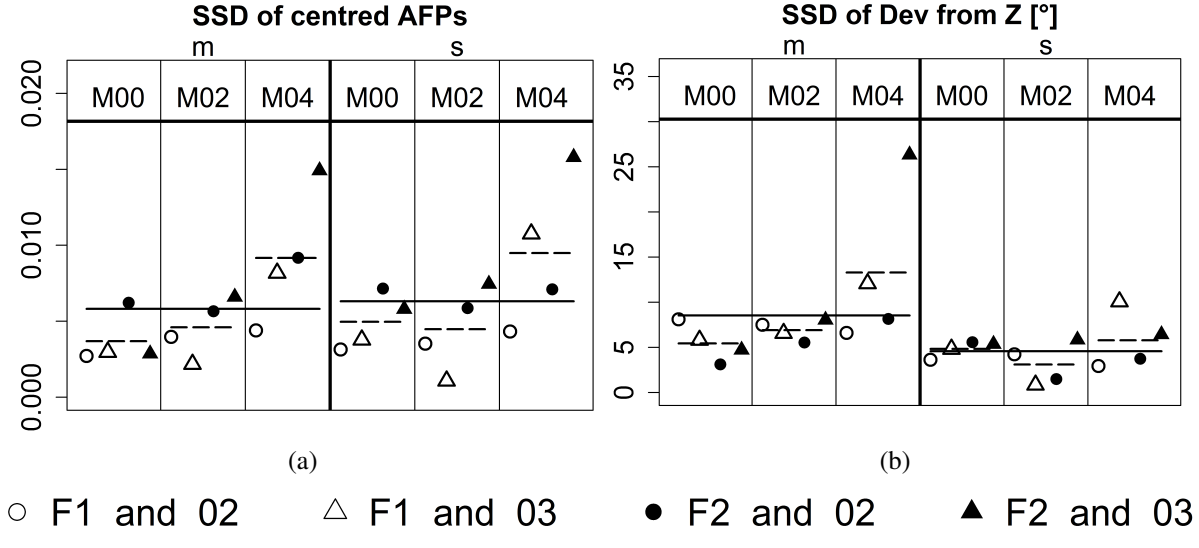

Figure 6.7: SSD of the centred AFP (a) and the deviation of the fibre orientation from the Z-axis (b) along the Y-direction. Dashed lines describe mean values in subgroups with fixed casting point and plasticiser content but varying fibre parameters.

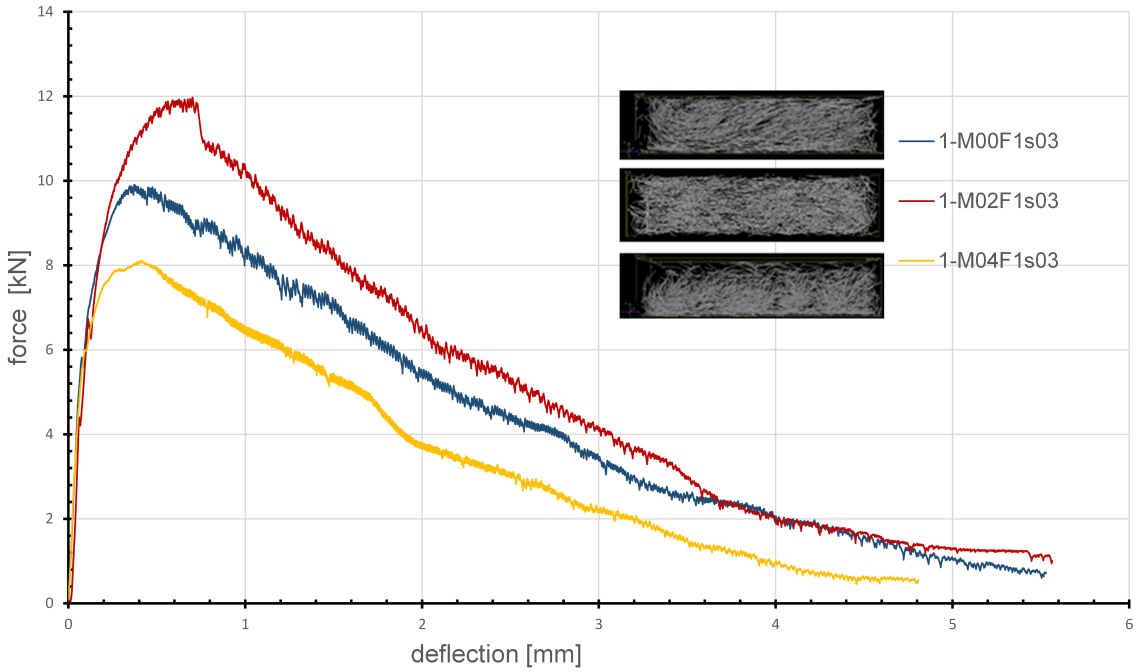

Figure 6.8: Load-midspan deflection curves for the specimens M00F1s03, M02F1s03 and M04F1s03

specimen is the dominant mechanism such that a crack width law can be assumed. This is in line with Prudencio et al. (2006) [111] and the AFGC-Recommendation (2013) [99]. The residual width of the other cracks depends on the deformation degree reached before, which could be elastic or elastoplastic. Figure 6.8 shows the load-midspan deflection curves for different consistencies of F1-specimens. Maximal force values are observed for the M02-specimen which has the most homogeneous fibre system. In contrast, the M04-specimen with strong sedimentation of fibres is least stable. Similar results have been obtained for F2-specimens cast from the middle.

The load-deflection curves for all specimens are shown in Figure 6.9. Typically, the first crack occurs at a deflection between 0.06 and 0.08 mm and the maximum linear stress is reached at a deflection between 0.17 and 0.22 mm. In all cases, specimens with higher fibre volume fraction (F2, dark colours) turn out to be more stable than those with only 1% volume fraction (F1, bright colours). For fixed volume fraction, specimens with thin (hence, more) fibres yielded better bending performance than specimens with thick fibres. M04-specimens clearly show a reduced mechanical stability while M00- and M02-specimens are comparable. The variation between the curves for the three specimens with the same parameters is small compared to the overall variability.

In general, the m-specimens show reduced elastic strengths compared to s-specimens. The difference between m- and s-specimens reduces when increasing the fibre volume fraction. For fixed fibre volume fraction, the specimens with reduced fibre diameter, hence, containing more fibres, show a better performance. Irrespectively of the casting method and the fibre parameters, the maximal elastic flexural strength is obtained for the M02-specimens. The difference between M00-specimens and M02-specimens is typically small. M04-specimens show the lowest strength which can be explained by the inhomogeneities in the fibre system due to sedimentation.

6.1.3 Discussion

The casting process causes a turbulence in the vicinity of the casting point, which produces a heterogeneous fibre geometry in this region. The flux seems to get laminar a few centimetres (around 2-6 cm) after the casting point. The spatial fibre distribution becomes homogeneous and the fibres align in flow

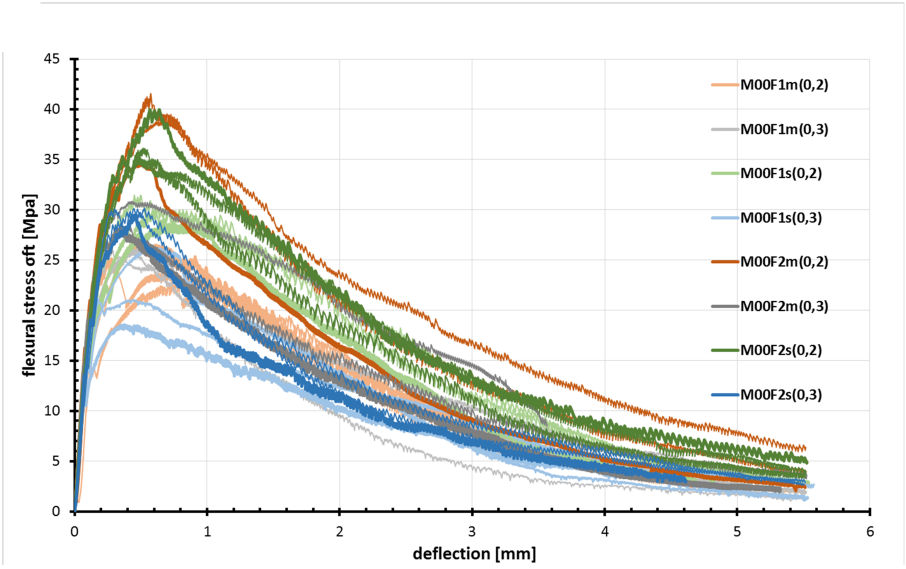

(a)

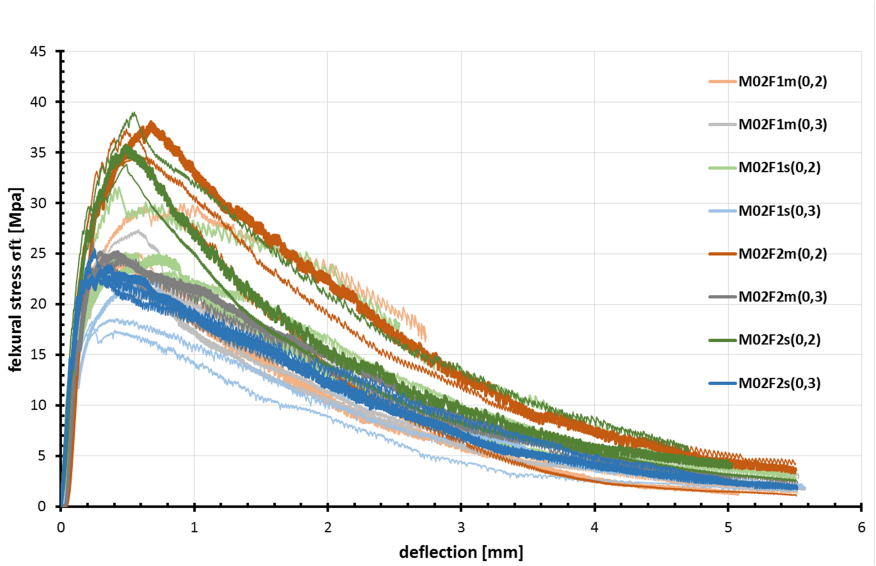

(b)

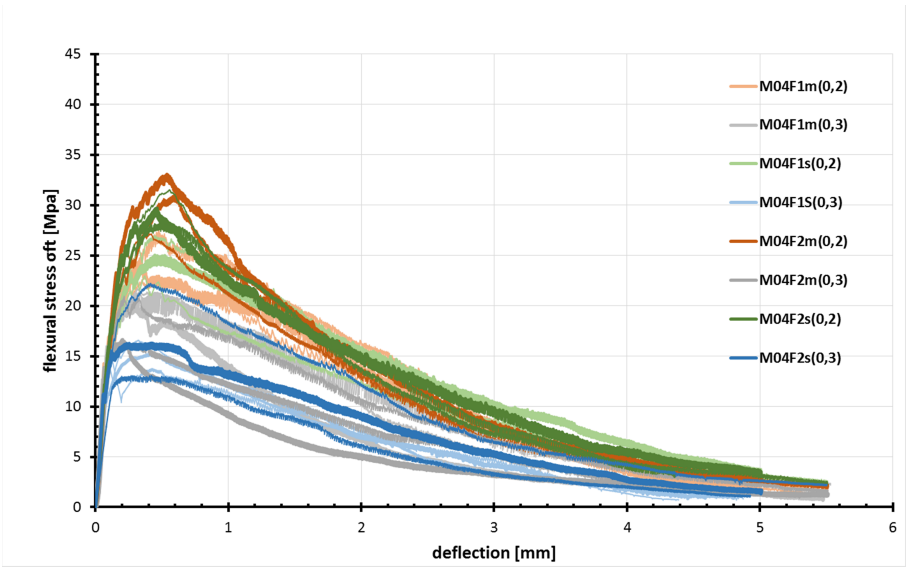

(c)

Figure 6.9: Flexural stress–deflection curves of all tested specimens grouped by consistencies M00 (a), M02 (b) and M04 (c)

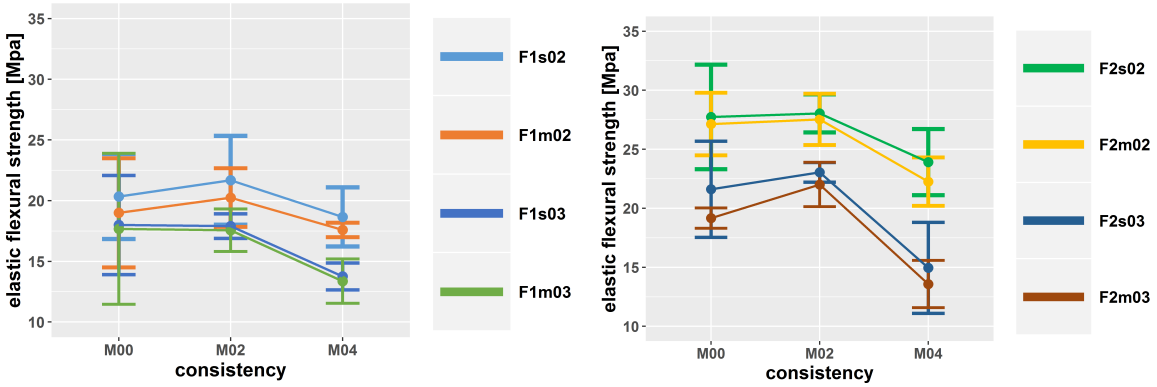

(a) (b)

Figure 6.10: Correlation between the studied parameters and elastic flexural strength. Dots are the means of the elastic flexural strengths of the three specimens with equal parameters. The error bars represent the 95% confidence interval of the mean

direction. The degree of alignment depends mainly on the consistency of the mixture.

Fibres in M00-specimens keep their orientation caused by turbulent flux in the vicinity of the casting point because the viscosity of the matrix is high enough to prevent the realignment of the fibres by their own weight. This realignment is possible with consistency M02 resulting in homogeneous fibre systems even close to the casting point. In contrast, the very low viscosity of the M04-mixture leads to fluctuations and sedimentation. The flexural strength observed during the bending test correlates well with the observed homogeneity of the specimens. M02-specimens achieved the highest strength followed by M00-specimens.

6.2 Conclusion

We investigated the influence of production parameters on the fibre geometry and, as a consequence, on the flexural behaviour of UHPFRC. The fibre geometry in specimens with different production parameters was investigated by means of micro-computed tomography. Subsequently, the flexural behaviour of the specimens was investigated in four point bending tests. The following conclusions could be drawn:

- Casting from the side results in a more homogeneous fibre geometry than casting from the middle. This results in a better mechanical performance.
- Increasing the fibre radius from d_f = 0.2 mm to d_f = 0.3 mm increases the inhomogeneity in the fibre systems. In particular, sedimentation is more pronounced for thicker fibres.
- Fibre orientation stabilises after a certain distance from the casting point. This is consistent with findings by Vandewalle et al. (2008) [67] and Ferrara et al. (2011) [68]. In our experiments, a unidirectional alignment of the fibres with deviations of a few degrees from the flow direction can be assumed approx. 2-6 cm after the casting point for not too fluid consistencies (M00 or M02).
- The most homogeneous fibre systems resulting in the highest flexural strength were obtained using the M02 mixture with a spread flow (Hagermann cone) between 27 and 28 cm. Mixtures with lower spread flow (25-27 cm) can deliver good results, too. If the spread flow exceeds 28 cm, significant sedimentation of the fibres is observed which decreases the flexural strength. These findings are in line with the results by Wang et al. (2017) [65] and Stähli et al. (2008) [66].
- A wall effect could be observed close to the boundary of the formwork (5 -10 mm). Wall effects are stronger for increasing volume fraction and decreasing fibre diameter. Casting from the middle

results in reduced wall effects compared to casting from the side. This is probably correlated with the lower flow distance of the material.

To allow for an investigation of concrete elements (e.g. beams), models and methods from spatial statistics could be used to predict the concrete geometry at a given position from a limited number of samples. Numerical flow simulation provides an alternative approach for predicting the fibre geometry of UHPFRC samples for given production parameters [112, 113]. Simulation based approaches can reduce the effort of such investigations compared to the production, characterisation and testing of large amounts of concrete samples. However, the simulations should be validated by experiments. The image analysis tools presented (AFP, Dev) yield statistical information that can be compared to fibre parameters observed in simulations.

Chapter 7

Influence of specimen size on the fibre geometry and tensile strength of UHPFRC

In the previous section, we investigated the influence of production parameters on fibre geometry and correlated it with the bending behaviour of the specimens. It remains an open question to which extent our findings can be generalised to larger specimens, see Herrmann et. al (2019) [114] for a discussion. To investigate this question in the framework presented here, we produced M02F2s02 production equivalent specimens of five different sizes. Due to the limited sample size that can be handled by μCT, specimens have to be cut into smaller cuboids before scanning.

7.1 Results

Recall that the Z-axis of the coordinate system corresponds to the flow direction during casting and to the tensile axis in the tensile tests.

Stress-strain curves are shown in Figure 7.1. In general, the tensile behaviour of all subspecimens looks similar and the initial stiffness is almost identical. However, there are obvious differences in tensile strength of the different subspecimens. In the following, each specimen will be discussed separately.

7.1.1 Specimen 4x4x16

This specimen is of the same size as the specimens investigated in Chapter 6. It mainly serves as a baseline and to ensure reproducibility of the production and the analysis protocols. Indeed, the plots for the AFP and the fibre orientation deviation shown in Figure 7.2 are similar for 4x4x16 and specimen M02F2s02 used in Chapter 6. The stress strain curve shown in Figure 7.1a cannot be compared to M02F2s02 since 4x4x16 was tensioned and M02F2s02 was bended.

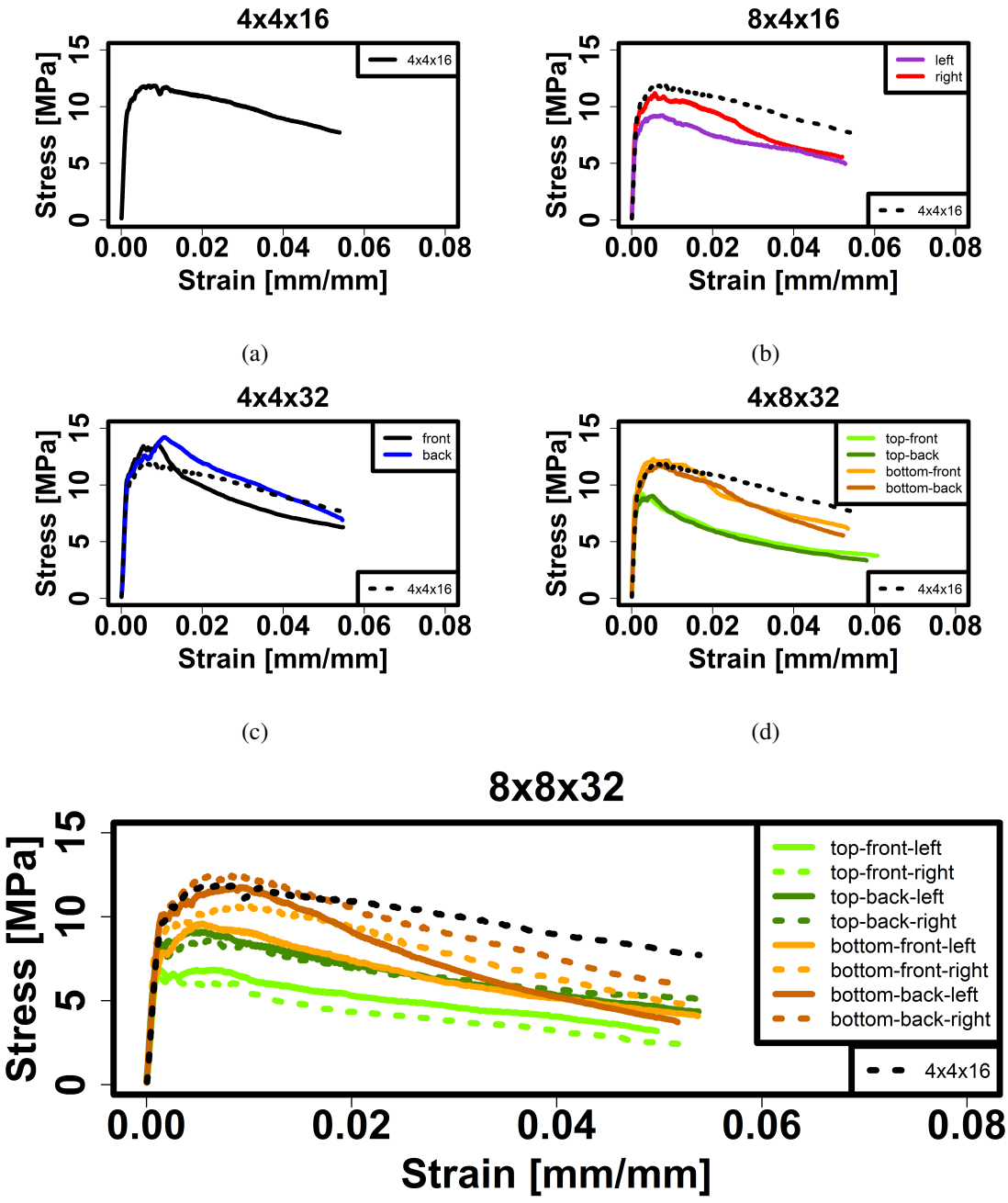

Figure 7.1: Stress-strain curves for all specimens.

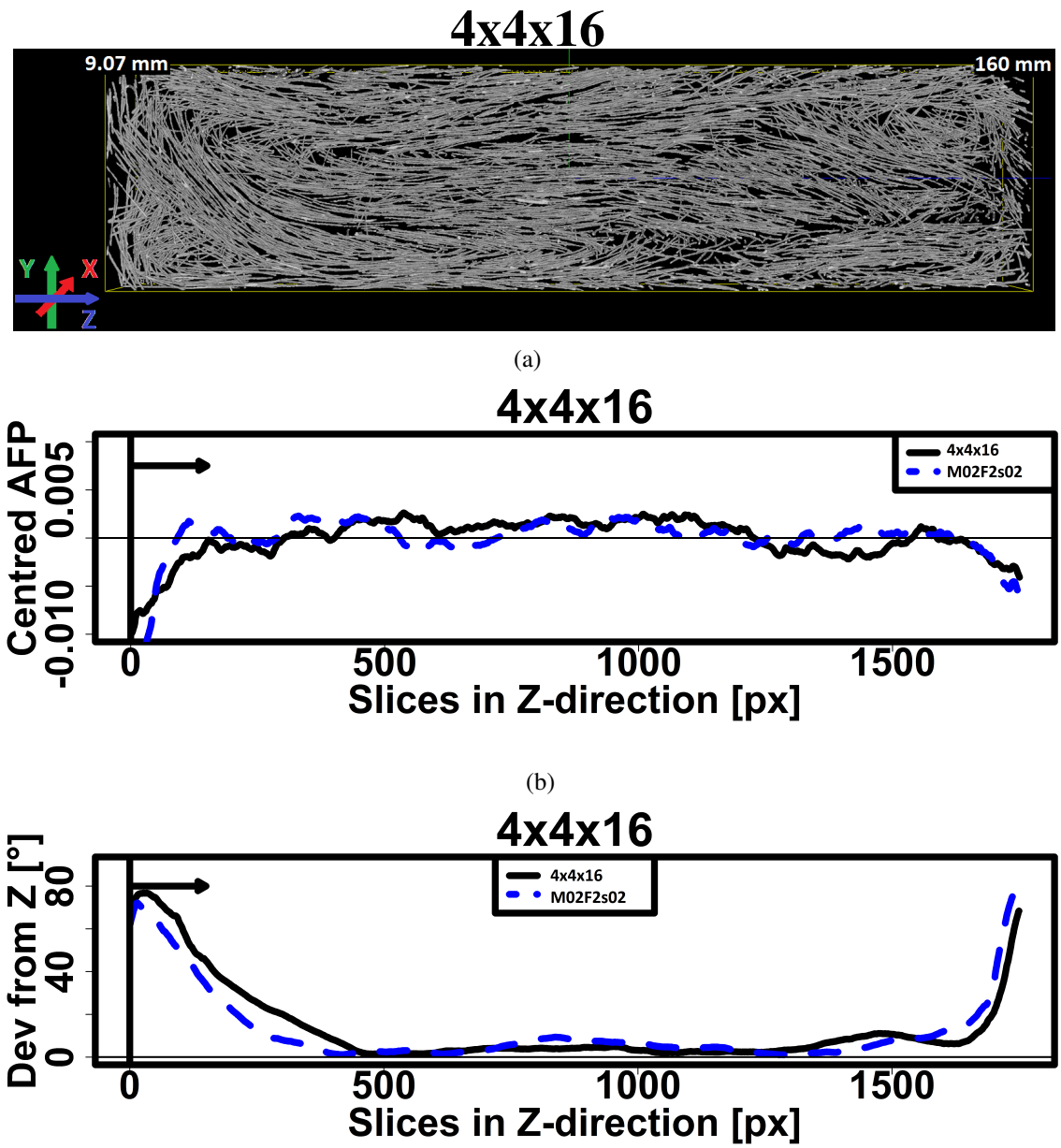

Figure 7.2: Specimen 4x4x16: Subvolume rendering (a), centred AFP (b), and deviation of the fibre orientations from the Z-axis (c) along the Z-direction. The curves obtained for specimen M02F2s02 in Chapter 6 are shown as dashed blue lines. The casting point is marked with a vertical line and the flow direction is illustrated by an arrow.

7.1.2 Specimen 8x4x16

The stress strain curves of specimen 8x4x16 are shown in Figure 7.1b. Based on the production process, similar results for the left and the right specimen are expected. The observation that the left specimen is weaker than the right one can be explained by the presence of a large agglomeration of silica fume in the left part of the specimen, see Figure 7.3.

Both specimen parts are slightly weaker than specimen 4x4x16 which may be explained by a larger variability of the local fibre geometry. In particular, we observe slightly stronger fibre misalignment than in specimen 4x4x16, see Figure 7.4. Additionally, fibre misalignment is observed in the bottom part of the specimen, see Figure 7.5. Due to the increased specimen width, flow lines to the side are observed

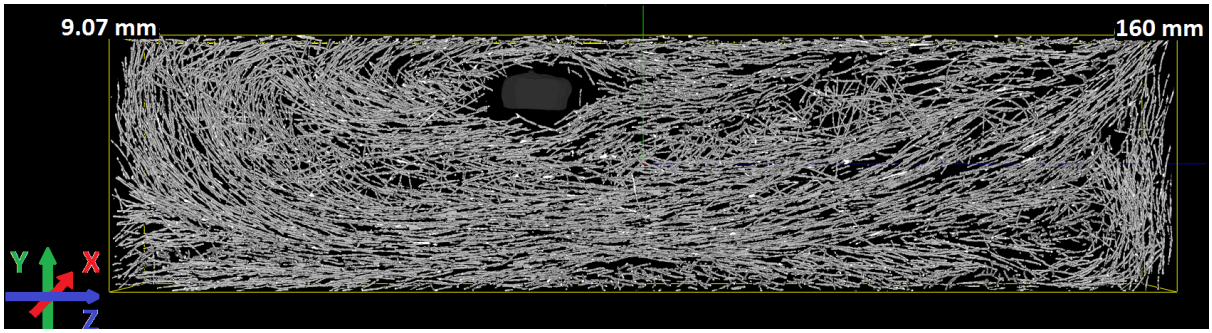

(a)

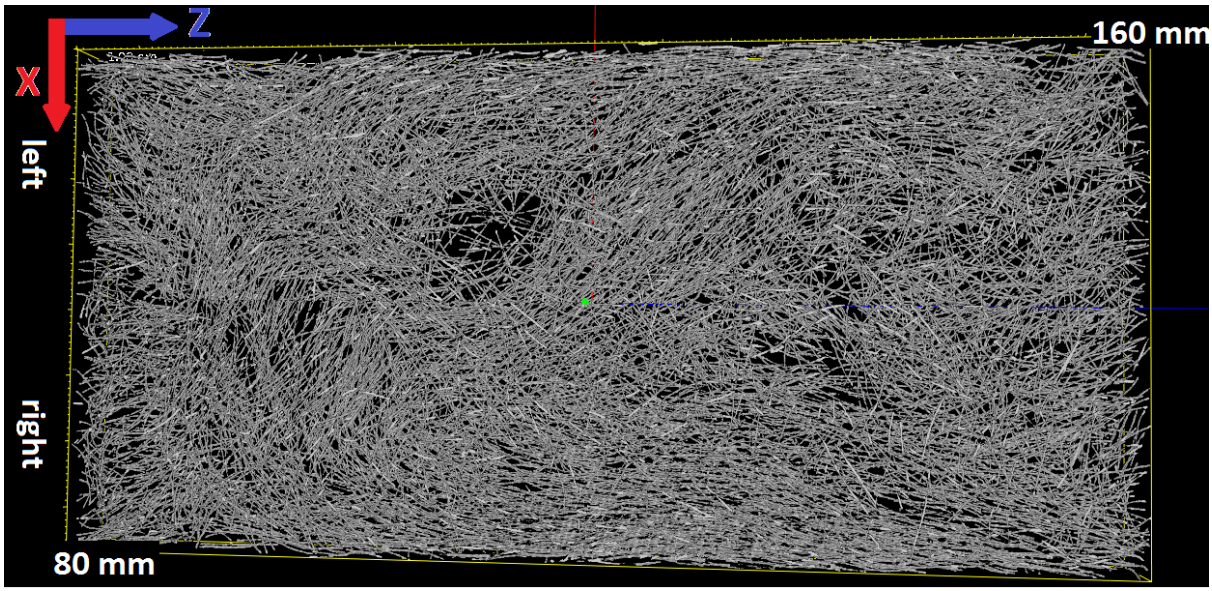

(b)

Figure 7.3: Silica agglomeration (dark grey) located in the upper left part of specimen 8x4x16. View from the side (a). View from the top (b).

resulting in fibres pointing towards the outer edge of the samples in X-direction. The fibre content is reduced in the left specimen part which may partially be explained by a displacement of the fibres to the right due to the silica agglomeration (Figure 7.5c). It seems that this displacement also leads to the fibre misalignment towards the right edge of the specimen (Figure 7.5d).

This could mean that the increasing fibre fraction at the bottom (Figure 7.5a) should not be interpreted as fibre sedimentation. The consistency of the mixture is very stable and the fibre geometry shown in Figure 7.3 does not indicate fibre sedimentation. In contrast, the fibre geometry looks integrated, coherent and harmonious as expected for the given flow direction and casting point. The large deviation of the fibres from the Z-direction in the bottom part is probably caused by the interaction between the first concrete layers during the casting process, when the fibre concrete of the new layer flows over the previous one. This also applies to all following specimens.

7.1.3 Specimen 4x4x32

The stress strain curves shown in Figure 7.1c show a similar tensile behaviour in the front and the back part with the back being slightly stronger. The back part shows a lower fibre content than the front part, but a better alignment of the fibres in the tensile direction, see Figure 7.6. Additionally, fibres are more homogeneously distributed over the sample height in the back part, see Figure 7.7.

Both specimens show a reduced fibre density in the upper part. The effect is more pronounced in the front part than in the back part. Orientations are very homogeneous over the complete height with no

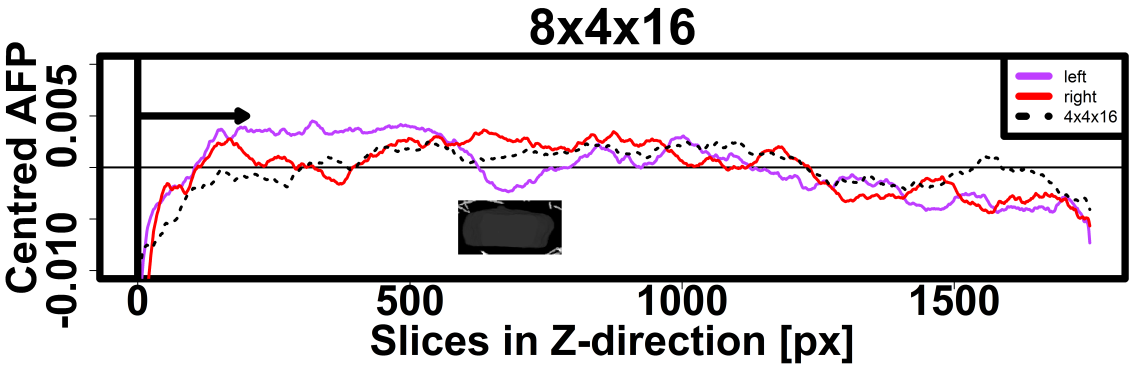

(a)

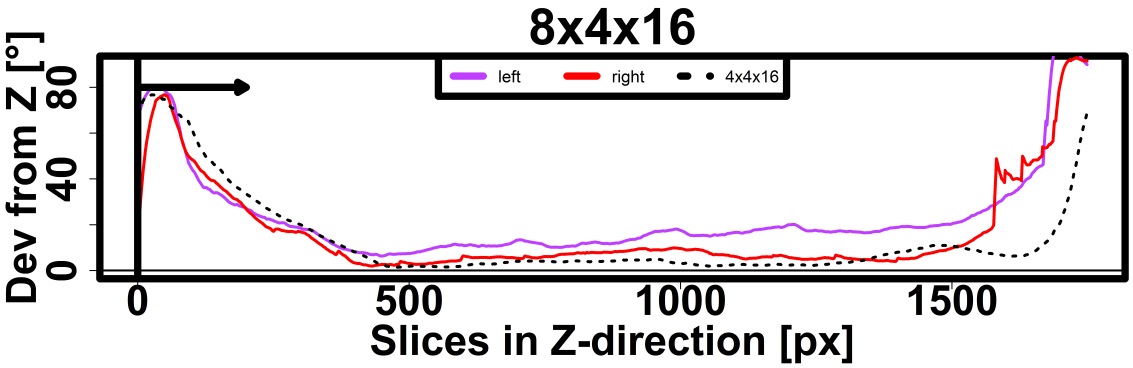

(b)

Figure 7.4: Specimen 8x4x16: Centred AFP along the Z-direction (a), and deviation of the fibre orientations from the Z-axis (b) along the Z-direction. The position of the silica fume agglomeration is shown in dark grey. The casting point is marked with a vertical line and the flow direction is illustrated by an arrow.

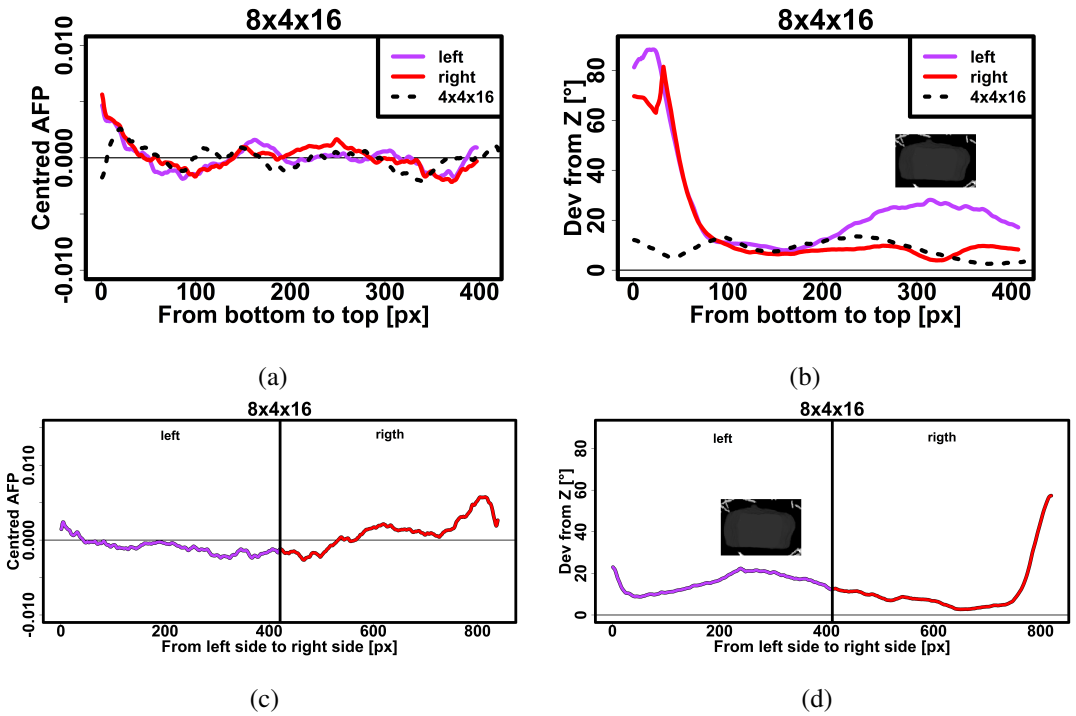

Figure 7.5: Specimen 8x4x16: Centred AFP (a,c) and deviation of the fibre orientations from the Z-axis (b,d) along Y-direction (a,b) and along the X-direction (c,d). The position of the silica agglomeration is shown in dark grey.

significant differences between front and back part. The profiles in X-direction show a symmetric and very homogeneous structure both regarding fibre content and fibre orientation, see Figure 7.7.

7.1.4 Specimen 4x8x32

According to the stress strain curves, see Figure 7.1d, the two lower subspecimens are more tensile than the two upper ones. This observation can be explained by a reduced fibre density and poorer fibre alignment in the top part compared to the bottom, see Figures 7.8 and 7.9. There is no significant deviation between front and back parts. The fibre geometry is symmetric along its width.

7.1.5 Specimen 8x8x32

The stress strain curves for the eight subsamples of this specimen are shown in Figure 7.1e. In general, there are no significant differences between subsamples on the left and their counterparts on the right. In the remaining directions, the order from weakest to strongest is front top, back top, front bottom, and back bottom. Hence, the subvolumes from the bottom are stronger than those from the top of the specimen. This can be explained by the lower fibre density and larger deviation from Z-axis in the top parts compared to the bottom, see Figures 7.10 and 7.11. Additionally, the back part is stronger than the front. The reason for this is less obvious. The volume rendering in the side view shown in Figure 7.10 shows a wavelike pattern with strong orientational deviations in the front and in the upper back part. The trends in the curves are similar to those obtained for the 4x8x32 specimen.

7.1.6 Comparison of specimens

The calculated elastic and ultimate tensile strengths of the subspecimens and the corresponding strains are plotted in Figure 7.12. The elastic tensile strain ranges between 0.85 ‰ and 1.9 ‰ (mean value approx.1.3 ‰) and the ultimate tensile strain ranges between 2.6 ‰ and 10.65 ‰ (mean value approx.

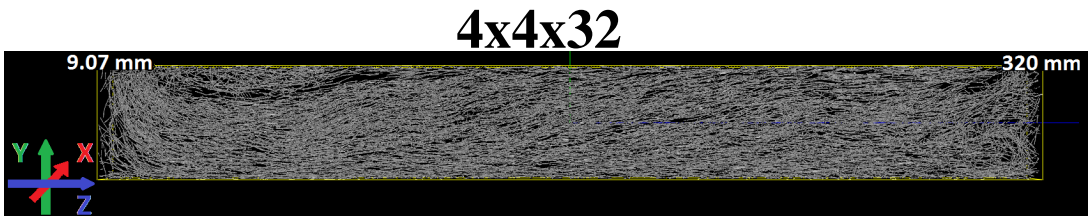

(a)

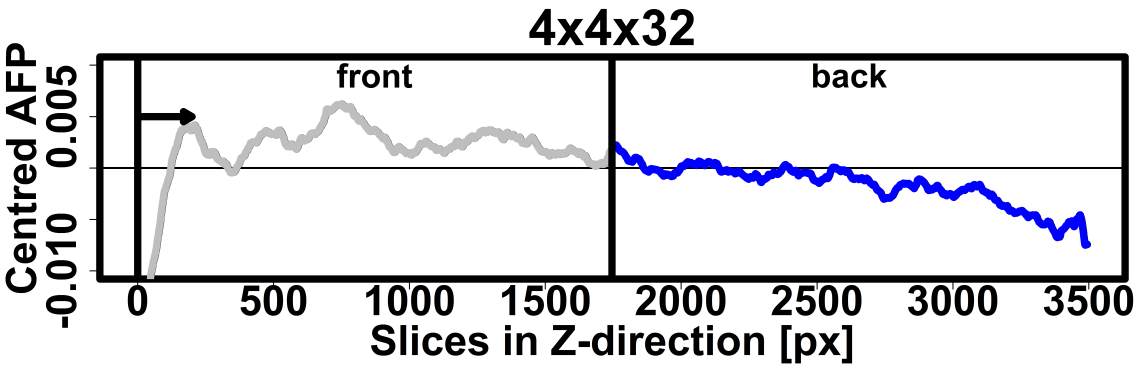

(b)

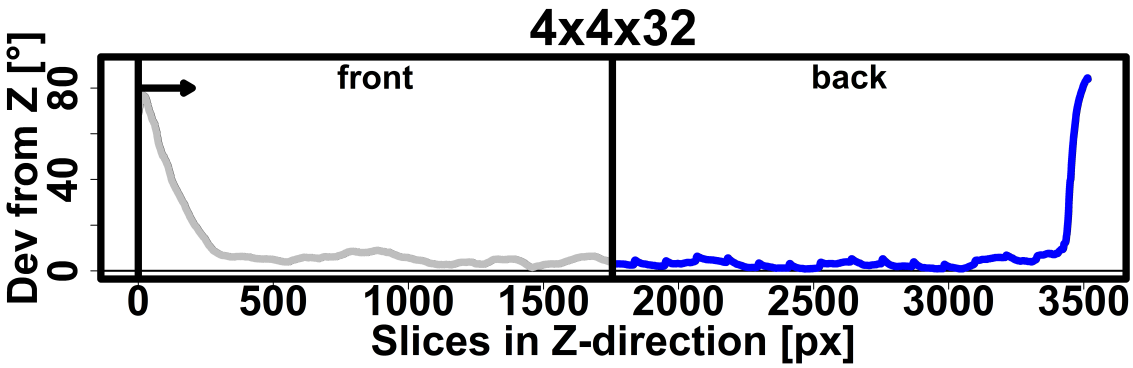

(c)

Figure 7.6: Specimen 4x4x32: Subvolume rendering (a), centred AFP (b) and deviation of the fibre orientations from the Z-axis (c) along the Z-direction. The casting point is marked with a vertical line and the flow direction is illustrated by an arrow.

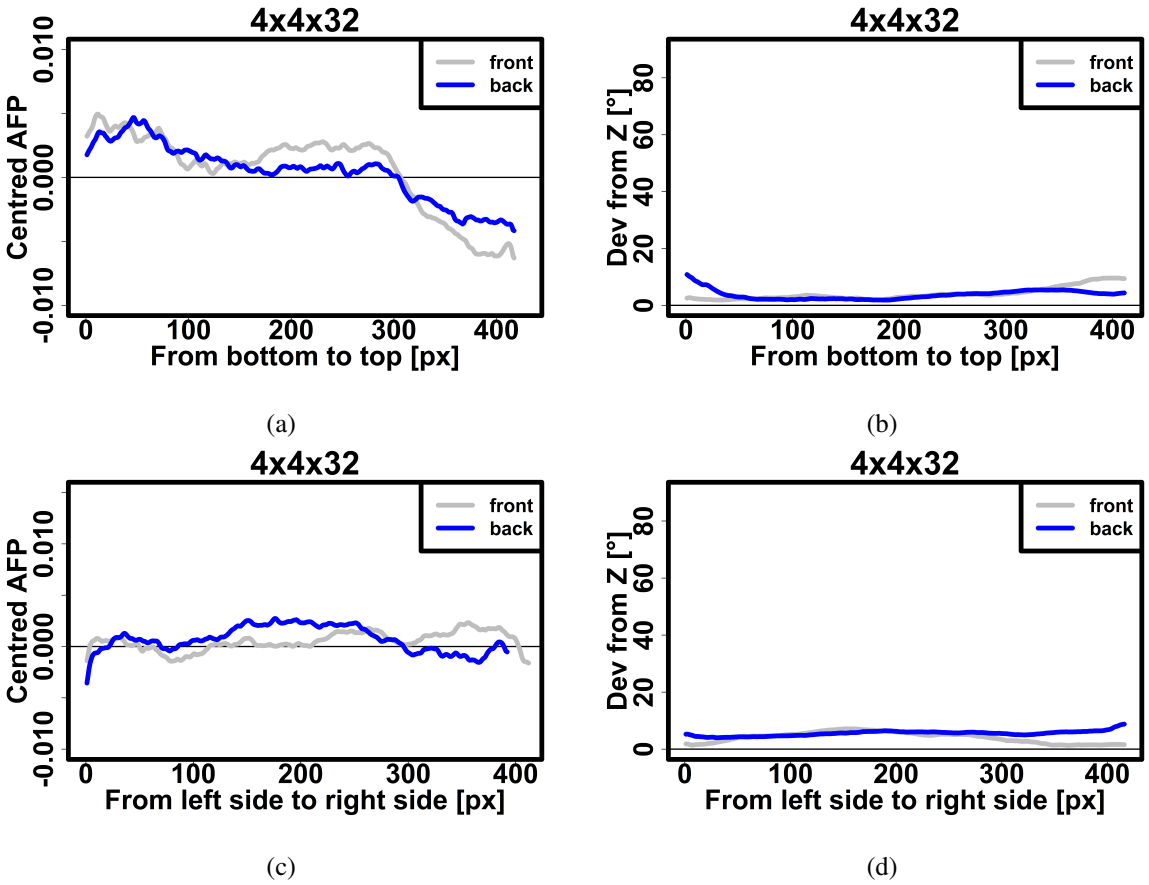

Figure 7.7: Specimen 4x4x32: Centred AFP (a,c) and deviation of the fibre orientations from the Z-axis (b,d) along Y-direction (a,b) and along the X-direction (c,d).

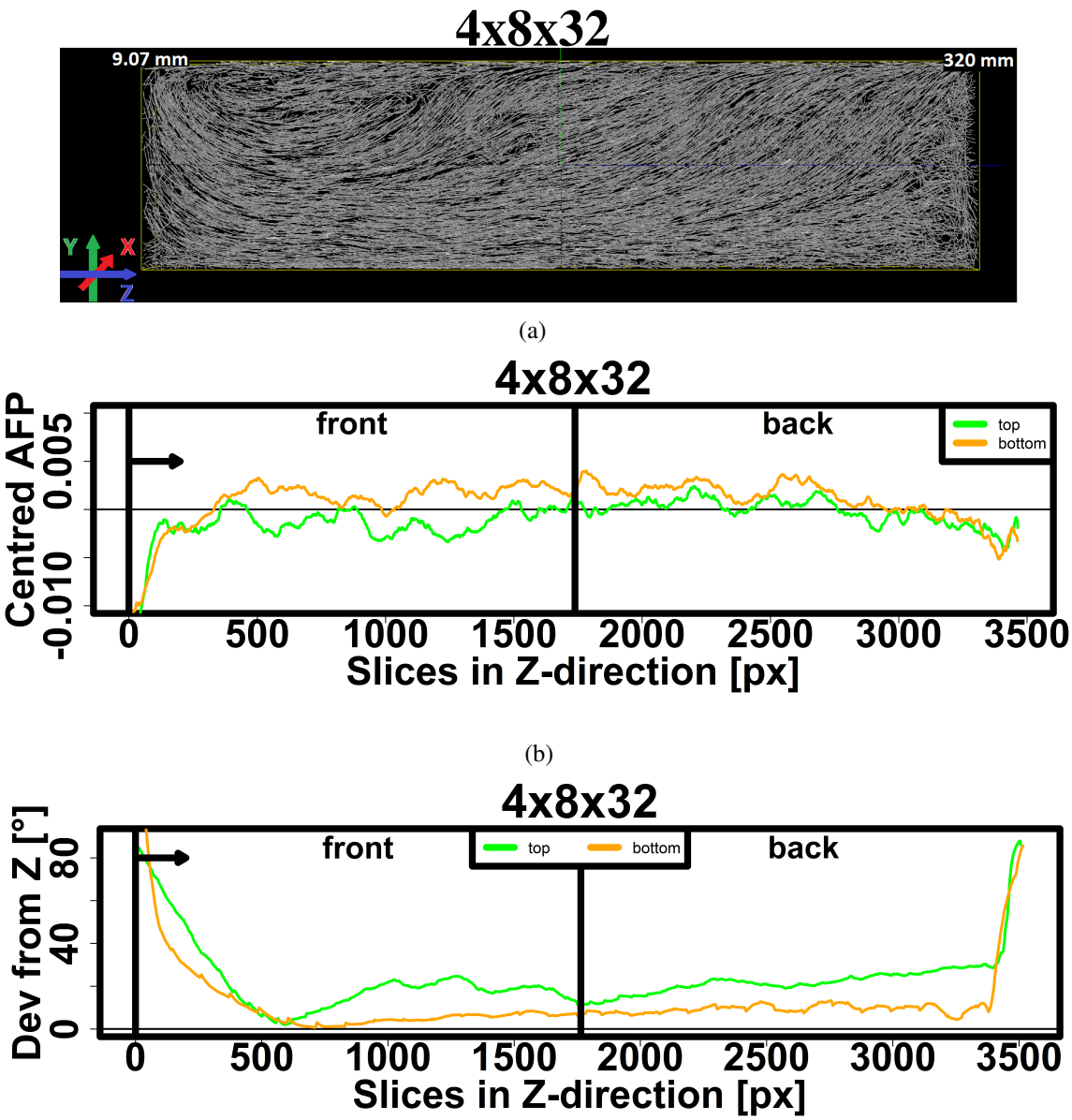

Figure 7.8: Specimen 4x8x32: Subvolume rendering (a), centred AFP (b) and deviation of the fibre orientations from the Z-axis (c) along the Z-direction. The casting point is marked with a vertical line and the flow direction is illustrated by an arrow. The subvolume rendering shows less fibres in the top front part of the specimen than in the bottom front part.

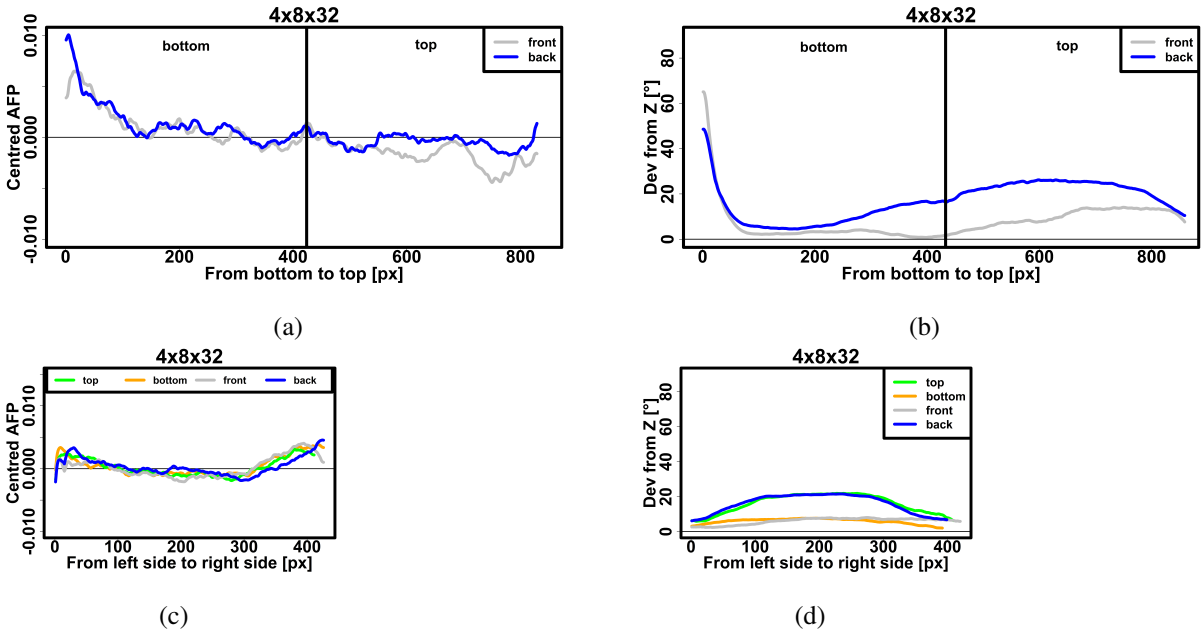

Figure 7.9: Specimen 4x8x32: Centred AFP (a,c) and deviation of the fibre orientations from the Z-axis (b,d) along Y-direction (a,b) and along the X-direction (c,d).

6.5 ‰). As mentioned, the results cannot be used to evaluate the size effect on the original specimens. They rather illustrate the influence of the specimen size on the local strength due to local variations in the fibre geometry. Figure 7.12 shows that the subspecimens in the top tend to have reduced elastic and ultimate strength compared to those in the bottom. In the same way, subspecimens from the front show a smaller strength than those from the back. The difference between the left and right subspecimens seems to be negligible. Subspecimens of specimen 4x8x32 are stronger than the corresponding subspecimens of the enlarged specimen 8x8x32. Subspecimens of the smaller specimens 4x4x16 and 4x4x32 show a higher strength than those from the large specimens.

7.2 Conclusion

We investigated the influence of the specimen size on the fibre geometry in fine-grained UHPFRC blended with 2 Vol.-% straight micro-fibres. Specimens were produced in five sizes and cut into subspecimens of equal size. The subspecimens were imaged by micro-computed tomography. The fibre system was characterised slice-wise by computing the local fibre content (AFP) and fibre alignment (deviation from the Z-axis). Correlations between the fibre geometry and the tensile strength of the subspecimens were investigated. The general finding is that the fibre geometry changes locally when increasing the specimen size. This change depends on the direction in which the sample is enlarged, i.e., increasing the width has a different effect than increasing the length or depth. The following conclusions can be drawn:

- Up to reflection, the fibre geometries in the left and the right subspecimen show the same behaviour. Hence, also the results of the tensile tests are similar for left and right subspecimens. An exception was specimen 8x4x16 which contained an abnormally large silica fume agglomeration. In absence of such anomalies, increasing the width of the specimen will most likely have a negligible influence, if the casting is performed over the whole specimen width.

- Wavelike patterns induced by the flow lines close to the casting point are more pronounced in higher and longer specimens. This resulted in a reduced tensile strength of the front subspecimens in specimens 4x8x32 and 8x8x32.

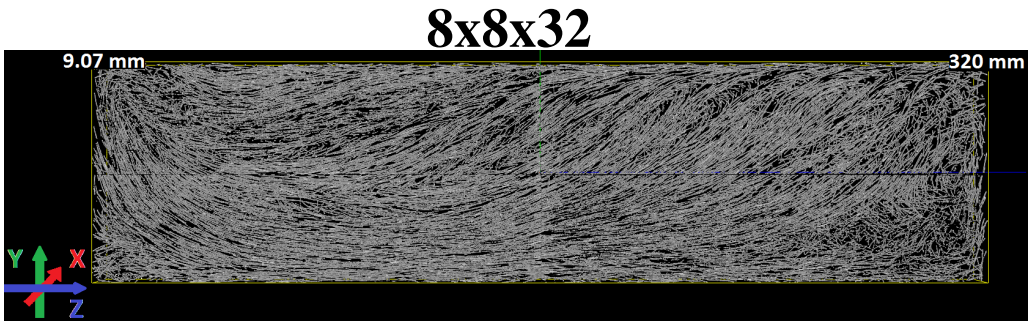

(a)

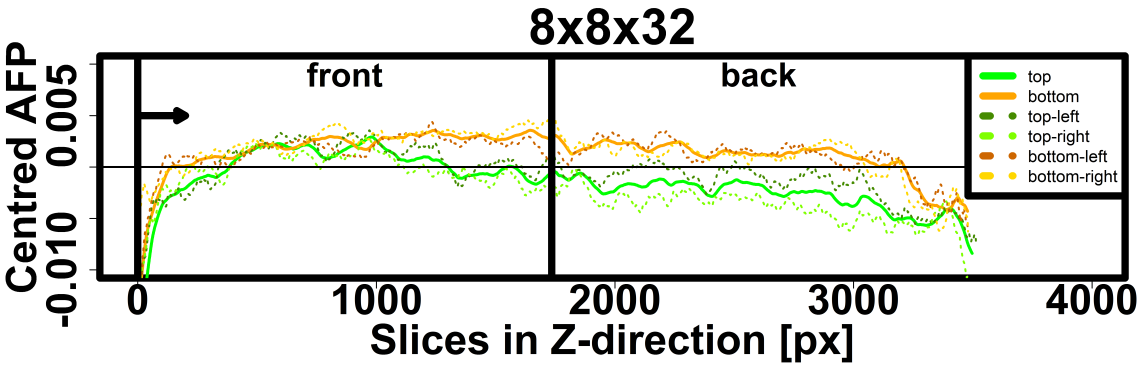

(b)

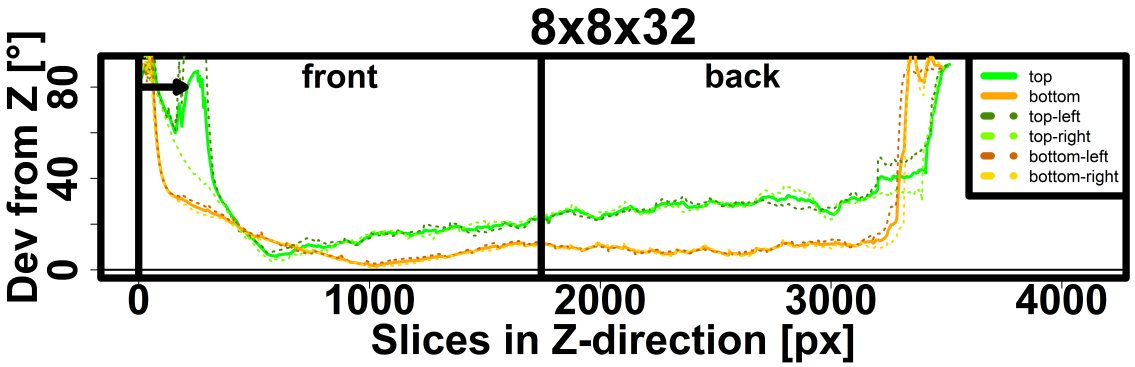

(c)

Figure 7.10: Specimen 8x8x32: Subvolume rendering (a), centred AFP (b) and deviation of the fibre orientations from the Z-axis (c) along the Z-direction. The casting point is marked by a vertical line and the flow direction is illustrated by an arrow.

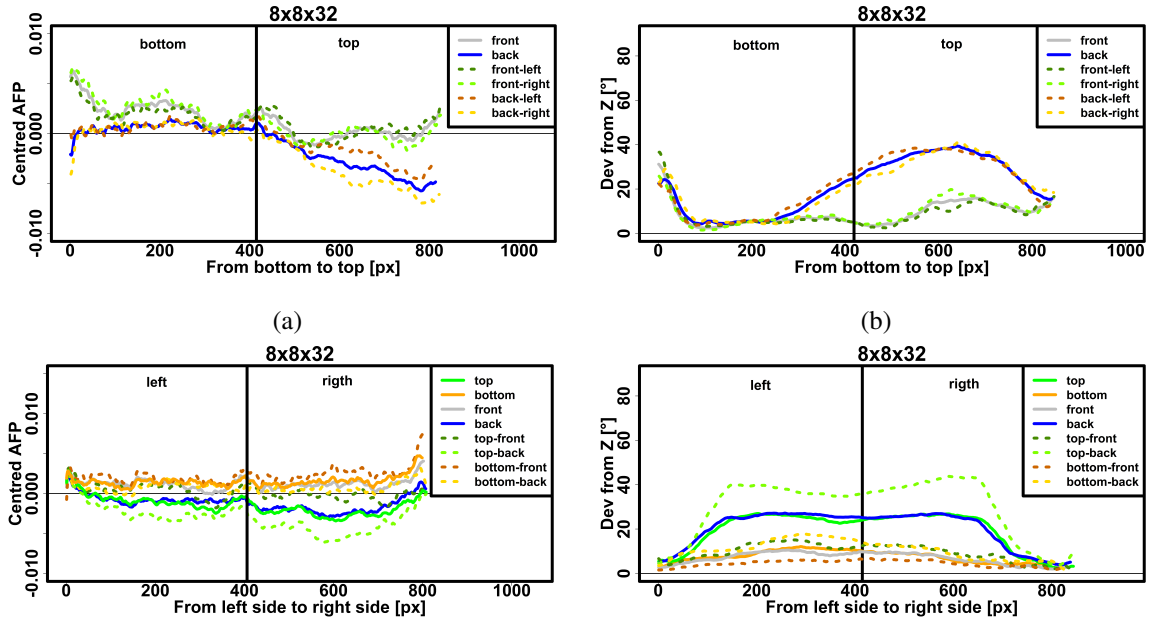

(a) (b)

(c) (d)

Figure 7.11: Specimen 8x8x32: Centred AFP (a,c) and deviation of the fibre orientations from the Z-axis (b,d) along Y-direction (a,b) and along the X-direction (c,d).

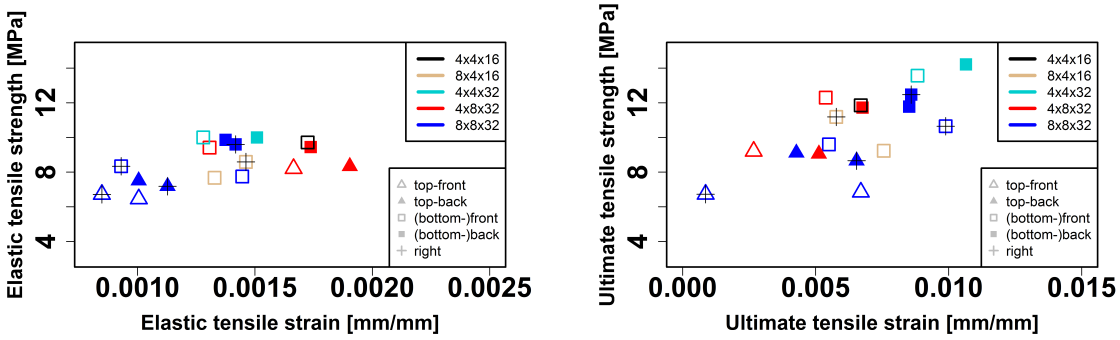

(a) (b)

Figure 7.12: Correlations between elastic stress σ_{el}^{exp} (a) and ultimate stress σ_{ult}^{exp} (b) as well as the corresponding strain values. Note that 4x4x16 belongs to the black square without content (see the sign for (bottom-)front in the legend below).

- For fixed cross-section size, increasing the specimen length gradually decreases the fibre content along the Z-axis. However, the alignment to the Z-axis improves.
- Edge effects of different magnitude were observed close to the sides and the bottom in all specimens.
- Local changes in the fibre geometry resulted in varying tensile strength of the subspecimens. Subspecimens showed an increased tensile strength in the bottom and back parts and a decreased tensile strength in the top and front parts. This is consistent with findings in [114, 115].
- Compared to the smallest specimen 4x4x16, subspecimens of the larger specimens showed a slight reduction in the tensile strength.

In conclusion, changing the specimen size causes local changes in the fibre geometry which influences the tensile strength. Specimen height appears to be the most determining parameter followed by specimen length. Specimen width seems to be less important. For further investigation of the size effect on the flexural behaviour of UHPFRC, mechanical tests could be performed on a series of specimens of different sizes. Such tests may also reveal to which extent the mechanical strength of a large specimen can be inferred from information on the subspecimens.

Chapter 8

Predicting the tensile behaviour of UHPFRC from single fibre pull-out tests

The results from Chapter 6 and 7 gave us a deeper understanding of the influence of production parameters and specimen size on fibre geometry and mechanical properties. This knowledge can be used to fit a stochastic geometry model to the observed microstructures, e.g. a system of cylinders of random orientation and position, see Redenbach and Vecchio (2011) [116]. Such models allow for the generation of virtual concrete samples with a large range of geometric characteristics. From these, mechanical properties of the concrete can be predicted.

8.1 Methods

8.1.1 Single fibre segmentation

For calculating the tensile force contribution of single 02-fibres in a loaded composite, the individual 02-fibres have to be separated in the segmentation. Due to the coarse image resolution, the space between touching fibres is not sufficiently resolved. Hence, labelling the connected components of the fibre system leads to the formation of fibre clusters. For separating fibres in the clusters, a particle separation based on the watershed transform was applied [117]. During this procedure, fibres were split into segments which were merged manually to reconstruct the single fibres.

After CT scanning, a four point bending test (see Section 4.3) was performed on the sample M02F2s02. During this test, the specimen developed an approximately planar crack parallel to the XY-plane in the CT image. The location of this crack was identified in the CT scan. Due to the complexity of the single fibre segmentation, the analysis was restricted to the vicinity of the crack plane such that orientation and embedded length of fibres crossing the crack could be determined.

8.1.2 Modelling single-fibre pull-out curves

For performing single-fibre pull-out tests, individual fibres were embedded in a concrete slab. The same M02 concrete mixture and 02-fibres as described in Section 4.1 were used. The length $\mathrm{l_e}$ of the fibre part embedded in the concrete and the inclination angle θ of the fibres with respect to the pull-out direction were varied. The embedded length $\mathrm{l_e}$ was chosen as one half, one third or one sixth of the fibre length, i.e. $\mathrm{l_e}$ is $l_f/2 = 6.25$ mm, $l_f/3 \approx 4.17$ mm or $l_f/6 \approx 2.08$ mm. The inclination angle θ was varied from 0° to 80° in steps of 10°. For testing, the free end of the fibre was clamped between two metal jaws of the testing machine and pulled out while rigidly fixing the concrete slab. During the procedure, force-slip curves reporting the force P applied and the slip s were recorded. At least six fibres were tested for each combination $(\theta, \mathrm{l_e})$ resulting in more than 162 single-fibre pull-out curves.

Figure 8.1 shows the force-slip curves $P_i(s, \theta, \mathrm{l_e}),\ i = 1, \ldots, 6$, of the six tested fibres with $\theta = 10^\circ$ and $\mathrm{l_e} = l_f/2$. We denote by $\dot{P}(s, \theta, \mathrm{l_e})$ the median curve which is the point-wise median of the six

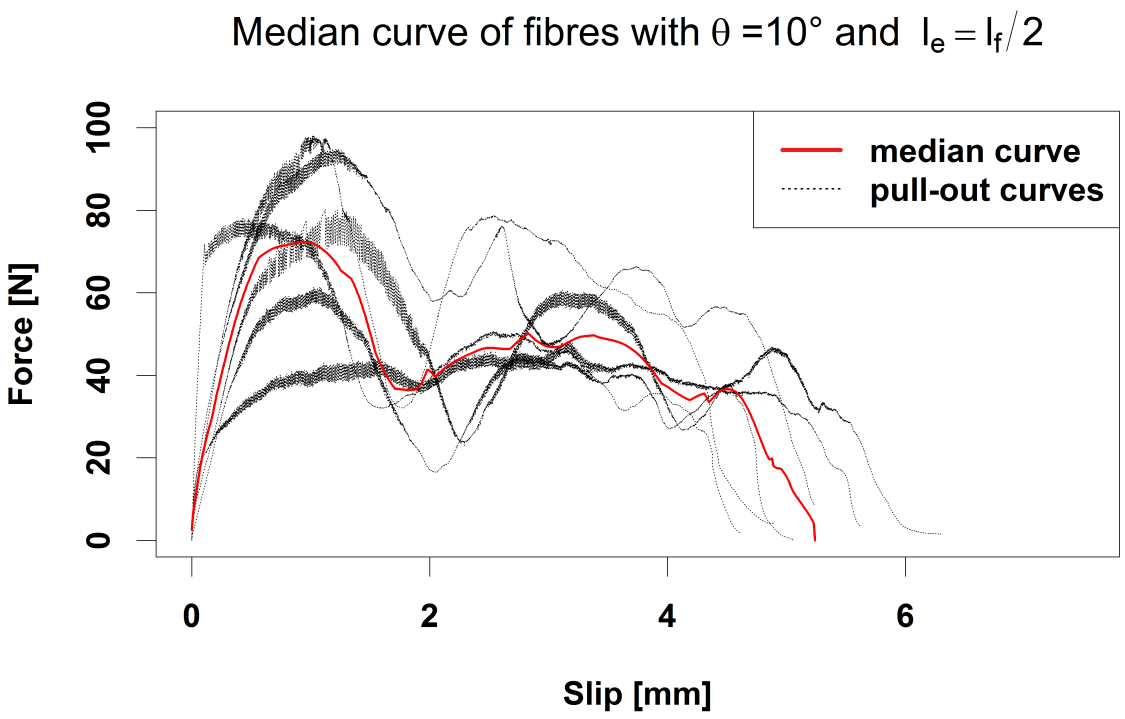

Figure 8.1: Median curve (red solid) of the single-fibre pull-out force curves (black dotted) with angle $\theta = 10°$ and $\mathrm{l_e} = l_f/2$.

single-fibre pull-out curves for a fixed combination $(\theta, \mathrm{l_e})$, i.e.

$$\dot{P}(s, \theta, \mathrm{l_e}) = med\left(P_1(s, \theta, \mathrm{l_e}), \ldots, P_6(s, \theta, \mathrm{l_e})\right), \; s \in [0, \mathrm{l_e}]. \tag{8.1}$$

In the next step, we fit a piecewise linear model to the observed force-slip curves. In the literature, several approaches (bilinear, trilinear, exponentially decreasing) for modelling single-fibre pull-out curves have been suggested, see [96]. Based on the results of our single fibre pull-out tests, we decided to use a three-phase model. Phase I represents the linear elastic part of the curve up to the yield strength P_{el} that is reached at slip s_{el}. Phase II is the nonlinear part up to the ultimate force P_{ult} at slip s_{ult}. For simplicity, this part is also described by a linear model. Phase III is a linear descending branch up to complete fibre pullout at slip s_{tot}, i.e., the last recorded slip value. See Figure 8.2 for an illustration of the model.

For fitting the model, the force and slip values derived from the six fibre-pullout tests per combination $(\theta, \mathrm{l_e})$ are averaged. We use the median values

$$\begin{aligned}
P_{el,med}(\theta, \mathrm{l_e}) &= med(P_{el,1}(\theta, \mathrm{l_e}), \ldots, P_{el,6}(\theta, \mathrm{l_e})) \\
P_{ult,med}(\theta, \mathrm{l_e}) &= med(P_{ult,1}(\theta, \mathrm{l_e}), \ldots, P_{ult,6}(\theta, \mathrm{l_e})) \\
s_{el,med}(\theta, \mathrm{l_e}) &= med(s_{el,1}(\theta, \mathrm{l_e}), \ldots, s_{el,6}(\theta, \mathrm{l_e})) \\
s_{ult,med}(\theta, \mathrm{l_e}) &= med(s_{ult,1}(\theta, \mathrm{l_e}), \ldots, s_{ult,6}(\theta, \mathrm{l_e})) \\
s_{tot,med}(\theta, \mathrm{l_e}) &= med(s_{tot,1}(\theta, \mathrm{l_e}), \ldots, s_{tot,6}(\theta, \mathrm{l_e})).
\end{aligned}$$

The numerical values are given in Appendix D Table D.1.

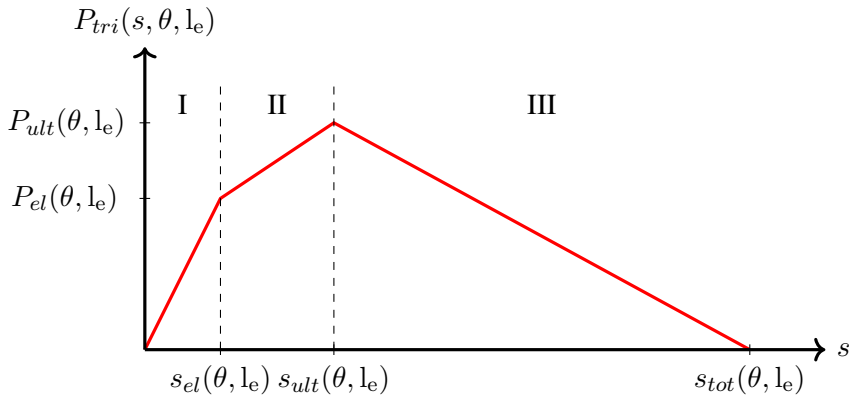

Figure 8.2: Simplified single-fibre pull-out force. Phase I and II given as linear increasing branches and phase III given as linear descending branch.

In summary, the model reads

$$P_{tri}(s,\theta,\mathrm{l_e}) = \begin{cases} p_1 \cdot s & 0 \le s \le s_{el,med}(\theta,\mathrm{l_e}) \\ & \text{(phase I)} \\ p_2 \cdot s + r_1 & s_{el,med}(\theta,\mathrm{l_e}) \le s \le s_{ult,med}(\theta,\mathrm{l_e}) \\ & \text{(phase II)} \\ p_3 \cdot s + r_2 & s_{ult,med}(\theta,\mathrm{l_e}) \le s \le s_{tot,med}(\theta,\mathrm{l_e}) \\ & \text{(phase III).} \end{cases} \tag{8.2}$$

Formulas and estimates of the parameters $p_1, p_2 > 0, p_3 < 0$, and $r_1, r_2 \in \mathbb{R}$ are summarised in Appendix D Table D.2. Figure 8.3 illustrates the model for $\theta = 10°$ and $\mathrm{l_e} = l_f/2, l_f/3, l_f/6$.

8.1.3 Prediction model for tensile stress

We assume the following (see also [98, 118]):

- The UHPC matrix is a statistically homogeneous material [119, p.28].
- Fibres are straight with cylindrical geometry. The fibres have fixed length l_f and diameter d_f.
- The spatial distribution of the fibre positions in the UHPC is statistically homogeneous [119, p.28].
- The fibre orientation is random following a given probability density function (p.d.f.) p.
- The specimen is uniaxially strained.
- During loading, the specimen develops a planar crack C of width w and area A_C orthogonal to the tension axis, see Figure 8.4.
- With growing crack width, the shorter fibre end is pulled out of the concrete matrix. The longer end is not affected.
- The fibres behave linearly elastic.
- The matrix deformation and the Poisson effect of the fibres during pull-out are neglected. The fibre-matrix bond is frictional.

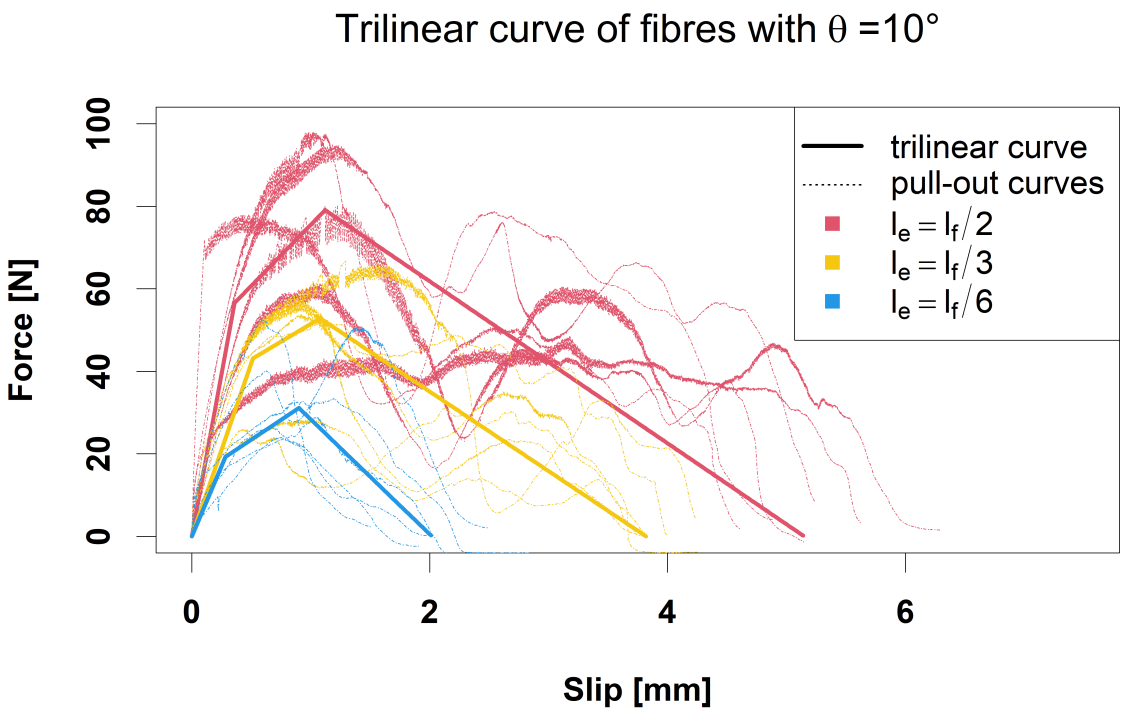

Figure 8.3: Trilinear curves (solid) of the single-fibre pull-out force curves (dotted) with angle $\theta = 10°$ and embedded lengths $\mathrm{l_e} = l_f/2$, $\mathrm{l_e} = l_f/3$, $\mathrm{l_e} = l_f/6$.

If the strain ϵ exceeds ϵ_r, the strain at the uniaxial tensile strength of the UHPC, a crack starts to form. The crack width w is given by

$$w = \begin{cases} 0, & \epsilon \leq \epsilon_r \\ (\epsilon - \epsilon_r) \cdot L, & \epsilon > \epsilon_r \end{cases}$$

with $L = 40$ mm and $\epsilon_r = 0.00087$ (see Table 4.3). Fibres crossing the crack are divided into the two segments to the left and to the right of the crack plane. We denote the length of the shorter segment by l_e, see Figure 8.4, such that $l_e \in [0, l_f/2]$. With increasing crack width w, the shorter fibre end is pulled out of the concrete until the fibre gets detached at $w > l_e$.

For predicting the stress evolution for increasing crack width w, the single pull-out forces $P(s, \theta, \mathrm{l_e})$ of the fibres crossing the crack have to be taken into account. Due to the assumption that only the shorter fibre end is pulled out of the concrete, the slip s corresponds to the crack width w. Furthermore, $\mathrm{l_e}$ in the single-fibre pull-out tests corresponds to the embedded length l_e. Thus, we use $s = w$ and $\mathrm{l_e} = l_e$ in (8.2).

Assume that the planar crack C is crossed by N fibres with given inclination angles and embedded lengths $(\theta_1, l_{e,1}), \ldots, (\theta_N, l_{e,N})$. As experimental single-fibre pull-out curves are only available for a discrete set of θ and l_e values, the forces $P(w, \theta, l_e)$ of fibres in C are binned into classes as given in Table 8.1.

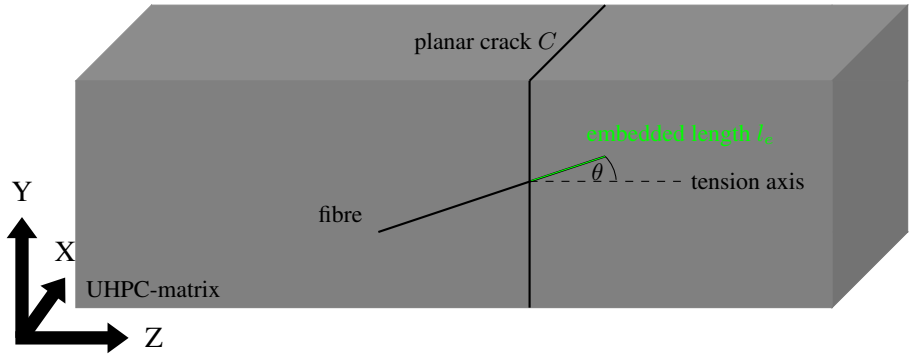

Figure 8.4: UHPC-matrix with one fibre intersecting a planar crack C (assumed to be embedded in the XY-plane) at crack width $w = 0$. The crack divides the fibre in two parts. The embedded length l_e is the length of the shorter (green) fibre part. The angle between fibre and tension axis (assumed to be the Z-axis) is denoted by θ.

Table 8.1: Binning of embedded length l_e and inclination angle θ.

class	**interval**	$P(w, \theta, l_e)$
T_1	$\theta \in [\,0°; 5°)$	$P(w,\ 0°, l_e)$
T_2	$\theta \in [5°; 15°)$	$P(w, 10°, l_e)$
$\vdots$	$\vdots$	$\vdots$
T_9	$\theta \in [75°; 90°]$	$P(w, 80°, l_e)$
L_1	$l_e \in$ [0 mm; 2.5mm)	$P(w, \theta, 2.08)$
L_2	$l_e \in$ [2.5 mm; 5mm)	$P(w, \theta, 4.17)$
L_3	$l_e \in$ [5 mm; 6.25mm)	$P(w, \theta, 6.25)$

Fibres crossing the crack counteract the opening of the crack. According to [95, 98], the composite stress (or mean resistance force per unit area) at crack width w is obtained by

$$\sigma_{ct}(w) \quad = \quad \lambda_c \int_0^{\frac{l_f}{2}} \int_0^{\frac{\pi}{2}} P(w, \theta, l_e) p_c(\theta, l_e)\, d\theta\, dl_e, \tag{8.3}$$

where $p_c(\theta, l_e)$ denotes the joint probability density of inclination angle and embedded length of crack-crossing fibres. λ_c is the mean number of fibres per unit area in C.

We approximate $\sigma_{ct}(w)$ by first replacing the integral in (8.3) by a sum over all fibres observed in the crack. In the second step, angles and embedded lengths are binned such that model (8.2) can be applied.

$$\sigma_{ct}(w) \quad \approx \quad \frac{1}{A_C} \sum_{k=1}^{N} P(w, \theta_k, l_{e,k}) \tag{8.4}$$

$$\approx \quad \frac{1}{A_C} \sum_{i=1}^{9} \sum_{j=1}^{3} N_{T_i, L_j} \tilde{P}(w, \theta_i, l_{e,j}). \tag{8.5}$$

Here, N_{T_i,L_j} denotes the number of fibres in C with $\theta_k \in T_i$ and $l_{e,k} \in L_j$, $k \in \{1, \ldots, N\}$, $i \in \{1, \ldots, 9\}$, $j \in \{1, 2, 3\}$. $\tilde{P}$ is a prediction of P by the median curve or by the trilinear model. We will denote the prediction based on $\tilde{P} = \dot{P}$ by $\sigma_{ct}^{med}(w)$ and the prediction based on $\tilde{P} = P_{tri}$ by $\sigma_{ct}^{tri}(w)$.

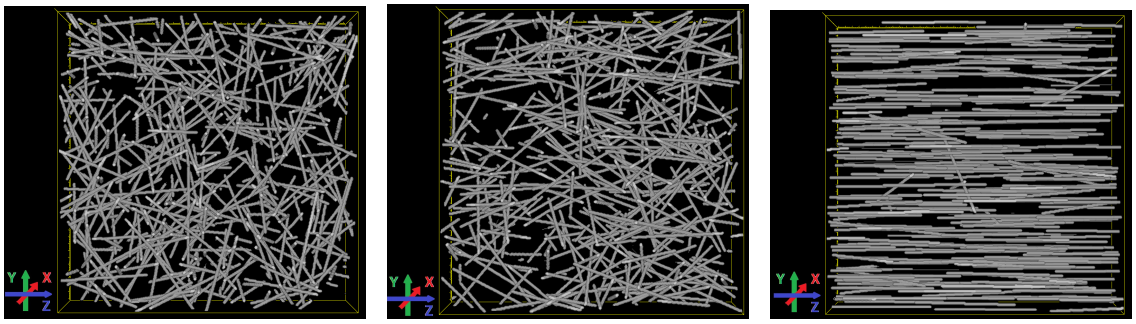

(a) $\beta = 1$ (isotropic) (b) $\beta = 0.5$ (c) $\beta = 0.01$

Figure 8.5: Realisations of the fibre model for different anisotropy parameters β.

8.1.4 Stochastic fibre model

In the following, we introduce a stochastic fibre model to generate 3D fibre systems of virtual specimens. Their tensile behaviour can then be predicted with our stress prediction model.

The fibre system is modelled by a Boolean model [106] as follows: The positions of fibres are indicated by their midpoints which are modelled by a Poisson point process. That is, the number N of fibre midpoints (x, y, z) in a given volume V follows a Poisson distribution with parameter $\lambda \cdot V$, where $\lambda > 0$ is the mean number of fibres per unit volume. Locations of fibre midpoints are drawn independently from a uniform distribution on the volume of interest.

The orientation of a fibre is independent of its location and can be described in spherical coordinates with co-latitude angle $\theta \in [0, \pi/2)$ and longitude angle $\varphi \in [0, 2\pi)$. Assuming the Z-axis to be the tension axis, θ corresponds to the inclination angle of the fibre with respect to the tension axis. The longitude angle φ does not influence the force contribution of a fibre. Hence, we consider φ to be uniformly distributed on $[0, 2\pi)$ such that the probability density function of the fibre orientation is a function $p(\theta)$ depending only on θ.

We assume that θ follows a one-parametric orientation distribution described by the p.d.f

$$p(\theta) = \frac{\beta \sin(\theta)}{(1 + (\beta^2 - 1)\cos^2(\theta))^{\frac{3}{2}}}, \quad \theta \in \left[0, \frac{\pi}{2}\right], \quad \beta > 0, \tag{8.6}$$

see [116, 117, 120, 121] for details and applications. The anisotropy parameter β[1] controls the alignment of the fibres. For $\beta = 1$, the fibres are isotropically oriented. For decreasing β, the fibres tend to be aligned along the Z-axis, see Figure 8.5. For $\beta > 1$, the fibre orientations are concentrated in a plane. This case is not considered here.

For fitting the model to a given concrete sample, the characteristics λ and β can be obtained from μCT images, see [116, 117, 122]. Due to the low fibre volume fraction, we assume that overlap of fibres in the model is negligible. Hence, the fibre intensity λ can be computed from the fibre volume fraction V_V, the fibre length l_f and cross-sectional area A_f via

$$\lambda = \frac{V_V}{l_f A_f}.$$

If a single fibre segmentation is available, an estimate of the anisotropy parameter β can be determined from the sample $\theta_1, \ldots, \theta_N$ of inclination angles by using the maximum likelihood method as described in [120]. An estimate of β based on the method of moments is given by (see Section 8.1.5.2)

$$\hat{\beta}_{mom} = \frac{N}{\sum_{i=1}^{N} \cos(\theta_i)} - 1. \tag{8.7}$$

[1]Note that the anisotropy parameter has nothing to do with the ovalness parameter from the standardised Kent distribution in Example 2.2.1.

The Boolean model described so far yields a stochastic fibre system in 3D. The prediction model outlined in Section 8.1.3 requires only inclination angles θ and embedded lengths l_e of the fibres intersecting the crack plane C. Due to the spatial homogeneity of the model, C can be assumed to be contained in the XY-plane.

In the Boolean model, fibre position and orientation are independent. Hence, l_e and θ are independent. Thus, the joint p.d.f. of θ and l_e for crack-crossing fibres fulfils $p_c(\theta, l) = p_c(\theta)p_{l_e}(l)$ where $p_c(\theta)$ is the p.d.f. of inclination angles θ of fibres crossing the crack and $p_{l_e}(l)$ is the p.d.f. of l_e. The spatial homogeneity of the Boolean model implies that l_e is uniformly distributed on $[0, l_f/2]$. The planar characteristics are related to the spatial characteristics as follows [98, 106, 117]

$$p_{l_e}(l) = \frac{2}{l_f}, \qquad l \in [0, l_f/2] \tag{8.8}$$

$$p_c(\theta) = (1+\beta)p(\theta)\cos(\theta) \tag{8.9}$$

$$\lambda_c = \frac{\lambda l_f}{1+\beta} \tag{8.10}$$

where λ_c is the expected number of fibres per unit area in C.

Note that the difference between (8.6) and (8.9) can be explained as follows [98, 123]: The p.d.f. $p(\theta)$ takes every fibre in the reinforced concrete into account whereas $p_c(\theta)$ accounts only for fibres intersecting the crack plane. A fibre is more likely to hit the crack plane if its inclination angle θ is small. The assumption that the distribution $p_c(\theta)$ is equal to $p(\theta)$ is a common misunderstanding that leads to incorrect interpretations of measurement results (see [86, 96, 124]).

If a single fibre segmentation of fibres in a crack is available, an estimate of the anisotropy parameter β can be determined from the sample $\theta_{c,1}, \ldots, \theta_{c,N}$ of inclination angles of crack-crossing fibres by using a modified version of the maximum likelihood estimator given in [120]. An estimator of β based on the method of moments is given by

$$\hat{\beta}_{c,mom} = \frac{N}{\sum_{i=1}^{N} \cos^2(\theta_{c,i})} - 1, \tag{8.11}$$

see Section 8.1.5.2 for details.

The fibre orientation coefficient η_θ is a widely established characteristic for the distribution of fibre orientation in a crack [86, 88, 96, 117, 125, 126, 127]. η_θ is the second moment of the angular deviation of the crack-crossing fibre from the tension axis. Here, it is possible to calculate η_θ in closed form

$$\eta_\theta = \int_0^{\frac{\pi}{2}} p_c(\theta)\cos^2(\theta)\, d\theta = \frac{1}{1+\beta} = \frac{\lambda_c}{\lambda l_f}.$$

For an isotropic fibre orientation ($\beta = 1$), which is assumed in several studies [79, 86, 95, 96], it follows that $\lambda_c = \frac{1}{2}\lambda l_f$, $p_c(\theta) = 2\sin(\theta)\cos(\theta) = \sin(2\theta)$ and $\eta_\theta = \frac{1}{2}$. In the extreme case that all fibres are aligned along the tension axis ($\beta = 0$), it follows that $\lambda_c = \lambda l_f$, and $\eta_\theta = 1$.

8.1.5 Parameter estimation for anisotropy parameter β

We consider a fibre system as described in Section 8.1.4. The random angular deviation between a fibre and the Z-axis is described by its inclination angle. A random inclination angle in space is denoted by Θ and a random inclination angle of a fibre intersecting the XY-plane by Θ_c.

Θ follows a distribution with density (8.6) and Θ_c follows a distribution with density (8.9). For a fibre system of N fibres, we denote a sample of spatial inclination angles by $\theta_1, \ldots, \theta_N$ and a sample of inclination angles of fibres intersecting the XY-plane by $\theta_{c,1}, \ldots, \theta_{c,M}$, $M \leq N$.

8.1.5.1 Maximum likelihood estimator $\hat{\beta}_{c,mle}$ for β

The maximum likelihood estimator (mle) estimates the parameters of a probability distribution by maximising its likelihood function for observed data. The maximiser of the likelihood function is called the maximum likelihood estimator ($\hat{\beta}_{mle}$). The following is based on the findings in [120]. The maximum likelihood estimator $\hat{\beta}_{mle}$ given in [120] considers the spatial inclination angles.

We introduce a mle $\hat{\beta}_{c,mle}$ for fibres intersecting the XY-plane: Consider $\Theta_{c,1}, \ldots, \Theta_{c,M}$ independent and identically distributed (i.i.d.) with density $p_c(\theta)$. The log-likelihood function reads

$$\begin{aligned} l(\beta|\Theta_{c,1}, \ldots, \Theta_{c,M}) &= \log \prod_{i=1}^{M} p_c(\Theta_{c,i}) \\ &= \log \prod_{i=1}^{M} (1+\beta) p(\Theta_{c,i}) \cos(\Theta_{c,i}) \\ &= M \log(1+\beta) + \sum_{i=1}^{M} \log(p(\Theta_{c,i})) + \sum_{i=1}^{M} \log(\cos(\Theta_{c,i})) \\ &= M \log(1+\beta) + \sum_{i=1}^{M} \log(\cos(\Theta_{c,i})) \\ &\quad + M \log(\beta) + \sum_{i=1}^{M} \left(\log(\sin(\Theta_{c,i})) + \frac{3}{2} \log(1 + (\beta^2 - 1)\cos^2(\Theta_{c,i})) \right) \end{aligned}$$

To compute the maximum of $l(\beta|\Theta_{c,1}, \ldots, \Theta_{c,M})$, we compute its derivative w.r.t. β

$$\frac{\partial l(\beta|\Theta_{c,1}, \ldots, \Theta_{c,M})}{\partial \beta} = \frac{M}{1+\beta} + \frac{M}{\beta} - 3\beta \sum_{i=1}^{M} \frac{\cos^2(\Theta_{c,i})}{1 + (\beta^2 - 1)\cos^2(\Theta_{c,i})}. \tag{8.12}$$

In the following, we use a numerical procedure based on Newton's method because we are not able to compute the roots of (8.12) analytically. For $\beta > 0$, define $h(\beta) = -\beta \frac{\partial l}{\partial \beta}$ such that the root of (8.12) can be calculated by solving $h(\beta) = 0$. Now, $h(0) = -M$ and $h(\beta) = M$ for $\beta \to \infty$. Hence, h has at least one root. In contrast to [120], there exists $\beta > 0$ such that $h'(\beta) = \frac{\partial}{\partial \beta} h \not> 0$. Thus, local extrema of the likelihood function can exist, and candidates for the maximum likelihood estimator $\hat{\beta}_{c,mle}$ of β have to be checked, e.g. via the second derivative. Using Newton's method, we can approximate the root of (8.12) iteratively by

$$\beta_{t+1} = \beta_t - \frac{h(\beta_t)}{h'(\beta_t)}.$$

Because h can have several roots, the solution obtained by Newton's method could depend on the choice of the initial value β_{init} for β. We, therefore, recommend the choice of different initial values and repeated runs of the Newton method. A simulation study of $\hat{\beta}_{c,mle}$ for $M = 10, 100, 600, 1000$ and $\beta = 0.1, 0.3, 0.5, 0.9, 1$, is given in Section 8.1.5.3.

8.1.5.2 Method of moments estimators $\hat{\beta}_{mom}$, $\hat{\beta}_{c,mom}$ for β

The method of moments (mom) is based on the approximation of sample moments with theoretical moments (via the law of large numbers (LLN)). If the theoretical moments are functions of a parameter, the sample moments are functions of the parameter's estimate. Here, the parameter of interest is the anisotropy parameter β. Assume that $\Theta_1, \ldots, \Theta_N$ i.i.d. with density $p(\theta)$ such that for suitable function g we have $\mathbb{E}(\Theta_i^k) = g_k(\beta) < \infty$. Then an estimator $\hat{\beta}_{mom}$ can be obtained as solution of $\overline{\Theta^k}_N = \frac{1}{N} \sum_{i=1}^{N} \Theta_i^k = g_k(\hat{\beta}_{mom})$. We apply the cosine to the angles in the following. Thus,

$\cos(\Theta_1), \ldots, \cos(\Theta_N)$ are i.i.d. with

$$\mathbb{E}(\cos(\Theta_i)) = \int_0^{\frac{\pi}{2}} \cos(\theta) p(\theta)\, d\theta = \frac{1}{1+\beta} \tag{8.13}$$

and $g(\beta) = \frac{1}{1+\beta}, \beta > 0$. Therefore,

$$\hat{\beta}_{mom} = \frac{1}{\overline{\cos(\Theta)}_N} - 1 \tag{8.14}$$

with $\overline{\cos(\Theta)}_N = \frac{1}{N} \sum_{i=1}^{N} \cos(\Theta_i)$. For $\Theta_{c,1}, \ldots, \Theta_{c,M}$ i.i.d. it follows analogously

$$\mathbb{E}(\cos^2(\Theta_{c,i})) = \int_0^{\frac{\pi}{2}} \cos^2(\theta) p_c(\theta)\, d\theta = (1+\beta) \int_0^{\frac{\pi}{2}} \cos^3(\theta) p(\theta)\, d\theta = \frac{1}{1+\beta} \tag{8.15}$$

Therefore,

$$\hat{\beta}_{c,mom} = \frac{1}{\overline{\cos^2(\Theta_c)}_M} - 1. \tag{8.16}$$

8.1.5.3 Comparison of the maximum likelihood estimator $\hat{\beta}_{c,mle}$ with the method of moments estimator $\hat{\beta}_{c,mom}$ for β based on fibres intersecting the XY-plane

We simulated $K = 100$ samples $\theta_{c,1}^{(k)}, \ldots, \theta_{c,M}^{(k)}$, $k = 1, \ldots, K$, for each combination of β = 0.1, 0.22, 0.3, 0.5, 0.9 and M = 10, 100, 1000. For each sample we calculate $\hat{\beta}_{c,mle}^{(k)}$ and $\hat{\beta}_{c,mom}^{(k)}$ (with $\beta_{init} = 0.1, 0.5, 1$), $k = 1, \ldots, K$. To compare the accuracy of $\hat{\beta}_{c,mle}$ and $\hat{\beta}_{c,mom}$, we compute the mean value and standard deviation (SD) of $K = 100$ estimates for each parameter combination. The mean values and SDs are given in Table 8.2 and Table 8.3. The results indicate that both methods work well for large sample sizes M and anisotropic samples but $\hat{\beta}_{c,mle}$ has a lower SD and is closer to the true value than $\hat{\beta}_{c,mom}$. For a small sample size or especially an isotropic sample, $\hat{\beta}_{c,mom}$ has a lower SD and is closer to the true β than $\hat{\beta}_{c,mle}$. The initial value β_{init} has little influence on the result of $\hat{\beta}_{c,mle}$. Apart from that, $\hat{\beta}_{c,mom}$ needs neither an initial value nor a numerical method. Therefore, we would recommend $\hat{\beta}_{c,mom}$ due to its simplicity and sufficient accuracy.

Table 8.2: Mean and standard deviation (SD) of $\hat{\beta}_{c,mle}$ for various β, β_{init} and M

β		0.1	0.22	0.3	0.5	0.9	1
$(M, \beta_{init}) = (1000, 0.1)$	Mean	0.0999	0.2183	0.3011	0.5008	0.9004	0.9939
	SD	0.0036	0.0075	0.0120	0.0188	0.0327	0.0371
$(M, \beta_{init}) = (1000, 0.5)$	Mean	0.0999	0.2204	0.3008	0.4985	0.8926	0.9934
	SD	0.0034	0.0086	0.0117	0.0208	0.0310	0.0328
$(M, \beta_{init}) = (1000,\ 1)$	Mean	0.0999	0.2177	0.3004	0.5003	0.9001	0.9981
	SD	0.0037	0.0073	0.0104	0.0190	0.0305	0.0457
$(M, \beta_{init}) = (600, 0.1)$	Mean	0.1009	0.2203	0.2973	0.5000	0.8892	0.9984
	SD	0.0046	0.0092	0.0147	0.0228	0.0439	0.0417
$(M, \beta_{init}) = (600, 0.5)$	Mean	0.1001	0.2200	0.3011	0.4991	0.8957	0.9929
	SD	0.0046	0.0100	0.0128	0.0260	0.0431	0.0437
$(M, \beta_{init}) = (600,\ 1)$	Mean	0.1000	0.2191	0.3004	0.5034	0.9014	1.0009
	SD	0.0050	0.0108	0.0141	0.0264	0.0385	0.0447
$(M, \beta_{init}) = (100, 0.1)$	Mean	0.1017	0.2191	0.2998	0.4924	0.8579	1.0006
	SD	0.0117	0.0239	0.0337	0.0519	0.1005	0.1288
$(M, \beta_{init}) = (100, 0.5)$	Mean	0.1027	0.2209	0.2988	0.4940	0.8878	1.0103
	SD	0.0107	0.0224	0.0401	0.0568	0.1172	0.1213
$(M, \beta_{init}) = (100,\ 1)$	Mean	0.1017	0.2217	0.3020	0.4928	0.8781	0.9790
	SD	0.0125	0.0245	0.0315	0.0570	0.1069	0.1168
$(M, \beta_{init}) = (10, 0.1)$	Mean	0.1104	0.2382	0.2982	0.4334	0.7446	0.7903
	SD	0.0396	0.0849	0.1072	0.1269	0.2742	0.2899
$(M, \beta_{init}) = (10, 0.5)$	Mean	0.1265	0.2418	0.3198	0.4822	0.7215	0.7846
	SD	0.0474	0.0845	0.1160	0.1781	0.2698	0.4023
$(M, \beta_{init}) = (10,\ 1)$	Mean	0.1218	0.2358	0.3121	0.4749	0.7646	0.7915
	SD	0.0441	0.0856	0.1338	0.1684	0.2539	0.3242

Table 8.3: Mean and standard deviation (SD) of $\hat{\beta}_{c,mom}$ for various β and M

β		0.1	0.22	0.3	0.5	0.9	1
$M = 1000$	Mean	0.0998	0.2206	0.3020	0.4973	0.8999	1.0039
	SD	0.0057	0.0122	0.0138	0.0195	0.0353	0.0372
$M = 600$	Mean	0.1007	0.2205	0.2981	0.5021	0.8986	0.9992
	SD	0.0078	0.0127	0.0174	0.0245	0.0391	0.0494
$M = 100$	Mean	0.1037	0.2214	0.3017	0.5029	0.9029	1.0179
	SD	0.0183	0.0308	0.0459	0.0543	0.0995	0.1090
$M = 10$	Mean	0.1012	0.2490	0.3023	0.5351	1.0203	1.0421
	SD	0.0610	0.1390	0.1169	0.1776	0.3401	0.4120

8.2 Results

8.2.1 Image analysis

The crack observed in the imaged sample is approximated by a plane whose position is identified in the CT scan, see Figure 8.6a. Among the segmented fibres, $N = 598$ cross the crack plane. Inclination

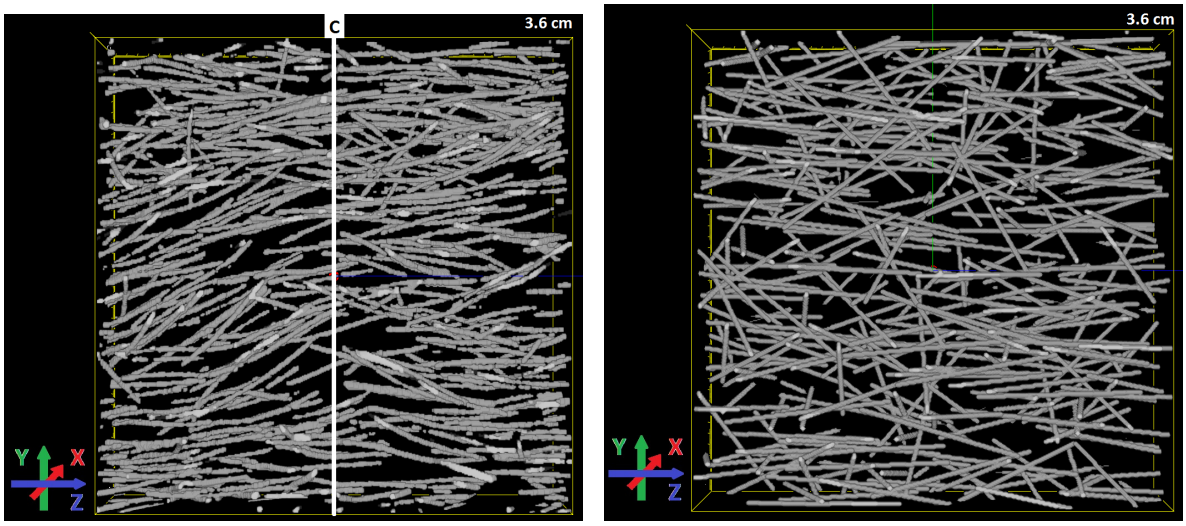

(a) (b)

Figure 8.6: Volume rendering of fibres in the crack area (a) and a fitted fibre system (b). The subvolume is of dimension 3.6 cm^2×0.45 cm. The position of C in (a) is indicated by a solid white line.

angles of the individual fibres are determined as described in Section 5.3. Fibre lengths can be measured by the maximal Feret diameter[2] [128]. By intersection with the crack plane, each fibre is split into two segments. The embedded length l_e is the maximal Feret diameter of the shorter one of these segments. From the inclination angles $\theta_{c,i}$, we obtain $\hat{\beta}_{c,mom} = 0.22$.

By Equation (8.10) with $\beta = 0.22$ the expected number of fibres in the cross section is $A_C \cdot \lambda_c = 834$. The observed number $N = 598$ is well below that value. There are several possible explanations. In [48], the fibre content at the crack location was observed to be about 5% lower than the theoretical value of V_V=0.02 (see Figure 6.4g at the approximate crack position in Slice 641). Additionally, according to the master datasheet of the fibres used, both, the diameter d_f mm and the fibre length l_f can deviate by 10%.

In Figure 8.7, the distributions of observed inclination angles and embedded lengths are compared with the fitted p.d.f.s $p_c(\theta)$ (with $\beta = 0.22$) and $p_{l_e}(l)$ given in (8.9) and (8.8), respectively. The inclination angles are well fitted. The distribution of the embedded length has an unexpected peak around 4.5 mm. A possible explanation is that short fibre segments (whose diameter in the μCT image corresponds to only 2 to 3 voxels) were missed. It should be noted that we are not aware of any practical way of estimating l_e from a 2D slice as was also mentioned in [86]. A fibre system simulated as a realisation of the Boolean model with $\beta = 0.22$, $l_f = 12.5$ mm, $d_f = 0.2$ mm, $V_V = 0.02$ is shown in Figure 8.6b.

8.2.2 Prediction of tensile stress

To predict the composite stress σ_{ct} using Equation (8.5), we need N_{T_i,L_j}, the number of crack-crossing fibres with (θ, l_e) in class (T_i, L_j), $i = 1, \ldots, 9$, $j = 1, 2, 3$. Based on the single fibre segmentation, we derive N_{T_i,L_j} as given in Table 8.4.

Experimental tensile tests were carried out on three specimens as described in Section 4.4. The ultimate tensile stress and the corresponding strain of the experimental tensile curves are given in Table 8.5.

The observed tensile curves are used to calibrate our prediction.

[2]Note that the Feret diameter is defined as the distance between two parallel tangents of a particle where the tangents are orthogonal to a specified direction and the maximal Feret diameter is the largest distance between two parallel tangents in any direction.

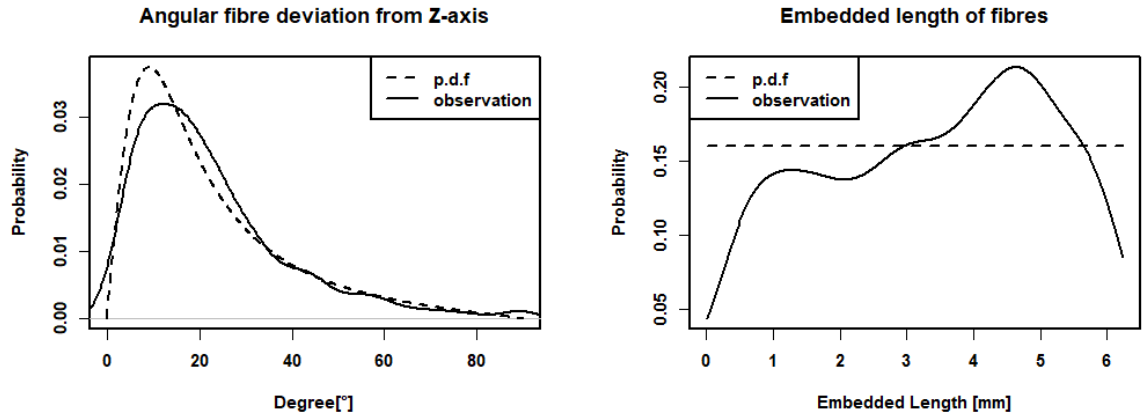

(a) (b)

Figure 8.7: Observed inclination angle (a) and embedded length (b) of the fibres intersecting the crack (solid lines) and the corresponding fitted p.d.f. $p_c(\theta)$ with $\beta = 0.22$ and $p_{l_e}(l)$ (dotted lines).

Table 8.4: Number of fibres in the (θ, l_e) bins as obtained from the single fibre segmentation of the μCT image.

L_j \ T_i	0°	10°	20°	30°	40°	50°	60°	70°	80°
$l_f/2$	10	52	39	14	6	6	3	1	0
$l_f/3$	20	92	91	35	20	9	6	1	1
$l_f/6$	14	48	44	34	16	14	8	6	8

Table 8.5: Ultimate tensile stress of three uniaxial loaded specimens.

	1	2	3	mean
σ_{ult}^{exp} [MPa]	10.97	11.21	12.34	$\overline{\sigma_{ult,exp}}$ = 11.51
ϵ_{ult}^{exp} [mm/mm]	0.01064	0.0010	0.0095	$\overline{\epsilon_{ult,exp}}$ = 0.0070

8.2.2.1 Prediction of tensile stress based on median curve

Here, we use the median curve to predict σ_{ct} by σ_{ct}^{med}. Figure 8.8a shows the prediction as well as the three experimental tensile curves. We see that the prediction overestimates the stress. The predicted ultimate tensile stress is 18.56 MPa which is reached at strain $\epsilon_{ult}^{med} = 0.0230$ [mm/mm].

To calibrate the curves, we follow [79, 86, 96, 129] and introduce suitable rescaling factors to match characteristic stress-strain points (i.e., ultimate tensile stress $\sigma_{ct,ult}$ or yield stress $\sigma_{ct,el}$) of experiments and predictions.

In the first step, we scale σ_{ct}^{med} by a stress scaling factor $\mathcal{S}_{ult}^{\sigma}$ such that the predicted and mean experimental ultimate stress coincide, i.e. $\mathcal{S}_{ult}^{\sigma}\sigma_{ct,ult}^{med} = \overline{\sigma_{ult,exp}}$. This is achieved for $\mathcal{S}_{ult}^{\sigma} = 0.61$, see Figure 8.8b. In the next step, the locations of the maxima have to be matched. To this end, we additionally scale the strain-axis by a strain scaling factor $\mathcal{S}_{ult}^{\epsilon}$. The choice $\mathcal{S}_{ult}^{\epsilon} = 0.42$ yields $\mathcal{S}_{ult}^{\epsilon}\epsilon_{ult}^{med} = \overline{\epsilon_{ult,exp}}$ such that the maxima are closer together (see Figure 8.8c). However, the slope of the curve after the maximum does not fit the experimental curves. A remedy is to restrict scaling of the strain-axis to the

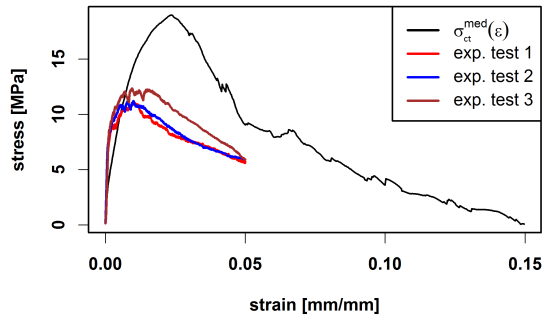

(a) Prediction of $\sigma_{ct}(\epsilon)$ by $\sigma_{ct}^{med}(\epsilon)$.

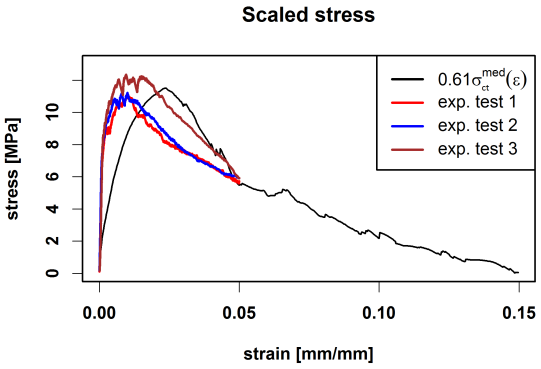

(b) Scaled stress $\mathcal{S}_{ult}^{\sigma}\sigma_{ct}^{med}(\epsilon)$.

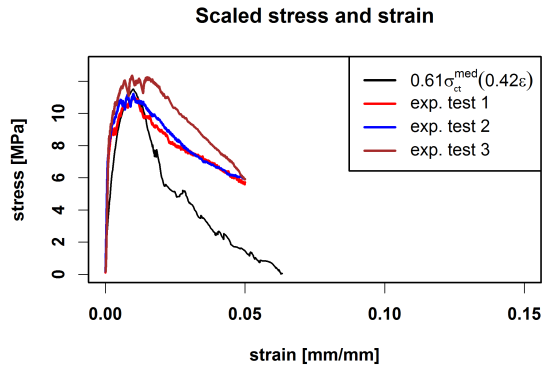

(c) Scaled stress and strain $\mathcal{S}_{ult}^{\sigma}\sigma_{ct}^{med}(\mathcal{S}_{ult}^{\epsilon}\epsilon)$.

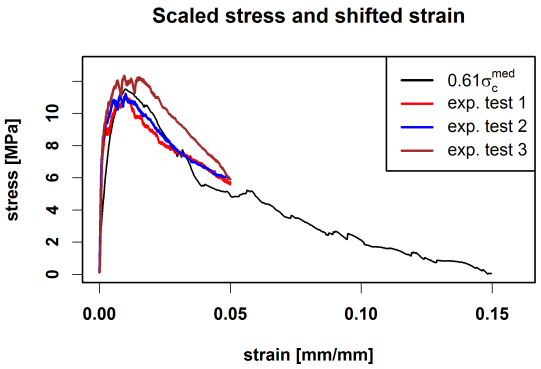

(d) Prediction based on Equation (8.17).

Figure 8.8: Prediction of composite stress $\sigma_{ct}(\epsilon)$ by $\sigma_{ct}^{med}(\epsilon)$ (a) compared with three experimental tensile curves. Scaled $\sigma_{ct}^{med}(\epsilon)$ by stress scaling factor $\mathcal{S}_{ult}^{\sigma} = 0.61$ (b) and additionally scaled strain by strain scaling factor $\mathcal{S}_{ult}^{\epsilon} = 0.42$ (c).

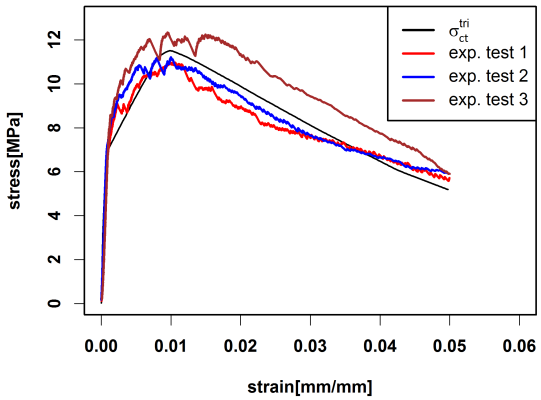

Figure 8.9: Prediction of composite stress $\sigma_{ct}(\epsilon)$ by $\sigma_{ct}^{tri}(\epsilon)$ based on the trilinear model.

region prior to the maximum, that is,

$$\sigma_c^{med,scale}(\epsilon) = \begin{cases} \sigma_{ct}^{med}\left(\frac{\epsilon}{\mathcal{S}_{ult}^{\epsilon}}\right) & ,\epsilon \in [0, \overline{\epsilon_{ult,exp}}] \\ \sigma_{ct}^{med}\left(\epsilon_{ult}^{med} + \frac{\epsilon_{tot}^{med}-\epsilon_{ult}^{med}}{\epsilon_{tot}^{med}-\overline{\epsilon_{ult,exp}}} \cdot (\epsilon - \overline{\epsilon_{ult,exp}})\right) & ,\epsilon \in \left(\overline{\epsilon_{ult,exp}}, \epsilon_{tot}^{med}\right], \end{cases} \tag{8.17}$$

where ϵ_{tot}^{med} is the last available strain value in the median curve. This way, both, the maximum location and the stress at the final point ϵ_{tot}^{med} are matched. The result shown in Figure 8.8d indicates that the drop after the ultimate tensile stress is flatter due to the fixation of ϵ_{tot}^{med}.

8.2.2.2 Prediction of tensile stress based on the trilinear model

Here, we use model (8.2) to predict σ_{ct} by σ_{ct}^{tri}. As for the median curve we need to modify the prediction. Instead of piecewise scaling equivalent to Equation (8.17), we recompute (8.2) with new values for slip and force given by

$$\begin{aligned} s_{el,med}^{\circ}(\theta, l_e) &= 0.072 \cdot s_{el,med}(\theta, l_e) \\ s_{ult,med}^{\circ}(\theta, l_e) &= 0.36 \cdot s_{ult,med}(\theta, l_e) \\ s_{tot,med}^{\circ}(\theta, l_e) &= s_{tot,med}(\theta, l_e) \\ P_{el,med}^{\circ}(\theta, l_e) &= 0.66 \cdot P_{el,med}(\theta, l_e) \\ P_{ult,med}^{\circ}(\theta, l_e) &= 0.66 \cdot P_{ult,med}(\theta, l_e) \end{aligned}$$

where $s_{el,med}(\theta, l_e), s_{ult,med}(\theta, l_e), s_{tot,med}(\theta, l_e), P_{el,med}(\theta, l_e), P_{ult,med}(\theta, l_e)$ are given in Table D.1. The new parameters $(p_1^{\circ}, p_2^{\circ}, p_3^{\circ}, r_1^{\circ}, r_2^{\circ})$ are calculated as in Appendix D.2. The prediction is given in Figure 8.9. The factors are chosen such that $\sigma_{ct,ult}^{tri} = \overline{\sigma_{ult,exp}}$ and $\epsilon_{ct,ult}^{tri} = \overline{\epsilon_{ult,exp}}$.

In the interval between yield and ultimate stress, the predicted curve is straighter than the experimental stress curves which can be explained by the use of a linear model. Furthermore, the maximal peak is more pronounced than in the experimental tests. This may be due to the replacement of the individual single-fibre pull-out forces P_i by average forces P_{tri} obtained from the trilinear model. To overcome this problem, we propose a model based on randomised single fibre contributions in the following section.

8.2.2.3 Prediction of tensile curves based on randomised trilinear model

In order to model the random variations in the tensile curves, we consider $s_{ult,med}$ as random following a uniform distribution and add normally distributed residuals to the yield and the ultimate force. This

way, individual functions $\dot{P}$ are simulated for each fibre in the crack. The range of values of the required random variables is inferred from the single fibre pull-out experiments.

Prediction study part 1: Stress prediction with randomised strain shifts

We define the interval

$$I_{ult}(\theta, l_e) = \left[\min_{i=1,\dots,6} (s_{ult,i}(\theta, l_e)) \,;\, \max_{i=1,\dots,6} (s_{ult,i}(\theta, l_e)) \right]$$

and choose

$$\begin{aligned} s^*_{ult,med}(\theta, l_e) &\sim \mathcal{U}(I_{ult}(\theta, l_e)) \\ r_{P_{el,med}}(\theta, l_e) &\sim \mathcal{N}(0, \mathrm{sd}^2_{P_{el,med}}(\theta, l_e)) \\ r_{P_{ult,med}}(\theta, l_e) &\sim \mathcal{N}(0, \mathrm{sd}^2_{P_{ult,med}}(\theta, l_e)), \end{aligned}$$

where the minimum and maximum values of $s_{ult,i}$ and the sample standard deviations $\mathrm{sd}_{P_{el,med}}$ and $\mathrm{sd}_{P_{ult,med}}$ for each combination (θ, l_e) are given in the Appendix D Table D.1. Then, we recompute the trilinear curve with

$$\begin{aligned} s^\circ_{el,med}(\theta, l_e) &= 0.072 \cdot s_{el,med}(\theta, l_e) \\ s^\circ_{ult,med}(\theta, l_e) &= 0.36 \cdot s^*_{ult,med}(\theta, l_e) \\ s^\circ_{tot,med}(\theta, l_e) &= s_{tot,med}(\theta, l_e) \\ P^\circ_{el,med}(\theta, l_e) &= 0.68 \cdot P_{el,med}(\theta, l_e) + r_{P_{el,med}}(\theta, l_e) \\ P^\circ_{ult,med}(\theta, l_e) &= 0.68 \cdot P_{ult,med}(\theta, l_e) + r_{P_{ult,med}}(\theta, l_e). \end{aligned}$$

$M = 10$ predictions based on the fibre system observed in the CT image are shown in Figure 8.10a. The predictions reproduce the stress profile better than the deterministic predictions.

Prediction study part 2: Stress prediction of virtual specimens with varying production parameters

We use the prediction regime from *Prediction study part 1* and the stochastic fibre model from Section 8.1.4 to generate a fibre systems of virtual specimens. From the virtual fibre systems, we derive (θ, l_e) of fibres in some cross-section. These simulate the crack-crossing fibres. Figure 8.10b shows a tensile prediction of ten virtual fibre systems. The input parameters are determined from the crack-crossing fibres of the scanned specimen.

Predictions for virtual samples with modified orientation distribution and volume fraction V_V are shown in Figure 8.10. Note that the fibre parameters d_f and l_f were not varied since the single-fibre pull-out tests were restricted to fibres with $d_f = 0.2$ mm and $l_f = 12.5$ mm. Figure 8.10c shows that a fibre orientation along the tensile axis increases the tensile stress compared to an isotropic fibre orientation. This is in accordance with [86, 96]. Figure 8.10d reveals that the influence of the volume fraction also behaves as expected: Fewer fibres decrease and more fibres increase the tensile stress.

8.3 Conclusion

We presented a tensile behaviour prediction model of UHPFRC-specimens based on statistical information on the fibre system (obtained by quantitative analysis of a μCT image) and extensive single fibre pull-out tests. The model is calibrated by comparing the prediction to the results of experimental uniaxial tensile tests. The introduced stochastic fibre model generates fibre systems of virtual specimens which can be used for the prediction of the tensile behaviour. Through experimental and theoretical investigations, the following conclusions are drawn:

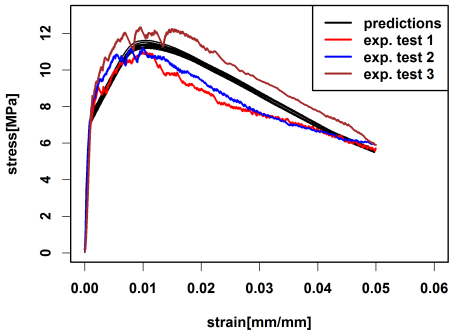

(a) Based on fibre system from CT scan.

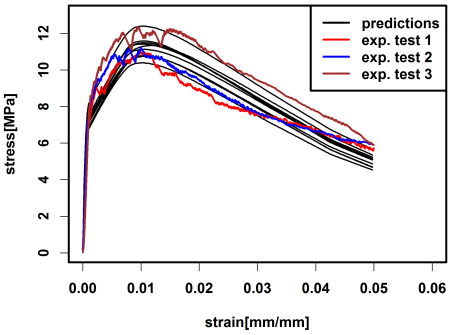

(b) Based on stochastic fibre systems.

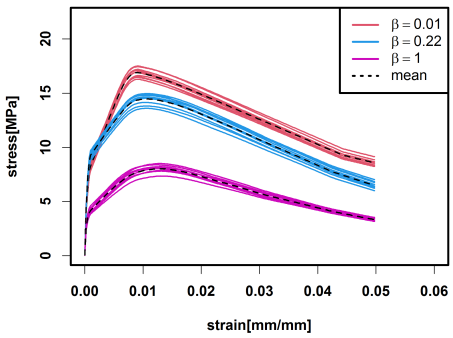

(c) $\beta = 0.01, 0.22, 1$

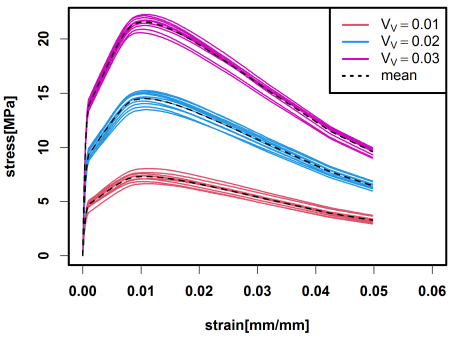

(d) $V_V = 0.01, 0.02, 0.03$

Figure 8.10: Prediction of $M = 10$ tensile curves (a) based on the scanned fibre system summarised in Table 8.4, (b) tensile prediction of 10 virtual specimens with fibre system generated by the stochastic fibre model from Section 8.1.4 with input parameters determined from the scanned fibre system. The predictions are compared with the three experimental tensile curves. (c) and (d) Tensile prediction of 10 virtual specimens with varied parameters. (c) β is varied and V_V is fixed. (d) β is fixed and V_V is varied. The mean of the tensile predictions per varied parameter is given as a dotted line.

- The fibre system in the concrete is modelled by a Boolean model of straight cylinders. The fibre orientation distribution is represented by a one-parametric distribution family. Its parameter β controls the anisotropy of the fibre orientation. Both, the case of total alignment and isotropy are included in the model as special cases. The widely used reference value η_θ (fibre orientation factor) can be calculated directly from β. In particular, the relationship of fibre orientation of the full 3D fibre system and of crack-crossing fibres is examined. Furthermore, we emphasised the difference between the p.d.f. for the fibre orientation of all fibres in the reinforced concrete and the p.d.f. for the fibre orientation of fibres intersecting a crack plane. The assumption that the p.d.f.s are equal is a common misunderstanding that leads to incorrect interpretations of measurement results (see [86, 96, 124]).

- Estimators for β are presented and analysed. We recommend the estimator $\hat{\beta}_{c,mom}$. It estimates accurately, no numerical method is required (like a gradient descent algorithm in [116]) and only the fibre angles in 2D cross-sections are needed. The latter means that fibre orientations observed in a crack are sufficient to estimate the anisotropy parameter β for the stochastic fibre model and no μCT imaging is needed.

- In contrast to 2D imaging methods, μCT allows for a determination of the embedded length of fibres in cracks since the whole 3D fibre system is observable. In particular, this allows for the validation of the fundamental assumption of a uniformly distributed embedded length l_e for the widespread tension-softening model in [118]. Furthermore, using μCT overcomes the accuracy disadvantage of fibre orientation estimation in 2D sections as discussed in [86].

- The presented prediction model uses the stochastic fibre model combined with a statistical analysis and modelling of the single fibre pull-out tests. Predictions are calibrated by using experimental tensile curves. Furthermore, running the prediction on virtual specimens with varied production parameters led to reasonable stress-strain curves.

Conclusion

In this work, we introduced mathematical morphology and statistical methods for the analysis of directional data. Directional data are sets of unit vectors that we encounter in many applications such as engineering.

In part I, we introduced mathematical morphology for directional images and an extension of directional quantiles from Ley et al. [11]. The definition of morphological operators and filters required an ordering structure between unit vectors. An ordering was determined via the theory of statistical depth functionals and related to h-ordering. The h-ordering ensures that the defined morphological operators are h-adjunctions and, therefore, well-defined. Furthermore, we introduced a background/foreground representation for directional images and other grey-scale image counterparts. We extended the morphological operators to multi-scale morphological operators via a redefined structuring function. The structuring function applied on a vector corresponds to a vector rotation where the scale parameter determines the rotation angle. Relations of introduced morphological operators to their grey-scale counterparts are emphasised. We used the operators to enhance regions of significant changes in a displacement field of a compressed glass foam.

The concept of quantiles and depth for directional data from Ley et. al. [11] was extended. These concepts provide useful geometric properties of the depth contours such as convexity and rotational equivariance, a Bahadur representation of the quantiles and are canonical for rotationally symmetric depth contours. However, it also produces rotationally symmetric depth contours even if the underlying distribution is not rotationally symmetric. Our extension solves this lack of flexibility for distributions with elliptical depth contours. Because of the similarities with the classical Mahalanobis depth, the introduced depth is called elliptical Mahalanobis depth. The basic idea is to deform the elliptical contours by a diffeomorphic mapping to rotationally symmetric contours, thus reverting to the canonical case in Ley et al. [11]. Furthermore, trimming of directional data is introduced. A Monte Carlo simulation study confirmed the results. The extension is used to analyse fibre directions in fibre-reinforced concrete.

In Part II, we elaborated interdisciplinary results in civil engineering which are partly published in [48, 78]. Our statistical analysis of the correlation between production parameters (fibre length, fibre diameter, fibre volume fraction as well as casting method, superplasticiser and specimen size) of ultra-high performance fibre reinforced concrete, and the fibre system (position and orientation) provides users with a better understanding of this relatively new composite material. Subsequently, the mechanical behaviour of the specimens was investigated and correlated with the fibre system. μCT imaging the specimens allowed a reconstruction of the fibre system. The fibre system was characterised slice-wise by computing the local fibre content (AFP) and fibre alignment (deviation from the Z-axis). The findings are in line with other work such as that fibre orientations stabilise after a certain distance from the casting point (see findings by Vandewalle et al. (2008) [67] and Ferrara et al. (2011) [68]). Furthermore, specimens of five different sizes were produced and cut into subspecimens of equal size (due to CT requirements). The general finding is that the fibre geometry changes locally when increasing the specimen size. This change depends on the direction in which the sample is enlarged, i.e., increasing the width has a different effect than increasing the length or depth. Local changes in the fibre geometry resulted in varying tensile strength of the subspecimens. These showed increased tensile strength in the bottom and back parts and a decreased tensile strength in the top and front parts. This is consistent with findings in [114, 115]. Specimen height appears to be the most determining parameter followed by

specimen length. Specimen width seems to be less important. Such tests may also reveal to what extent the mechanical strength of a large specimen can be inferred from information on the subspecimens.

Furthermore, we presented a tensile behaviour prediction model of UHPFRC-specimens and a stochastic fibre model. The prediction model is based on statistical information about the fibre system and extensive single fibre pull-out tests. We calibrated the model on the results of experimental uniaxial tensile tests. The stochastic fibre model generates fibre systems (Boolean model of straight cylinders) of virtual specimens. The fibre orientation distribution is represented by a one-parametric distribution family. Its parameter β controls the anisotropy of the fibre orientation. Estimators for β are presented and compared. For users in civil engineering the *method of moments* estimator $\hat{\beta}_{c,mom}$ is a good choice since it estimates accurately, no numerical method is required (like a gradient descent algorithm in [116]) and only the fibre angles in 2D cross-sections are needed. The latter means that fibre orientations observed in a crack are sufficient to estimate the anisotropy parameter β for the stochastic fibre model. The presented prediction model uses the stochastic fibre model combined with a statistical analysis and modelling of the single fibre pull-out tests. Predictions are calibrated by using experimental tensile curves. Furthermore, performing the prediction on virtual specimens with varied production parameters resulted in reasonable stress-strain curves.

Bibliography

[1] Matheron G. *Random sets and integral geometry*. Wiley New York, 1974.

[2] Serra J. *Image Analysis and Mathematical Morphology*. Academic Press, Inc., USA, 1983.

[3] Serra J. *Image Analysis and Mathematical Morphology. Volume 2: Theoretical Advances*. Academic Press, Inc., 1988.

[4] Soille P. *Morphological Image Analysis: Principles and Applications*. Springer-Verlag, Berlin, Heidelberg, 2 edition, 2003.

[5] Sternberg S. Grayscale morphology. *Computer Vision, Graphics, and Image Processing*, 35(3):333–355, 1986.

[6] Ronse C. Why mathematical morphology needs complete lattices. *Signal Processing*, 21(2):129–154, 1990.

[7] Goutsias J., Heijmans H., and Sivakumar K. Morphological operators for image sequences. *Comput. Vis. Image Underst.*, 62:326–346, 1995.

[8] Velasco-Forero S. and Angulo J. Random projection depth for multivariate mathematical morphology. *IEEE Journal of Selected Topics in Signal Processing*, 6(7):753–763, 2012.

[9] Liu R. Y. and Singh K. Ordering Directional Data: Concepts of Data Depth on Circles and Spheres. *The Annals of Statistics*, 20(3):1468 – 1484, 1992.

[10] Pandolfo G., Paindaveine D., and Porzio G. Distance-based depths for directional data. *Canadian Journal of Statistics*, 46, 09 2017.

[11] Ley C., Sabbah C., and Verdebout T. A new concept of quantiles for directional data and the angular Mahalanobis depth. *Electronic Journal of Statistics*, 8(1):795 – 816, 2014.

[12] Roerdink J.B.T.M. Mathematical morphology on the sphere. In Murat Kunt, editor, *Visual Communications and Image Processing '90: Fifth in a Series*, volume 1360, pages 263 – 271. International Society for Optics and Photonics, SPIE, 1990.

[13] Peters II R. A. Mathematical morphology for angle-valued images. In Edward R. Dougherty and Jaakko T. Astola, editors, *Nonlinear Image Processing VIII*, volume 3026, pages 84 – 94. International Society for Optics and Photonics, SPIE, 1997.

[14] Hanbury A.G. and Serra J. Morphological operators on the unit circle. *IEEE Transactions on Image Processing*, 10(12):1842–1850, 2001.

[15] Frontera-Pons J. and Angulo J. Morphological operators for images valued on the sphere. In *2012 19th IEEE International Conference on Image Processing*, pages 113–116, 09 2012.

[16] Andrew P. Witkin. Scale-space filtering. In *International Joint Conferences on Artificial Intelligence*, 1983.

[17] Jackway P. Morphological scale-spaces. In Peter W. Hawkes, editor, *Morphological Scale-Spaces*, volume 99 of *Advances in Imaging and Electron Physics*, pages 1–64. Elsevier, 1997.

[18] Jackway P. Morphological scale-space. In *Proceedings., 11th IAPR International Conference on Pattern Recognition. Vol. III. Conference C: Image, Speech and Signal Analysis,*, pages 252–255, 1992.

[19] Heijmans H.J.A.M. and van den Boomgaard R. Algebraic framework for linear and morphological scale-spaces. *Journal of Visual Communication and Image Representation*, 13(1):269–301, 2002.

[20] Vachier C. Morphological scale-space analysis and feature extraction. In *Proceedings 2001 International Conference on Image Processing (Cat. No.01CH37205)*, volume 3, pages 676–679 vol.3, 2001.

[21] Welk M. Families of generalised morphological scale spaces. In Lewis D. Griffin and Martin Lillholm, editors, *Scale Space Methods in Computer Vision*, pages 770–784, Berlin, Heidelberg, 2003. Springer Berlin Heidelberg.

[22] Angulo J. Morphological Scale-Space Operators for Images Supported on Point Clouds. In Springer-Verlag Berlin Heidelberg, editor, *5th International Conference on Scale Space and Variational Methods in Computer Vision*, volume LNCS 9087 of *Proc. of SSVM'15 (5th International Conference on Scale Space and Variational Methods in Computer Vision)*, Lège-Cap Ferret, France, June 2015.

[23] Fletcher P., Venkatasubramanian S., and Joshi S. Robust statistics on riemannian manifolds via the geometric median. *26th IEEE Conference on Computer Vision and Pattern Recognition, CVPR*, pages 1–8, 06 2008.

[24] Heijmans H.J.A.M. *Morphological Image Operators*. Advances in electronics and electron physics: Supplement. Academic Press, 1994.

[25] Blumenson L. E. A derivation of n-dimensional spherical coordinates. *The American Mathematical Monthly*, 67(1):63–66, 1960.

[26] Mardia K. V. and P. E. Jupp. *Directional Statistics*. Wiley, New York, 1999.

[27] García-Portugués E., Paindaveine D., and Verdebout T. On optimal tests for rotational symmetry against new classes of hyperspherical distributions. *Journal of the American Statistical Association*, 115(532):1873–1887, 2020.

[28] Zuo Y. and Serfling R. General notions of statistical depth function. *The Annals of Statistics*, 28(2):461 – 482, 2000.

[29] Tukey J. W. Mathematics and the picturing of data. In *Proceedings of the International Congress of Mathematicians (Vancouver, B. C., 1974)*, volume 2, page 523–531, 1975.

[30] Liu R. On a Notion of Data Depth Based on Random Simplices. *The Annals of Statistics*, 18(1):405 – 414, 1990.

[31] Donoho D. and Gasko M. Breakdown properties of location estimates based on halfspace depth and projected outlyingness. *Ann. Stat.*, 20, 12 1992.

[32] Vardi Y. and Zhang C. The multivariate l1-median and associated data depth. *Proceedings of the National Academy of Sciences of the United States of America*, 97:1423–6, 03 2000.

[33] Fisher N.I. Spherical medians. *Journal of the Royal Statistical Society. Series B (Methodological)*, 47(2):342–348, 1985.

[34] Fisher N.I., Lewis T., and Embleton B.J.J. *Statistical Analysis of Spherical Data*. Cambridge University Press, 1987.

[35] Koenker R. *Quantile Regression*. Cambridge University Press, 2005.

[36] Linglong Kong and Ivan Mizera. Quantile tomography: Using quantiles with multivariate data. *Statistica Sinica*, 22(4):1589–1610, 2012.

[37] Najman L. and Talbot H. *Mathematical Morphology: from theory to applications*. ISTE-Wiley, June 2010.

[38] Strömberg T. *The operation of infimal convolution*. Instytut Matematyczny Polskiej Akademi Nauk, 1996.

[39] Nogatz T., Redenbach C., and Schladitz K. 3d optical flow for large ct data of materials microstructures. *Strain*, page e12412, 2021.

[40] Kelker D. Distribution theory of spherical distributions and a location-scale parameter generalization. *Sankhyā: The Indian Journal of Statistics, Series A (1961-2002)*, 32(4):419–430, 1970.

[41] Cambanis S., Huang S., and Simons G. On the theory of elliptically contoured distributions. *Journal of Multivariate Analysis*, 11(3):368–385, 1981.

[42] Fang K., Kotz S., and Ng K. *Symmetric multivariate and related distributions*. Chapman & Hall, 1990.

[43] Leong P. and Carlile S. Methods for spherical data analysis and visualization. *Journal of Neuroscience Methods*, 80(2):191–200, 1998.

[44] Kent J. The Fisher-Bingham distribution on the sphere. *Journal of the Royal Statistical Society. Series B (Methodological)*, 44(1):71–80, 1982.

[45] Bahadur R. R. A Note on Quantiles in Large Samples. *The Annals of Mathematical Statistics*, 37(3):577 – 580, 1966.

[46] Pennec X. Intrinsic statistics on riemannian manifolds: Basic tools for geometric measurements. *Journal of Mathematical Imaging and Vision*, 25:127–154, 07 2006.

[47] Härdle W. and Simar L. *Applied Multivariate Statistical Analysis*. Springer-Verlag Berlin Heidelberg, 2003.

[48] Maryamh K., Hauch K., Redenbach C., and Schnell J. Influence of production parameters on the fiber geometry and the mechanical behavior of ultra high performance fiber-reinforced concrete. *Structural Concrete*, 22(1):361–375, 2021.

[49] Watson G.S. *Statistics on Spheres*. Wiley, New York, 1983.

[50] Tu L. W. *An Introduction to Manifolds*. Springer-Verlag, New York, 2011.

[51] Hauberg S. Directional statistics with the spherical normal distribution. *18th International Conference on Information Fusion*, pages 704–711, 07 2018.

[52] Bishop Y.M.M., Holland P., and Fienberg S.E. Discrete multivariate analysis: Theory and practice. 1975.

[53] Tsagris M., Athineou G., Sajib A., Amson E., and Waldstein M. J. *Directional: A Collection of R Functions for Directional Data Analysis*, 2021. R package version 5.0.

[54] Rao Jammalamadaka S. and Sengupta A. *Topics in Circular Statistics*. WORLD SCIENTIFIC, 2001.

[55] Fehling E., Schmidt M., Teichmann T., Bunje K., Bornemann R., and Middendorf B. *Entwicklung, Dauerhaftigkeit und Berechnung Ultrahochfester Betone (UHPC). Schriftenreihe Baustoffe und Massivbau, Heft Nr. 1*. kassel university press GmbH, 2005.

[56] Hoàng K. H. and Hadl P. A new mix design method for UHPC based on stepwise optimization of particle packing density. *First International Interactive Symposium on UHPC*, 2016.

[57] Stürwald S. *Rissentwicklung bei kombiniert bewehrten UHPC-Balken. 53. Forschungskolloquim DAfStb*. kassel university press GmbH, 2008.

[58] Leutbecher T. *Rissbildung und Zugtragverhalten von mit Stabstahl und Fasern bewehrtem Ultrahochfesten Beton (UHPC)*. kassel university press GmbH, 2008.

[59] DAfStb-Heft 561. *Sachstandsbericht Ultrahochfester Beton*. Beuth, 2008.

[60] Fröhlich S. and Schmidt M. *Rheologische Eigenschaften von Faserhaltigem Ultrahochfesten Beton. 53. Forschungskolloquim DAfStb*. kassel university press GmbH, 2008.

[61] Wille K. and Parra-Montesinos G. J. Effect of beam size, casting method, and support condition on flexural behavior of ultra-high-performance fibre-reinforced concrete. *ACI Materials Journal/May-June*, 109(3), 2012.

[62] Schnell J., Schladitz K., and Frank S. Richtungsanalyse von Fasern in Betonen auf Basis der Computer-Tomographie. *Beton- und Stahlbetonbau*, 105:72 – 77, 2010.

[63] Lange J., Rauscher S., Benning W., and Hegger J. Ellipsen- und Kreisdetektion zur Bestimmung der Orientierung von Stahl- und Glasfasern in Beton. *Tm-technisches Messen*, 75:529–536, 2008.

[64] Scheffler B. and Schmidt M. *Application of Ultra-High Performance Concrete for Multifunctional Road Pavements. In: Proceedings of Hipermat 2012 - 3rd International Symposium on UHPC and Nanotechnology for High Performance Construction Materials*. kassel university press GmbH, 2012.

[65] Rui Wang, Xiaojian Gao, Huanghuang Huang, and Guangshuai Han. Influence of rheological properties of cement mortar on steel fiber distribution in uhpc. *Construction and Building Materials*, 144:65 – 73, 2017.

[66] Stähli P., Custer R., and van Mier JGM. On flow properties, fibre distribution, fibre orientation and flexural behaviour of frc. *Mater Struct*, 41:189–196, 2008.

[67] Vandewalle L., Heirman G., and Van Rickstal F. Fibre orientation in self-compacting fibre reinforced concrete. In *Proceedings of the 7th international RILEM symposium on fibre reinforced concrete: design and applications*, pages 719–728, 2008.

[68] Ferrara L., Ozyurt N., and di Prisco M. High mechanical performance of fibre reinforced cementitious composites: the role of "casting-flow induced" fibre orientation. *Mater Struct*, 44:109–128, 2011.

[69] Larsen I.L. and Thorstensen R.T. The influence of steel fibres on compressive and tensile strength of ultra high performance concrete: A review. *Construction and Building Materials*, 256:119459, 2020.

[70] Goran H. Mahmud, Zhenjun Yang, and Aram M.T. Hassan. Experimental and numerical studies of size effects of ultra high performance steel fibre reinforced concrete (uhpfrc) beams. *Construction and Building Materials*, 48:1027 – 1034, 2013.

[71] Nguyen D.L., Kim D.J., Ryu G.S., and Koh K.T. Size effect on flexural behavior of ultra-high-performance hybrid fiber-reinforced concrete. *Composites Part B: Engineering*, 45(1):1104 – 1116, 2013.

[72] Sadegh K. and Adam L. Influence of specimen size and fiber content on mechanical properties of ultra-high-performance fiber-reinforced concrete. *Aci Materials Journal*, 109:675–684, 11 2012.

[73] Fládr J. and Bílý P. Specimen size effect on compressive and flexural strength of high-strength fibre-reinforced concrete containing coarse aggregate. *Composites Part B: Engineering*, 138:77 – 86, 2018.

[74] Yoo D., Banthia N., Kang S., and Yoon Y. Size effect in ultra-high-performance concrete beams. *Engineering Fracture Mechanics*, 157:86 – 106, 2016.

[75] Weibull W. A statistical distribution function of wide applicability. *Journal of Applied Mechanics*, 18:293–297, 1951.

[76] Bažant Z.P. Size effect in blunt fracture: Concrete, rock, metal. *Journal of Engineering Mechanics*, 110(4):518–535, 1984.

[77] Bažant Z.P. and Kazemi M. Determination of fracture energy, process zone length and brittleness number from size effect, with application to rock and concrete. *International Journal of Fracture*, 44:111–131, 1990.

[78] Maryamh K., Hauch K., Redenbach C., and Schnell J. Influence of specimen size on the fibre geometry and tensile strength of ultra-high-performance fibre-reinforced concrete. *Structural Concrete*, pages 1–14, 2021.

[79] Lee Y., Kang S.-T., and Kim J.-K. Pullout behavior of inclined steel fiber in an ultra-high strength cementitious matrix. *Construction and Building Materials*, 24(10):2030 – 2041, 2010.

[80] Jones P. A., Austin S. A., and Robins P. J. Predicting the flexural load–deflection response of steel fibre reinforced concrete from strain, crack-width, fibre pull-out and distribution data. *Materials and Structures*, 41:449–463, 2008.

[81] Naaman A.E., Namur G.G., Alwan J.M., and Najm H.S. Fiber pullout and bond slip. i: Analytical study. *Journal of Structural Engineering*, 117(9):2769–2790, 1991.

[82] Naaman A.E., Namur G.G., Alwan J.M., and Najm H.S. Fiber pullout and bond slip. ii: Experimental validation. *Journal of Structural Engineering*, 117(9):2791–2800, 1991.

[83] Shandarov Z., Mäder E., and Gohs U. Why should the "alternative" method of estimating local interfacial shear strength in a pull-out test be preferred to other methods? *Materials*, 11:2406, 11 2018.

[84] H-. Lee, Vimonsatit S., Mendis P., and Nassif A. Study of strain-hardening behaviour of fibre-reinforced alkali-activated fly ash cement. *Materials*, 12:23, 12 2019.

[85] Piggott M.R. The single-fibre pull-out method: its advantages, interpretation and experimental realization. *Composite Interfaces*, 1(3):211–223, 1993.

[86] Choi M.S., Kang S.-T., Lee B.Y, Koh K.-T., and Ryu G-S. Improvement in predicting the post-cracking tensile behavior of ultra-high performance cementitious composites based on fiber orientation distribution. *Materials*, 9(10), 2016.

[87] Moradi M., Bagherieh A. R., and Esfahani M. R. Tensile modeling of steel fiber reinforced concrete. *Asian Journal of Civil Engineering*, 20:269–280, 2019.

[88] Yoo D.-Y., Kang S.-T., and Yoon Y.-S. Effect of fiber length and placement method on flexural behavior, tension-softening curve, and fiber distribution characteristics of uhpfrc. *Construction and Building Materials*, 64:67–81, 2014.

[89] Habel K. and Gauvreau P. Response of ultra-high performance fiber reinforced concrete (uhpfrc) to impact and static loading. *Cement and Concrete Composites*, 30(10):938–946, 2008.

[90] Wille K., Tue N., and Parra-Montesinos G. Fiber distribution and orientation in uhp-frc beams and their effect on backward analysis. *Materials and Structures*, 47:1825–1838, 11 2013.

[91] Yoo D.-Y., Lee J.-H., and Yoon Y.-S. Effect of fiber content on mechanical and fracture properties of ultra high performance fiber reinforced cementitious composites. *Composite Structures*, 106:742–753, 2013.

[92] Kang S.-T., Lee Y., Park Y.-D., and Kim J.-K. Tensile fracture properties of an ultra high performance fiber reinforced concrete (uhpfrc) with steel fiber. *Composite Structures*, 92(1):61–71, 2010.

[93] Wuest J., Denarié E., and Brühwiler E. Model for predicting the uhpfrc tensile hardening response. *The Second International Symposium on Ultra High Performance Concrete, Kassel*, 01 2008.

[94] Kang S.-T. and Kim J.-K. The relation between fiber orientation and tensile behavior in an ultra high performance fiber reinforced cementitious composites (uhpfrcc). *Cement and Concrete Research*, 41:1001–1014, 10 2011.

[95] Li V.C., Wang Y., and Backer S. Effect of inclining angle, bundling and surface treatment on synthetic fibre pull-out from a cement matrix. *Composites*, 21(2):132 – 140, 1990.

[96] Yoo D.-Y., Banthia N., and Yoon Y.-S. Predicting the flexural behavior of ultra-high-performance fiber-reinforced concrete. *Cement and Concrete Composites*, 74:71 – 87, 2016.

[97] Kruschwitz S., Oesch T., Mielentz F., Meinel D., and Spyridis P. Non-destructive multi-method assessment of steel fiber orientation in concrete. *Applied Sciences*, 12(2), 2022.

[98] Matthes S., Ballani F., and Stoyan D. Modelling post-crack tension-softening behavior of fiber-reinforced materials. *Probabilistic Engineering Mechanics*, 45:157 – 163, 2016.

[99] AFGC Recommendation. Recommendations; association francais de genie civil (afgc). *Documents scientifiques et technique; Ultra High Performance Firbre-Reinforced Concrete.*, 2013.

[100] Department of Image Processing Fraunhofer Institute for Industrial Mathematics ITWM. *MAVI – Modular Algorithms for Volume Images*. Kaiserslautern, Germany.

[101] Fraunhofer ITWM. ToolIP tool for image processing. `itwm.fraunhofer.de/toolip`, 2020. Accessed: 2020-06-02.

[102] Herman G.T. Correction for beam hardening in computed tomography. *Physics in Medicine and Biology*, 24(1):81–106, jan 1979.

[103] Soille P. *Morphological Image Analysis*. Springer-Verlag, 2004.

[104] Otsu N. A threshold selection method from gray-level histograms. *IEEE Transactions on Systems, Man, and Cybernetics*, 9(1):62–66, 1979.

[105] Danielsson P. Euclidean distance mapping. *Computer Graphics and Image Processing*, 14(3):227 – 248, 1980.

[106] Chiu S.N., Stoyan D., Kendall W.S., and Mecke J. *Stochastic Geometry and Its Applications*. Wiley Series in Probability and Statistics. Wiley, 2013.

[107] Heckel F., Meine H., and Moltz J.H. et al. Segmentation-based partial volume correction for volume estimation of solid lesions in CT. *IEEE Transactions on Medical Imaging*, 33(2):462–480, 2014.

[108] R Core Team. *stats: R statistical functions*. R Foundation for Statistical Computing, Vienna, Austria, 2019.

[109] Pastorelli E. and Herrmann H. Time-efficient automated analysis for fibre orientations in steel fibre reinforced concrete. *Proceedings of the Estonian Academy of Sciences*, 65:28–36, 01 2016.

[110] Wirjadi O., Schladitz K., Easwaran P., and Ohser J. Estimating fibre direction distributions of reinforced composites from tomographic images. *Image Analysis and Stereology*, 35(3):167–179, 2016.

[111] Prudencio L., Austin S., Jones P., Armelin H., and Robins P. Prediction of steel fibre reinforced concrete under flexure from an inferred fibre pull-out response. *Materials and Structures*, 39(6):601–610, 2006.

[112] Gudžulić V., Dang T.S., and Meschke G. Computational modeling of fiber flow during casting of fresh concrete. *Comput Mech*, 63:1111–1129, 2019.

[113] Kang S. and Kim J. Numerical simulation of the variation of fiber orientation distribution during flow molding of ultra high performance cementitious composites (uhpcc). *Cement and Concrete Composites*, 34(2):208 – 217, 2012.

[114] Herrmann H., Goidyk O., Naar H., Tuisk T., and Braunbrück A. The influence of fiber orientation in self-compacting concrete on 4-point bending strength. *Proceedings of the Estonian Academy of Sciences*, 68:337–346, 08 2019.

[115] Leutbecher T. and Rebling J. Experimentelle untersuchungen zur ableitung der zentrischen nachrisszugfestigkeit von uhfb aus biegeversuchen. *Bauingenieur.*, 93(11):463–472, 2018.

[116] Redenbach C. and Vecchio I. Statistical analysis and stochastic modelling of fibre composites. *Composites Science and Technology*, 71(2):107 – 112, 2011.

[117] Ohser J. and Schladitz K. *3D Images of Materials Structures: Processing and Analysis*. Wiley, 2009.

[118] Li V. C., Wang Y., and Backer S. A micromechanical model of tension-softening and bridging toughening of short random fiber reinforced brittle matrix composites. *Journal of the Mechanics and Physics of Solids*, 39(5):607 – 625, 1991.

[119] Torquato S. *Random Heterogeneous Materials: Microstructure and Macroscopic Properties*. Springer, 2002.

[120] Franke J., Redenbach C., and Zhang N. On a mixture model for directional data on the sphere. *Scandinavian Journal of Statistics*, 43(1):139–155, 2016.

[121] Louis A., Riplinger M., Spiess M., and Spodarev E. Inversion algorithms for the spherical radon and cosine transform. *Inverse Problems - INVERSE PROBL*, 27, 03 2011.

[122] Weidemann G., Stadie R., Goebbels J., and Hillemeier B. Computed tomography study of fibre reinforced autoclaved aerated concrete. *Materials Testing*, 50(5):278–285, 2008.

[123] Matthes S. and Stoyan D. Planar sections through three-dimensional line-segment processes. *Image Analysis and Stereology*, 33(1):55–64, 2014.

[124] Fu S.-Y. and Lauke B. Effects of fiber length and fiber orientation distributions on the tensile strength of short-fiber-reinforced polymers. *Composites Science and Technology*, 56(10):1179–1190, 1996.

[125] Piggott M. Short fibre polymer composites: a fracture-based theory of fibre reinforcement. *Journal of Composite Materials*, 28(7):588–606, 1994.

[126] Parviz S. and Lee C. D. Distribution and orientation of fibers in steel fiber reinforced concrete. *Aci Materials Journal*, 87:433–439, 1990.

[127] Xia M., Hamada H., and Maekawa Z. Flexural stiffness of injection molded glass fiber reinforced thermoplastics. *International Polymer Processing*, 10(1):74–81, 1995.

[128] Ohser J. and Mücklich F. *Statistical analysis of microstructures in materials science*. Wiley, 2000.

[129] Markovic I. *High-performance Hybrid-fibre Concrete: Development and Utilisation*. Delft University Press, 2006.

Appendix A

Complement operator based on D_F

Here, we give another approach of a complement operator which is based on D_F. Let $i \in E$ and $x = I(i) \in \mathcal{S}^{d-1}$. We want to remind the reader on

$$D_F(x) = \arg\min_{\tau\in[0,1]}\{c_\tau \geq x^T\mu\}, \tag{A.1}$$

given in (1.28) and the tangent-normal decomposition of a vector $x \in \mathcal{S}^{d-1}$ w.r.t. $\mu \in \mathcal{S}^{d-1}$ given in (1.17)

$$x = (x^T\mu)\mu + (I_d - \mu\mu^T)x = (x^T\mu)\mu + z \tag{A.2}$$

with

$$z = (I - \mu\mu^T)x \tag{A.3}$$

and

$$||z||_2 = \sqrt{1 - (x^T\mu)^2}. \tag{A.4}$$

We define the complement of a pixel value x as

$$\mathrm{C}\, x := c_{1-D_F(x)}\mu + z_{\mathrm{C}} \tag{A.5}$$

with tangential part

$$z_{\mathrm{C}} := -z\frac{\sqrt{1 - c^2_{D_F(\mathrm{C}\, x)}}}{||z||_2}. \tag{A.6}$$

Then,

$$||z_{\mathrm{C}}||_2 \overset{(A.6)}{=} \sqrt{1 - c^2_{D_F(\mathrm{C}\, x)}} \tag{A.7}$$

It holds that

$$\frac{z_{\mathrm{C}}}{||z_{\mathrm{C}}||_2} \overset{(A.6),(A.7)}{=} -\frac{z}{||z||_2}. \tag{A.8}$$

The depth value of $\mathrm{C}\, x$ reads

$$\begin{aligned} D_F(\mathrm{C}\, x) &= D_F(c_{1-D_F(x)}\mu + z_{\mathrm{C}}) && \text{(A.9)}\\ &\overset{(A.1)}{=} \arg\min_{\tau\in[0,1]}\{c_\tau \geq \left(c_{1-D_F(x)}\mu + z_{\mathrm{C}}\right)^T\mu\}, \quad \mu^T\mu = 1,\ \mu^T z = 0 && \text{(A.10)}\\ &= \arg\min_{\tau\in[0,1]}\{c_\tau \geq c_{1-D_F(x)}\} && \text{(A.11)}\\ &= 1 - D_F(x) && \text{(A.12)} \end{aligned}$$

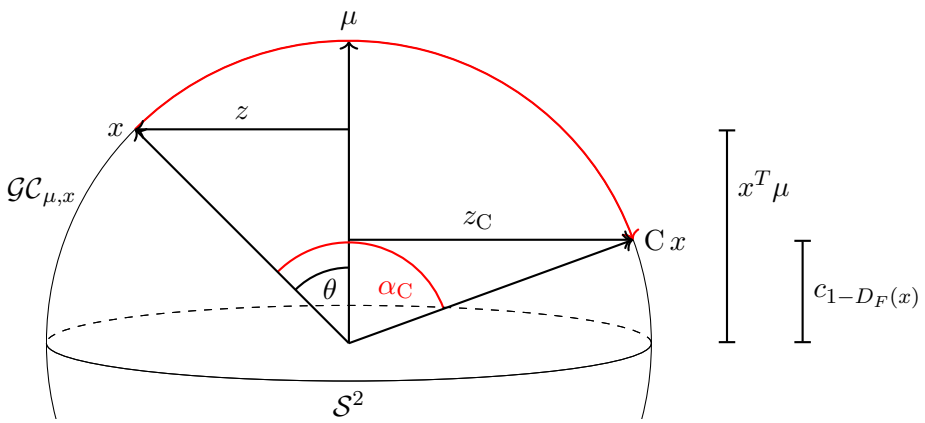

Figure A.1: Construction of complement $\mathrm{C}\,x$ of a unit vector $x \in \mathcal{S}^{d-1}$ using D_F. The angles $\theta = \arccos(x^T\mu)$ and $\alpha_{\mathrm{C}} = \arccos((\mathrm{C}\,x)^T\mu) = \theta + \arccos(c_{1-D_F(x)})$. The tangential parts are $z = (I - \mu\mu^T)x$ and $z_{\mathrm{C}} = (I - \mu\mu^T)\,\mathrm{C}\,x$. By construction $\mathrm{C}\,x$ lies on the great circle $\mathcal{GC}_{\mu,x}$.

where we see an analogy to (1.4) since $\max D_F = 1$. The interpretation of the complement is as follows: Reverse the sign of the tangential vector z and determine the angle between x and Cx by the depth of x. Note that a vector x which is central w.r.t. μ has a complement $\mathrm{C}\,x$ which is less central and vice versa. Figure A.1 illustrates $\mathrm{C}\,x$ and its relation to x for $d = 3$.

Further properties are:

- The complement of $x \in \mathcal{S}^{d-1}$ is again a unit vector $\mathrm{C}\,x \in \mathcal{S}^{d-1}$:

$$\begin{aligned}
||\,\mathrm{C}\,x||_2 &\overset{\text{(A.5),(A.6)}}{=} \left\| c_{1-D_F(x)}\mu - z\frac{||z_{\mathrm{C}}||_2}{||z||_2} \right\|_2 \\
&= \left(c^2_{1-D_F(x)}\mu^T\mu + 0 + 0 + z^T z \frac{||z_{\mathrm{C}}||_2^2}{||z||_2^2} \right)^{\frac{1}{2}} \\
&\overset{\text{(A.6)}}{=} \left(c^2_{1-D_F(x)} + 1 - c^2_{1-D_F(x)} \right)^{\frac{1}{2}} \\
&= 1
\end{aligned}$$

  with $\mu^T\mu = 1$, $\mu^T z = 0$ and $z^T z = ||z||_2^2$.

- The (natural) complement of μ is $-\mu$:

$$\begin{aligned}
\mathrm{C}\,\mu &\overset{\text{(A.5),(A.6)}}{=} c_{1-D_F(\mu)}\mu - z\frac{||z_{\mathrm{C}}||_2}{||z||_2} \\
&= (-1)\cdot\mu + 0_d \\
&= -\mu
\end{aligned}$$

  with $D_F(\mu) = 1$, $c_0 = -1$, $||z_{\mathrm{C}}||_2 \overset{\text{(A.7)}}{=} \sqrt{1 - c^2_{D_F(\mathrm{C}\,\mu)}} \overset{\text{(A.12)}}{=} 0$ and $\frac{z}{||z||_2}$ a unit vector.

- Note that the complement of the complement of x is not necessarily x. This is due to the inequality sign in the definition of D_F. If, however,

$$c_{D_F(x)} = x^T\mu, \tag{A.13}$$

it follows that

$$\begin{aligned}
\mathrm{C}\,(\mathrm{C}\,x) &\overset{(A.5),(A.6)}{=} c_{1-D_F(\mathrm{C}\,x)}\mu - z_{\mathrm{C}}\frac{\sqrt{1-c^2_{D_F(\mathrm{C}(\mathrm{C}\,x))}}}{||z_{\mathrm{C}}||_2} \\
&\overset{(A.12)}{=} c_{1-(1-D_F(x))}\mu - z_{\mathrm{C}}\frac{\sqrt{1-c^2_{1-D_F(\mathrm{C}\,x)}}}{||z_{\mathrm{C}}||_2} \\
&\overset{(A.12)}{=} c_{D_F(x)}\mu - z_{\mathrm{C}}\frac{\sqrt{1-c^2_{D_F(x)}}}{||z_{\mathrm{C}}||_2} \\
&\overset{(A.8)}{=} c_{D_F(x)}\mu + z\frac{\sqrt{1-c^2_{D_F(x)}}}{||z||_2} \\
&\overset{(A.13)}{=} (x^T\mu)\mu + z\frac{\sqrt{1-(x^T\mu)^2}}{||z||_2} \\
&\overset{(A.4)}{=} (x^T\mu)\mu + z \\
&\overset{(A.2)}{=} x.
\end{aligned}$$

The equality $c_{D_F(x)} = x^T\mu$ holds if we assume that $X^T\mu$ (with realisation $x^T\mu$) follows a continuous distribution. For a large number of pixel values, the equality is approximately fulfilled.

- The complement C can also be defined via a rotation matrix. Let $R_{\mu,x} \in SO(d)$ be a rotation matrix which rotates a vector x about $\mu \times x$ with $R_{\mu,x}(\theta)x = \mu$, $\theta = \arccos(x^T\mu)$. Then, $Cx = R_{\mu,x}(\alpha_{\mathrm{C}})x$ with $\alpha_{\mathrm{C}} = \theta + \arccos(c_{1-D_F(x)})$ as illustrated in Figure A.1 for $d = 3$. Note that x is rotated along the great circle $\mathcal{GC}_{\mu,x}$.

We want to examine the effect of this complement operator. For this purpose, we generate a 2-dimensional $\mathcal{S}^2$-valued image with a unit vector in each pixel. Figure A.2a shows such an image I mimicking direction vectors obtained from one fibre on a homogeneous background.. The image contains one object in the middle consisting of vectors with a small angular deviation from μ. This object is part of the image foreground. Vectors aligned more in a plane perpendicular to μ are part of the background. Thus, the image part above and below the object is image background. Figure A.2b shows the application of the complement operator C on I. The vectors of the object are rotated away from μ according to their depth value. The vectors in the two background areas from Figure A.2b are rotated towards μ. As expected, foreground becomes background and vice versa. Figure A.2c shows the application of the complement operator to A.2b. Figure A.2c corresponds nearly to the original image I (except for a few vectors). The reason for the difference lies in the definition of D_F as described in Section 1.3.2. Furthermore, the vectors that differ from the original image do not result in any new objects. No "holes" in the object occur and the shape of the object is not changed. The number of foreground and background vectors in Figure A.2b and Figure A.2c are the same.

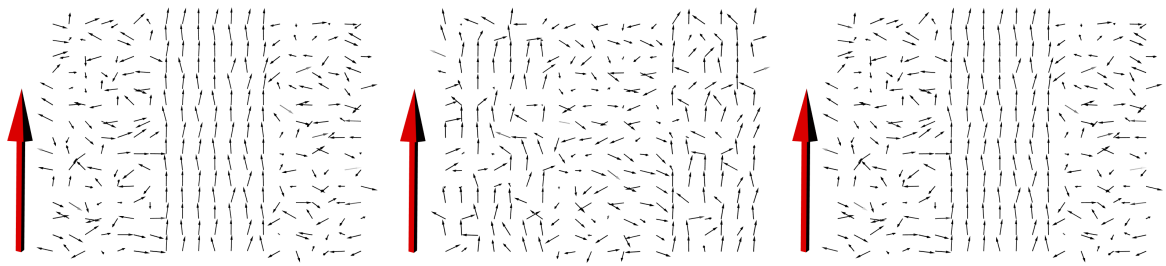

(a) $I \in \mathcal{S}^2$ (b) $\mathrm{C}\, I$ (c) $\mathrm{C}\,\mathrm{C}\, I$

Figure A.2: Original $\mathcal{S}^2$-valued image I (a), complement $\mathrm{C}\, I$ (b), and $\mathrm{C}\,\mathrm{C}\, I$ (c). The object vectors in I are rotationally symmetric around μ (large red vector). Their angular deviation from μ is uniformly drawn from $(0, \pi/8)$. Background vectors are also rotationally symmetric around μ. Their angular deviation from μ is uniformly drawn from $[\pi/8, 7\pi/10]$.

Appendix B

Goodness-of-fit test for $F_0 \in \mathcal{R}_\mu$

The goodness-of-fit test proposed in [11] considers the testing problem

$$H_0 : F = F_0 \text{ for some } F_0 \in \mathcal{R}_\mu \quad against \quad H_1 : F \neq F_0.$$

Consider $\tau = (\tau_1, \ldots, \tau_m) \in (0,1)^m$ and the statistic

$$T_\tau^{(n)} = \sqrt{n}((\hat{c}_{\tau_1} - c^0_{\tau_1}), \ldots, (\hat{c}_{\tau_m} - c^0_{\tau_m}))^T,$$

where $c^0_{\tau_i}$ is the projection quantile of order τ_i. It follows from in Proposition 2.2.3 [11, Proposition 3.2] that, under H_0, $T_\tau^{(n)}$ is asymptotically normal with mean zero and covariance matrix $\Sigma_{T_\tau^{(n)}} = (\Sigma_{i,j}) \in \mathbb{R}^{m\times m}$, with

$$\Sigma_{i,j} = \frac{\min(\tau_i, \tau_j) - \tau_i\tau_j}{f_{0,proj}(c^0_{\tau_i}) f_{0,proj}(c^0_{\tau_j})}, \tag{B.1}$$

where $f_{0,proj}(c^0_{\tau_i})$ stands for the density of the projections under F_0 evaluated at $c^0_{\tau_i}$. Note that the covariance matrix $\Sigma_{T_\tau^{(n)}}$ does not need to be estimated under the null hypothesis. Based on this joint asymptotic normality result which directly follows from the multivariate central limit theorem, a goodness-of-fit test is obtained by rejecting the null (at the nominal asymptotic level α) when

$$Q_\tau^{(n)} = (T_\tau^{(n)})^T \Sigma^{-1}_{T_\tau^{(n)}} T_\tau^{(n)}$$

exceeds the α-upper quantile of the chi-square distribution with m degrees of freedom.

Appendix C

Projected density and covariance matrix for von Mises-Fisher distributed random vectors

For $F_0 = M_3(\mu, \kappa) \in \mathcal{R}_\mu$, a simple expression for the projected density f_{proj} and the covariance matrix $\Sigma_{T_\tau^{(n)}}$ is given in the following.

C.1 Projected density for von Mises-Fisher distributed random vectors

For $X \sim M_3(\mu, \kappa)$ von Mises-Fisher and with Equation (2.14), $y = X^T\mu$ has the projected density

$$\begin{aligned} f_{proj}(y) &\overset{(2.14)}{=} \omega_2 c_{3,f_\mu} f_\mu(y) \\ &\overset{(2.16)}{=} \omega_2 c_{3,f_\mu} \cdot \exp(\kappa y) \\ &\overset{(2.15),(2.18)}{=} \frac{2\pi^{2/2}}{\Gamma(2/2)} \cdot \frac{\kappa^{3/2-1}}{(2\pi)^{3/2} I_{3/2-1}(\kappa)} \cdot \exp(\kappa y) \\ &= \frac{\sqrt{\kappa}}{\sqrt{2\pi} I_{0.5}(\kappa)} \exp(\kappa y). \end{aligned} \tag{C.1}$$

Furthermore, the projection quantile c_τ with $P(X^T\mu \leq c_\tau) = \tau$ is given by

$$\begin{aligned} \tau = P(X^T\mu \leq c_\tau) &\overset{(C.1)}{=} \int_{-1}^{c_\tau} \frac{\sqrt{\kappa}}{\sqrt{2\pi} I_{0.5}(\kappa)} \exp(\kappa y) dy \\ &= \frac{\sqrt{\kappa}}{\sqrt{2\pi} I_{0.5}(\kappa)} \frac{\exp(\kappa c_\tau) - \exp(-\kappa)}{\kappa} \\ \Rightarrow \quad c_\tau &= \frac{1}{\kappa} \log\left(\tau \sqrt{2\pi\kappa} I_{0.5}(\kappa) + \exp(-\kappa)\right) \end{aligned} \tag{C.2}$$

Thus,

$$
\begin{aligned}
f_{proj}(c_\tau) &\overset{\text{(C.1)}}{=} \frac{\sqrt{\kappa}}{\sqrt{2\pi} I_{0.5}(\kappa)} \exp\left(\kappa c_\tau\right) \\
&\overset{\text{(C.2)}}{=} \frac{\sqrt{\kappa}}{\sqrt{2\pi} I_{0.5}(\kappa)} \exp\left(\kappa \frac{1}{\kappa} \log\left(\tau\sqrt{2\pi\kappa} I_{0.5}(\kappa) + \exp\left(-\kappa\right)\right)\right) \\
&= \frac{\sqrt{\kappa}}{\sqrt{2\pi} I_{0.5}(\kappa)} \left(\tau\sqrt{2\pi\kappa} I_{0.5}(\kappa) + \exp\left(-\kappa\right)\right) \\
&= \tau\kappa + \frac{\sqrt{\kappa}}{\sqrt{2\pi}\exp\left(\kappa\right) I_{0.5}(\kappa)} \\
&\overset{*}{=} \tau\kappa + \frac{\kappa \exp\left(-\kappa\right)}{\exp\left(\kappa\right) - \exp\left(-\kappa\right)} \\
&= \kappa\left(\tau + \frac{1}{\exp\left(2\kappa\right) - 1}\right) \qquad \text{(C.3)} \\
&\overset{\kappa \geq 3}{\approx} \kappa\tau.
\end{aligned}
$$

Line $*$ holds by symbolic calculation (e.g. WolframAlpha). For $\kappa \geq 3$, it follows that $\frac{1}{\exp(2\kappa)-1} < 0.0025$.

C.2 Covariance matrix for von Mises-Fisher distributed random vectors

For $F_0 = M_3(\mu, \kappa) \in \mathcal{R}_\mu$, $c^0_{\tau_i}$ is given in (C.2) and $f_{0,proj}(c^0_{\tau_i})$ in (C.3). For large κ, we got a simple expression for the covariance matrix $\Sigma_{T^{(n)}_\tau} = (\Sigma_{i,j})$ in (B.1)

$$
\begin{aligned}
\Sigma_{i,j} &\overset{\kappa \geq 3}{\approx} \frac{\min(\tau_i, \tau_j) - \tau_i\tau_j}{\kappa^2 \tau_i \tau_j} \qquad \text{(C.4)} \\
&= \frac{1}{\kappa^2}\left(\frac{1}{\max(\tau_i, \tau_j)} - 1\right). \qquad \text{(C.5)}
\end{aligned}
$$

Consider w.l.o.g. that $0 < \tau_i < \tau_j < 1$ for $1 \leq i < j \leq m$ such that

$$
\Sigma_{T^{(n)}_\tau} \overset{\text{C.5}}{=} \frac{1}{\kappa^2}\left[\begin{pmatrix} 1/\tau_1 & 1/\tau_2 & \dots & 1/\tau_m \\ 1/\tau_2 & 1/\tau_2 & \dots & 1/\tau_m \\ \vdots & \vdots & \ddots & \vdots \\ 1/\tau_m & 1/\tau_m & \dots & 1/\tau_m \end{pmatrix} - 1_m 1_m^T\right].
$$

Since $x \mapsto 1/x$ tends to $+\infty$ for $x \to 0$ the matrix entries with small indices dominate the others in magnitude. Furthermore, $\kappa \to \infty$ would lead to a singular covariance matrix $\Sigma_{T^{(n)}_\tau}$ if $\max(\tau_i, \tau_j) \not\to 0$. Due to the special form of $\Sigma_{T^{(n)}_\tau}$ its determinant reads

$$
\det\left(\Sigma_{T^{(n)}_\tau}\right) = \frac{1}{\kappa^2}\frac{1-\tau_m}{\tau_1}\prod_{i=1}^{m-1}\frac{\tau_i - \tau_{i+1}}{\tau^2_{i+1}}.
$$

With Cramer's rule it follows that

$$
\Sigma^{-1}_{T^{(n)}_\tau} = \frac{1}{\det\left(\Sigma_{T^{(n)}_\tau}\right)} C^T,
$$

where $C = (C)_{i,j}$ is the matrix of cofactors with $C_{i,j} = (-1)^{i+j} M_{i,j}$, $M_{i,j}$ the (i,j)-minor with $M_{i,j} = \det\left(\left(\Sigma_{T_\tau^{(n)},p,q}\right)_{p\neq i, q\neq j}\right)$. Due to the special form of $\Sigma_{T_\tau^{(n)}}$ its (i,j)-minor is given by

$$M_{ij} = \frac{1-\tau_{\max(I)}}{\tau_{\min(I)}} \prod_{\substack{k=1 \\ i+1, i\neq \max(i,j)}}^{m-1} \frac{\tau_k - \tau_{k+1}}{\tau_{k+1}^2},$$

where $I = \{1,\dots,m\} \setminus \{\max(i,j)\}$.

Appendix D

Single fibre pull-out test results

Table D.1: Median values $s_{el,med}(\theta, l_e), P_{el,med}(\theta, l_e)$ (standard deviations given in brackets), $s_{ult,med}(\theta, l_e)$ (minimum and maximum values given in brackets), $P_{ult,med}(\theta, l_e)$ (standard deviations given in brackets), $s_{tot,med}(\theta, l_e)$. No values for $\mathrm{sd}_{P_{el,med}}$ and $\mathrm{sd}_{P_{ult,med}}$ were determined for the combination $(\theta, l_e) = (80°, l_f/6)$, as only one single fibre pull-out curve could be observed.

(θ, l_e)	$s_{el,med}$ [mm]	$P_{el,med}$ [N]	$s_{ult,med}$ [mm]	$P_{ult,med}$ [N]	$s_{tot,med}$ [mm]
$(0°, l_f/2)$	0.50	39.67 (32.73)	0.97 (0.76, 1.77)	47.52 (27.82)	5.68
$(0°, l_f/3)$	0.03	7.21 (18.80)	0.89 (0.69, 1.04)	53.30 (9.80)	4.82
$(0°, l_f/6)$	0.08	6.50 (13.70)	0.94 (0.46, 1.09)	23.82 (12.95)	1.82
$(10°, l_f/2)$	0.37	56.56 (15.69)	1.12 (0.42, 3.17)	87.52 (19.04)	5.15
$(10°, l_f/3)$	0.51	43.16 (10.30)	1.08 (0.93, 2.13)	52.85 (15.24)	3.82
$(10°, l_f/6)$	0.14	13.95 (15.16)	0.90 (0.60, 1.38)	27.62 (12.53)	2.02
$(20°, l_f/2)$	0.43	44.70 (8.59)	1.12 (0.65, 1.26)	66.68 (12.66)	5.77
$(20°, l_f/3)$	0.06	13.30 (5.93)	0.91 (0.77, 1.00)	39.86 (10.06)	3.46
$(20°, l_f/6)$	0.25	21.00 (4.49)	1.10 (0.73, 1.23)	24.10 (14.07)	1.67
$(30°, l_f/2)$	0.23	30.80 (5.62)	0.99 (0.66, 1.43)	56.90 (10.71)	4.91
$(30°, l_f/3)$	0.37	40.00 (18.23)	1.18 (0.63, 1.42)	52.74 (10.53)	2.61
$(30°, l_f/6)$	0.20	23.74 (9.09)	0.93 (0.83, 1.06)	44.70 (8.77)	1.70
$(40°, l_f/2)$	0.52	50.75 (14.04)	1.13 (0.73, 2.72)	71.35 (14.51)	4.99
$(40°, l_f/3)$	0.03	11.14 (6.63)	1.07 (0.66, 4.13)	63.52 (22.80)	3.45
$(40°, l_f/6)$	0.04	6.20 (8.70)	0.65 (0.28, 1.01)	23.78 (11.54)	1.42
$(50°, l_f/2)$	0.04	11.09 (14.00)	1.57 (1.38, 1.74)	53.34 (16.30)	4.59
$(50°, l_f/3)$	0.07	10.00 (7.70)	1.30 (0.97, 1.92)	44.85 (15.97)	2.48
$(50°, l_f/6)$	0.06	10.00 (27.88)	0.48 (0.35, 0.76)	25.41 (6.46)	0.88
$(60°, l_f/2)$	0.10	14.20 (6.18)	1.40 (1.17, 1.60)	68.25 (13.00)	4.96
$(60°, l_f/3)$	0.06	13.50 (44.59)	1.39 (1.33, 2.96)	56.71 (50.63)	2.60
$(60°, l_f/6)$	0.11	14.80 (5.22)	0.96 (0.63, 1.01)	36.79 (7.57)	1.23
$(70°, l_f/2)$	0.07	11.90 (18.93)	1.77 (1.64, 2.07)	59.29 (10.08)	4.16
$(70°, l_f/3)$	0.11	8.90 (3.87)	1.65 (0.84, 2.19)	44.99 (12.17)	2.51
$(70°, l_f/6)$	0.08	8.52 (3.52)	0.67 (0.38, 1.50)	20.73 (5.80)	1.11
$(80°, l_f/2)$	0.06	9.50 (5.24)	2.39 (1.17, 3.13)	54.94 (22.78)	3.77
$(80°, l_f/3)$	0.53	6.50 (2.81)	0.54 (0.02, 1.31)	7.27 (7.05)	0.69
$(80°, l_f/6)$	0.00	4.54 (-)	0.13 (0.13, 0.13)	4.55 (-)	0.37

Table D.2: Parameter values for $P_{tri}(w, \theta, l_e)$. No value for p_1 was determined for the combination $(\theta, l_e) = (80°, l_f/6)$, as no phase I could be observed.

(θ, l_e)	p_1	p_2	p_3	r_1	r_2
$(0°, l_f/2)$	79.34	16.30	-26.83	31.78	46.58
$(0°, l_f/3)$	250.41	53.42	-31.58	5.67	49.68
$(0°, l_f/6)$	80.25	20.15	-35.99	4.87	21.61
$(10°, l_f/2)$	152.59	41.31	-57.37	41.25	94.03
$(10°, l_f/3)$	84.04	17.14	-41.81	34.35	56.04
$(10°, l_f/6)$	103.13	17.84	-34.24	11.54	24.07
$(20°, l_f/2)$	105.09	31.73	-40.63	31.20	71.22
$(20°, l_f/3)$	207.58	31.36	-29.84	11.29	37.08
$(20°, l_f/6)$	85.4	3.61	-58.37	20.11	29.89
$(30°, l_f/2)$	131.09	34.77	-35.44	22.63	56.39
$(30°, l_f/3)$	107.83	15.81	-66.17	34.13	63.52
$(30°, l_f/6)$	119.58	28.52	-74.70	18.08	39.54
$(40°, l_f/2)$	98.36	33.39	-48.13	33.52	77.35
$(40°, l_f/3)$	404.92	50.37	-54.20	9.75	67.05
$(40°, l_f/6)$	139.23	29.15	-30.17	4.90	10.66
$(50°, l_f/2)$	282.54	27.68	-49.61	10.00	75.59
$(50°, l_f/3)$	151.83	28.24	-69.47	8.14	63.08
$(50°, l_f/6)$	181.48	36.50	-41.19	7.99	-5.04
$(60°, l_f/2)$	136.65	41.59	-54.03	9.88	86.58
$(60°, l_f/3)$	242.58	32.42	-90.14	11.70	86.3
$(60°, l_f/6)$	133.94	25.89	-150.39	11.94	30.63
$(70°, l_f/2)$	175.64	27.91	-69.22	10.01	98.67
$(70°, l_f/3)$	83.08	23.36	-107.43	6.40	98.92
$(70°, l_f/6)$	109.05	20.72	-40.51	6.90	4.34
$(80°, l_f/2)$	152.08	19.49	-121.31	8.28	160.83
$(80°, l_f/3)$	12.28	122.75	-29.50	-58.49	-11.14
$(80°, l_f/6)$	-	0.08	-4.29	4.55	-4.27

The parameters where determined as follows

$$p_1 = \frac{P_{el,med}(\theta, l_e)}{s_{el,med}(\theta, l_e)} \tag{D.1}$$

$$p_2 = \frac{P_{ult,med}(\theta, l_e) - P_{el,med}(\theta, l_e)}{s_{ult,med}(\theta, l_e) - s_{el,med}(\theta, l_e)} \tag{D.2}$$

$$p_3 = \frac{P_{ult,med}(\theta, l_e)}{s_{ult,med}(\theta, l_e) - s_{tot,med}(\theta, l_e)}, \tag{D.3}$$

$$r_1 = P_{el,med}(\theta, l_e) - p_2 \cdot s_{el,med}(\theta, l_e), \tag{D.4}$$

$$r_2 = P_{ult,med}(\theta, l_e) - p_3 \cdot s_{ult,med}(\theta, l_e). \tag{D.5}$$

Scientific career

Publications

- Maryamh, K., Hauch, K., Redenbach, C., Schnell, J.; Influence of production parameters on the fiber geometry and the mechanical behavior of ultra high performance fiber-reinforced concrete. *Structural Concrete*. 2021; doi:10.1002/suco.202000105

- Maryamh, K., Hauch, K., Redenbach, C., Schnell, J.; Influence of specimen size on the fibre geometry and tensile strength of ultra-high-performance fibre-reinforced concrete. *Structural Concrete*. 2021; doi:https://doi.org/10.1002/suco.202000753

- Hauch, K., Maryamh, K., Redenbach, C., Schnell, J.; Predicting the Tensile Behaviour of Ultra-High Performance Fibre-Reinforced Concrete from Single-Fibre Pull-Out Tests. *Materials*. 2022; doi:10.3390/ma15145085

- Hauch, K., Redenbach, C.; Mathematical morphology on directional data. *25th International Conference on Information Fusion*. 2022; https://ieeexplore.ieee.org/document/9841314

Academic background

since October 2017	PhD studies	
	Technische Universität Kaiserslautern	
October 2017	Master thesis	
	Technische Universität Kaiserslautern	
	Title:	»Goodness-of-Fit Tests for Spherical Data«
	Supervisor:	Prof. Dr. C. Redenbach
2015–2017	Master studies in mathematics with minor in physics	
	Technische Universität Kaiserslautern	
September 2015	Bachelor thesis	
	Title:	»Richtungstensoren für parametrische Verteilungsmodelle auf der Sphäre«
	Supervisor:	Prof. Dr. C. Redenbach, Dr. O. Wirjadi and Dr. K. Steiner
2012–2015	Bachelor studies in mathematics with minor in physics	
	Technische Universität Kaiserslautern	
2012	Abitur at Gymnasium Birkenfeld, Birkenfeld	

Akademischer Werdegang

seit Oktober 2017	Promotionsstudium Technische Universität Kaiserslautern
Oktober 2017	Masterarbeit Technische Universität Kaiserslautern *Titel:* »Goodness-of-Fit Tests for Spherical Data« *Betreuer:* Prof. Dr. C. Redenbach
2015–2017	Masterstudium in Mathematik mit Nebenfach Physik Technische Universität Kaiserslautern
September 2015	Bachelorarbeit *Titel:* »Richtungstensoren für parametrische Verteilungsmodelle auf der Sphäre« *Betreuer:* Prof. Dr. C. Redenbach, Dr. O. Wirjadi and Dr. K. Steiner
2012–2015	Bachelorstudium in Mathematik mit Nebenfach Physik Technische Universität Kaiserslautern
2012	Abitur at Gymnasium Birkenfeld, Birkenfeld